



PETROPHYSICS FOR UPSCALING WITH APPLICABILITY TO ASSESSMENT  
OF ENHANCED OIL RECOVERY

Tatiana Lipovetsky

Tese de Doutorado apresentada ao Programa de Pós-graduação em Engenharia Civil, COPPE, da Universidade Federal do Rio de Janeiro, como parte dos requisitos necessários à obtenção do título de Doutor em Engenharia Civil.

Orientadores: Paulo Couto

José Luis Drummond Alves

Luca Moriconi

Rio de Janeiro  
Dezembro de 2020

PETROPHYSICS FOR UPSCALING WITH APPLICABILITY TO ASSESSMENT  
OF ENHANCED OIL RECOVERY

Tatiana Lipovetsky

TESE SUBMETIDA AO CORPO DOCENTE DO INSTITUTO ALBERTO LUIZ  
COIMBRA DE PÓS-GRADUAÇÃO E PESQUISA DE ENGENHARIA DA  
UNIVERSIDADE FEDERAL DO RIO DE JANEIRO COMO PARTE DOS  
REQUISITOS NECESSÁRIOS PARA A OBTENÇÃO DO GRAU DE DOUTOR EM  
CIÊNCIAS EM ENGENHARIA CIVIL.

Orientadores: Paulo Couto

José Luis Drummond Alves

Luca Moriconi

Aprovada por: Prof. Paulo Couto

Prof. José Luis Drummond Alves

Prof. Luca Moriconi

Dra. Elizabeth May Braga Dulley Pontedeiro

Prof. Martinus Theodorus van Genuchten

Prof. Behzad Ghanbarian

Prof. Juliana Souza Baioco

RIO DE JANEIRO, RJ – BRASIL

DEZEMBRO DE 2020

Lipovetsky, Tatiana

Petrophysics For Upscaling with Applicability To  
Assessment of Enhanced Oil Recovery / Tatiana Lipovetsky.

– Rio de Janeiro: UFRJ/COPPE, 2020.

XXXIV, 214 p.: il.; 29,7 cm.

Orientadores: Paulo Couto

José Luis Drummond Alves

Luca Moriconi

Tese (doutorado) – UFRJ/ COPPE/ Programa de  
Engenharia Civil, 2020.

Referências Bibliográficas: p. 160-177.

1. Upscaling. 2. Carbonates. 3. Petrophysics. I. Couto, Paulo  
*et al.* II. Universidade Federal do Rio de Janeiro, COPPE,  
Programa de Engenharia Civil. III. Título.

I dedicate the days and nights spent on this work to my beloved ones:

Tim, for always holding my hand with so much love;

Mom and dad, for allowing me every possible experience;

Grandparents, for being admirable role models;

And my babies, for being an endless source of joy and love.

This work is just as mine as it is yours.

All I do is for you and because of you.

Dedico os dias e noites gastos nesta obra aos meus amados:

Tim, por sempre segurar minha mão com muito amor;

Mãe e pai, por me permitirem todas as experiências possíveis;

Avós, por serem exemplos de vida que tanto admiro;

E meus bebês, por serem uma fonte inesgotável de alegria e amor.

Este trabalho é tão meu quanto de vocês.

## ACKNOWLEDGEMENT

“We should be taught not to wait for inspiration to start a thing. Action always generates inspiration. Inspiration seldom generates action.” by Frank Tibolt

I had no idea what it was going to be like... A PhD transcends science. It evolves not only scientifically and professionally, but personally... How to not acknowledge the ones involved?

I would like to thank my family that stayed back in my hometown, especially my parents, grandparents, puppies and sister. My babies Flor and Polenta, for the constant companion and joyful moments. Thank you for your support, for calming me down when I needed it, for guidance when I asked your help, and for all the love.

I would like to thank “the” very important person, crucial to all what I am and can be, who never stepped away from my side, shared all of my harsh and happy times, faced every challenge with me (and sometimes for me), always brought out the best of me, and never lacked love and patience. Tim, I am really lucky to have you!

My supervisors, Paulo Couto, Luca Moriconi and José Luis Drummond Alves, thank you for making a difference since my Master’s degree! Paulo, thank you for believing in me and encouraging me to dive into any topic I would like to pursue. Thank you for being a caring person, for the opportunity of doing part of my research at Utrecht University, and for funding my attendance at conferences in Brazil and overseas. Luca, thank you for looking so closely at my work, for reading and discussing every aspect of my research, for the hours spent with me on fractals and percolation theory, and for facing my bad moments during research with so much patience. Zé, thank you for being such a spirited person, never letting a mistake pass by, and for being available whenever I needed your feedback. It has been an honor!

Betty May Pontedeiro, you have the gift of guidance! Thank you so much for your friendship, for picking me up from the floor when I was hopeless and full of uncertainties, and for keeping me on track. I will always be grateful for having you as “our Post-Doc”, head of the “Musketeers”. Rien, the famous van Genuchten, I have no words when it

comes to the privilege of having the chance to work with you, and learn directly from you. It has been a pleasure and I am glad to tell everyone that a legend like you was responsible for many of the bricks that built my thesis and knowledge. Austin Boyd, thank you for being our Petrophysics guru, so easy-going and with a broad view. You were always up for any challenge, shared your extremely solid background, and worked hands-on with me on so many different problems. Behzad Ghanbarian, you brought me to a higher level when it comes to upscaling. Thank you for always finding a spot for me in your extremely busy agenda, for looking at my calculations and data, for supervising my laboratory experiments in the USA, for the lessons held in person during the 100<sup>th</sup> AGU meetings in San Francisco and through Skype. Amir Raouf, thank you so much for sharing your expertise with so much energy and enthusiasm, and the hospitality when I arrived in Utrecht. You were always very open for discussing any idea and brainstorming. Luwen Zhuang and Mahin Bagheri, thank you for accepting the challenge to test a rock sample using HYPROP in Utrecht, for sharing your experience on this matter and being so responsive! Wenceslau Teixeira, I really appreciate the afternoons you dedicated to my research on WP4C with rock samples, allowing me to test them at EMBRAPA, and the time dedicated to reading my texts and analyzing my data – it was quite a challenge! I profoundly admire all of you!

During my thesis development I was fortunate to work with incredible people: Rodrigo Bagueira, from UFF, thank you for providing the Indiana Limestone samples and always being open for collaborative work. Giovanna Carneiro, from Schlumberger, thank you for data support and for being so responsive. Santiago Drexler, thank you for guiding me through my first steps in EOR and for still being a friend and professor I could count on! William Godoy, thank you for introducing us to the early aspects of PNM and the Utrecht team! Thanks also to Patrick Corbett from Heriot-Watt University who has been guiding and following my work since 2012, Juan Mateo from CMG, Enno de Vries from UU, Eduardo Ribeiro (who has rescued me several times from my *coding* problems), Bárbara Esteves (my dear friend from the “next desk”), Thais Márcia Silveira (with me since our Schlumberger and MSc days), Carol Dias, Edmilson Rios, Rodrigo Bayão, Denise Nunes, Felipe Eler, Carlos Jr., Adilson Jr., Adriano Rocha, Mateus Ramirez, Thiago Carvalho, Camila Bezerra-Coelho, Gilson Francisco Jr. and Prof. Amaro from the Department of Chemistry, Thiago Pereira and Amanda Ribeiro.

I must not forget to mention my PhD colleagues, brainstorm buddies and dearest friends Fernanda Hoerlle and Maira Lima (“O Bonde do LRAP”, or The LRAP Tram) that were my company and provided loyal friendship during this journey in Brazil and overseas. The three of us and Betty May entitled ourselves “The Musketeers”, a team of girls striving in science through mutual support, hard work and true friendship. You have a very special place in my heart.

I also need to include my lifetime friends and those who I have met while in this journey, that have always cheered for me. You were all essential!

I also would like to thank the TESCAN team in Czech Republic for scanning my samples and for the CoreTOM courses they provided, as well as the CoreLab team in the USA for the laboratory routines. I would also like to thank Ricardo Tadeu and his team (Alessandra Machado, Olga Oliveira and Caio Sorrentino) from LIN/UFRJ, for providing data for my samples with their tomograph. Special thanks to the professors, students and staff from UFRJ, COPPE/UFRJ, PEC/COPPE/UFRJ, LRAP/UFRJ, LAMAS/EMBRAPA, and the Universiteit Utrecht Aardwetenschappen Afdeling (Department of Earth Sciences of the Utrecht University).

My gratitude also goes to CNPq, CAPES and Shell for their financial support. To Frances Abbotts, Jacyra Monteiro and Moisés Silva, from Shell, for all their support during my PhD research. To the examining board for the detailed review and discussions during the defense of this work!

Thank you all for nourishing every crazy idea, for the instructions, meetings during lunch, late night calls, emails, messages, weekend discussions, fun times, laughs and even for the corrections I needed now and then!

Resumo da Tese apresentada à COPPE/UFRJ como parte dos requisitos necessários para a obtenção do grau de Doutor em Ciências (D.Sc.)

PETROFÍSICA PARA UPSCALING COM APLICAÇÃO À AVALIAÇÃO DE  
RECUPERAÇÃO AVANÇADA DE PETRÓLEO

Tatiana Lipovetsky

Dezembro/2020

Orientadores: Paulo Couto

José Luis Drummond Alves

Luca Moriconi

Programa: Engenharia Civil

Este trabalho apresenta métodos de avaliação de amostras de rochas carbonáticas visando a obtenção de *rock typing* de rochas e valores de permeabilidade efetiva em conformidade com seus correspondentes volumes elementares representativos para auxiliar na avaliação da recuperação avançada de petróleo (RAP) em reservatórios. Por meio da coleta de dados experimentais a partir de rotinas petrofísicas, é conduzida uma pesquisa com o fim de caracterizar as formações rochosas e implementar de técnicas de *upscaling*. O resultado é uma integração confiável entre rotinas experimentais, análises matemáticas e simulações computacionais que fornecem informações sobre meios porosos, propostas para apoiar operações de RAP em reservatórios carbonáticos, como as bacias do Pré-sal brasileiro. Este trabalho avalia o uso de várias técnicas de caracterização petrofísica para melhorar o *rock typing* e estimativa de permeabilidade. O objetivo final da pesquisa apresentada é aprimorar os esforços de recuperação de fluidos, extensíveis à técnica de injeção de água-gás alternado (WAG) e outras aplicações de RAP nas formações do Pré-sal no Brasil.



Abstract of Thesis presented to COPPE/UFRJ as a partial fulfilment of the requirements for the degree of Doctor of Science (D.Sc.)

PETROPHYSICS FOR UPSCALING WITH APPLICABILITY TO ASSESSMENT  
OF ENHANCED OIL RECOVERY

Tatiana Lipovetsky

December/2020

Advisors: Paulo Couto

José Luis Drummond Alves

Luca Moriconi

Department: Civil Engineering

This work presents methods for evaluating carbonate rock samples to obtain rock types and effective permeabilities in conformance with their corresponding representative elementary volumes to aid in the enhanced oil recovery (EOR) of oil reservoirs. Experimental data from petrophysical laboratory measurements were analyzed to characterize the formations and evaluation of upscaling techniques. The results integrate experimental routines, mathematical analyses, and computer simulations that provide information on porous media to support EOR operations in carbonate reservoirs, such as the Brazilian Pre-salt basins. This work evaluates the use of several petrophysical characterization techniques to improve rock typing and permeability estimation. The ultimate objective of the presented research was to enhance fluid recovery efforts, extendible to water-alternating-gas (WAG) injection technique, and other EOR applications for the Brazilian Pre-salt formations.

# SUMMARY

|  |          |
|--|----------|
| LIST OF FIGURES.....   | xiii     |
| LIST OF TABLES .....   | xxiv     |
| LIST OF ABBREVIATIONS, SYMBOLS, AND UNITS.....                       | xxvii    |
| <b>1 Introduction.....</b>   | <b>1</b> |
| 1.1 <i>Motivation</i> .....  | 1        |
| 1.2 <i>Thesis proposal</i> .....                                     | 3        |
| 1.3 <i>Objectives</i> .....  | 3        |
| 1.4 <i>Contribution and Originality</i> .....                        | 4        |
| 1.5 <i>Thesis organization</i> .....                                 | 4        |
| <b>2 Literature Review .....</b>                                     | <b>6</b> |
| 2.1 <i>Carbonate rocks</i> .....                                     | 6        |
| 2.1.1 <i>Indiana Limestone</i> .....                                 | 6        |
| 2.2 <i>Porosity</i> .....  | 8        |
| 2.2.1 <i>Dual-porosity systems</i> .....                             | 8        |
| 2.3 <i>Permeability and hydraulic conductivity</i> .....             | 9        |
| 2.4 <i>Formation Factor</i> .....                                    | 10       |
| 2.5 <i>Capillary pressure and wettability</i> .....                  | 11       |
| 2.6 <i>Mercury capillary pressure curve</i> .....                    | 12       |
| 2.7 <i>Evaporation and chilled-mirror dew point techniques</i> ..... | 15       |
| 2.7.1 <i>The van Genuchten-Mualem model</i> .....                    | 16       |
| 2.7.2 <i>The dual-porosity van Genuchten model of Durner</i> .....   | 19       |
| 2.8 <i>Micro-Computerized Tomography</i> .....                       | 20       |
| 2.9 <i>Nuclear Magnetic Resonance</i> .....                          | 23       |
| 2.10 <i>Representative Elementary Volume</i> .....                   | 29       |
| 2.11 <i>Fractals</i> .....   | 31       |

|          |   |           |
|----------|---|-----------|
| 2.11.1   | Linear regression.....  | 37        |
| 2.12     | <i>Permeability models based on The Thomeer Hyperbola .....</i> | 37        |
| 2.13     | <i>Permeability models based on single MICP points .....</i>    | 42        |
| 2.13.1   | Swanson Model .....   | 43        |
| 2.13.2   | Winland Model .....   | 43        |
| 2.14     | <i>Percolation Theory and Critical Path Analysis .....</i>      | 44        |
| 2.14.1   | Background of Critical Path Analysis.....                       | 44        |
| 2.14.2   | Percolation Threshold.....                                      | 47        |
| 2.14.3   | Parametrization of pore size distribution .....                 | 48        |
| 2.14.4   | Single-Phase Permeability from CPA .....                        | 48        |
| 2.14.5   | Critical radius for CPA .....                                   | 51        |
| 2.15     | <i>Pore Network Modeling .....</i>                              | 54        |
| <b>3</b> | <b>Materials and Methods .....</b>                              | <b>58</b> |
| 3.1      | <i>Studied Samples .....</i>                                    | 58        |
| 3.2      | <i>Basic Petrophysics Routine Core Analysis.....</i>            | 58        |
| 3.2.1    | Porosity and Permeability .....                                 | 58        |
| 3.3      | <i>Water retention curve and hydraulic conductivity.....</i>    | 60        |
| 3.3.1    | The HYPROP setup .....  | 61        |
| 3.3.2    | HYPROP hydraulic measurements.....                              | 64        |
| 3.3.3    | WP4C .....  | 65        |
| 3.4      | <i>Imaging techniques.....</i>                                  | 67        |
| 3.4.1    | $\mu$ CT.....   | 67        |
| 3.4.2    | Thin Sections.....  | 72        |
| 3.4.3    | Box Counting.....   | 75        |
| 3.5      | <i>NMR and NMR Fractal dimension.....</i>                       | 79        |
| 3.6      | <i>Permeability computations based on MICP .....</i>            | 81        |
| 3.6.1    | Thomeer-Swanson spreadsheets .....                              | 82        |
| 3.6.2    | Critical Path Analysis.....                                     | 83        |
| 3.7      | <i>Workflow.....</i>  | 85        |
| <b>4</b> | <b>Results and Discussion.....</b>                              | <b>87</b> |
| 4.1      | <i>Routine core analysis and formation factor .....</i>         | 87        |

|          |  |            |
|----------|--|------------|
| 4.2      | <i>Thin Sections</i> .....                                 | 88         |
| 4.3      | <i>REV Permeability Calculations</i> .....                 | 92         |
| 4.3.1    | Thomeer-Swanson spreadsheet permeability.....              | 92         |
| 4.3.2    | Critical Path Analysis Permeability .....                  | 103        |
| 4.3.3    | Summary tables .....                                       | 111        |
| 4.4      | <i>Indiana Limestone High</i> .....                        | 113        |
| 4.4.1    | Basic Petrophysics for IH .....                            | 113        |
| 4.4.2    | Formation Factors for IH.....                              | 114        |
| 4.4.3    | Mercury Porosimetry: pore throat distributions for IH..... | 115        |
| 4.4.4    | Mercury injection for IH permeability estimations .....    | 120        |
| 4.4.5    | NMR Pore Size Distributions.....                           | 134        |
| 4.4.6    | IH Fractal Dimension from NMR.....                         | 141        |
| 4.4.7    | Water retention curve: HYPROP-WP4C.....                    | 143        |
| 4.4.8    | $\mu$ CT Permeability .....                                | 150        |
| 4.4.9    | $\mu$ CT <i>Df</i> .....                                   | 153        |
| <b>5</b> | <b>Conclusions and Considerations</b> .....                | <b>155</b> |
| 5.1      | <i>Future work</i> .....                                   | 159        |
|          | <b>Bibliography</b> .....                                  | <b>160</b> |
|          | <b>Appendix A</b> .....                                    | <b>178</b> |
|          | <b>Appendix B</b> .....                                    | <b>180</b> |

## LIST OF FIGURES

|  |    |
|--|----|
| Figure 1 – SEM photomicrograph of Indiana Limestone 1 (left) and 2 (right), samples studied by CHURCHER <i>et al.</i> (1991). .....  | 7  |
| Figure 2 – Figure showing a dual-porosity porous medium generated with the PoreFlow PNM software (RAOOF & HASSANIZADEH, 2010b). Two porosity subdomains are generated and superimposed: macropores are represented as red pore bodies, while aggregates (micropores) are in blue. Pore throats connect the pore bodies. This image was extracted from DE VRIES <i>et al.</i> (2017). ..... | 9  |
| Figure 3 – Example of a mercury capillary pressure plot showing related saturation parameters. Imaged extracted from CHURCHER <i>et al.</i> , (1991).....  | 12 |
| Figure 4 – Idealization of mercury injection capillary pressure curve shapes. Note that all of the curves have identical displacement pressures and minimum unsaturated (residual) pore volumes but that the saturation profiles would differ dramatically due to differences in pore volumes. ....  | 14 |
| Figure 5 – (A) Nuclear magnetic moments randomly distributed, with no interaction with the static magnetic field (image from DUNN <i>et al.</i> , 1994); (B) Hanson distribution sphere formed by vectors pointing out, for a given number of nuclei when the magnetic moments are transferred to the origin, showing the null result of the system (image from LEVITT, 2001).....         | 24 |
| Figure 6 – Schematic of the spin precession movement of the center $^1\text{H}$ . $B_0$ is represented by the yellow arrow (image from COATES <i>et al.</i> , 1993). ....  | 24 |
| Figure 7 – (A) Spin precession under two energy states: low energy and high energy, (B) schematic design demonstrating preferential alignment of the spins in the direction of $\beta_0$ , (C) resulting magnetization from the $\mu_0$ system due to preferential orientation of the spins (images adapted from COATES <i>et al.</i> , 1993). ....  | 25 |
| Figure 8 – Schematization of the transversal relaxation process, which happens spirally (image adapted from DUNN <i>et al.</i> , 2002).....  | 27 |

|   |    |
|---|----|
| Figure 9 – Schematization of NMR signal generation: the magnetic flow produced during the relaxation process induces an electric current inside the detection coil, which exponentially leaves free induction decay (FID) signals (image adapted from DUNN <i>et al.</i> , 2002).....   | 27 |
| Figure 10 – Definition of the Representative Elementary Volume (REV) for a particular petrophysical parameter (Image from SILVA <i>et al.</i> , 2018). .....  | 30 |
| Figure 11 – In Euclidean geometry, the area of a square varies according to its side length to the second power. ....   | 33 |
| Figure 12 – Generation of a Sierpinski Carpet through iterations. Holes are in black...   | 34 |
| Figure 13 – Section of Sierpinski Carpet .....  | 35 |
| Figure 14 – Comparison of two Euclidean geometry cubes that sample the fractal set. Volume is a function of the lateral length to the $n$ th power (where $n$ is an integer), and a constant that varies with the shape of the object. ....   | 36 |
| Figure 15 – When plotted on log-log axes, the MICP capillary pressure $P_c$ versus bulk volume $BV$ curve generally resembles a hyperbola. ....   | 38 |
| Figure 16 – Left-skewed pore throat histogram (LSPTH), shown in red, derived from MICP data (black) of pressure and incremental bulk volume converted into pore throat diameters (CLERKE; MARTIN, 2004; THOMEER, 1983, 1960). ....  | 39 |
| Figure 17 – The shortest tortuous path from A to B, corresponding to the percolation path of a liquid passing through a porous carbonate rock. The ratio $L_d/L$ for carbonates with angular grains is usually around 2. For rounded grains, the ratio varies between 1.3 and 1.6 (extracted from BUITING & CLERKE, 2013). ....                         | 41 |
| Figure 18 – Plots showing, from left to right, probability density function curves based on Eqs. (2.52), (2.53) and (2.54), respectively. ....  | 46 |
| Figure 19 – MICP experimental results of percolation. The percolation threshold, $P_c$ , occurs at the inflection point of the curve, represented in red, when a sample-spanning cluster formed by mercury-filled pores first emerges. Image has been adapted from DAIGLE (2016). $P_c, Hg$ is the mercury pressure at the critical radius $r_c$ . .... | 48 |

Figure 20 – MICP cumulative mercury saturation curve (Hg Sat) and its first and second derivatives. This graph confirms that the peak of the pore size distribution corresponds to the MICP inflection point of the cumulative saturation curve. .... 52

Figure 21 – Schematic of a network consisting of three pore bodies in each of 13 directions. Numbers inside squares represent the possible throat directions. Numbers without squares represent pore bodies. Only pore body number 14 in the center has its connections (pore throats) to other pores shown. This figure was extracted from RAOOF & HASSANIZADEH (2012, 2010b)..... 56

Figure 22 – Schematic of the HYPROP system as applied to the Indiana limestone sample (adapted from Schindler *et al.*, 2010). .... 62

Figure 23 – (A) Actual sample used for the HYPROP measurements; notice the two drilled holes for the tensiometers. (B) Plugs used to cap the holes after installation of the tensiometers. .... 63

Figure 24 – Pictures of the TESCAN CoreTOM microtomography equipment. FOV stands for field of view, characterizing the area available to scanning (TESCAN, 2020). .... 67

Figure 25 – Picture showing that the resolution of a sample is a function of geometric magnification ( $M$ ), which is the ratio between SDD (source-detector distance) and SOD (source-object distance), X-ray spot size ( $s$ ) and detector pixel size ( $d$ ). Note that it is possible to obtain larger geometric magnifications of smaller samples as long as the sample fully fits in the X-ray cone generated from the X-ray source that reaches the detector, thus allowing better resolutions (TESCAN, 2020). .... 68

Figure 26 – Illustration of ImageJ processing: (A) Limestone blue-stained thin section, showing pores in blue; (B) segmentation procedure using ImageJ, showing pores in red; (C) binary image generated after segmentation, showing pores in black (Courtesy of World Wide Rock Catalog, by CoreLab). .... 73

Figure 27 – Feret numbers of a pore..... 74

Figure 28 – Schematics showing the process of dividing images, starting from the first iteration, and proceeding to the second and third iterations. The image in the center corresponds to  $\mu$ CT section 10 in the XY plane of Indiana Limestone IH-2. Pores are in

black, solid material (rock) is in lighter colors of the grey scale. In this example, the first iteration contains 1 square, and hence only 1 square contains pores. The second iteration has all 4 squares contain pores. The third iteration shows that only 4 out of 16 squares contain pores..... 76

Figure 29 – On the left, a representative zoom showing a division in squares after the  $n$ th iteration (here,  $n=3$ ). The image shows a zoomed shot of slice 1427, in the YZ plane, of an Indiana Limestone IH-2 sample..... 77

Figure 30 – Box counting iterations for divisions that do not return an integer length: (A) the first iteration (in red) works well since no division is made; (B) the second iteration returns a non-integer length. The squares must be replaced by integer-sided ones, leading to the next step; (C) The closes smallest integer is taken by the squares, leaving the image not covered by the boxes (in shaded grey). Hence, more squares of the same lengths must be added; (D) newly added squares of the same length. A similar approach applies to three-dimensional images. .... 78

Figure 31 – Plot of  $\varnothing r^2 \Delta r$  as a function of  $r$ ..... 81

Figure 32 – Log-log plot representing Eq. (3.18). The fractal dimension equals the slope of the straight line (in red). .... 81

Figure 33 – Thesis workflow. The white boxes show the main parameters and outputs of each step, while the pink boxes indicate calculated or measured permeabilities. The red dashed lines indicate routines performed only on Indiana Limestone. .... 86

Figure 34 – Thin section of L20B, zoomed in 128 times before segmentation (A), and after segmentation and binarization (B). Pores are shown by the black color. .... 89

Figure 35 – Pore size distribution curves from a thin section (orange) of L20B (L20 zoomed in 128 times) and MICP (blue) before (A) and after (B) applying the BTR factor to the MICP curve (the BTR, in this case, equals to 8). .... 90

Figure 36 – Results for thin sections L07 (A) and L20B (B) and their contrasts with the MICP data. The pore size distributions (T-Section, in orange) were smoothed (TS5lv1, in grey). Average AR values are shown in yellow. The MICP curve multiplied by BTR (8 in this case) is shown in blue. .... 90



Figure 37 – Plots showing closure corrections (red vertical bars) of zero for sample L20 (A) and 0.20 for sample L05 (B). ..... 93

Figure 38 – Thomeer hyperbola (red dashed lines) fitted to MICP data (black dots) of (A) unimodal sample L20 having G-factor,  $(BV)P_{\infty}$  and  $P_d$  values equal to 0.23, 60 and 32, respectively, and (B) bimodal sample L05 having G-factor,  $(BV)P_{\infty}$  and  $P_d$  values equal to 0.73, 20.30 and 3.06, respectively for PS1, and 0.10, 5.0 and 233, respectively, for PS2. .... 93

Figure 39 – Capillary pressure curves of unimodal sample L20 (A) and bimodal sample L05 (B), showing water saturation values versus water pressure head in feet. .... 94

Figure 40 – The logarithms of the calculated permeabilities are plotted against the logarithms of the measured permeabilities for the full-histogram Thomeer-based approaches discussed above, for the 30 limestone samples. Dashed lines indicate theoretical predictions within a 20% range of precision. .... 95

Figure 41 – Plots showing calculated versus measured permeability values of 30 limestones, assuming the presence of one or two pore systems. Results are for (A) the Thomeer Buiting-Clerke model, (B) the Thomeer Buiting-Clerke integral model and (C) the Thomeer monomodal model. Dashed lines indicate theoretical predictions within a 20% range of precision. .... 95

Figure 42 – Swanson point selection view window for samples L20 (A) and L05 (B). The Swanson point is the highest value of the  $(BV)P_c/P_c$  ratio, located at the peak of the curve. .... 96

Figure 43 – Plot showing Swanson calculated permeabilities of the 30 limestone samples. The number of pore systems (unimodal or bimodal) per sample was obtained according to the best fit of the Thomeer hyperbolae. Dashed lines indicate theoretical predictions within a 20% range of precision. .... 97

Figure 44 – View of the raw and closure corrected  $P_c$  data, and results of the Thomeer fits using up to three pore systems for sample L20 (A) and sample L05 (B). The left axis shows equivalent pressure heads (in feet), the right axis the capillary pressure (in psi), the bottom axis the injected bulk volume, and the top axis mercury saturation. .... 98

Figure 45 – Plot showing Winland calculated permeabilities for the 30 samples. The number of pore systems per sample was obtained according to the best fit of the Thomeer hyperbolae. Dashed lines indicate theoretical predictions within a 20% range of precision. .... 99

Figure 46 – Plot comparing radii corresponding to the Swanson parameter versus Winland radii at the 35<sup>th</sup> percentile for samples with one pore system (unimodal) and two pore systems (bimodal)..... 100

Figure 47 – Critical radii per pore system (red dots) for sample L05. The values of 0.43  $\mu\text{m}$  and 12.55  $\mu\text{m}$  for this case were chosen visually from the peaks of the MICP derived pore size distribution. .... 103

Figure 48 – L05 MICP data as input for RETC (circles), and the fitted van Genuchten equation. The fitted equation enables two different methods for calculating the critical radius: (a) from the inflection point based on Dexter’s equation, and (b) from the fitted  $\alpha$  van Genuchten parameter. .... 104

Figure 49 – Results for (A) independent and (B) self-similar porous systems via the Skaggs CPA calculations, with the critical radius chosen visually from the graph. Dashed lines indicate theoretical predictions within a 20% range of precision. .... 105

Figure 50 - Results for independent (A) and self-similar (B) pore systems via the Skaggs CPA calculations, with the critical radius being equated to the inverse of the van Genuchten  $\alpha$  value. Dashed lines indicate theoretical predictions within a 20% range of precision. .... 105

Figure 51 - Results for independent (A) and self-similar (B) pore systems via the Skaggs CPA calculations, with the critical radius estimated using Dexter’s equation. Dashed lines indicate theoretical predictions within a 20% range of precision..... 106

Figure 52 - Results for independent (A) and self-similar (B) porous systems via the Skaggs CPA calculations, with the critical radius calculated using a fractal approach formula. Dashed lines indicate theoretical predictions within a 20% range of precision. .... 106

Figure 53 – Black circles show the measured data of the water content as a function of the pressure head of a bimodal sample. The black line is the bimodal van Genuchten

equation fitted to the data. The bimodal van Genuchten fitted curve is the sum of contributions from the microporosity system and the macroporosity system. Figure was obtained using the RETC software (VAN GENUCHTEN *et al.*, 1991). ..... 107

Figure 54 - Results for self-similar and independent porous systems via the Skaggs CPA calculations, considering the micro- and macro-pore parts in parallel according to the formation factor defined as in Test A (plot A) and Test B (plot B). Dashed lines indicate theoretical predictions within a 20% range of precision. .... 108

Figure 55 – (A) Dimension of the IH2, IH3 and IH6 plugs. (B) Pictures of the Indiana Limestone plugs..... 113

Figure 56 – Results of mercury (Hg) intrusion and extrusion experiments using the IH2 sample. The graph shows the mercury bulk volume (%) versus injection pressure for intrusion and extrusion. .... 116

Figure 57 – Wetting fluid saturation versus pore throat radius for mercury intrusion and pore body radius from mercury extrusion. During intrusion, the wetting fluid saturation decreases as mercury saturation increases in the pore throats. Afterwards, during extrusion, mercury saturation decreases as water saturation increases in pore bodies. 117

Figure 58 – Pore Throat Size Distribution obtained from intrusion and extrusion of mercury in the IH2 sample. (A) shows incremental volume and (B) shows differential saturation per natural logarithm of differential of pressure. Plot shows mercury intrusion in blue, representing pore throats, and mercury extrusion in orange, representing pore bodies. BTR is given by the ratio between pore body and throat radii from mercury porosimetry tests, equal to 2 for IH2. Dashed line shows intrusion data corrected using a BTR of 2. .... 118

Figure 59 – Indiana Limestone High thin section. Pores are dyed in blue. Scales represent (A) IH1-A with scale in red of 500  $\mu\text{m}$ , (B) IH1-B with scale in red of 0.5 mm and (C) IH1-C with scale in red of 0.5 mm. .... 118

Figure 60 – Thin Section Histograms for IH1-A, IH1-B and IH1-C. .... 119

Figure 61 – Histogram of intruded mercury and thin section analysis (green dashed line) obtained for Indiana High. To match the thin section distributions, intrusion data were multiplied by a factor of 2, equal to the BTR. .... 119

Figure 62 – IH1-A thin section analysis. The green curve shows the histogram (incremental volume distribution) from the image analysis, the blue curve is the 5-level average of the incremental volume distribution, and the yellow curve shows the average aspect ratio per pore diameter..... 120

Figure 63 – IH2 MICP results for the incremental and cumulative intruded pore space, classified according to the pore scale. Graphs provided by Core Laboratories. .... 121

Figure 64 – IH2 permeability distribution according to the mercury injection experiment. Graph provided by Core Laboratories. .... 121

Figure 65 – Incremental bulk volume data versus pore throat diameter for IH2. The graph allows correction and verification of calculated geometric factors. These factors define the shape of the left-skewed Thomeer hyperbola (red dashed line) fitted to the measured data (black dots). Two hyperbolae are apparent, one per pore system..... 122

Figure 66 – Closure correction indicated by the vertical red line. The blue line represents experimental data of IH2. The red dashed line is the left-skewed Thomeer hyperbola fitted to the experimental data..... 123

Figure 67 – Plots of the IH2 capillary pressure, represented in terms of height above a free water level, versus water saturation. .... 123

Figure 68 – Plots of  $BvQ$  ( $\%BV_{occ} CORR$ ) and  $e - 2DfQ$  ( $\exp(-2D\lambda Q)$ ) used for the Buiting-Clerke tortuous and relative fractal tubular bundle integral. The Swanson point is also indicated in this graph. .... 125

Figure 69 – Plot showing that the Swanson point of IH2 can be obtained by finding the coordinates that have the largest  $BV/Pc$  ratio..... 125

Figure 70 – View of the raw, and closure-corrected  $Pc$  data and results for the Thomeer fits using up to three pore systems for IH2. The left axis shows the equivalent pressure head (feet), the right axis the capillary pressure (psi), the bottom axis the injected bulk volume and the top axis mercury saturation. .... 126

Figure 71 – Mercury (A) intrusion and (B) extrusion derivative data. Red points at the peaks correspond to inflection points on the porosimetry curves. .... 128

Figure 72 – MICP results for IH2 compared with NMR data for IH2 and IH3. The curves show normalized values. By matching the MICP and NMR peaks, it was possible to

|   |     |
|---|-----|
| obtain a NMR surface relaxivity, $\rho$ , of 24 $\mu\text{m/s}$ needed to translate relaxation times into radii.....  | 135 |
| Figure 73 – Plots on the left show NMR results of IH2, and plots on the right show NMR results of IH3. A1 and B1: NMR data of amplitude (units of amplitude) versus relaxation time (milliseconds). A2 and B2: NMR data for the incremental porosity (pore units) versus radii (micrometers). A3 and B3: NMR data for the cumulative porosity (%) versus radii (micrometers). The surface relaxivity $\rho$ was 24 $\mu\text{m/s}$ for both IH2 and IH3.....  | 136 |
| Figure 74 – Distribution of pore sizes from tests performed on Indiana Limestone. The MICP curve shows a PSD associated more with the throats. All curves are corrected to the experiment’s porosity, accordingly. NMR has been adjusted according to MICP, with no allowance from BTR ( $\rho = 24 \mu\text{m/s}$ ).....   | 137 |
| Figure 75 – MICP, NMR and Thin Section histograms as a function of pore body radius. The MICP curve was adjusted to show pore bodies with a BTR of 2, and with NMR surface relaxivity ( $\rho$ ) values equal to 24 $\mu\text{m/s}$ for IH3 and 45 $\mu\text{m/s}$ for IH2. All curves were corrected to the experiment’s porosity.....   | 137 |
| Figure 76 – Plots on the left show NMR results of IH2, and plots on the right show NMR results of IH3. A1 and B1: NMR data of amplitude (units of amplitude) versus relaxation time (milliseconds). A2 and B2: NMR data for incremental porosity (pore units) versus radii (micrometers). A3 and B3: NMR data for cumulative porosity (%) versus radii (micrometers). Surface relaxivity $\rho$ of 45 $\mu\text{m/s}$ for IH2 and 34 $\mu\text{m/s}$ IH3.....   | 138 |
| Figure 77 – Indiana Limestone NMR experimental data showing diffusive coupling (e.g., diffusion between large and small pores) for two different simulated NMR results, one of which eliminated diffusive coupling. The vertical axis is the NMR amplitude. This graph was extracted from the work by CARNEIRO <i>et al.</i> (2014). Differently from the study presented in this work, surface relaxivity in their study was equal to 8 $\mu\text{m/s}$ , based on the works by Souza (SOUZA <i>et al.</i> , 2013; SOUZA, 2012). ..... | 141 |
| Figure 78 - Graphical comparison between NMR porosity and corresponding calculated fractal dimension. ....  | 142 |
| Figure 79 – Plots used to estimate the fractal dimension of the micropore and macropore systems of (A) IH2 and (B) IH3. Results do not vary substantially between NMR   |     |

|  |     |
|--|-----|
| measurements, which were obtained after saturation in 2015, after confinement stress in 2017 and after saturation in 2017. ....  | 143 |
| Figure 80 – Observed HYPROP evaporation (circles) and WP4C (triangles) water retention (A) and hydraulic conductivity data as a function of volumetric water content (B) and pF (C). ....  | 145 |
| Figure 81 – Observed HYPROP (circles) and WP4C (triangles) volumetric water retention data fitted with the standard ( $m=1-1/n$ ), and variable (independent $m$ and $n$ ) van Genuchten and PDI hydraulic functions. The plots show results for (A) the unimodal van Genuchten functions, (B) the unimodal PDI functions, (C) the bimodal van Genuchten functions and (D) the bimodal PDI functions.....  | 146 |
| Figure 82 – Comparison between distributions of the HYPROP and WP4C data (black lines), thin section (dark green dashed lines) and (A) mercury extrusion (orange lines) and (B) mercury intrusion (blue lines). ....   | 148 |
| Figure 83 – Observed HYPROP hydraulic conductivity curves fitted with the unimodal and bimodal van Genuchten equations assuming $m=1-1/n$ . ....   | 149 |
| Figure 84 – (A) Sample being prepared for image acquisition using CoreTOM, carried out in Brno, Czech Republic. (B) Image provided by TESCAN during an online seminar held in May 2020, showing how the zoom is done without damaging the sample. ....   | 150 |
| Figure 85 – Segmentation process using the Avizo software. Left image shows a random slice of the IH2 zoom (solid material is in grey color, and pores in black). Right image shows the resulted segmentation (pores are represented in blue).....   | 151 |
| Figure 86 – Illustration of the implementation of boundary condition in POREFLOW to define pores destined for fluid entry and for fluid exit.....  | 152 |
| Figure 87 – ParaView visualization of (A) Representation of pore bodies (spherical pores) and pore throats (cylinders) of the examined cube, with the scale in millimeters (pore radii varied from 4.3 $\mu\text{m}$ to 240 $\mu\text{m}$ , and throat radii from 4.3 $\mu\text{m}$ to 230 $\mu\text{m}$ .) (B) All clusters of connected pores, (C) Largest cluster of connected pores, (D) Pressure distribution, which varied from 100 psi (blue) to 170 psi (red)..... | 153 |
| Figure 88 – Virtual cut (limited by the green marks) inside of the IH2 zoom stack for posterior calculation of the fractal dimension. (A) superior view, (B) interior view on 3-   |     |

D perspective, (C) interior view showing orthogonal slices in the Y plane, (D) cylinder within the cut at the end of the procedure. .... 154

Figure 89 – Fractal dimension calculations using linear fitting.  $N$  is the number of cycles (iterations) and  $L$  the division between the size of the image and the edge of the cube. .... 154

Figure 90 – Normalized incremental saturations or porosities versus pore radius for NMR (yellow and blue) with their respective values of the relaxation time, MICP corrected using BTR (orange), thin section A (green) and HYPROP + WP4C (black). .... 158

## LIST OF TABLES

|  |     |
|--|-----|
| Table 1 – Area calculations for Euclidean geometry. The Euclidean dimension $\tau$ is an integer. ....   | 34  |
| Table 2 – Calculation of fractal dimension $\alpha$ for the Sierpinski Carpet and its components (hole and outer squares) based on a small section of the $n$ th iteration. ....   | 35  |
| Table 3 – Table exemplifying harmonic and arithmetic averages based on resistors ( $R$ ) with the same length ( $l$ ). Similar approaches are applicable to pore throat calculation for estimating the permeability. Pore throat radii control permeability and can be interpreted as resisting flow. .... | 72  |
| Table 4 – Calculations of $N$ and $L$ for 2-D (thin section) and 3-D ( $\mu$ CT) images. ....  | 77  |
| Table 5 – Basic petrophysical data and the formation factor ( $F$ ) of the tested limestones. Porosities ( $\emptyset$ ) are in percentages and the permeabilities ( $k$ ) in milliDarcies. ....   | 88  |
| Table 6 – Summary of the thin section results .....  | 91  |
| Table 7 – Calculated permeabilities* and main parameters of the Thomeer-Swanson and Thomeer-Winland approaches. The number of pore systems was defined according to the Thomeer fitting function which produced the best results for each sample. ....   | 101 |
| Table 8 – Summary of parallelism tests that resulted in the plots of Figure 54. ....   | 107 |
| Table 9 – Results of CPA-based approaches using the independent and self-similar equations of Skaggs .....   | 109 |
| Table 10 – RMSLE values obtained using the implemented Thomeer spreadsheet. ...  | 111 |
| Table 11 – RMSLE calculations for the implemented CPA-based methods. ....  | 111 |
| Table 12 – Average permeability error calculations for the implemented Thomeer spreadsheet. ....   | 112 |
| Table 13 – Average permeability error calculations for the implemented CPA-based methods. ....   | 112 |



|   |     |
|---|-----|
| Table 14 – Poropermeameter data obtained for Indiana Limestone High (IH) cylindrical samples IH2, IH3 and IH6. Permeability tests were performed under a pressure of 500 psi. ....  | 114 |
| Table 15 – Formation and cementation factors of Indiana limestone samples IH2 and IH3 .....   | 114 |
| Table 16 – Formation and cementation factor of Indiana limestone sample IH2 used for the CPA-based approach. ....   | 114 |
| Table 17 – Calculated geometric factors per pore system from MICP performed on Indiana Limestone High using the developed Mathematica® code.....  | 122 |
| Table 18 – Obtained results for the air permeability based on the Thomeer-Swanson and Winland spreadsheet and comparison against permeabilities measured using basic petrophysics done immediately prior to the mercury intrusion experiments. ....   | 127 |
| Table 19 – Summary of Skaggs-CPA air permeability results for the intrusion and extrusion experiments, with the critical radius extracted from differential graph as described in the text.....   | 128 |
| Table 20 – Summary of Skaggs-CPA air permeability results for the intrusion and extrusion experiments, with the critical radius extracted from the differential graph as described above. Results are compared against previous permeability measurements in terms of percentual error..... | 129 |
| Table 21 –The Skaggs-CPA results are compared against the average of permeability measurements from samples IH2, IH3 and IH6 in terms of percentual error. ....   | 129 |
| Table 22 – Summary of best Skaggs-CPA calculation method, based on errors presented, for critical radii ( $r_c$ ) obtained visually from the graphs in Figure 71.....   | 130 |
| Table 23 – Estimated values of the van Genuchten parameter $\alpha$ (inverse of the pressure head) and $h$ (the pressure head) for a bimodal distribution of pore sizes and the equivalent pore radii ( $r$ ).....  | 131 |
| Table 24 – Estimated permeabilities and corresponding errors for the critical radius as estimated from the air entry pressure, considering the medium to be independent and self-similar. ....  | 131 |

|   |     |
|---|-----|
| Table 25 – van Genuchten parameters used for estimating radii at the inflection points and radii based on Dexter’s equation for the macropore and micropore systems. ....   | 131 |
| Table 26 – Estimated permeability values and corresponding errors of the critical radius calculated with Dexter’s equation, considering the medium to be independent and self-similar. ....   | 132 |
| Table 27 – Variables used for the parallelism test based on van Genuchten’s bimodal equation fitted to the IH water retention data. $\emptyset$ is the porosity, $F$ is the formation factor, $w$ and $m$ are van Genuchten parameters, and the subscripts mic and mac represent the micropore and macropore subsystems, respectively. .... | 132 |
| Table 28 – Parallelism test’s estimated permeability values and corresponding errors for critical radius calculated from Dexter’s derivation, for Test A, considering the medium to be independent and self-similar. $F_{mic}$ and $F_{mac}$ were used instead of $F_{total}$ . ....  | 133 |
| Table 29 – Parallelism test’s estimated permeability values and corresponding errors for critical radius calculated using Dexter’s equation for Test B, considering the medium to be independent and self-similar. $F_{total}$ were used instead of $F_{mic}$ and $F_{mac}$ . ....  | 133 |
| Table 30 – Comparison tables of IH2 and IH3 NMR data and corresponding calculated fractal dimensions obtained using Mathematica. Data are shown chronologically from left to right. NMR measurements were obtained (A) after saturation in 2015, (B) after confinement stress in 2017 and (C) after saturation in 2017. ....                | 142 |
| Table 31 – Fitted parameter values for the van Genuchten (VG) and PDI unimodal and bimodal hydraulic formulations assuming the VG constraint that $m=1-1/n$ . Fixed values are indicated by an asterisk (*). ....   | 147 |
| Table 32 – Statistical analysis of the fitted water retention and hydraulic conductivity models. ....   | 147 |

# LIST OF ABBREVIATIONS, SYMBOLS, AND UNITS

## Abbreviations

|               |   |   |
|---------------|---|---|
| <i>AR</i>     | - | Aspect ratio  |
| <i>aveAR</i>  | - | Average Aspect ratio  |
| <i>BTR</i>    | - | Body to throat ratio  |
| <i>AICc</i>   | - | Akaike information criterion that has a correction for small sample sizes |
| <i>CF</i>     | - | Corrected Feret   |
| <i>CFM</i>    | - | Corrected Feret Minimum   |
| <i>CPA</i>    | - | Critical Path Analysis  |
| <i>EOR</i>    | - | Enhanced Oil Recovery   |
| <i>Eq.</i>    | - | Equation  |
| <i>FID</i>    | - | Free induction decay  |
| <i>FR</i>     | - | Frequency radio   |
| <i>IH</i>     | - | Indiana Limestone High  |
| <i>L</i>      | - | Limestone   |
| <i>LSPTH</i>  | - | left skewed pore throat histogram   |
| <i>MICP</i>   | - | Mercury Injection Capillary Pressure                                      |
| <i>NMR</i>    | - | Nuclear Magnetic Resonance  |
| <i>PDF</i>    | - | Probability density function  |
| <i>PNM</i>    | - | Pore-Network Modeling   |
| <i>PSD</i>    | - | Pore size distribution  |
| <i>REV</i>    | - | Representative Elementary Volume  |
| $R^2$         | - | Statistical R-square  |
| <i>RGB</i>    | - | Red-green-blue spectrum   |
| <i>RMSE</i>   | - | Root mean square error  |
| <i>RMSLE</i>  | - | Root mean square log-transformed error                                    |
| <i>SEM</i>    | - | Scanning Electron Microscope  |
| <i>SI</i>     | - | International System  |
| <i>TS</i>     | - | Thin Section  |
| <i>TS5lvl</i> | - | Thin section 5-level averaging  |

|                  |                                 |
|------------------|---------------------------------|
| <i>T-Section</i> | - Thin Section                  |
| <i>WAG</i>       | - Water-Alternating-Gas         |
| <i>μ-CT</i>      | - Micro-computerized Tomography |

## Symbols

|   |   |
|---|---|
| <i>A</i>                                      | - Cross-section area of the column or tube                                  |
| <i>A<sub>s</sub></i>                          | - Surface area  |
| <i>A<sub>p</sub></i>                          | - Cross-sectional area of the porous medium                                 |
| <i>A<sub>N</sub></i>                          | - Normalization constant  |
| <i>a<sub>K</sub></i>                          | - Klein-Nishina coefficient   |
| <i>a</i>                                      | - Constant in Archie's Law (tortuosity factor)                              |
| $\vec{B}_0$                                   | - Magnetic field  |
| $\vec{B}_1$                                   | - Oscillating magnetic field perpendicular to $\vec{B}_0$                   |
| <i>BV</i>                                     | - Bulk volume   |
| $\tilde{B}_v^Q$                               | - Integral transform of the MICP fractional bulk volume BV                  |
| <i>C<sub>s</sub></i>                          | - Curve shape parameter   |
| <i>C<sub>PDF</sub></i>                        | - Constant found by taking the integral of the probability density function |
| <i>c</i>                                      | - Pore geometry dependent coefficient                                       |
| <i>CT</i>                                     | - X-ray numerical values (Hounsfield unit)                                  |
| <i>c<sub>KT</sub></i>                         | - Constant defined by Katz and Thompson for CPA                             |
| <i>c<sub>S</sub></i>                          | - Constants defined by Skaggs for CPA                                       |
| <i>d</i>                                      | - Diameter  |
| <i>d<sub>P<sub>1</sub>P<sub>2</sub></sub></i> | - Euclidean distance between the center of the pores                        |
| <i>D<sub>f</sub></i>                          | - Fractal dimension   |
| <i>E</i>                                      | - Energy  |
| <i>e<sub>h</sub></i>                          | - Relevant spectrum of high energy  |
| <i>e<sub>l</sub></i>                          | - Relevant spectrum of low energy   |
| <i>F</i>                                      | - Formation factor  |
| <i>F<sub>mac</sub></i>                        | - Formation factor related to macropores                                    |

|             |   |   |
|-------------|---|---|
| $F_{mic}$   | - | Formation factor related to micropores                        |
| $F_{total}$ | - | Total formation factor  |
| $f(r)$      | - | Volumetric PDF of pore sizes in the medium                    |
| $G$         | - | Pore geometrical factor                                       |
| $g_a$       | - | Acceleration due to gravity                                   |
| $g$         | - | Conductance   |
| $g_c$       | - | Critical conductance  |
| $g_c^e$     | - | Critical electrical conductance                               |
| $g_c^h$     | - | Critical hydraulic conductance                                |
| $g^e$       | - | Electrical conductance  |
| $g^h$       | - | Hydraulic conductance   |
| $g_{ij}$    | - | Conductance of pore throat ij                                 |
| $g_m$       | - | Macroscopic conductance                                       |
| $h$         | - | Height above the free surface or pressure head                |
| $h_s$       | - | Thickness of homogeneous sample                               |
| $h_p$       | - | Planck's constant   |
| $h_a$       | - | Air entry pressure  |
| $H^+$       | - | Hydrogen proton   |
| $Hg$        | - | Mercury   |
| $\bar{h}^i$ | - | Medial water tension between two evaluated points             |
| $h_j^i$     | - | Water tension at depth j, time i.                             |
| $I$         | - | Remaining intensity after the X-ray passes through the object |
| $I_0$       | - | Incident X-ray intensity                                      |
| $I_p$       | - | Quantum spin number of the nucleus                            |
| $j^e$       | - | Electrical current  |
| $K$         | - | Hydraulic conductivity  |
| $k$         | - | Permeability  |
| $k_{air}$   | - | Air permeability  |
| $k_B$       | - | Boltzmann constant  |
| $k_{BC}$    | - | Buiting-Clerke air permeability                               |
| $k_{cal}$   | - | Calculated permeability                                       |

|             |   |   |
|-------------|---|---|
| $k_{mac}$   | - | Permeability proveniente from macropores  |
| $k_{meas}$  | - | Measured permeability   |
| $k_{mic}$   | - | Permeability proveniente from micropores  |
| $K_s$       | - | Hydraulic conductivity at full saturation   |
| $K_r$       | - | Relative hydraulic conductivity   |
| $k_{total}$ | - | Total permeability of pore systems  |
| $K^i$       | - | Hydraulic conductivity ( $\text{cm h}^{-1}$ )   |
| $L_{SD}$    | - | Distance between source and detector in X-ray   |
| $L_n$       | - | Length of PNM network   |
| $L$         | - | Outer length of the sample (external size)  |
| $l$         | - | Length of object  |
| $l_f$       | - | Size of fractal object  |
| $l_{fl}$    | - | Length in flow direction  |
| $L_d$       | - | Length of the first percolation path or the shortest flow path associated with the largest tube of radius $r_d$ |
| $L_i$       | - | Integer number of divisions   |
| $l_{ij}$    | - | Length of pore throat with a cylindrical cross-section  |
| $m_c$       | - | Cementation exponent (Porosity exponent in Archie's Law)  |
| $m$         | - | van Genuchten parameter   |
| $M_{xy}$    | - | Resulting magnetization on the $x$ - $y$ plane  |
| $M_z$       | - | Final magnetization at the $z$ -axis  |
| $N$         | - | Number of fractal objects   |
| $N_p$       | - | Amount of protons   |
| $N_s$       | - | Number of samples   |
| $n$         | - | van Genuchten parameter (shape factor)  |
| $N_i$       | - | Number of boxes or squares  |
| $P$         | - | Pressure  |
| $P_c$       | - | Capillary pressure  |
| $P_{cr}$    | - | Critical probability from percolation theory  |
| $P_{c,Hg}$  | - | Mercury pressure calculated based on the critical radius of the sample  |
| $P_d$       | - | Extrapolated displacement pressure in Thomeer hyperbola function  |

|             |   |   |
|-------------|---|---|
| $pF$        | - | Logarithm of pressure head (h)  |
| $P_{Hg}$    | - | Mercury capillary pressure  |
| $P_i$       | - | Confinement pressure in core holder   |
| $p_i$       | - | Fluid pressures in pore i   |
| $P_\infty$  | - | Extrapolated infinite capillary pressure  |
| $Q$         | - | Q-domain: $Q=\ln(P)$ , P is pressure  |
| $q$         | - | Fluid's flux  |
| $q_{ij}$    | - | Total volumetric flow rate through pore throat ij                               |
| $q^i$       | - | Water flow in time  |
| $R$         | - | Resistance of resistor  |
| $RF$        | - | Recovery factor   |
| $r$         | - | Radius  |
| $r_0$       | - | Smallest pore radius  |
| $r_{35}$    | - | Pore throat radius at the 35th percentile of pore throat cumulative bulk volume |
| $r_{cap}$   | - | Capillary tube radius   |
| $r_c$       | - | Critical radius   |
| $r_d$       | - | Radius (from diameter d) of breakthrough percolation pore                       |
| $r_i$       | - | Pore radius from discrete distribution  |
| $r_{ij}$    | - | Radius of pore throat with a cylindrical cross-section                          |
| $r_m$       | - | Largest pore radius   |
| $r_{c,mac}$ | - | Critical radius from macropores system  |
| $r_{max}$   | - | Radius of the largest accessible pore in the medium                             |
| $r_{c,mic}$ | - | Critical radius from micropores system  |
| $r_{min}$   | - | Radius of the smallest accessible pore in the medium                            |
| $s$         | - | Shape factor (for cylinder, $s = 2\pi$ )  |
| $S/V$       | - | Geometrical factor which models pore geometry (surface area/volume)             |
| $S_e$       | - | Effective saturation  |
| $S_{Hg}$    | - | Mercury saturation  |
| $S_{o,r}$   | - | Residual oil saturation   |
| $S_{w,irr}$ | - | Irreducible water saturation  |

|           |   |   |
|-----------|---|---|
| $T$       | - | Absolute temperature  |
| $T_1$     | - | Polarization time   |
| $T_2$     | - | Relaxation time   |
| $t^i$     | - | Time  |
| $V$       | - | Volume of pores   |
| $V_s$     | - | Volume of sample  |
| $v$       | - | Fluid's velocity  |
| $\bar{v}$ | - | Average pore velocity   |
| $V_F$     | - | Total volume of the fluid   |
| $V_G$     | - | Total volume occupied by the grains   |
| $V_i$     | - | Volume of the sample, grains, core holder or injected gas   |
| $V_P$     | - | Porous volume   |
| $V_R$     | - | Volume of the rock  |
| $V_t$     | - | Total volume  |
| $w$       | - | van Genuchten parameter for bimodal distribution that defines the proportion between micro and macropores |
| $W(r)$    | - | Probability density function for pore radius distribution   |
| $x, y, z$ | - | Cartesian coordinates of pore   |
| $Z$       | - | Effective atomic number   |
| $z_{c,i}$ | - | Coordination number or pore $i$   |
| $z_i$     | - | Depth of tensiometers   |

## Greek symbols

|                  |   |  |
|------------------|---|--|
| $\alpha$         | - | Shape parameter related to the inverse of the air entry pressure |
| $\beta$          | - | Pore-solid fractal parameter                                     |
| $\Delta P_{PNM}$ | - | Pressure difference between inlet and outlet of the network      |
| $\Delta P$       | - | Pressure drop across the pore                                    |
| $\Delta r$       | - | Radius increment   |
| $\Delta t^i$     | - | Interval time between two evaluation points                      |
| $\Delta V$       | - | Voltage drop across the pore                                     |



|                     |   |   |
|---------------------|---|---|
| $\Delta V^i$        | - | Water loss (cm <sup>3</sup> )                   |
| $\Delta z$          | - | Distance between the tensiometers (cm)          |
| $\varepsilon$       | - | Surface tension                                 |
| $\varepsilon_d$     | - | Detector's efficiency                           |
| $\gamma$            | - | Magnetogyric ratio of the nucleus               |
| $\theta_c$          | - | Interface contact angle                         |
| $\theta$            | - | Water content                                   |
| $\theta_s$          | - | Water content at full saturation                |
| $\theta_r$          | - | Water content at residual saturation            |
| $\mu$               | - | Dynamic viscosity                               |
| $\mu_B$             | - | Linear attenuation coefficient                  |
| $\mu_0$             | - | Liquid magnetization                            |
| $\mu_w$             | - | Water linear attenuation coefficient            |
| $\rho_b$            | - | Bulk density                                    |
| $\rho$              | - | Fluid's density                                 |
| $\rho_s$            | - | Surface relaxivity                              |
| $\rho_{nw}$         | - | Density of non-wetting fluid                    |
| $\rho_w$            | - | Density of wetting fluid                        |
| $\tau$              | - | Euclidean dimension                             |
| $\sigma$            | - | Interfacial tension                             |
| $\sigma_b$          | - | Bulk electrical conductivity                    |
| $\sigma_w$          | - | Electrical conductivity of the saturating fluid |
| $\emptyset$         | - | Porosity  |
| $\emptyset_{mac}$   | - | Porosity related to macropores                  |
| $\emptyset_{mic}$   | - | Porosity related to micropores                  |
| $\emptyset_{total}$ | - | Total porosity                                  |

## Units

|            |   |                           |
|------------|---|---------------------------|
| <i>cm</i>  | - | Centimeter                |
| <i>cP</i>  | - | Centipoise                |
| <i>D</i>   | - | Darcy                     |
| <i>m</i>   | - | Meter                     |
| <i>mm</i>  | - | Millimeter                |
| <i>mD</i>  | - | MilliDarcy                |
| <i>MHz</i> | - | Megahertz                 |
| $\mu m$    | - | Micrometer ( $10^{-6}$ m) |
| <i>H</i>   | - | Hounsfield                |
| <i>kg</i>  | - | Kilogram                  |
| <i>psi</i> | - | Pound per square inch     |

# 1 Introduction

Carbonate reservoirs contain more than 50% of the world's remaining conventional hydrocarbon reserves but have relatively low recovery factors (ADAMS, 2005; ODDONE, 2017, 2018). As the era of “easy oil” (easy exploitation of conventional oil and natural gas) phases out, EOR (Enhanced Oil Recovery) becomes increasingly important to maintain and extend the production of existing oil reservoirs (MASALMEH *et al.*, 2015). It is estimated that a large amount of the original oil in place is left behind when conventional production methods are used to exploit the hydrocarbon. Nevertheless, when applying EOR methods, special attention should be paid to sweep efficiency (efficiency of displacing oil from a formation by a flooding fluid) and thief zones (formations encountered during drilling into which circulating fluids can be lost). The sweeping efficiency may be affected by fingering due to heavier oil viscosities in contrast to injected fluid viscosities, while thief zones are a challenge when formations are very heterogeneous. Therefore, learning how a reservoir might respond to EOR stimulations is of great importance, even if this may take many years of integrated studies before field applications (JING, 2018).

Carbonate reservoirs can be very heterogeneous with often very complex pore systems involving double or even triple porosity (matrix-vug-fracture) and mixed oil-wet characteristics. These characteristics, especially permeability heterogeneity and wettability, tend to significantly change well and reservoir performances due to their impact on capillary pressure, relative permeability and residual oil saturation, which may affect remaining oil distributions, oil recovery rates and the sweep efficiency (MASALMEH *et al.*, 2014, 2015). These various aspects encouraged this study of petrophysical and related parameters, including their upscaling to actual carbonate rock formations to understand better and control EOR processes.

## 1.1 Motivation

The Brazilian National Agency of Petroleum (ANP) stated in a report presented by ODDONE (2018) that by the first semester of 2018, 56% of the country's total production of oil and gas was obtained from pre-salt reservoirs along the South-eastern coast of

Brazil. The ANP report showed that the average recovery factor in Brazil is approximately 21% compared to a worldwide average of 35%. A previous report (ODDONE, 2017) also stated that increasing the recovery factor by 1% would represent an investment of approximately 18 million dollars, leading to an increment of 2.2 billion barrels of oil and an increase in petroleum royalties to 11 billion dollars, as estimated according to the average dollar quotation and the price of a barrel of oil in 2017. The report further stated that in 2016, Brazil accounted for the largest share (32%) of the global deep-water crude oil production. In February 2018, average oil production per well in pre-salt reservoirs was in the order of 17,000 bpd, with other conventional offshore production being 1,632 bpd and onshore 17 bpd. Therefore, it is of crucial importance to understand carbonate formations so as to improve oil recovery (related to the amount of oil extracted from a reservoir) and the fluid extraction efficiency (related to the method chosen for the oil recovery).

Characterizing carbonate reservoirs is a great challenge given their ubiquitous heterogeneity. The Brazilian Pre-salt holds more than 50% of the country's proven oil reserves. Oil production from the pre-salt tripled from 500,000 bbl/d in 2014 to 1,500,000 bbl/d in 2018 (PETROBRAS, 2019). Worldwide, carbonate rocks contain up to 25% of known oil reserves according to BOGGS JR. (2006), representing 50% of the remaining conventional oil reserves according to ADAMS (2005). To optimize production and increase recovery, it is necessary to acquire knowledge regarding the formations involved, including their interaction with fluids such as those used for enhanced oil recovery (EOR). Knowing the properties of a formation is critical for understanding how reservoirs respond to enhanced oil recovery efforts and for increasing recovery factors. Since after a few years of production, a considerable amount of oil remains in the reservoirs and cannot be produced by natural processes, or only partially with the help of well intervention, it is necessary to implement secondary and tertiary recovery methods, such as EOR. Knowing ahead of time how a reservoir and its fluids respond to such methods could substantially increase overall production, minimize energy and capital investments, and reduce pollution. Since oil-bearing carbonate reservoirs are unusually complex, efforts are needed in both industry and academia to increase our understanding of these complex formations, which is key for their optimal development. For these various reasons, research documented in this thesis is focused on improved descriptions

of reservoir properties based on petrophysics, the use representative elementary volumes (REV), and upscaling to field-scale settings.

## **1.2 Thesis proposal**

This thesis evaluates carbonate rock samples with the aim to obtain rock types and effective permeability values in conformance with their corresponding representative elementary volumes to aid in reservoir EOR assessments. For this purpose, experimental data obtained from petrophysical routines are used to characterize the samples and posteriorly used in upscaling techniques. Evaporation and chilled-mirror dew point techniques are employed for the first time to obtain capillary pressure curves in terms of water contents using a rock sample. This and other techniques integrating experimental routines, mathematical analyses, and computer simulations provide reliable porous media information supporting EOR operations in carbonate reservoirs, such as the Brazilian Pre-salt basins. The research links studies of the representative elementary volume (REV) to obtain permeability estimates under laboratory-scale conditions and for alternative mathematical techniques.

## **1.3 Objectives**

The objective of this work was to investigate carbonate rocks that may be subject to EOR in the near future. The study is part of integrated work carried out by the Enhanced Oil Recovery Laboratory (LRAP) at COPPE/UFRJ in Rio de Janeiro to investigate EOR techniques for carbonate rock formations. For this purpose, a series of petrophysical laboratory routines were implemented on carbonate samples. Since water-alternating-gas (WAG) injection is a popular form to improve recovery, laboratory techniques involving water were used and thoroughly tested for the petrophysical characterizations. Results were then upscaled into REVs that allow posterior reservoir characterization emphasizing permeability estimation. This work aims to contribute to improved recovery factors of Brazilian petroleum reservoirs by better understanding their oil-bearing carbonate formations.

## **1.4 Contribution and Originality**

Research documented in this thesis consists of testing carbonate formation samples in the laboratory and their use to obtain REV scale information through upscaling techniques. Basic petrophysics, mercury intrusion/extrusion capillary pressure, nuclear magnetic resonance, and micro-computerized tomography techniques were performed on carbonate rock samples. The water retention curve of a rock sample was measured for the first time in the laboratory using a combination of advanced evaporation (HYPROP) and dew-point mirror (WP4C) techniques. While these techniques have become relatively popular in soil hydrology for unconsolidated media, they are still without precedence for consolidated media within the oil and gas industry.

Upscaling techniques have recently found wide application in hydrogeologic studies. Unfortunately, they have been applied nearly exclusively to single-porosity systems, but not frequently to carbonate rocks which often exhibit bimodal or trimodal properties involving two or three interacting pore systems within a sample or formation. Understanding the behavior of fluids within such multimodal systems at the reservoir scale becomes more tangible through petrophysical analyses in conjunction with upscaling techniques. The suggested approaches assist EOR assessments as they help to understand the rock characteristics and fluid dynamics in reservoirs, as well as to estimate REV-scale permeabilities obtained through different techniques.

## **1.5 Thesis organization**

This thesis is organized in terms of an Introduction, a Literature review, a Materials and methods section, Results and discussion, and a Conclusions and considerations section. The Introduction explains the motivation, the proposed research, the contribution and originality of the research, and the thesis organization.

In the section comprising the Literature Review, concepts regarding carbonate rocks, petrophysics and related techniques of rock typing for permeability measurements, and upscaling techniques are presented. That section also contains a brief description of the van Genuchten-Mualem approach since the model is applied later to the dual-porosity unsaturated hydraulic properties of a carbonate rock sample. The model has been applied

to rock samples in several papers, but to the best of the author's knowledge, this is the first time the model is applied to a dual-porosity rock medium in conjunction to the evaporation and chilled-mirror dewpoint laboratory techniques presented in the Materials and Methods section.

In the Materials and Methods section, two sets of samples are presented: 29 limestone formation samples representing different carbonate reservoirs from around the world, and Indiana Limestones samples acquired from Kocurek Industries that were used for more detailed analysis. Then an overview of laboratory experiments is given, such as basic petrophysics, nuclear magnetic resonance (NMR), mercury intrusion (MICP) and extrusion capillary pressure, formation factor measurements, thin section analysis, and micro-computerized tomography ( $\mu$ -CT), which provide input to upscaling techniques and pore network modeling (PNM) tools for simulating fluid flow in porous media. Evaporation and chilled-mirror dewpoint techniques are described next to obtain capillary pressure-saturation (water retention) data of tested samples using the HYPROP and WP4C techniques. Capillary pressure-saturation measurements were obtained from mercury intrusion and extrusion experiments. The objective is to show how the van Genuchten water retention function equation can be used to describe the hydraulic properties of porous media at the macroscopic (continuum) level.

The Results and Discussion section presents results separately: firstly, the limestones from carbonate reservoirs (L samples) are analyzed and discussed, followed by the Kocurek Indiana Limestone (IH samples) for which more data were available. Finally, the Conclusions and Considerations chapter summarizes the research and discusses remaining observations and possible future research by assessing the most important features and results from the techniques used.

## 2 Literature Review

### 2.1 Carbonate rocks

Carbonate rocks are sedimentary rocks, originated by precipitation of minerals from water through various chemical or biochemical processes. They usually contain significant amounts of non-skeletal organic matter in addition to various amounts of siliciclastic or chemical (*e.g.*, carbonate) constituents and represent the most abundant type of chemical/biochemical sedimentary rock. Carbonate rocks represent 20% to 25% of all sedimentary rocks and, based on mineralogy, are divided between limestones and dolomites/dolostones. Limestones are composed mainly of the mineral calcite, while dolomites or dolostones are mostly composed of dolomite (BOGGS JR., 2006). Carbonates, along with sandstones, represent the most common oil-bearing reservoir types found in nature (TIAB & DONALDSON, 2003), corresponding to 66% of the known petroleum reserves (ZINSZNER & PELLERIN, 2007). Carbonates are mainly composed of calcium carbonate ( $\text{CaCO}_3$ ), which dictates the physical-chemical behavior of the rocks. Carbonate rocks are typically found in shallow sedimentary basins with great amounts of organic matter responsible for secreting calcium monoxide or lime ( $\text{CaO}$ ). After deposition,  $\text{CaO}$  contacts water, which may contain carbonic acid, resulting in calcium carbonate ( $\text{CaCO}_3$ ) (SOUZA, 2012).

#### 2.1.1 Indiana Limestone

Understanding rock properties is essential to determine rock-fluid interactions that occur in a reservoir or during laboratory or field experimentation. Indiana Limestone is one of the standard carbonate rocks often used for porous media laboratory experiments. As an inexpensive, readily available and relatively homogeneous rock, the outcrops of producing subsurface formations have been used by the oil industry for years, although little has been published about their petrographic and petrophysical characteristics (CHURCHER *et al.*, 1991).

Indiana Limestone is a calcite cemented grainstone from the state of Indiana, USA. The rock consists of fossil fragments and concentrically lamellar calcium carbonate particles



(oolites) (Indiana Limestone Handbook, 1975). Colors in the quarry can vary with depth from gray to buff-colored, representing respectively lower to higher permeabilities and porosities at deeper to shallower depths. The gray-colored variant is usually found below a water table because of reducing conditions, while the buff-colored one occurs above a current water table due to oxidation (STEVENSON, 1978). Petrographic analyses indicate that Indiana Limestone is composed of the minerals calcite (99%) and quartz (1%) (CHURCHER *et al.*, 1991).

Analyses of thin sections and Scanning Electron Microscope (SEM) images have shown that the porosity and permeability of Limestones is mainly controlled by the distribution of coarse, pore-filling calcite cement. Also, permeability variations may be due to chemical weathering, which generally leads to higher permeabilities (CHURCHER *et al.*, 1991). A photomicrograph of an Indiana Limestone sample is provided in Figure 1.

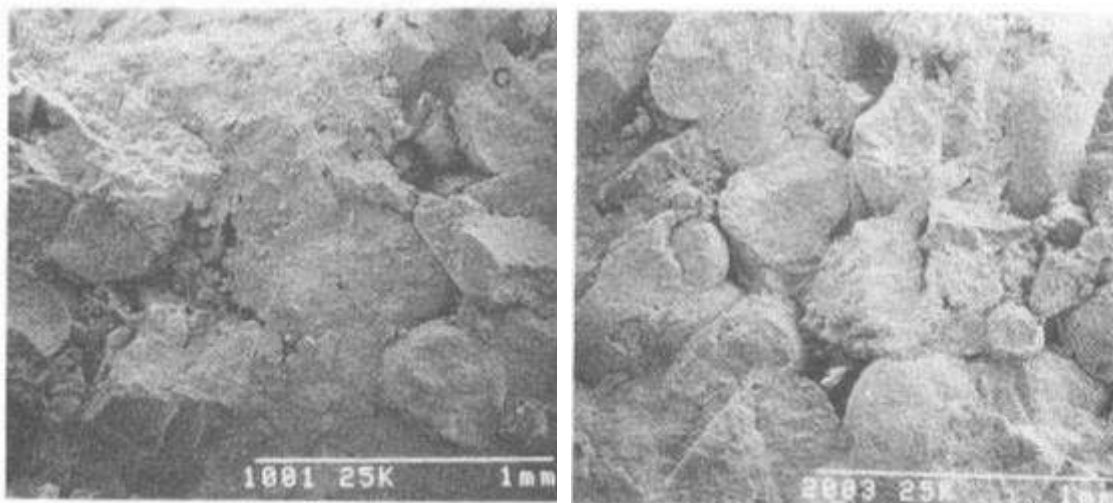


Figure 1 – SEM photomicrograph of Indiana Limestone 1 (left) and 2 (right), samples studied by CHURCHER *et al.* (1991).

Mercury intrusion capillary pressure (MICP) tests performed by CHURCHER *et al.* (1991), CARNEIRO *et al.* (2014) and SAYEDAKRAM *et al.* (2016) on Indiana Limestone samples indicated bimodal pore throat-size distributions in two samples. The bimodal pore throat-size distributions are thought to be a result of the distribution of fine calcite crystals lining the pores, thereby creating microporosity. The microporosity could have originated also due to intra-particle porosity in some of the fossil fragments and oolites. Indiana Limestone usually shows favorable pore-throat size distributions, which may be reflected by its high final mercury recovery efficiency (WARDLAW *et al.*, 1987).

## 2.2 Porosity

Total porosity is the void fraction that measures the volume of voids over the total volume, characterizing the fluid storage capacity of a rock (TIAB & DONALDSON, 2003). By definition, porosity  $\emptyset$  is given by:

$$\emptyset = \frac{V_R - V_G}{V_R} = \frac{V_P}{V_R}, \quad (2.1)$$

where  $V_R$  is the volume of the rock,  $V_G$  is the total volume occupied by the grains and  $V_P$  is the pore volume. Porosity is governed by uniformity, cementation and compaction of grains and can be divided into primary and secondary types. Primary porosity is formed due to deposition, while secondary porosity is generally formed due to diagenetic processes after deposition, such as dissolution. Secondary porosity is more commonly found in carbonate rocks as compared to sandstones due to carbonate chemistry and its formation process. Microporosity in carbonates generally is associated with intraparticle porosity, while vugs are associated with interparticle spaces, usually called meso- or macropores (SOUZA, 2012; TIAB & DONALDSON, 2003). Total porosity is given by the sum of the inter- and intra-aggregate porosity.

### 2.2.1 Dual-porosity systems

A dual-porosity rock is characterized by both primary porosity (from the original deposition) and secondary porosity (originated by some other mechanism). In this type of system, most of the flow towards a well effectively occurs through one of the porosity systems, while most of the fluid generally is stored and supplied by the other. Naturally fractured reservoirs and vugular carbonates often behave as dual-porosity reservoirs, since they show contrasts between high-permeability and low-permeability layers. Such a system typically exhibits mathematical bimodal behavior at the larger scale.

As explained by GONG (1997), when a porous medium contains natural fractures or highly conductive channels, dual-porosity models provide the most realistic approach for modeling fluid flow. In such models, flow within the matrix is mostly dissociated from that within highly conductive channels. This concept was introduced by BARENBLATT

& ZHELTOV (1960), who formulated a set of equations for slightly compressible single-phase fluid flow in both the fractures and the matrix, while transfer between them was assumed to occur in a pseudo-steady state manner.

Dual-porosity systems are typically composed of macropores, micropores and pore throats. Pore bodies, larger in size, control the porosity of the medium and are then divided into two sub-domains: macropore, fracture or inter-aggregate domains and micropore, matrix or intra-aggregate domains. Pore throats with their smaller sizes control then the hydraulic connection between the larger pores. An example of a dual-porosity pore network model (PNM) can be seen in Figure 2.

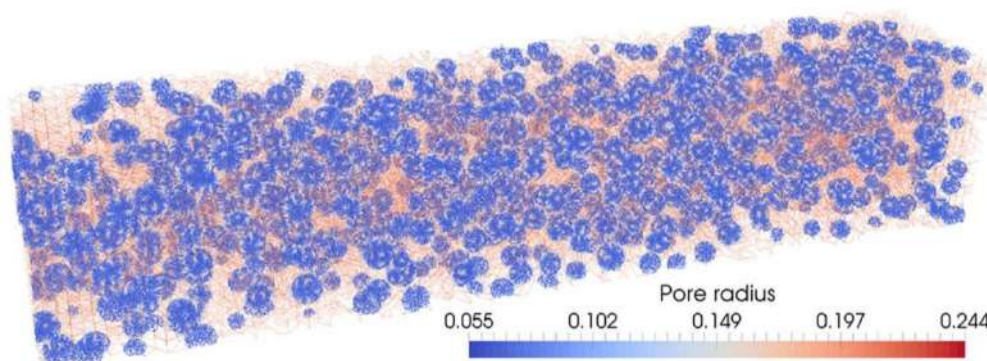


Figure 2 – Figure showing a dual-porosity porous medium generated with the PoreFlow PNM software (RAOOF & HASSANIZADEH, 2010b). Two porosity subdomains are generated and superimposed: macropores are represented as red pore bodies, while aggregates (micropores) are in blue. Pore throats connect the pore bodies. This image was extracted from DE VRIES *et al.* (2017).

### 2.3 Permeability and hydraulic conductivity

Permeability is a parameter reflecting the ability of a rock (or another porous medium) to transmit fluids (water, oil and/or air), commonly represented in terms of Darcy (D) or millidarcy (mD) units, but sometimes also in  $m^2$  ( $\sim 10^{12}$  darcys). Permeability is the proportionality constant in Darcy's law, which relates the flow of fluid to the fluid physical properties (notably the viscosity) with a pressure gradient applied to the porous medium:

$$q = \frac{Q}{A} = -\frac{k}{\mu} \frac{dP}{dl_{fl}} , \quad (2.2)$$

where  $q$  is the flux,  $Q$  is the flow rate,  $A$  is the cross-sectional area of the porous medium,  $k$  is the permeability,  $\mu$  is the dynamic viscosity,  $P$  is pressure and  $l_{fl}$  is the length of the porous medium in the flow direction.

The hydraulic conductivity,  $K$ , is the proportionality constant specifically defined for the flow of water through a porous medium, with permeability being only a portion of this by being a property of the porous medium only, not of the fluid. Given the value of hydraulic conductivity for a pore system, the permeability can be calculated as follows:

$$k = K \frac{\mu}{\rho g_a} , \quad (2.3)$$

where  $\rho$  is the fluid density and  $g_a$  the acceleration due to gravity.

## 2.4 Formation Factor

The formation factor ( $F$ ) is the ratio of the resistivity, or inverse of the electric conductivity, of a rock filled with water to the resistivity, or inverse of the conductivity, of that water. ARCHIE (1942) introduced a classical empirical model based on a set of relationships between formation resistivity, porosity and water saturation for shale-free sands. WINSAUER *et al.* (1952) modified the Archie's formula by introducing tortuosity factor  $a$ , into the relationship between porosity and formation factor. The formation factor  $F$  can be related to porosity  $\emptyset$  by:

$$F = a\emptyset^{-m} , \quad (2.4)$$

where  $m$  is the porosity exponent and  $a$  is a constant.

Since conductance in natural porous media relates to critical conductance, the effective or upscaled permeability needs information about the electrical conductivity to be solved:

$$\frac{\sigma_b}{\sigma_w} = \frac{1}{F}, \quad (2.5)$$

where  $\sigma_b$  is the bulk electrical conductivity and  $\sigma_w$  the electrical conductivity of the saturating fluid (e.g., water). This value ( $F$ ), when not measured, can also be estimated from mercury intrusion (KATZ & THOMPSON, 1987) or water-expulsion porosimetry (NISHIYAMA & YOKOYAMA, 2014).

## 2.5 Capillary pressure and wettability

Capillary pressure is the result of the interaction of forces within and between contacting fluids and bounding solids. Surface, interfacial and liquid-solid forces dictate the capillary pressure and wettability. When the liquid-solid forces are greater than the surface plus interfacial forces, the liquid is wetting the solid; if not, the liquid is non-wetting. Wettability is described by the contact angle ( $\theta_c$ ) between the fluid-fluid interface and the solid, measured through the fluid of higher density.

When a capillary tube is placed vertically in a fluid, its wall attracts the wetting fluid ( $w$ ) by drawing it up, but repels the non-wetting fluid ( $nw$ ), until all forces are balanced. Due to the difference in density  $\rho$  between the fluids, different pressure gradients result. The difference between pressures across the tube's meniscus formed between the fluids is the capillary pressure ( $P_c$ ). Hence, capillary pressure is the non-wetting phase's extra pressure needed to overcome the balance between forces and displace the wetting phase within the tube. The Washburn equation, given by Eq. (2.6), provides a simple relationship to convert mercury pressure into a pore size and is a special case of the Young-Laplace equation (GREGG; SING, 1982):

$$P_c = (\rho_w - \rho_{nw})g_a h = \frac{2\sigma \cos\theta_c}{r_{cap}}, \quad (2.6)$$

where  $g_a$  is the acceleration due to gravity,  $h$  is the height above the free surface,  $\sigma$  is interfacial tension and  $r_{cap}$  is the capillary tube radius.

## 2.6 Mercury capillary pressure curve

One of the most popular ways to measure a capillary pressure curve in the petroleum industry is through mercury intrusion, occasionally followed by extrusion, into a wetting fluid-saturated rock sample, with mercury being the non-wetting phase and gas the wetting phase, as presented in Figure 3. The distribution of the fluids as they migrate throughout a rock is typically controlled by wetting characteristics prior to movement. This is an important feature which mercury intrusion and extrusion provides, thus serving as a guide to fluid injection and production and aiding in reservoir engineering and petrophysical characterizations.

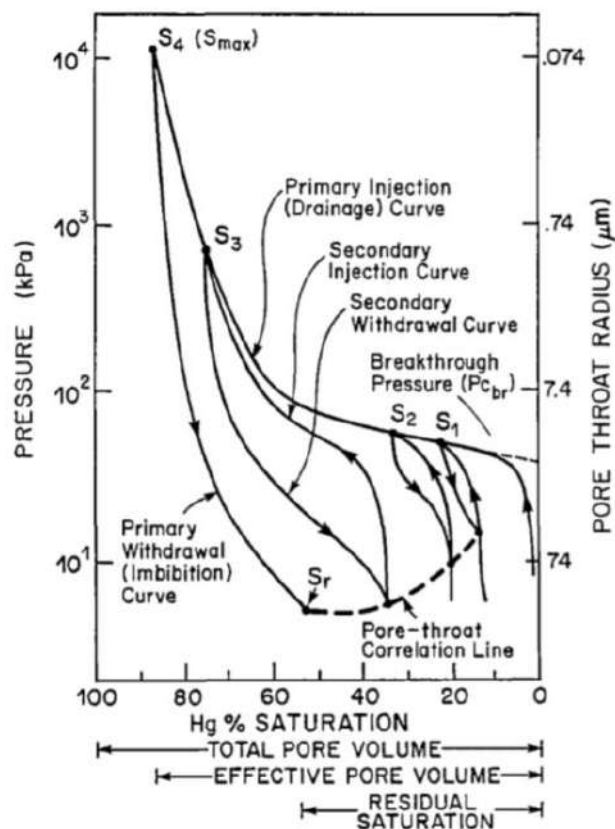


Figure 3 – Example of a mercury capillary pressure plot showing related saturation parameters. Imaged extracted from CHURCHER *et al.*, (1991).

To perform the mercury intrusion experiments, incremental pressures are applied to the non-wetting phase as it enters the sample's initially evacuated pores. Since the pressure steps are performed sequentially, mercury progressively fills (“conforms” or “closes around”) the chamber where the sample is placed and any surface irregularities of the

sample. The pressure at which mercury first intrudes the sample is the displacement pressure, the initial pore entry pressure, or the closure pressure. All intrusion data recorded up to the closure pressure are subtracted from the following mercury injection capillary pressure (MICP) raw data, as the closure correction (SHAFER & NEASHAM, 1999). At atmospheric pressure, mercury only enters pores larger than  $\sim 14 \mu\text{m}$ , and thus typically surrounds the sample particles. For every increase in pressure, the percentage of rock pore volume occupied by mercury is measured at equilibrium.

After the maximum pressure of mercury injection is reached, the pressure is reduced, thus allowing the wetting phase to imbibe the sample and initializing the extrusion part of the experiment. The extruded mercury is measured per percentage bulk volume (or total pore volume) per pressure step until residual mercury saturation (WARDLAW & TAYLOR, 1976).

Through the mercury injection curve, it is possible to obtain the effective pore throat distribution using the equation for capillary pressure described by Eq. (2.6) (WARDLAW & TAYLOR, 1976). On the other hand, the mercury extrusion curve provides the distribution of pore bodies (GIESCHE, [s.d.]) due to the decrease in pressure leading to the expulsion of mercury driven by capillary forces. Comparison between these curves provides valuable information regarding the porous medium such as trapped fluids, the flux, the aspect ratio, the body to throat ratio and the recovery factor.

The mercury injection pressure versus mercury saturation also provides information about the pore throat size distribution. The shape of the curve provides information about the sample, which can be unsorted, poorly sorted, well-sorted or even have a bimodal or multimodal pore-size distribution, as seen in Figure 4.

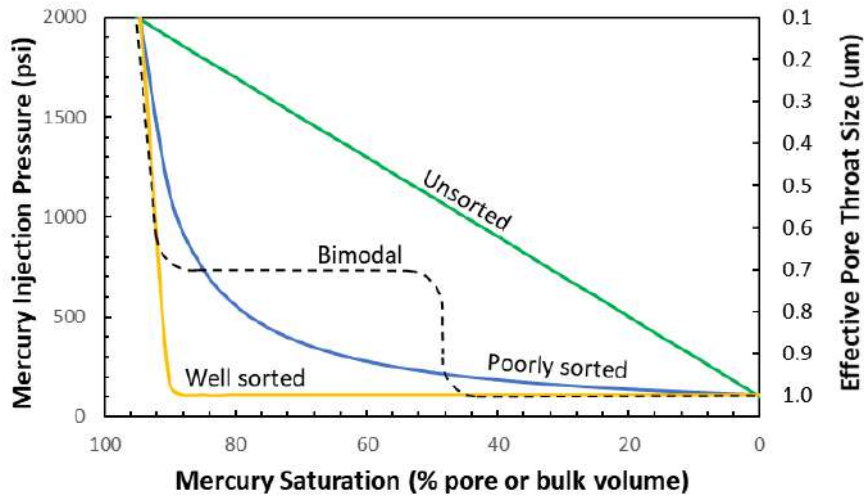


Figure 4 – Idealization of mercury injection capillary pressure curve shapes. Note that all of the curves have identical displacement pressures and minimum unsaturated (residual) pore volumes but that the saturation profiles would differ dramatically due to differences in pore volumes.

Mercury intrusion is considered to be an additional technique supplementing X-ray tomography since the latter neglects pores smaller than its resolution. With MICP it is possible to obtain a more realistic value of the pore volume of aggregates or micropores (DAL FERRO *et al.*, 2013).

Mercury capillary pressure analyses can be used to determine pore geometry and to predict the behavior of immiscible fluid pairs in the porous medium (CHURCHER *et al.*, 1991). The pressure-saturation data defining the injection curve can be used to generate a pore size distribution based on Eq. (2.6), where  $P_c$  is the capillary pressure (e.g., in kPa),  $\sigma$  is the surface tension between air and mercury (480 mN/m),  $\theta$  is the contact angle (equal to  $140^\circ$  for air-mercury) and  $r_{cap}$  is the pore throat radius ( $\mu m$ ).

The above techniques serve as indirect methods to measure porosity. They are limited to problems related to porosity data generated during the injection process but are not able to directly observe individual pores (REIS NETO *et al.*, 2011).



## 2.7 Evaporation and chilled-mirror dew point techniques

This section discusses the HYPROP evaporation and WP4C chilled-mirror dew point laboratory routines, as well as related mathematical approaches for measuring the hydraulic properties of unsaturated porous media. The unsaturated hydraulic properties of soil and rock formations are an important part of theoretical and practical investigations of single- and multiphase fluid flow studies in the soil, hydrogeologic and petroleum engineering disciplines. A large number of experimental methodologies have been developed and tested over the years to estimate the water retention and unsaturated hydraulic conductivity relationships (DANE & HOPMANS, 2002; KLUTE & DIRKSEN, 1986), alternatively termed the capillary pressure-saturation ( $P_c$ - $S$ ) and relative permeability curves, respectively.

A direct approach for estimating the water retention curve, especially popular in the soil hydrology literature, is to measure a series of water content ( $\theta$ ) and pressure head ( $h$ ) pairs, and then to fit a particular function to the data. Direct measurement techniques include methods using a hanging water column or sandbox, pressure cells, pressure plate extractors, suction tables, soil freezing, and many other approaches as reviewed by BITTELLI & FLURY (2009); DANE & HOPMANS (2002) and LOONEY & FALTA (2000), among others. Once the pairs of  $\theta$  and  $h$  data are obtained, the results may be analyzed in terms of specific analytical functions such as those by BROOKS & COREY (1964), or VAN GENUCHTEN (1980). Similar direct approaches involving pairs of conductivity and pressure head or water content data are in principle also possible for the  $K(h)$  or  $K(\theta)$  functions (DANE & HOPMANS, 2002), including for the saturated hydraulic conductivity,  $K_s$ .

Since pairs of  $K(h)$  or  $K(\theta)$  data are not easily obtained in the very dry range, more specialized approaches are often used such as hot-air, centrifugation, or dew-point techniques (ARYA, 2002; NIMMO *et al.*, 2002; SCANLON *et al.*, 2002). Consequently, unsaturated hydraulic conductivity properties are still often estimated using laboratory- or field-scale inverse parameter estimation procedures (e.g., HOPMANS *et al.* (2002) and ŠIMŮNEK *et al.* (1998)). Most of these techniques pertain to unconsolidated media, generally soils. While some of the techniques can also be applied to consolidated rocks,

different approaches have been considered to be more suitable for such media like mercury intrusion porosimetry, water adsorption or desorption measurements, centrifuge methods, core flooding, and related approaches (DULLIEN, 1979; HAGHI *et al.*, 2020; LIU *et al.*, 2016; PURCELL, 1949).

Evaporation and chilled-mirror dew point laboratory methods are used to improve the petrophysical characterization of an Indiana Limestone carbonate rock sample through the van Genuchten-Mualem models, presented below, fitted to observed pressure head (water capillary pressure) versus water content data.

### **2.7.1 The van Genuchten-Mualem model**

MUALEM (1976) presented a model for predicting the hydraulic conductivity from water retention curves and the electric conductivity at saturation. His model uses a simple integral formula for the unsaturated hydraulic conductivity, which enables derivation of closed-form analytical expressions, provided that suitable equations for the soil-water retention curves are available. GHANBARIAN-ALAVIJEH & HUNT (2012a) define the Mualem model as a theoretical approach developed to estimate the unsaturated hydraulic conductivity from the pore size distribution. VAN GENUCHTEN & NIELSEN (1985) indicated that the Mualem theory was applicable to a wider variety of soils than the BURDINE (1953) theory, commonly used in conjunction with the BROOKS & COREY (1964) equation for water retention.

VAN GENUCHTEN (1980) derived closed-form analytical expressions for estimating the unsaturated hydraulic conductivity function from the soil-water retention curve, the latter being a curve with a continuous slope. The resulting conductivity models generally have three independent parameters, which may be obtained by matching the proposed soil-water retention curve to experimental data. This section is based on his work and serves as a model to fit water retention data of rock samples. The work is important since direct measurements of the unsaturated hydraulic conductivity curve can be very time consuming and expensive, the highly nonlinear nature of the curve, as well as its extensive variability in natural field settings. Nevertheless, the unsaturated conductivity can be calculated if a more easily measured soil-water retention curve is available.

The relative hydraulic conductivity ( $K_r$ ), according to MUALEM (1976), is given by:

$$K_r(S_e) = S_e^{1/2} \left[ \int_0^{S_e} \frac{1}{h(x)} dx / \int_0^1 \frac{1}{h(x)} dx \right]^2, \quad (2.7)$$

where  $h$  is the pressure head and  $S_e$  is effective fluid saturation given by:

$$S_e(h) = \frac{\theta(h) - \theta_r}{\theta_s - \theta_r}, \quad (2.8)$$

in which  $\theta$  is the volumetric water content, and the subscripts  $r$  and  $s$  denote residual and saturated values of the water content, respectively. Mathematically,  $h$  is defined as the fluid pressure divided by its density and the acceleration due to gravity, as explained in section 2.3.

Eq. (2.7) is used here in conjunction with the water retention (or capillary pressure – saturation) curve of VAN GENUCHTEN (1980):

$$S_e = \left[ \frac{1}{1 + (\alpha h)^n} \right]^m, \quad (2.9)$$

where  $\alpha$ ,  $m$  and  $n$  are undetermined parameters, and  $h$  is assumed to be positive.

The water content as a function of the pressure head is given by Eq. (2.8) and Eq. (2.9), i.e., by:

$$\theta = \theta_r + \frac{(\theta_s - \theta_r)}{[1 + (\alpha h)^n]^m}, \quad h > 0; m = 1 - \frac{1}{n}. \quad (2.10)$$

The saturated water content  $\theta_s$  is easily obtained experimentally since it equates to the porosity (assuming no entrapped or dissolved air in the sample). By contrast, the residual water content  $\theta_r$  is generally poorly defined, especially when relatively dry samples are considered (e.g., PETERS, 2013; RUDIYANTO *et al.*, 2020). Usually  $\theta_r$  is obtained by extrapolating available water retention data towards the lower water contents, where the slope ( $d\theta/dh$ ) becomes zero.

Simple, closed-form expressions for  $K_r(S_e)$  can be derived when certain conditions are imposed on the values of  $m$  and  $n$  in Eq. (2.9), resulting in:

$$K_r(S_e) = S_e^{\frac{1}{2}} \left[ \frac{f(S_e)}{f(1)} \right]^2, \quad (2.11)$$

where for the most general case with independent  $m$  and  $n$  parameters

$$f(S_e) = \int_0^{S_e} \left[ \frac{x^{1/m}}{1 - x^{1/m}} \right]^{1/n} dx. \quad (2.12)$$

By using  $y = x^m$  in Eq. (2.12):

$$f(S_e) = m \int_0^{S_e^{\frac{1}{m}}} y^{m-1+\frac{1}{n}} (1-y)^{-\frac{1}{n}} dy, \quad (2.13)$$

For all integer values of  $k = m - 1 + 1/n$  the integration of Eq. (2.13) can be carried out without difficulties. For the particular case when  $k = 0$  (i.e.,  $m = 1 - 1/n$ ), integration of Eq. (2.13) yields:

$$f(S_e) = 1 - \left( 1 - S_e^{\frac{1}{m}} \right)^m, \quad m = 1 - \frac{1}{n}. \quad (2.14)$$

Because  $f(1) = 1$ , Eq. (2.11) becomes:

$$K_r(S_e) = S_e^{1/2} \left[ 1 - \left( 1 - S_e^{1/m} \right)^m \right]^2, \quad m = 1 - \frac{1}{n}; 0 < m < 1. \quad (2.15)$$

The relative hydraulic conductivity can also be expressed in terms of the pressure head by substituting Eq. (2.9) into (2.15):

$$K_r(h) = \frac{\{1 - (\alpha h)^{n-1} [1 + (\alpha h)^n]^{-m}\}^2}{[1 + (\alpha h)^n]^{m/2}}, \quad m = 1 - \frac{1}{n}. \quad (2.16)$$

From the hydraulic conductivity and the soil-water retention curve, it is also possible to derive an expression for the soil-water diffusivity ( $D$ ):

$$D(S_e) = K(S_e) \left| \frac{dh}{d\theta} \right|, \quad (2.17)$$

which leads to:

$$D(S_e) = \frac{(1-m)K_s}{\alpha m(\theta_s - \theta_r)} S_e^{\frac{1}{2}-\frac{1}{m}} \left[ \left(1 - S_e^{\frac{1}{m}}\right)^{-m} + \left(1 - S_e^{\frac{1}{m}}\right)^m - 2 \right], \quad (2.18)$$

where  $K_s$  is the hydraulic conductivity at full saturation when  $S_e = 1$ .

Nonlinear least-squares curve-fitting techniques may be used to obtain simultaneous estimates of  $\theta_r$ ,  $\alpha$  and  $n$ . The entire measured water retention curve can then be used in the parameter estimation procedure. A detailed description and listing of the non-linear least-squares curve-fitting program RETC used for this purpose is given by VAN GENUCHTEN *et al.* (1981). The method is also used by the HYPROP-FIT software (PERTASSEK *et al.*, 2015) to analyze water retention data in terms of the van Genuchten and Brooks-Corey models, as well as the PDI model to be discussed later.

The  $n$  and  $m$  parameters have an undefined relationship with the pore size distribution. The relationship with  $n$  and  $m$  regards the curvatures at large and small saturations. These curvatures are related as the percolation constraints on the air (water) phase must affect the limits at large (small) saturations (HUNT *et al.*, 2014).

### 2.7.2 The dual-porosity van Genuchten model of Durner

The bimodal van Genuchten water retention model, as formulated by Durner (DURNER, 1994), is a weighted superposition of two van Genuchten type functions. The dual-porosity (bimodal) formulation accounts for the presence of distinct but interacting macropore and micropore regions in macropores soils or fractured rock, as well as in general for porous media showing heterogeneous pore- and/or particle size distributions:

$$S_e(h) = \sum_{i=1}^2 w_i \left[ \frac{1}{1 + (\alpha_i |h|)^{n_i}} \right]^{m_i}, \quad (2.19)$$

where  $\alpha_i$  ( $cm^{-1}$ ) and  $n_i$  (dimensionless) are shape factors (Eq. (2.9)), and  $m_i = 1 - 1/n_i$ , with  $w_1$  and  $w_2$  representing weighting factors representing the macropore and micropore regions, respectively ( $w_1$  and  $w_2$  add up to unity, i.e.,  $w_2 = 1 - w_1$ ). PRIESACK & DURNER (2006) showed that combination of the bimodal water retention model given

by Eq. (2.29) with the Mualem conductivity model will lead to the following closed-form expression for  $K(S_e)$ :

$$K(S_e) = K_s \frac{(w_1 S_1 + w_2 S_2)^L \left\{ w_1 \alpha_1 [1 - (1 - S_1^{1/m_1})^{m_1}] + w_2 \alpha_2 [1 - (1 - S_2^{1/m_2})^{m_2}] \right\}^2}{(w_1 \alpha_1 + w_2 \alpha_2)^2} \quad (2.20)$$

The combined dual-porosity water retention and hydraulic conductivity functions now contain a total of seven independent parameters ( $w_1$ ,  $\alpha_1$ ,  $\alpha_2$ ,  $n_1$ ,  $n_2$ ,  $K_s$  and  $L$ ).

## 2.8 Micro-Computerized Tomography

The use of 3-D microtomography and other associated techniques has been enormously helpful to obtain non-destructive information about the pore structure of porous media (ALLAIRE *et al.*, 2009; DAL FERRO *et al.*, 2013; MANGALASSERY *et al.*, 2013; SAN JOSÉ MARTÍNEZ *et al.*, 2015; ZHOU *et al.*, 2013), including for studies about fluid flow and structural dynamic processes (CNUUDE & BOONE, 2013; WILDENSCHILD & SHEPPARD, 2013). Information obtained at the pore-scale allows the estimation of macroscopic properties related to the fundamental physical pore-scale processes, pore size distributions and connectivities (RAOOF & HASSANIZADEH, 2013; 2010b). Non-destructive imaging techniques generate cross-sectional pictures by measuring the attenuation of a beam of X-rays as the equipment is rotated around the sample at angular increments within a single place (AKIN & KOVSCEK, 2003).

Radiological imaging using computer tomography (CT) scanners was first introduced by HOUNSFIELD (1975). The scanners create cross-sectional images of the object by measuring the attenuation of a beam of X-rays as the object is rotated at angular increments within a plane. The full image is reconstructed afterwards through the use of algorithms based on Fourier transforms (AKIN & KOVSCEK, 2003).

When running a CT scanner, X-rays penetrate a thin volumetric slice of an object at different angles as this object, located between the source and detector, is rotated. The detector records the intensity of the received X-rays. Many different X-ray attenuations are available for mathematical reconstruction and enhancement. The basic quantity

measured in each voxel (each volume element) of a CT image is the linear attenuation coefficient, defined by Beer's law as:

$$\frac{I}{I_0} = \exp^{-\mu_B h_s}, \quad (2.21)$$

where  $I_0$  is the incident X-ray intensity,  $I$  is the remaining intensity after the X-rays pass through a thickness  $h_s$  of a homogeneous sample, and  $\mu_B$  is the linear attenuation coefficient. For heterogeneous media, the energy transmitted along a particular ray path is:

$$\ln\left(\frac{I}{I_0}\right) = \int_0^{L_{SD}} \mu_B(h_s(x, y)) dh_s, \quad (2.22)$$

where  $h_s(x, y)$  are the coordinates of the attenuation coefficient in two dimensions,  $L_{SD}$  is the distance between source and detector, and  $dh_s$  is a distance along this path length.

Beer's law assumes a narrow X-ray beam and monochromatic radiation. This, even though the actual beam, which is polychromatic consisting of a spectrum of photons ranging from 20 keV to 120 keV, is responsible for the generation of imaging artifacts. Detectors also have an associated efficiency dependent upon energy. Hence, the remaining intensity of the X-rays can be more accurately represented by

$$I = \int_{e_l}^{e_h} \frac{dI_0}{dE} \varepsilon_d(E) \exp\left(-\int_0^{h_s} \mu_B(x, y, E) dL\right) dE, \quad (2.23)$$

where  $dI_0/dE$  is the spectral distribution of the incident radiation,  $\varepsilon_d(E)$  is the detector's efficiency at energy  $E$ , and  $e_l$  and  $e_h$  are the relevant spectrum of energy, with subscripts  $l$  and  $h$  meaning low and high, respectively. Eq. (2.23) presents the attenuation coefficient as a function of position and energy.

In practice, Eq. (2.22) is discretized into  $n$  volume elements, each with an unknown attenuation coefficient, to be used for reconstructing images, while assuming some particular effective energy for the X-ray beam as a whole. Measurement of the attenuation of multiple ray projections provides data to solve multiple equations for attenuation.

After image reconstruction, the relative values of the linear attenuation coefficient are known for each pixel. These values are converted into numerical values (CT) through normalization using the water linear attenuation coefficient:

$$CT = 1000 \frac{(\mu_B - \mu_w)}{\mu_w} . \quad (2.24)$$

Eq. (2.24) is expressed in Hounsfield (H) units, which represent a 0.1% change in density with respect to the calibration density scale. The higher the CT number, the higher the material's mass density.

The linear attenuation coefficient is a function of the electron density (or the bulk density,  $\rho_b$ ) and the effective atomic number,  $Z$  (VINEGAR & WELLINGTON, 1987):

$$\mu = \rho_b (a_K + bZ^{3.8}/E^{3.2}) \quad (2.25)$$

where  $a_K$  is the Klein-Nishina coefficient and  $b$  a constant. This equation states that the heavier the elements, the greater the photoelectric cross-section, with the fraction of photoelectric contribution increase as the energy decreases.

Once the CT numbers are known, porosity can be estimated. The porosity analysis provides measurements of the void fraction and characterization of the empty space. In petroleum engineering, studies of pore connectivity are of great importance since connectivity is a primary determinant of the flow of liquids. To do so, the porosity analysis is done by accounting for the empty space. A pore can be open, meaning that it connects to the space outside the object or sample, or closed, meaning that it is fully enclosed by the material. The microtomography images, when treated, give information regarding porosity and connectivity that can later be used to calculate, for example, the permeability and geometric tortuosity.

Through an analysis of hundreds of high-resolution images, non-destructive approaches allow studies of microtomographic sections and three-dimensional visualizations of the internal structures of a sample, thus making it possible to quantify areas and volumes of voids and solid material. The analysis provides qualitative and quantitative information regarding the shape, size, distribution, volume, area and connectivity of pores at the



microscale (REIS NETO *et al.*, 2011). The techniques are limited by the maximum reachable resolution by the equipment (CNUdde *et al.*, 2006).

As mentioned earlier,  $\mu$ CT has been used extensively in the petroleum industry to quantify porosity and other properties, although one important aspect that may impact porosity calculations is the invoked resolution of computerized tomography. The closer the zoom-in (i.e., the closer the X-ray source is to the object), the better the resolution to allow smaller pores to be captured and accounted for. Poor resolutions, on the contrary, may not be capable to capture the microporosity of a sample. There are also some limitations of higher resolutions (more zoomed-in images) in that the captured sample must be smaller, while lower resolutions allow for larger samples to be fully imaged. The resolution also defines the thickness of scanned sections.

## **2.9 Nuclear Magnetic Resonance**

NMR techniques are based on the response of the interaction (spins) of atomic nuclei to external magnetic fields. The possibility of manipulating these spins in one or more dimensions allows the deployment of the technique in many experiments, giving NMR a unique, versatile feature compared to other spectroscopic techniques. Being the most abundant element contained in fluids analyzed by the industry, the  $^1\text{H}$  isotope is the most used by the technique. Its nucleus is formed by a single proton that has an intrinsic angular momentum known as spin and a magnetic moment that causes it to behave like a magnetic bar, containing north and south poles, aligning with the magnetic moment direction. This effect occurs because the magnetic moment and spin are parallel and related through a proportionality constant denominated magnetogyric ratio. This ratio is specific for each nucleus and each isotope can be observed by NMR in their specific own value. When the proton spin is observed along the direction of the external magnetic field, quantum mechanics states that there are only two possible measurement outcomes: either the proton's spin is parallel or antiparallel to the magnetic field, being the magnetogyric factor constant, independent from the magnetic field.

When a system of many hydrogen atoms is without the influence of an external magnetic field, the orientation of the spins is chaotic and governed by the dynamics of Brownian

movement (COATES *et al.*, 1993). As a consequence, the resulting magnetization of this system is null at any time, as depicted in Figure 5.

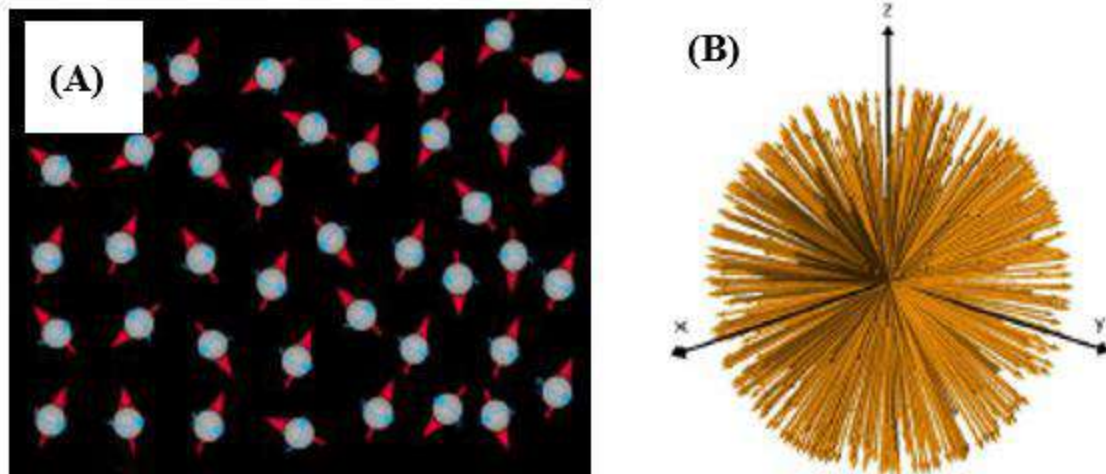


Figure 5 – (A) Nuclear magnetic moments randomly distributed, with no interaction with the static magnetic field (image from DUNN *et al.*, 1994); (B) Hanson distribution sphere formed by vectors pointing out, for a given number of nuclei when the magnetic moments are transferred to the origin, showing the null result of the system (image from LEVITT, 2001).

When the saturated sample is subjected to an external magnetic field ( $\vec{B}_0$ ), the magnetic moments test a torque, but do not align with that field. In fact, the torque exerted on these moments, associated with the spin causes a precession movement around  $\vec{B}_0$  (Figure 6).

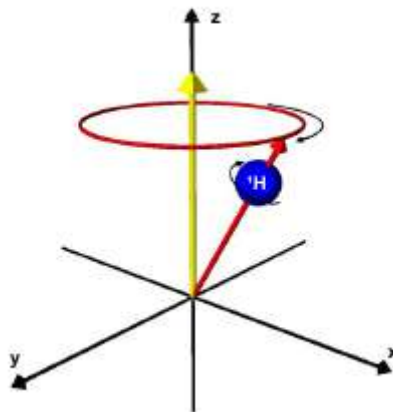


Figure 6 – Schematic of the spin precession movement of the center  $^1\text{H}$ .  $\vec{B}_0$  is represented by the yellow arrow (image from COATES *et al.*, 1993).

Since each isotope has its own value of the magnetogyric ratio, its nuclei are precessed with a specific frequency for each element having a magnetic field of the same intensity. The frequency of Resonance or Larmor Frequency is in the radio frequency range (MHz), being precessed at millions of cycles per second around  $\vec{B}_0$ . The importance of this frequency within an NMR experiment is that it allows the spins to absorb/release electromagnetic radiation (energy) with maximum efficiency (MESQUITA, 2017), thereby permitting the tool to interact specifically with a certain type of atomic nucleus.

Taking into account that each nucleus precesses differently, both in terms of intensity and direction, each nucleus tends to reorient itself around  $\vec{B}_0$  over time depending upon molecular thermal agitation, thereby differentiating the precession angles and resulting in two distinct energy states. The magnetic moments reorient, mostly in a direction parallel to  $\vec{B}_0$  when the magnetic energy is low, and in a direction anti-parallel to the field when magnetic energy is high. The redistribution of these moments is called polarization, being subtle, capable of generating a liquid magnetization  $\mu_0$ , resulting from the vector sums of the magnetic moments, having the same direction as  $\vec{B}_0$ , as seen in Figure 7.

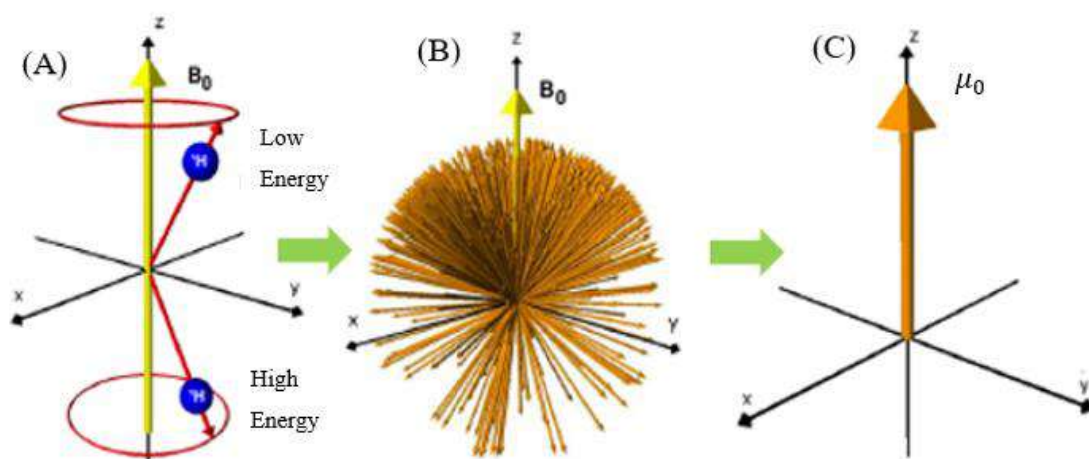


Figure 7 – (A) Spin precession under two energy states: low energy and high energy, (B) schematic design demonstrating preferential alignment of the spins in the direction of  $\vec{B}_0$ , (C) resulting magnetization from the  $\mu_0$  system due to preferential orientation of the spins (images adapted from COATES *et al.*, 1993).

The intensity of  $\mu_0$  can be observed and is proportional to the number of protons in the system ( $N_p$ ), the magnetogyric ratio of the nucleus ( $\gamma$ ), the intensity  $\vec{B}_0$ , and the inverse of the absolute temperature of the system ( $T$ ) through Curie's law as follows:

$$\mu_0 = N_p \frac{\gamma^2 h_p^2 I_p (I_p + 1)}{3T (4\pi^2) kB} B_0 \quad (2.26)$$

where  $kB$  is the Boltzmann constant,  $h_p$  is the Planck constant and  $I_p$  is the quantum spin number of the nucleus (COATES *et al.*, 1993).

The polarization phenomenon does not occur instantly. The entire process occurs exponentially over time, causing the magnetization to grow to a maximum equilibrium value  $\mu_0$ , which can be described as a function of  $M_z$  (final magnetization at the  $z$ -axis):

$$\frac{dM_z}{dt} = \frac{M_z - \mu_0}{T_1} \quad (2.27)$$

$$M_z(t) = \mu_0 \left( 1 - e^{-\frac{(t-t_i)}{T_1}} \right) \quad (2.28)$$

where  $t_i$  is the initial time of exposure of the sample to the field  $\vec{B}_0$ , and  $T_1$  is the time constant with which the magnetization grows exponentially until equilibrium, called the longitudinal relaxation time. The term “relaxation” is used to indicate the new state of equilibrium in which the system finds itself, caused by disturbance of the external magnetic field  $\vec{B}_0$ .

Even though it is possible to detect the NMR signal through longitudinal magnetization, its realization is not trivial. Therefore, in conventional NMR applications, the resulting magnetization is reoriented, leaving it parallel to the  $xy$  plane and the return is detected until the equilibrium condition. For this new reorientation, an oscillating magnetic field  $\vec{B}_1$ , perpendicular to the position  $\vec{B}_0$ , moves the protons aligned from the longitudinal direction (direction of  $\vec{B}_0$ ) to the transverse plane.  $\vec{B}_1$  is generated by providing a radiofrequency pulse, with the specific Larmor frequency of the proton, with sufficient duration for the nuclei to incline in relation to the  $\vec{B}_0$ . The result is the proton precession at Larmor frequency perpendicular to  $\vec{B}_0$  having its maximum NMR signal when tilted at  $90^\circ$  (Figure 8).

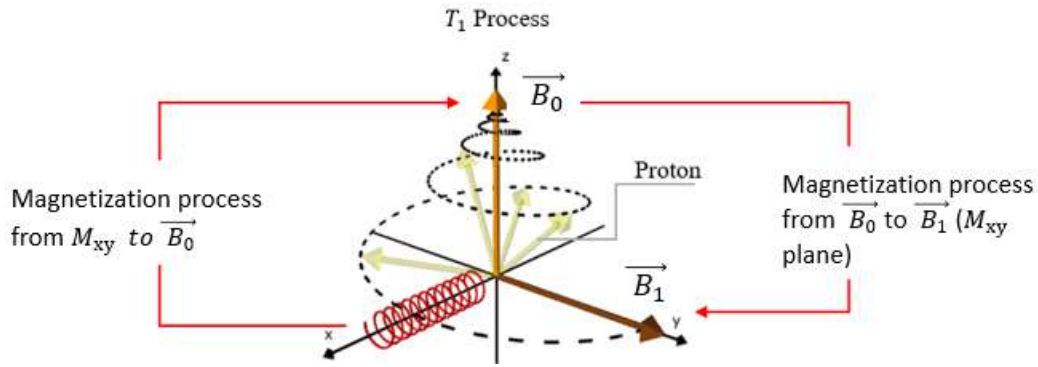


Figure 8 – Schematization of the transversal relaxation process, which happens spirally (image adapted from DUNN *et al.*, 2002).

In an NMR laboratory routine, the samples are saturated by a fluid, such as water or oil, wrapped in Teflon to prevent desaturation, and then introduced into the NMR spectrometer. Internally, the equipment has a radio frequency (FR) coil positioned perpendicularly between two permanent magnets, with opposite polarizations, for the generation of  $\vec{B}_0$ . The coil is connected to electronic circuits responsible for the emission of the FR pulses from the oscillating field  $\vec{B}_1$  and the detection of the signal induced by the projection of the resulting magnetization on the  $xy$  plane ( $M_{xy}$ ). The circuits are connected to a computer that controls the application of the pulse sequences and receives the digitalized free induction decay (FID) signals, being the record of the damping of the intensity of this current over time Figure 9.

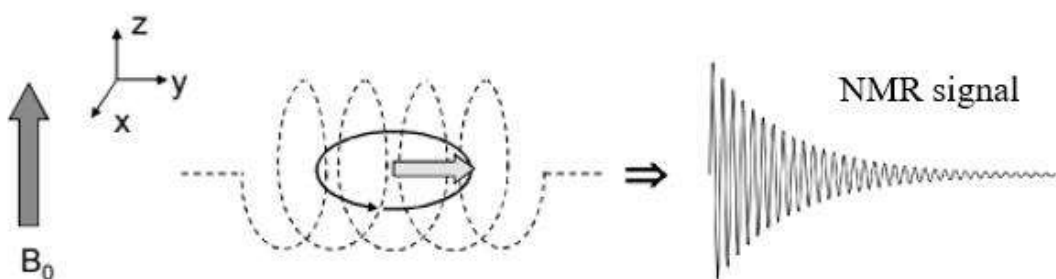


Figure 9 – Schematization of NMR signal generation: the magnetic flow produced during the relaxation process induces an electric current inside the detection coil, which exponentially leaves free induction decay (FID) signals (image adapted from DUNN *et al.*, 2002).

It is important to mention that when starting an NMR routine, the nuclei can either be at the lower or the higher energy state, although there is an excess of nuclei in the lower energy spin state. The sample is hit by a short pulse with different frequency ranges, causing the mentioned excess of nuclei to absorb the energy and flip from the lower to the higher spin state energy. When the nuclei fall back from the higher to the lower energy spin state, the NMR equipment detects the energy given off and gives a signal on an NMR spectrum. The signals (or peaks) on the intensity versus frequency graph represent a certain frequency, with intensity being the number of absorptions per frequency.

Since NMR tools operate based on hydrogen proton spin behavior by subjecting a brine-saturated rock to a strong magnetic field, the  $H^+$  ions in the liquid align themselves to the magnetic field, representing the so-called “polarization time”, or  $T_1$ . A second magnetic field perpendicular to the first field is produced and then interrupted. The time required for the protons to return to their original polarized state in the first field is the “relaxation time”, or  $T_2$ , measured in micro- or milliseconds. Energy absorbed from the magnetic field is proportional to the density of the  $H^+$  nuclei and proportional to the porosity of the rock. The ratio between  $T_1$  and  $T_2$  is proportional to the pore volume and is reported as a distribution curve of pore volumes along a time axis. Absolute volumes of the pore size classes are calculated based on some assumption about the shape factor and diffusion effects. Since  $T_2$  is a measure of the surface-to-volume ratio, rapid-relaxation times (short values of  $T_2$ ) correspond to smaller pore sizes, while longer relaxation times (large values of  $T_2$ ) correspond to larger pores (ADAMS, 2005).

Nuclear magnetic resonance provides information regarding porosity versus relaxation time through the absorption of electromagnetic radiation by certain atomic nuclei. A short relaxation time corresponds to small pores and a large relaxation time to large pores. The relaxation time referred to in this work is the transversal relaxation time ( $T_2$ ), responsible for reestablishing the initial condition of the resulting magnetization projection in the  $xy$  plane (LACERDA JR., 2018), which can be related to pore sizes and the free and bound fluid fractions (CARNEIRO *et al.*, 2014). The transversal relaxation time is transformed into pore radius, while frequency is transformed into incremental porosity for a given sample through mathematical relations.

Pore sizes are determined from NMR  $T_2$  distributions resulting from the interaction of the  $H^+$  protons at the rock/pore interface. The distributions of the  $T_2$  values are then converted into distributions of pore volumes using the relaxivity equation (ADAMS, 2005):

$$\frac{1}{T_2} = \rho_s(S/V) \quad (2.29)$$

where  $T_2$  is the transversal relaxation time (milliseconds),  $\rho_s$  is the surface relaxivity (micrometers/seconds) reflecting the ability of a rock surface to enhance relaxation, depending upon mineralogy, and  $S/V$  is a geometric factor accounting for the pore geometry (surface area per volume ratio). For spherical pores,  $S/V = 6/d$ , for cylindrical pores,  $S/V = 4/d$  and for sheet-like pores,  $S/V = 2/d$ , where  $d$  is the pore diameter. The complete relaxation equation is:

$$\frac{1}{T_{2(\text{measured})}} = \frac{1}{T_{2(\text{surface})}} + \frac{1}{T_{2(\text{bulk})}} + \frac{1}{T_{2(\text{diffusion})}}, \quad (2.30)$$

Reformulating Eq. (2.29) in terms of the pore radius using the measured  $T_2$  (seconds) gives

$$r = \rho_s T_2 n, \quad (2.31)$$

where  $r$  is pore radius in micron-meters and  $n$  is the shape factor (i.e., for cylindrical geometry,  $r = \rho_s T_2 2$ ).

## 2.10 Representative Elementary Volume

A representative elementary volume (REV) can be defined as the volume which captures a representative quantity of a sample's heterogeneity (BEAR, 1972). In other words, REV is that volume at which macroscopic properties, such as porosity or permeability become insensitive to small changes in the volume of the analyzed sample (SILVA *et al.*, 2018) and region of interest (ROI) within the sample (CORBETT *et al.*, 2015). REV's can vary in size according to the petrophysical property of interest (VIK *et al.*, 2013a; VIK *et al.*, 2013b). Figure 10 shows how one can define an REV: a petrophysical property is

measured for two different ROIs (within the blue and red squares) with varying volumes ( $V_1, V_2, V_3\dots$ ). REV is the minimum volume above which the petrophysical property with different ROIs does not change substantially. This means that a value for a given property has been found from the smallest possible sample, effectively representing the macroscopic medium that does not significantly change within a given size interval. The graph in Figure 10 shows the petrophysical property as a function of sample volume of two different regions of interest (ROIs), shown for simplicity in 2D.

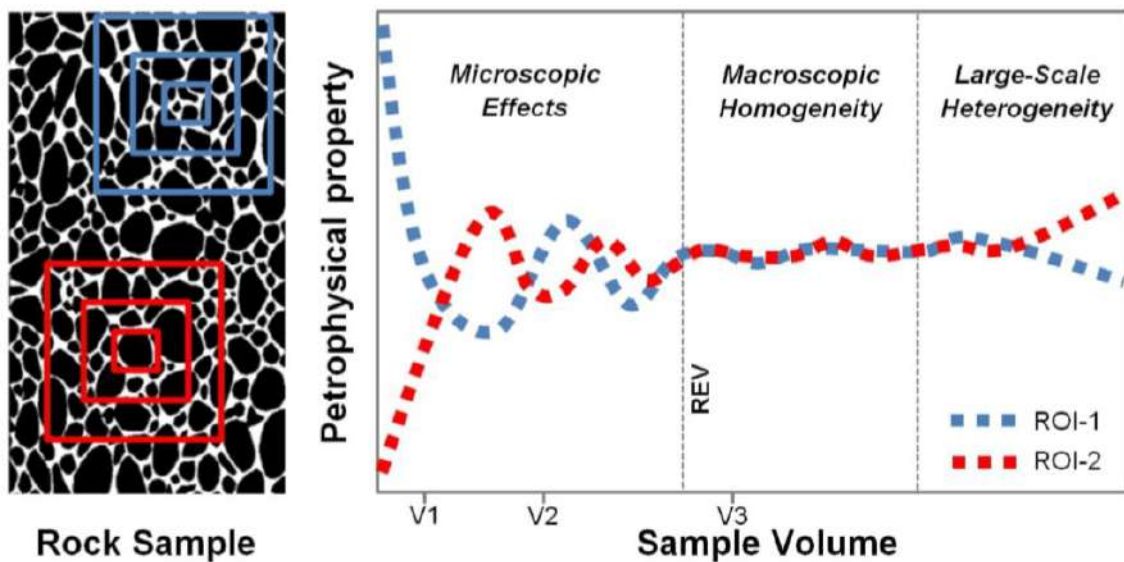


Figure 10 – Definition of the Representative Elementary Volume (REV) for a particular petrophysical parameter (Image from SILVA *et al.*, 2018).

REVs were investigated recently by DA SILVA (2019) by submitting varying sizes of Kocurek Industries limestone samples to NMR,  $\mu$ CT and basic petrophysics. They found that for the limestones they studied, specifically Edward Brown limestone, the sample volume should be larger than  $6,000 \text{ mm}^3$  ( $6 \text{ cm}^3$ ) for the porosity REV (within a confidence percentage of 93.5%). They also simulated permeabilities using a pore network modeling computational code, PoreFlow (RAOOF & HASSANIZADEH, 2013, 2010b; RAOOF *et al.*, 2010), for different sample sizes. Samples larger than  $6,900 \text{ mm}^3$  were found to have permeability values of the same order of magnitude as those from basic petrophysical routine core analysis in the laboratory. However, only samples larger



than 13,700 mm<sup>3</sup> were able to closely reproduce the laboratory permeability values (DA SILVA, 2019).

The limestones investigated in this work through NMR,  $\mu$ CT, the evaporation method, mercury porosimetry, and basic petrophysics were larger than the smallest REV's researched by da Silva in 2019. The studied samples are hence expected to be REV-representative in terms of their petrophysical properties, thus making it possible to reliably address upscaling techniques.

## 2.11 Fractals

As noted by HUNT *et al.* (2014), porous media have been modeled in many different ways: as random or regular sphere packs, as bundles of capillary tubes, as pore networks, and with fractal concepts. The term fractal comes from the Latin “fractus”, which by definition means a broken part or a piece. In mathematics, fractals are self-similar geometrical sets which are associated with generalizations of the concept of spatial dimensions. The fractal dimension represents the degree of occupation of the fractal geometry in space, indicating the irregularities of the geometrical figure. If the fractal geometry is inserted on a plane, its fractal dimension is between 1 and 2. If inserted in three-dimensional space, the fractal dimension is between 2 and 3.

For decades it was believed that the heterogeneities of porous media were random and uncorrelated, and would change significantly over length scales much smaller than the media's linear extent. Evidence accumulated over the years suggest, however, that natural porous media may exhibit correlations in the spatial distribution of their properties at multiple length scales. This finding can be analyzed by using fractal distributions to describe how the properties of a porous medium depend on the observation scale, how the properties are correlated and how to correctly model the correlations (HUNT & SAHIMI, 2017). Because of the self-similarity of fractals, it is possible to use fractal dimensions to aid in upscaling. Hence, to upscale flow or transport properties of a porous medium from small samples to the continuum scale, percolation theories and other techniques use fractal dimensions and the basic concepts of self-similarity.

The concept of fractals was firstly introduced in the 1960s by Mandelbrot (MANDELBROT, 1967) and since then has been extensively used in many fields of science. While fractal models introduced later, in the 1990s, can represent complex natural media successfully in terms of predicting the porosity and water retention curve, their application to flow properties such as the permeability is still somewhat less accurate (HUNT *et al.*, 2014).

The question remains of how to best model fluid movement in a porous medium. Fractal concepts have been introduced and presented as a well-suited approach for flow modeling because of their simple description of highly ramified spaces. Fractal theories offer a propitious framework for addressing the complexity of disordered, heterogeneous, hierarchical porous media, though porous media can at best only be approximated using these models since the natural objects are only statistically self-similar (HUNT *et al.*, 2014).

Power-law functions are often used in fractal analyses. A particularity of power-law functions is that they are linear when plotted on a log-log scale. The power-law function for describing a fractal number-size distribution is the number of fractal objects with size equal or greater than  $l_f$  is given by (HUNT *et al.*, 2014):

$$N(\geq l_f) = k l_f^{-D_f} \quad \text{with } l_{f,min} < l_f < l_{f,max} , \quad (2.32)$$

where  $k$  is a constant and  $D_f$  is the fractal dimension of the porous medium.

The probability density function (PDF) of fractals  $f(l_f)$ , i.e., the number of objects with size between  $l_f$  and  $l_f + dl_f$ , is proportional to the first derivative of Eq. (2.32):

$$f(\geq l_f) \propto l_f^{-1-D_f} . \quad (2.33)$$

which can be written in the form:

$$f(l_f) = C_{PDF} l_f^{-1-D_f} \quad \text{with } l_{f,min} < l_f < l_{f,max} , \quad (2.34)$$

where  $C_{PDF}$  is a constant, found by taking the integral of the probability density function  $f(l_f)$  from  $l_{f,min}$  to  $l_{f,max}$  and setting it equal to 1 (the area below the PDF curve should be equal to 1):

$$C_{PDF} = \frac{D}{l_{f,min}^{-D_f} - l_{f,max}^{-D_f}} \quad \text{with } l_{f,min} \ll l_{f,max} . \quad (2.35)$$

Primary fractal models account for two phases (pore and solid) and may be either pore fractal or solid fractal models. In a model, the solid or pore matrix is fractal with the number-size and probability density distributions both following a power-law distribution. Even though the pore phase may not be geometrically fractal, its number-size distribution can be given by a power-law function (as by Eq. (2.32)).

Below is a simple comparison between Euclidean and fractal dimensions. In a homogeneous system, the Euclidean volume scales up with the cubic power of their linear dimension. This may not be true for heterogeneous (fractal) systems. Consider a square with sides of length  $l$ , as well as a set of squares of side lengths equal to  $nl$ , where  $n$  is an integer, that forms larger figures as shown in Figure 11.

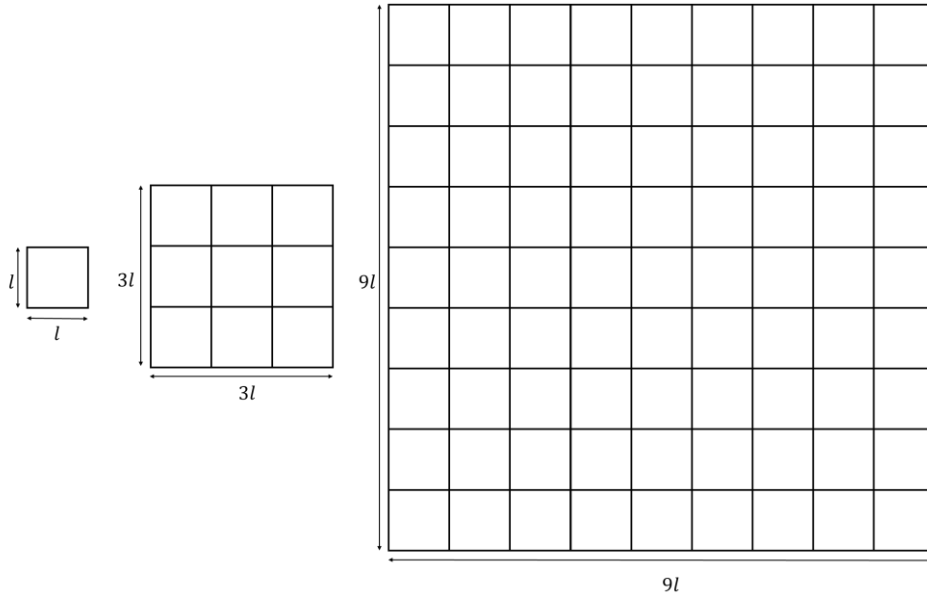


Figure 11 – In Euclidean geometry, the area of a square varies according to its side length to the second power.

For a square with sides of length  $l$ , one has:

$$A_s = cl^\tau , \quad (2.36)$$

where  $A_s$  is the area, and where the constant  $c$  is equal to 1 and exponent  $\tau$  equal to 2 for squares. Hence, from left to right, the area of the squares in Figure 11 can be calculated

as shown in Table 1 (assuming  $l = 1$ ). For more complicated Euclidean objects, the constant  $c$  changes according to the shape, and  $\tau$  according to the dimension. For example,  $c = \frac{\pi}{2}, \tau = 2$  for a half circle;  $c = \frac{\sqrt{3}}{4}, \tau = 2$  for an equilateral triangle;  $c = 1, \tau = 3$  for a sphere; and  $c = \frac{4\pi}{3}, \tau = 3$  for a pyramid.

Table 1 – Area calculations for Euclidean geometry. The Euclidean dimension  $\tau$  is an integer.

| $L = l$         | $L = 3l$        | $L = 9l$        |
|-----------------|-----------------|-----------------|
| $A_s = cL^\tau$ | $A_s = cL^\tau$ | $A_s = cL^\tau$ |
| $A_s = 1.1^2$   | $A_s = 1.3^2$   | $A_s = 1.9^2$   |
| $A_s = 1$       | $A_s = 9$       | $A_s = 81$      |

Fractal objects, on the contrary, behave differently. The Sierpinski Carpet, for example, is a flat fractal figure (ANTON & RORRES, 2001). The set can be understood as the gathering of eight non-congruent and non-overlapping subsets, each of which is congruent to the contraction of the original set by a factor of  $1/3$ . The construction of the Sierpinski Carpet starts from a two-dimensional Euclidean figure (a square). This square is subdivided into nine parts, from which the central part is being removed to obtain eight remaining small squares. Each square is then subdivided again into nine parts, with the central part being removed. This iteration process can be repeated infinitely as shown by Figure 12.

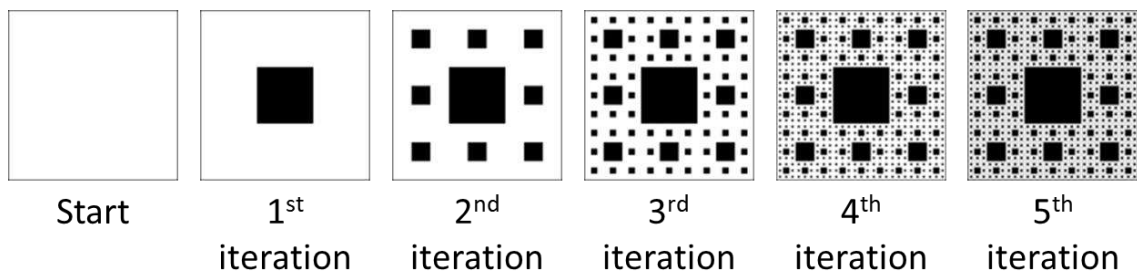


Figure 12 – Generation of a Sierpinski Carpet through iterations. Holes are in black.

To calculate the fractal dimension of the Sierpinski Carpet, one small section of the  $n^{th}$  iteration is analyzed as follows (see also Figure 13). The dimension  $\alpha$  of the Sierpinski Carpet can be obtained from the inserted Euclidean figures. The areas of the hole (with  $L = l$ ) and the surrounding outer square (with  $L = 3l$ ) minus the hole are given by

the entries in Table 2 (again assuming  $l = 1$ ). Since the Sierpinski Carpet is self-similar, the fractal dimension calculated for a given section is representative for the fractal geometry after  $n$  iterations.

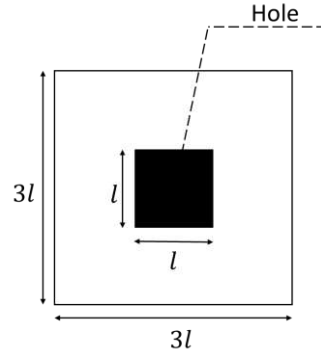


Figure 13 – Section of Sierpinski Carpet

Table 2 – Calculation of fractal dimension  $\alpha$  for the Sierpinski Carpet and its components (hole and outer squares) based on a small section of the  $n^{th}$  iteration.

| <i>Hole</i>                      | <i>Outer Square</i>     | <i>Outer Square – Hole</i>               |
|----------------------------------|-------------------------|--|
| $A = cL^\alpha$                  | $A = cL^\alpha$         | $A = cL^\alpha$                          |
| $1 \times 1 = 1 \times 1^\alpha$ | $A = 1 \cdot L^\alpha$  | $A = 1 \cdot L^\alpha$                   |
| $\alpha = 2$                     | $3 \times 3 = 3^\alpha$ | $(3 \times 3) - (1 \times 1) = 3^\alpha$ |
|                                  | $\alpha = 2$            | $8 = 3^\alpha$                           |
|                                  |                         | $\alpha \approx 1.893$                   |

For spatially heterogeneous fractal figures, e.g. a cube with porosity  $\emptyset$  as in a three-dimensional Sierpinski cube, consider the Euclidean example in Figure 14. The first cube on the left is multiplied by a constant, so it becomes the cube on the right, representing the upscaling technique. The volume of each cube can be given by:

$$V_s(L_0) = V_0, \tag{2.37}$$

$$V_s(L_1) = V_{s1},$$

and the volume of the upscaled Euclidean cubic object is:

$$V_s(L) = \frac{V_{s0}}{L_o^3} L_1^3. \tag{2.38}$$

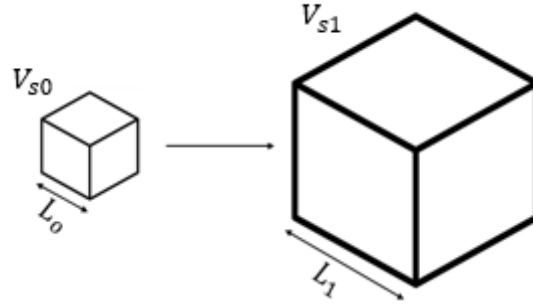


Figure 14 – Comparison of two Euclidean geometry cubes that sample the fractal set. Volume is a function of the lateral length to the  $n^{th}$  power (where  $n$  is an integer), and a constant that varies with the shape of the object.

The term  $\frac{V_{s0}}{L_0^3}$  in Eq. (2.37) is a constant and the dimension is equal to 3, where  $V_{s0}$  and  $L_0$  are the initial volume and side length, respectively.  $L_1$  is the length of the upscaled object. For a more general fractal system, one must have:

$$V_s(L) = \frac{V_{s0}}{L_0^D} L_1^{D_f}, \quad (2.39)$$

where  $D_f$  is the fractal dimension,  $\frac{V_{s0}}{L_0^D}$  is the multiplying constant with  $V_{s0}$  and  $L_0$  representing the initial volume and side length, respectively, and  $L_1$  is the length of the upscaled object.

Given these statements, a fractal cubic object can have its upscaled porosity given by:

$$\emptyset = \frac{V_s(L)}{L^3} = \frac{V_{s0}}{L_0^D} L^{D_f-3} = \frac{V_{s0}}{L_0^3} \left(\frac{L}{L_0}\right)^{D_f-3} \quad \text{or} \quad \emptyset(L) = \emptyset_o \left(\frac{L}{L_0}\right)^{D_f-3}, \quad (2.40)$$

where  $\emptyset(L)$  is the upscaled porosity and  $\emptyset_o$  the initial porosity. Eq. (2.40) shows that if  $D_f = 3$ , the upscaled porosity is the same as the initial porosity.

Fractal analysis is a useful tool to facilitate the definition of an REV. This study shows how the fractal dimension connects with REV and the formulation of permeability models. The fractal dimension shows how the pores permeate through the medium, which can be bidimensional or tridimensional, allowing one to interpret the rock volumes being studied and information to be obtained from those volumes.

### **2.11.1 Linear regression**

To find the fractal dimension of a given structure described by a power-function, such as those given by Eqs. (2.31) to (2.33) and (2.35), the exponent must be calculated. The fractal dimension is found by plotting the power-law function and corresponding data on logarithmic scales, and subsequently fitting a linear equation to the plotted data. The linear coefficient equals the fractal dimension. The  $R$ -squared ( $R^2$ ) statistical measure then informs how well the fitted regression line represents the measured data on the logarithmic scale linearized data. The closer to unity, the better the fit. The straight line on a logarithmic plot is a fitted linear regression and the data may fall close to the line when  $R^2 \rightarrow 1$ . Such relationships are often typical of power functions.

## **2.12 Permeability models based on The Thomeer Hyperbola**

It is also possible to estimate the permeability based on the entire pore (body or throat) size distribution of a sample. The following approaches make use of the full MICP pore throat distribution to do so.

### **2.12.1.1 Pore throat distribution Thomeer hyperbola**

Before reviewing calculations of the permeability from a MICP pore throat distribution in this section, the representation of the MICP pore throat distribution as a Thomeer hyperbola must be discussed. When the capillary pressure and corresponding bulk volume of mercury injection capillary pressure (MICP) are plotted on a log-log scale, a smooth curve approximating a hyperbola is generally obtained (THOMEER, 1960), as shown in Figure 15. The asymptotes  $(BV)_{P_\infty}$  and  $P_d$  in this figure are the bulk volume occupied by mercury at infinite pressure and the extrapolated displacement pressure, respectively.

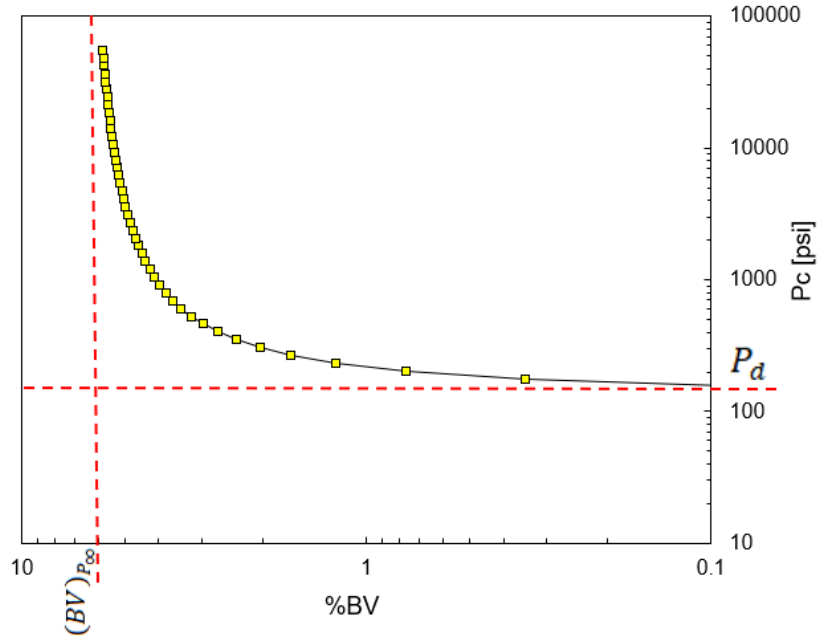


Figure 15 – When plotted on log-log axes, the MICP capillary pressure  $P_c$  versus bulk volume  $BV$  curve generally resembles a hyperbola.

Given the MICP data of pressure and bulk volume, the hyperbola equation in Figure 15 can be written as:

$$\frac{(BV)_{P_c}}{(BV)_{P_\infty}} = e^{-G(\log P_c/P_d)}, \quad (2.41)$$

where  $G$  is the pore geometrical factor, a function of the constant  $C_s$  that defines the shape of the curve:

$$G = \frac{C_s^2}{2.303}. \quad (2.42)$$

When the capillary pressure  $P_c$  versus  $(BV)_{P_c}$  is plotted on a logarithmic scale, it is possible to fit a hyperbola to the points. This allows the hyperbola in Figure 15 to be rewritten as:

$$(\log P_c - \log P_d)(\log(BV)_{P_c} - \log(BV)_{P_\infty}) = -C_s^2, \quad (2.43)$$



where  $P_c$  is the capillary pressure,  $(BV)_{P_c}$  is the bulk volume of injected mercury, and  $(BV)_{P_\infty}$  and  $P_d$  are the asymptotes as shown in Figure 15. Taking the derivative of (2.43) with respect to  $P_c$  eliminates  $P_d$  from the equation to give a linear equation:

$$\log(BV)_{P_c} = \log(BV)_{P_\infty} + C \sqrt{\frac{P_c}{(BV)_{P_c}} \frac{d(BV)_{P_c}}{dP_d}} . \quad (2.44)$$

Values of  $(BV)_{P_\infty}$  and  $C$  can be obtained from Eq. (2.44). Afterwards,  $G$  is easily estimated from Eq. (2.42). Replacing these values in Eq. (2.43) returns the value of  $P_d$ . The values of  $P_d$ ,  $(BV)_{P_\infty}$  and  $G$  can then be used to place the fitted hyperbola on top of the data.

The derivative of the fitted hyperbola of the cumulative bulk volume occupied by mercury versus the injection pressure, with bulk volumes converted to pore throat diameters ( $\mu\text{m}$ ), is best represented by a left-skewed pore throat histogram (LSPTH) (BUTING; CLERKE, 2013), as shown by the example in Figure 16. The filling of pores by mercury as it is injected defines the declining left-skewed tail of the LSPTH and the  $G$  parameter described above. The latter controls the distribution width and skewness of the LSPTH.

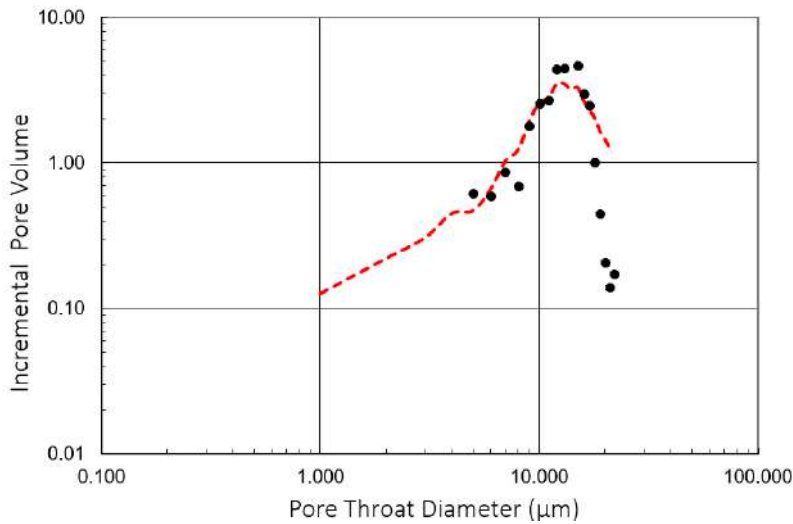


Figure 16 – Left-skewed pore throat histogram (LSPTH), shown in red, derived from MICP data (black) of pressure and incremental bulk volume converted into pore throat diameters (CLERKE; MARTIN, 2004; THOMEER, 1983, 1960).

### 2.12.1.2 Permeabilities estimated from the Thomeer hyperbola (Thomeer Monomodal K)

The Thomeer approach (THOMEER, 1983) requires that the closure correction and entry pressure ( $P_d$ ) values are defined. This can be done using a spreadsheet (CLERKE & MARTIN, 2004) that uses the Thomeer calculations and allows for multiple quick iterations to assess and determine the closure correction and the mercury entry pressure value. With these values and the LSPTH, a fitted Thomeer function can be used to calculate the air permeability. Assuming a fixed value of 2 for the exponent of  $BV/P_d$ , THOMEER (1983) found the following equation for the air permeability (in millidarcies) from a regression analysis of data from 165 siliciclastic and 114 carbonate samples:

$$k_{air} = 3.8068 \{BV/P_d\}^2 G^{-1.3334} . \quad (2.45)$$

The Thomeer model for the air permeability assumes that if the pore throat distribution is properly described by a Thomeer function, then the permeability model treats the cumulative pore volume ( $BV$ ) and the mercury entry pressure ( $P_d$ ) when mercury first enters the largest pore throats, in a symmetrical inverse manner after squaring.  $G$  values smaller than 1 (enhanced sorting and a narrow pore throat distribution) indicate a permeability enhancement above  $3.8068 \{BV/P_d\}^2$ , while  $G$  values larger than 1 (poor sorting and a wide pore throat distribution) indicate a permeability penalty. The permeability enhancement or penalty is controlled by  $G^{-1.3334}$ . When  $G$  is equal to unity, the permeability distribution is controlled only by  $3.8068 \{BV/P_d\}^2$ , with the pore throat distribution having no effect on the calculated permeability.

### 2.12.1.3 Buiting-Clerke tortuous and relative fractal tubular bundle model (B-C k integral)

BUITING & CLERKE (2013) expanded the tubular bundle model of Purcell for the permeability (PURCELL, 1949) to a fractal tubular bundle. The model assumes that the tubes responsible for breakthrough percolation are those with the largest diameter  $d$  (radius  $r_d$ ) with a tortuosity given by  $\frac{L}{L_d}$ , where  $L_d$  is the length of the first percolation

path (or the shortest flow path associated with the largest tube of radius  $r_d$ ) and  $L$  is the outer length of the sample (Figure 17). Tortuosity can be considered as a fractal-like property, with fractal dimension  $D_f$  between 1 and 2 (MANDELBROT, 1967). The subscripts  $d$  refer to the largest pores with diameter  $d$  that lead to breakthrough percolation

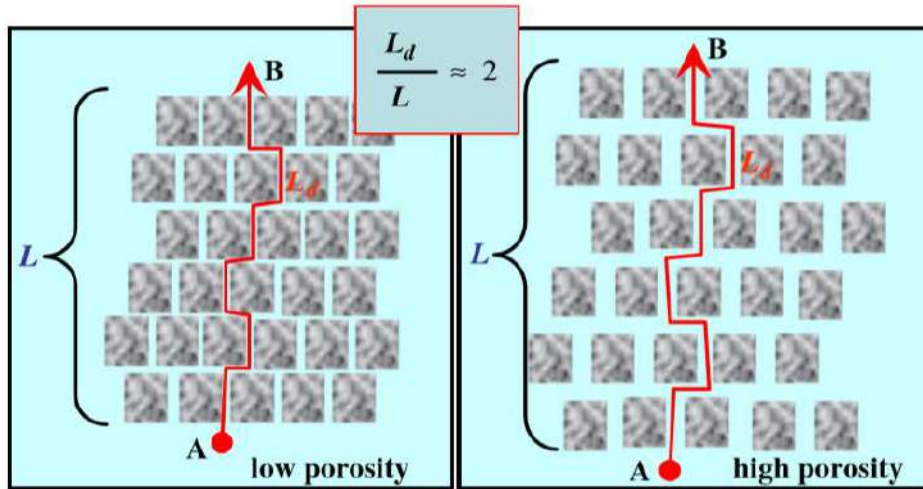


Figure 17 – The shortest tortuous path from A to B, corresponding to the percolation path of a liquid passing through a porous carbonate rock. The ratio  $L_d/L$  for carbonates with angular grains is usually around 2. For rounded grains, the ratio varies between 1.3 and 1.6 (extracted from BUITING & CLERKE, 2013).

Using the fractal argument and appropriate rod length, an expression relating the diameter of the tubes to their lengths has been proposed to calculate the permeability. The general expression for permeability in terms of the general Thomeer bulk volume curve of an MICP experiment is given by (BUITING; CLERKE, 2013):

$$k = \frac{\varepsilon^2}{4} D_f^{-2(1-D_f)} Q_d \left( \frac{L}{L_d} \right)^2 \hat{B}_v^Q(2D_f), \quad (2.46)$$

where  $\varepsilon = 2[\sigma \cos \theta]_{Hg-Air} = 734 \frac{\text{dyn}}{\text{cm}} = 107 \text{ psi } \mu\text{m}$ ,  $P$  is the pressure of the injected mercury,  $Q = \ln(P)$  and hence  $Q_d = \ln(P_d)$ .  $\hat{B}_v^Q(2D_f)$  is obtained through the analysis of  $\tilde{B}_v^Q(2D_f)$ , which is an integral transform of the MICP fractional bulk volume  $BV$  in the  $Q$ -domain, given by:

$$\tilde{B}_v^Q(2D_f) \equiv \int_{Q=Q_d}^{\infty} B_v^Q(2D_f) e^{-2D_f Q} dQ, \quad (2.47)$$

which is an incomplete Laplace transform since the integration starts at  $Q_d \neq 0$ . Nevertheless, it is possible to use a normal Laplace transform for  $Q_d > 0$  since  $BV(Q < Q_d) = 0$ :

$$\tilde{B}_v^Q(2D_f) \equiv \int_{Q=Q_d}^{\infty} B_v^Q(2D_f)e^{-2D_f Q} dQ \equiv \hat{B}_v^Q(2D_f). \quad (2.48)$$

### **2.12.1.1 Thomeer-based Buiting-Clerke permeability estimation (B-C k fit)**

It is possible to obtain a permeability value for the single Thomeer fitted hyperbola. Considering Eq. (2.46) and assuming  $L_d/L = 2$  and  $D_f = 1.56$  (common values for carbonates), the permeability of the unimodal pore system is given by (BUITING & CLERKE, 2013):

$$k_{BC} \approx 506 \frac{BV^\infty}{P_d^2} e^{-4.43\sqrt{G}}. \quad (2.49)$$

## **2.13 Permeability models based on single MICP points**

To estimate permeability, the unspecified pore volume flow paths must be specified by a model, while respecting the total porosity and the pore (body or throat) distribution function. The permeability of porous media is known to be governed primarily by pore throats instead of pore bodies. For this reason, the MICP pore throat distribution should better correlate with the permeability.

The Carman-Kozeny (CARMAN, 1937, 1956; J. KOZENY, 1927) and Purcell (PURCELL, 1949) capillary bundle models for granular porous media are frequently used to compute the permeability. These models represent good approximations for MICP tests performed on regularly shaped cuttings without measurement artifacts. Their application to pore throat distributions from less accurate and precise data sources have spurred the use of the single point permeability models of Swanson (SWANSON, 1981) and Winland (KOLODZIE, 1980; PITTMAN, 1992). These models do not require much computational

effort since they consider one single point on the pore throat distribution away from the entry pressure. This since the MICP closure correction can be difficult and time consuming to implement, but still frequently necessary for irregular cuttings from exploration wells (CLERKE & MARTIN, 2004). Details of the Swanson and Winland models are provided next.

### 2.13.1 Swanson Model

The Swanson formula (SWANSON, 1981) for air permeability focuses on plotting the bulk volume ( $BV$ , in percentage) of the pore throat distribution versus capillary pressure ( $P_c$ ). The Swanson point is obtained by finding the coordinates that give the largest  $BV/P_c$  ratio. Hence, the air permeability (millidarcy) is then given by:

$$k_{air} = 399 \left\{ \left| \frac{BV(P_c)}{P_c} \right|_{max} \right\}^{1.691}, \quad (2.50)$$

where the prefactor 399 and the exponent 1.691 were obtained after fitting the formula to data from 116 carbonates and 203 sandstones.

### 2.13.2 Winland Model

In an study of 322 samples, Winland (KOLODZIE, 1980; PITTMAN, 1992) correlated the pore throat radius of slices through the pore throat distribution at the 35<sup>th</sup> percentile of the pore throat cumulative bulk volume (35% of mercury saturation),  $r_{35}$ , to the uncorrected air permeability (milliDarcy) and the total porosity (percentage) to obtain:

$$\log(r_{35}) = 0.732 + 0.588 \log(k_{air}) - 0.864 \log(\emptyset). \quad (2.51)$$

The  $r_{35}$  value is significantly above the closure correction and entry pressure region (PITTMAN, 1992) and assumes that the pore throat diameter at the 35<sup>th</sup> percentile along the total porosity ( $\emptyset$ ) coordinate contains information necessary to compute the pore system air permeability.

## 2.14 Percolation Theory and Critical Path Analysis

### 2.14.1 Background of Critical Path Analysis

When a sufficient fraction of sites (or bonds) is locally connected to form a global connection, the system is said to be at percolation, or to percolate, as defined by HUNT *et al.* (2014). Percolation theory is an approach developed to study electronic transport in amorphous semiconductors. Several researchers (e.g., AMBEGAOKAR *et al.*, 1971), however, noticed that the technique's main concept is applicable to a broader class of disordered media when they developed Critical Path Analysis (CPA). CPA is a powerful analytical tool, based on percolation theory, which aims to predict permeability and electrical conductivity of porous media with a broad pore-size distribution (PSD) (GHANBARIAN *et al.*, 2016a). Among many theoretical approaches used to model permeability, such as capillary bundle theories and effective media approximations, critical path analysis from percolation theory is thought to be a reliable method, especially for heterogeneous and disordered media (GHANBARIAN *et al.*, 2016b). The tool has shown to be promising for determining permeability in strongly heterogeneous media where fluid flow occurs only through a small subset of the highest-conductance pores (DAIGLE, 2016; FRIEDMAN & SEATON, 1998; HUNT, 2001; SKAGGS, 2011).

AMBEGAOKAR *et al.* (1971) noted that fluid flow in disordered porous media with a broad conductance distribution is dominated by pores having conductances larger than a given critical value  $g_c$ , corresponding to a critical pore radius  $r_c$ , where  $g_c$  is the smallest conductance among the set of conductances forming a sample-spanning cluster (*i. e.*,  $g > g_c$  or  $r > r_c$ ). This means that the pore with radius  $r_c$  is the smallest pore in the sample-spanning cluster. According to CPA, pores with sizes corresponding to  $r < r_c$  do not contribute significantly to the overall (or effective) permeability. The elimination of these pores with  $r < r_c$  reduces the medium to a percolation system (SAHIMI, 2011). This means that hydraulic or electric conduction, as per definition in CPA, occurs mainly through the larger pores of the medium since they have the higher conductivities.

In CPA, the porous medium is assumed to be composed of flow pathways (pores) with different conductances (*i. e.*, having different abilities to transmit flow). The conductance is a function of the pore size. Since larger pores have higher conductances due to capillary

forces, most of the flow happens in high-conductance pathways that comprise a fraction of the total volume available to flow (DAIGLE, 2016). Macroscopic flow is hence dictated by the low-conductivity restrictions along these pathways (HUNT, 2001).

Before continuing, the definition of probability density function becomes necessary. Probability density functions (PDFs), fundamental parts of the field of statistics, can be used to describe pore size distributions (or histograms). Some examples of PDFs are exponential, Gaussian or normal, power-law, log-normal and Weibull. PDFs can be used to specify the probability of a random variable falling within a particular range of values, as opposed to taking on a single value. This probability is given by the integral of the PDF over that range of values (GRINSTEAD & SNELL, 2009). A random variable is a measurable function defined on a probability space, whose outcomes are typically real numbers (STEIGERWALD, [s.d.]). In other words, a PDF is a function used to describe the pore size distribution in a continuous form.

For illustration, consider a discrete distribution of pore size classes over a range of pore sizes,  $r_i$ , within  $r_0 \leq r_i \leq r_m$  where  $r_0$  and  $r_m$  are the smallest and largest pore radii, respectively. The discrete size classes  $r_i$  are defined as  $r_i = q^i r_m$  with  $q < 1$  and distributed according to a function such as the power-law probability function,  $PDF(r) \propto r^{-D_f}$ , where  $D_f$  is the fractal dimension. To translate the discrete function into a continuous one, a probability density function is used (HUNT, 2001; HUNT & GEE, 2002) for the pore radius  $r$ . For a power-law distribution function, the probability density function for the pore radius distribution would be  $W(r) = A_N r^{-D-1}$ , where  $A_N$  is a normalization constant.

HUNT *et al.* (2014) describe that for the bond percolation problem, a PDF denoted as  $f(g)$  is used to find the conductance between two arbitrary nearest neighbor sites with values between  $g$  and  $g + dg$ . Normalization of this PDF leads to:

$$\int_0^{\infty} f(g) dg = 1. \quad (2.52)$$

The median conductance is the smallest conductance that cannot be avoided by the current; this value is known as the critical conductance ( $g_c$ ). The critical conductance value can be obtained from:

$$\int_{g_c}^{\infty} f(g)dg = P_{cr} , \quad (2.53)$$

where  $P_{cr}$  is the critical probability from percolation theory, the value at which a sample-spanning cluster forms with a minimum number of connecting parts necessary for percolation. Conductance is intrinsically related to pore radii and the pore size distribution (PSD). CPA defines then the critical pore radius ( $r_c$ ) as the pore radius below which pores do not substantially contribute to fluid flow and permeability, as discussed above. Permeability reportedly is strongly related to the critical pore radius  $r_c$  (GHANBARIAN *et al.* (2016b) and references therein). Let  $f(r)$  be the volumetric PDF of pore sizes in the medium. Considering pores as cylinders with radius  $r$ , a critical pore size,  $P_{cr}$ , can be defined by

$$\int_{r_c}^{\infty} f(r)dr = P_{cr} . \quad (2.54)$$

The critical pore size represents the smallest restriction along the sample-spanning cluster (HUNT *et al.*, 2014), and is related to the critical conductance ( $g_c$ ). If  $P_{cr}$  and  $f(r)$  are known, it is possible to estimate permeability from the critical hydraulic conductance, minding the dependence of the relationship on pore size distribution and connectivity of the pore system (HALPERIN, 1989). Eqs. (2.52), (2.53) and (2.54) are graphically represented in Figure 17, where the shadowed area A for each curve represents the total area according to the limits of each integral. Plot C shows that the critical radius corresponds to the mode of the PSD.

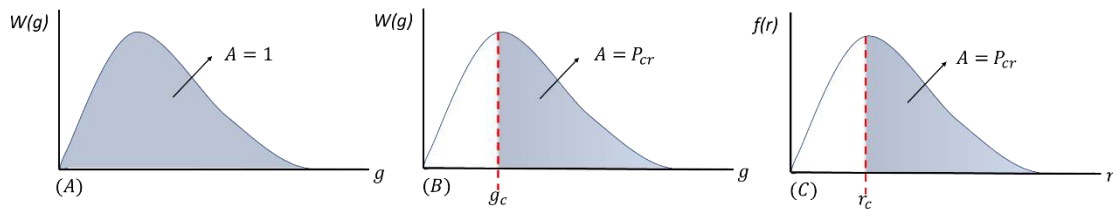


Figure 18 – Plots showing, from left to right, probability density function curves based on Eqs. (2.52), (2.53) and (2.54), respectively.

Because the relationship between the macroscopic hydraulic and electrical conductances is assumed to be the same as the pore-scale distribution of the hydraulic and electrical



conductances (HUNT, 2001; SKAGGS, 2011), predicting permeability at larger scales from pore-scale distributions becomes easier. Electrical and hydraulic conductances usually relate differently with pore size, but considering that hydraulic conductance is defined by Poiseuille's law and electrical conductance by Ohm's law, the ratio of the critical electrical and critical hydraulic conductances ( $g_c^e$  and  $g_c^h$ ) in a cylindrical pore is proportional to  $r_c^2$  (BANAVAR & JOHNSON, 1987; DAIGLE, 2016; FRIEDMAN & SEATON, 1998; HUNT, 2001; SKAGGS, 2011). This proportionality provides a relationship between permeability and electrical conductivity. Based on this relationship, many CPA based methods for estimating permeability have been proposed and proven to be satisfactory and consistent with other methods that use electrical conductivity to estimate permeability (DAIGLE, 2016).

CPA has been shown to predict permeability remarkably well for samples or formations covering nearly 4 (DAIGLE, 2016) to 6 (HUNT & GEE, 2002) orders of magnitude in length. To reach this conclusion, the Friedman & Seaton method (FRIEDMAN & SEATON, 1998) that estimates permeability from the ratio  $g_c^h/g_c^e$  was used in conjunction with a percolation theory-based description of electrical conductivity, allowing the Friedman & Seaton method to be extended to media with significant surface conductivity.

### 2.14.2 Percolation Threshold

Flow in disordered systems of nearly any structure is dominated by connecting paths near the percolation threshold (HUNT *et al.*, 2014). As per definition, the percolation threshold is the fraction of pore volume that must be occupied for a sample-spanning cluster to form. In other words, the percolation threshold is the incremental pore volume (or porosity) of the connecting pathway that first leads the sample to percolation. This fraction can be easily obtained from the inflection point of the cumulative pore volume versus mercury pressure curve obtained from a mercury injection experiment (KATZ & THOMPSON, 1987). Figure 19 illustrates how to obtain  $P_{c,Hg}$ , mercury pressure values based on the critical radius of a sample. KATZ & THOMPSON (1986) argued that the

inflection point of the MICP porosimetry curve corresponds to the critical pore radius and the saturation at which the sample-spanning cluster first occurs.

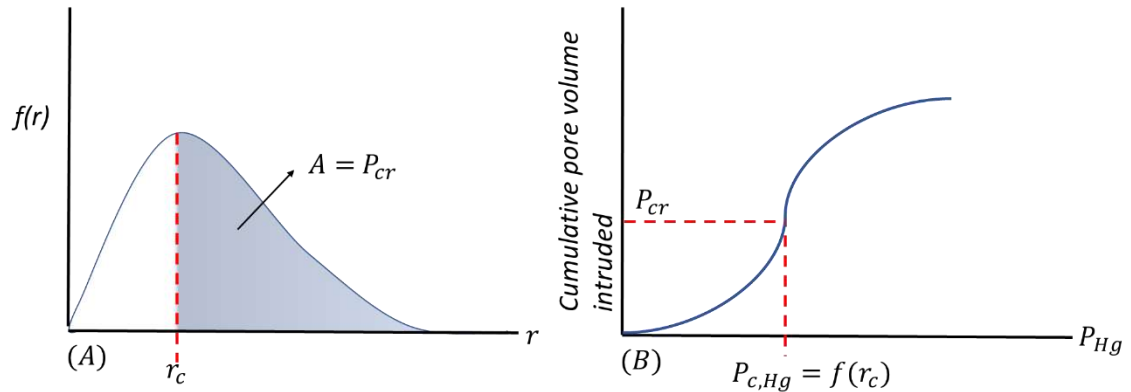


Figure 19 – MICP experimental results of percolation. The percolation threshold,  $P_c$ , occurs at the inflection point of the curve, represented in red, when a sample-spanning cluster formed by mercury-filled pores first emerges. Image has been adapted from DAIGLE (2016).  $P_{c,Hg}$  is the mercury pressure at the critical radius  $r_c$ .

### 2.14.3 Parametrization of pore size distribution

Pore size distributions can be parametrized using different pore size volumetric probability density functions (PDFs), such as power-law, lognormal, or bimodal distributions. Substituting the selected volumetric PDF,  $f(r)$ , into Eq. (2.54) gives then the porosity for the interval defined in the integral. The critical pore size can be calculated by rearranging  $\int_{r_c}^{\infty} f(r)dr = P_c$  for  $r_c$ . Given  $r_c$ , for example from the MICP pore size distribution model or the intruded cumulative pore volume inflection point, it is possible to calculate  $P_c$ .

### 2.14.4 Single-Phase Permeability from CPA

According to studies by BANAVAR & JOHNSON (1987), FRIEDMAN & SEATON (1998) and SKAGGS (2011), among others, application of Ohm's law to a pore with radius  $r$  gives the electrical conductance  $g^e$  of the pore:

$$j^e(r) = g^e(r)\Delta V, \quad (2.55)$$

where  $j^e(r)$  is the electrical current and  $\Delta V$  the voltage drop across the pore. The hydraulic conductance,  $g^h$ , follows from Poiseuille law as:

$$j^h(r) = g^h(r)\Delta P , \quad (2.56)$$

where  $j^h(r)$  is the volumetric flow rate and  $\Delta P$  the pressure drop across the pore. For cylindrical pores, the electrical conductance  $g^e(r)$  is given by (FRIEDMAN & SEATON, 1998):

$$g^e(r) = \frac{\pi r^2 \sigma_w}{l} , \quad (2.57)$$

and the hydraulic conductance for a cylindrical pore by:

$$g^h(r) = \frac{\pi r^4}{8\mu l} , \quad (2.58)$$

where  $\sigma_w$  is the electrical conductivity of the saturating fluid,  $\mu$  is its dynamic viscosity, and  $l$  is the pore length. Although FRIEDMAN & SEATON (1998) also studied slit-shaped pores, their approach is not presented here since MICP, NMR, microtomography and pore network modeling all consider cylindrical pore radius distributions. Moreover, cylindrical geometries are understood to work better for carbonate rocks (A. BOYD, *personal communication*).

The critical conductances are  $g_c^e = g^e(r_c)$  and  $g_c^h = g^h(r_c)$  (HUNT *et al.*, 2014). The critical ( $g_c$ ) and macroscopic ( $g_m$ ) conductances of natural porous media proportionally relate as  $g_m \approx g_c$  (HUNT, 2001). Based on this, KATZ & THOMPSON (1986, 1987) were the first to use critical path analysis to relate permeability to the electrical conductivity.

The Katz & Thompson approach (KATZ & THOMPSON, 1986, 1987) links permeability  $k$  to the electrical conductivity and the critical pore radius,  $r_c$ . They assumed that pores were cylindrical with radii approximately proportional to length ( $r \propto l$ ). The effective, or upscaled, permeability is then given by:

$$k = \frac{1}{C_{KT,r}} \frac{\sigma_b}{\sigma_w} r_c^2 = \frac{1}{56.5 F} \frac{1}{F} r_c^2 , \quad (2.59)$$

in which  $\sigma_b$  is the bulk electrical conductivity,  $\sigma_w$  is the saturating fluid electrical conductivity,  $r_c$  is the critical pore radius, and  $c_{KT} = 56.5$  is a constant as specified by Katz & Thompson, although other authors have used different values. Eq. (2.59), like others based on CPA, requires estimates of the electrical conductivity and the inverse of the formation factor,  $F$ :

$$\frac{\sigma_b}{\sigma_w} = \frac{1}{F} . \quad (2.60)$$

The method proposed by FRIEDMAN & SEATON (1998) is a common CPA-based approach, among other approaches using the assumption that  $g_m \approx g_c$  (e.g., BANAVAR & JOHNSON (1987) and LE DOUSSAL (1989)), which leads to the following equation:

$$\frac{K}{\sigma_b} = \frac{g_c^h}{g_c^e} = \frac{\pi r_c^4}{8\mu l} \frac{l}{\pi r_c^2 \sigma_w} = \frac{r_c^2}{8\mu \sigma_w} , \quad (2.61)$$

where  $K$  is the hydraulic conductivity and  $\sigma_b$  the bulk electrical conductivity. The ratio of  $K$  over  $\sigma_b$  is equal to the ratio of the critical conductances.

Assuming that the permeability  $k$  is given by  $k = \mu K$  (HUNT, 2001; SKAGGS, 2011), Eq. (2.61) may be defined in terms of the permeability as:

$$k = \frac{r_c^2}{8} \frac{\sigma_b}{\sigma_w} . \quad (2.62)$$

This equation allows measurements of the permeability in terms of the electrical conductivity and the pore size distribution (DAIGLE, 2016). The macroscopic permeability can now be expressed in terms of a pore size (in this case  $r_c$ ) and pore connectivity (in this case  $\frac{\sigma_b}{\sigma_w}$ ) (DAIGLE, 2016; KATZ & THOMPSON, 1986). It is important to emphasize that the initial assumption leading to Eq. (2.62), of having the same critical pore size for both electrical and hydraulic conductance, is valid only for porous media with negligible surface conductivity.

More recently, other authors revisited the work by KATZ & THOMPSON (1986) by investigating relationships to estimate the permeability from pore size properties. These

methods are reviewed by GHANBARIAN *et al.*, (2016b). The latest study (SKAGGS, 2011) proposed the relationship:

$$k = \frac{1}{32} \left( \frac{\gamma_h}{\gamma_e} \right)^{-y} \frac{\sigma_b}{\sigma_w} d_c^{\gamma_h - \gamma_e} = \frac{1}{c_S} \frac{\sigma_b}{\sigma_w} d_c^2, \quad (2.63)$$

in which  $c_S = 53.5$ ,  $\gamma_h = 4$  and  $\gamma_e = 2$  for independent  $l$  and  $d$  parameters, and  $c_S = 72.2$ ,  $\gamma_h = 3$  and  $\gamma_e = 1$  for a self-similar medium, with related  $l$  and  $d$  ( $d \propto l$ ) (HUNT, 2001; HUNT *et al.*, 2014; KATZ & THOMPSON, 1986), and with  $y$  being a prefactor exponent. SKAGGS (2003) showed that  $y = 0.74 \pm 0.01$  by means of Monte-Carlo simulations.

### 2.14.5 Critical radius for CPA

Unspecified flow paths must be specified using a model while respecting the total porosity and the pore (throat or body) size distribution. Only then is it possible for a permeability value to be computed (CLERKE & MARTIN, 2004). For instance, CPA-based approaches allow calculations of the effective permeability after obtaining the critical pore radius and the electrical conductivity (or formation factor).

The critical radius can be obtained from the inflection point of MICP data. The inflection point of the cumulative mercury saturation curve occurs where the second derivative is zero, while the first derivative (the slope of the curve) is zero where the peak of the incremental PSD data occurs. The set of data hence has to be numerically differentiated. This can be seen in Figure 20.

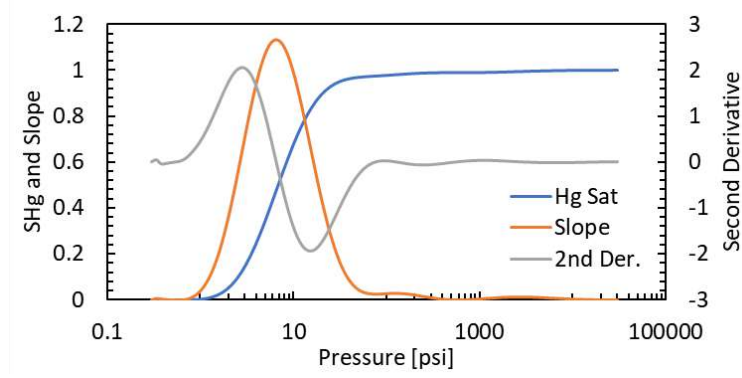


Figure 20 – MICP cumulative mercury saturation curve (Hg Sat) and its first and second derivatives. This graph confirms that the peak of the pore size distribution corresponds to the MICP inflection point of the cumulative saturation curve.

The critical radius can also be obtained from an equation proposed by GHANBARIAN-ALAVIJEH & HUNT (2012a), based on an earlier work by HUNT & GEE (2002):

$$r_c = r_{max} \left( 1 - \frac{\theta_s}{\beta} \right)^{\frac{1}{3-D_f}}, \quad (2.64)$$

where  $r_{max}$  is the radius of the largest accessible pore in the medium,  $D_f$  is the fractal dimension,  $\theta_s$  is the water content at full saturation, equal to porosity  $\Phi$ , and  $\beta$  is a pore-solid fractal parameter, represented by (GHANBARIAN *et al.*, 2017) as:

$$\beta = \frac{s c_p r_{max}^{3-D_f}}{3-D_f} = \frac{(\Phi - \theta_r) r_{max}^{3-D_f}}{r_{max}^{3-D_f} - r_{min}^{3-D_f}} ; \Phi < \beta < 1, \quad (2.65)$$

in which  $s$  is a shape factor (for cylinders,  $s = 2\pi$ ),  $\theta_r$  is the residual water content,  $r_{min}$  is the radius of the smallest accessible pore in the medium and

$$c_p = \frac{D_f}{r_{min}^{-D_f} - r_{max}^{-D_f}}. \quad (2.66)$$

The fractal dimensionality may be calculated from (HUNT & GEE, 2002):

$$3 - D = \frac{\log(1 - \Phi)}{r_{min}^{-D_f} - r_{max}^{-D_f}}. \quad (2.67)$$

The critical radius can also be obtained from the van Genuchten (VAN GENUCHTEN, 1980) water retention curve when fitted to the MICP data. This is an interesting approach for scattered data since the data are then smoothed by the van Genuchten model (GHANBARIAN *et al.*, 2016). The inflection point can be calculated based on the derivation proposed by (DEXTER, 2004).

DEXTER (2004) assumed that every pore of radius  $r$  is emptied at pressure head  $h = r/C$ , where  $C$  is a pore geometry dependent coefficient, equal to  $2\sigma$ , being  $\sigma$  the surface tension of water. Let the incremental volume  $V$  of pores be a function of the natural logarithm of the pore radius  $r$ . One has then

$$\frac{dV}{d(\ln r)} = \frac{dV}{dr} \frac{dr}{d(\ln r)} = \frac{dV}{dr} r. \quad (2.68)$$

Application of Eq. (2.68) to the water retention equation by VAN GENUCHTEN (1980), i.e., Eq. (2.10), results in:

$$\frac{dV}{d(\ln r)} = V_t(\theta_s - \theta_r)nm(\alpha C)^n \left[ 1 + \left( \frac{\alpha C}{r} \right)^n \right]^{-(m+1)} r^{-n} \quad (2.69)$$

And

$$\begin{aligned} \frac{d^2V}{d(\ln r)^2} \propto (m+1)n(\alpha C)^n \left[ 1 + \left( \frac{\alpha C}{r} \right)^n \right]^{-(m+2)} r^{-2n} \\ - n \left[ 1 + \left( \frac{\alpha C}{r} \right)^n \right]^{-(m+1)} r^{-n} \end{aligned} \quad (2.70)$$

where  $m=1-1/n$ . The inflection point of the PSD curve occurs when Eq. (2.70) equals zero, which implies that:

$$(\alpha C)^n n(m+1)r^{-n} - n \left[ 1 + \left( \frac{\alpha C}{r} \right)^n \right] = 0 \quad (2.71)$$

or

$$\{(\alpha C)^n n(m+1)r^{-n} - n(\alpha C)^n\}r^{-n} = n \quad (2.72)$$

from which one obtains:

$$r = \alpha C m^{1/n} \quad (2.73)$$

Eq. (2.73) is comparable with the pressure head  $h_i$  at the inflection point of the water retention curve:

$$h_i = \frac{1}{\alpha} \left[ \frac{1}{m} \right]^{1/n} \quad (2.74)$$

Eq. (2.74) shows that the inflection point coincides with the maximum of the PSD when expressed as a function on the logarithm of pore size (its radius). It is also possible to obtain the pressure head at the inflection point when the PSD (or water retention curve) is plotted on a regular scale. This was done by WANG *et al.* (1997) who obtained

$$h_i = \frac{1}{\alpha} m^{1/n} \quad (2.75)$$

This equation may be more suitable for relatively coarse-textured media such as sandstones and other media that lose their water more quickly when they dry out.

## 2.15 Pore Network Modeling

A (pore) network model is a detailed model of a porous medium, generally incorporating pore-scale descriptions of the medium and the physics of pore-scale events (BERKOWITZ & EWING, 1998). Pore network modeling (PNM) has been widely used to simulate flow in porous media at the pore scale (BULTREYS *et al.* (2016); RAOOF *et al.* (2012)). Percolation theory and network modeling are closely related. As stated by BERKOWITZ & EWING (1998), while network models yield insight into the behavior at the pore scale, percolation theory brightens the larger-scale behavior as it considers randomness in the geometry of the porous medium, the fluid properties and interactions between them. The two techniques are briefly compared below.

With PNM, a node can be a pore channel (a narrow opening, or throat) or a pore intersection (a larger opening, or a pore body). Numerical discretization within a PNM is based on the topology (physical structure) of the porous medium, while not being able to



explicitly capture gradients below the adopted pore scale. Under these conditions, it is possible to upscale parameters in these models (RAOOF & HASSANIZADEH, 2010a). Nevertheless, the models allow the use of a simplified description of the porous medium, thereby making it possible to scale up from the pore scale to a representative elementary volume (REV), with statistically meaningful averages and parameters.

The PNM approach has been used for many purposes, such as for single- and multi-phase flow in petroleum engineering (JOEKAR-NIASAR *et al.*, 2010; RAOOF & HASSANIZADEH, 2012; REEVES & CELIA, 1996) and in hydrology and soil physics (BERKOWITZ & BALBERG, 1993; EWING & GUPTA, 1993a, 1993b; FERRAND & CELIA, 1992), as well as for upscaling reactive/adsorptive transport (ACHARYA *et al.*, 2005; KÖHNE *et al.*, 2011; RAOOF & HASSANIZADEH, 2010a).

RAOOF *et al.* (2012) compared PNM with continuum scale models that use macro-scale parameters such as porosity, permeability, and tortuosity, as well as constitutive relationships such as the permeability and diffusivity as a function of fluid saturation, and their variations due to changes in the pore geometry as a result of precipitation or dissolution processes (e.g., PFINGSTEN, 2002).

The PNM methodology is used by PoreFlow (RAOOF *et al.*, 2012), a computational code that reproduces the microstructure of real porous media. To represent the topology of a porous medium in a typical PNM, it is necessary to provide the pore coordination number,  $z_c$ , which is the number of pore throats connected to an individual pore body. In the network model of RAOOF & HASSANIZADEH (2012), pore throats can be oriented in 13 directions, thereby allowing a maximum coordination number value of 26. This can be seen by the schematic in Figure 21.. A coordination number equal to zero means that the pore body has been eliminated from that lattice point.

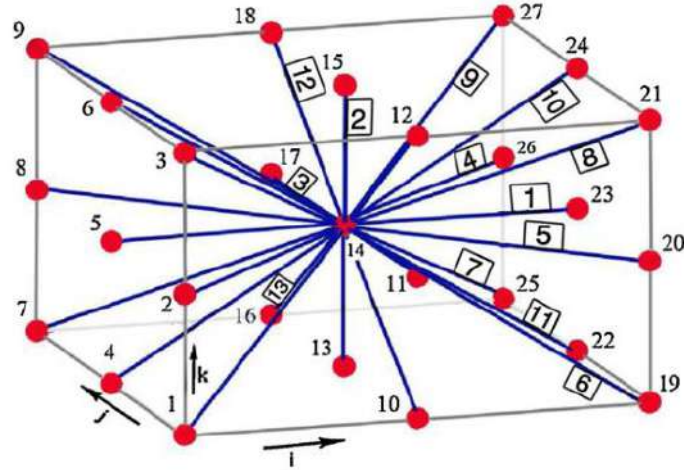


Figure 21 – Schematic of a network consisting of three pore bodies in each of 13 directions. Numbers inside squares represent the possible throat directions. Numbers without squares represent pore bodies. Only pore body number 14 in the center has its connections (pore throats) to other pores shown. This figure was extracted from RAOOF & HASSANIZADEH (2012, 2010b).

A pressure gradient can be applied between two opposite vertical boundaries of the pore network, thus causing the fluid to flow across the network. Boundaries parallel to flow are considered as no-flow boundaries. Discharge through a pore throat can be described with the Hagen-Poiseuille equation, which is valid for laminar flow:

$$q_{ij} = g_{ij}(p_j - p_i), \quad (2.76)$$

where the total volumetric flow rate through pore throat  $ij$ , given by  $q_{ij}$ , is proportional to the conductance of pore throat  $ij$ ,  $g_{ij}$ , and where  $p_i$  and  $p_j$  are the fluid pressures in pores bodies  $i$  and  $j$ , respectively. The conductance of a pore throat having a cylindrical cross-section with a radius  $r_{ij}$ , a fluid dynamic viscosity  $\mu$  and length  $l_{ij}$ , is given by:

$$g_{ij} = \frac{\pi r_{ij}^4}{8\mu l_{ij}}. \quad (2.77)$$

Assuming incompressible, steady-state flow, the sum of discharges of pore throats connected to a pore body must be zero:

$$\sum_{j=1}^{z_i} q_{ij} = 0, j = 1, 2, \dots, z_{c,i} , \quad (2.78)$$

where  $z_{c,i}$  is the coordination number for pore body  $i$ . Eq. (2.78) is applied to all pores except those on the inflow and outflow boundaries where pressure values are usually specified (the flow boundaries). By combining Eqs. (2.76) and (2.78) for every pore, a linear system of equations with a sparse and symmetrical positive-definite coefficient matrix is defined. The system of equations is solved for values of the pore body pressure. The flow velocity in every pore throat can be calculated with Eq. (2.76). If the network is an elementary representative volume (REV), the average pore water velocity,  $\bar{v}$ , is given by:

$$\bar{v} = \frac{(dQ/dt)L_n}{V_F} , \quad (2.79)$$

where  $dQ/dt$  is the time-derivative of the total discharge through the network,  $L_n$  is the length of the network and  $V_F$  is the total volume of fluid. From the total discharge, the pore network permeability can be calculated at a given time using Darcy's law:

$$k = \frac{\mu(dQ/dt)}{A_p \Delta P_{PNM} / L_n} , \quad (2.80)$$

in which  $\mu$  is the viscosity,  $k$  the intrinsic permeability,  $A_p$  the cross-sectional area of the network and  $\Delta P_{PNM}$  the pressure difference between the inlet and outlet boundaries of the network.

## **3 Materials and Methods**

### **3.1 Studied Samples**

This work analyzed limestone carbonate rock samples from one quarry and 29 petroleum reservoirs. Indiana Limestone High samples acquired from Kocurek Industries were obtained from a quarry, while another 29 limestones were obtained from diverse oil fields catalogued in the World Wide Rock Catalogue (WWRC), a commercial product by Core Laboratories (Houston, USA). The Indiana Limestones High samples from Kocurek were labeled “IH”, while limestones from WWRC were labeled “L”, all followed by a number for identification. Limestones from WWRC had their original formation names modified due to confidentiality matters.

The Kocurek Indiana Limestone samples were the only samples thoroughly examined using micro-tomography, HYPROP, WP4C and mercury extrusion techniques. The remaining laboratory routines and analyses were performed on all samples. All routines are explained below.

### **3.2 Basic Petrophysics Routine Core Analysis**

Basic petrophysical analyses serve as indirect methods for measuring porosity and permeability since they are limited by problems related to inefficient gas penetration and incapability to directly observe the pores (REIS NETO *et al.*, 2011).

#### **3.2.1 Porosity and Permeability**

The permeability and porosity were measured using the DV-4000 Poropermeameter equipment by Weatherford Laboratories (WEATHERFORD LABORATORIES, 2017), which is an advanced automatic steady-state gas (nitrogen) permeameter – helium porosimeter system. The equipment produces estimates of the porosity based on Boyle-Mariotte’s Law, which considers the pressure-volume product to be constant within a closed system at a constant temperature. Two cells with known volumes communicate within the system. Since one of them (the core-holder, with volume  $V_1$ ) holds the sample (with volume  $V_{sample}$ ) inside the core-holder, gas is injected in the other vase (volume

$V_2$ ) at known confined pressure  $P_2$ . The gas then expands and migrates to the core-holder vase. The final pressure  $P_f$  is measured as:

$$P_i V_i = P_f V_f , \quad (3.1)$$

where

$$P_i V_i = P_2 V_2 , \quad (3.2)$$

and

$$P_f V_f = P_f (V_1 + V_2 - V_{grains}) , \quad (3.3)$$

where  $V_{grains}$  is the grain volume within the sample:

$$V_{grains} = V_1 + V_2 - \left( \frac{P_2 V_2}{P_f} \right) . \quad (3.4)$$

The above information makes it possible to calculate the porosity:

$$\phi = 100 \left( \frac{V_{sample} - V_{grains}}{V_{sample}} \right) . \quad (3.5)$$

The equipment first measures the absolute permeability for air using Eq. (2.2). The Klinkenberg correction (KLINKENBERG, 1941) is subsequently used to reduce the air permeability to an equivalent liquid permeability by correcting for the effects of "slippage" of air in the sample, which does not happen with liquids. The Klinkenberg permeability is hence the corrected air permeability disregarding slippage (i.e., the liquid permeability, by varying the flowing pressure and extrapolating to infinite pressure).

This work does not consider directional permeability since the heterogeneity found in carbonates makes it impractical when layers are not found within the formations. Horizontal and vertical permeabilities have more impact on layered systems, such as sandstones.

The hydraulic conductivity ( $K$ ) can be obtained for both water (or liquids) and air (or gases) using the relation  $K = k \rho g_a / \mu$ , where  $k$  is permeability,  $\rho$  is the fluid density,  $g_a$  is the gravitational acceleration and  $\mu$  is fluid viscosity.

### 3.3 Water retention curve and hydraulic conductivity

The hydraulic properties of unsaturated porous media provide important information about single- and multi-phase fluid flow in the subsurface. They are critical to addressing many theoretical and practical studies in the soil, hydrogeologic, agricultural, civil and petroleum engineering disciplines. A large number of experimental methodologies has been developed and tested over the years to estimate the water retention,  $\theta(h)$ , and unsaturated hydraulic conductivity,  $K(h)$  or  $K(\theta)$ , relationships, where  $\theta$  is the volumetric water content,  $h$  is pressure head, and  $K$  the hydraulic conductivity. Most of the standard techniques, especially for the hydraulic conductivity, are suitable for intermediate or relatively wet conditions (DANE & HOPMANS, 2002; DURNER & LIPSIUS, 2005; LOONEY & FALTA, 2000), although some can also be applied to the dry range, such as hot-air, centrifugation, or dew-point methodologies (ARYA, 2002; DURNER & LIPSIUS, 2005; NIMMO *et al.*, 2002; SCANLON *et al.*, 2002).

To obtain water retention and related curves, the evaporation method has been widely used in the soils and hydrology literature, with studies starting as early as in the 1960s (GARDER & MIKLICH, 1962; WIND, 1968), followed by many others (e.g., IDEN & DURNER, 2008; and WENDROTH *et al.*, 1993, and references therein). Evaporation methods involve measurements of the pressure head at distinct depths within a cylindrical sample which, together with the measured evaporation rate from the top of the sample, make it possible to directly or inversely estimate the water retention and unsaturated hydraulic conductivity curves. The HYPROP system (PETERS & DURNER, 2008; PETERS *et al.*, 2015; SCHINDLER *et al.*, 2010, and others) is a widespread recent version of the evaporation method that involves semi-automated direct measurements of water retention and conductivity pairs over a wide range of pressure heads (the capillary pressure in terms of length units).

Numerous studies positively tested the HYPROP evaporation method against multi-step outflow and other methods (e.g., SCHELLE *et al.*, 2010; ZHUANG *et al.*, 2017). Synthetic data generated with the Richards unsaturated flow equation were also used successfully to test the HYPROP methodology (e.g., BEZERRA-COELHO *et al.*, 2018; IDEN *et al.*, 2019). The majority of these and other studies used the van Genuchten-Mualem expressions (VAN GENUCHTEN, 1980; VAN GENUCHTEN & NIELSEN,

1985) for the unsaturated hydraulic properties, while PETERS *et al.* (2015) used the equations of KOSUGI (1996) as well as the PDI model of Peters and colleagues (IDEN & DURNER, 2014; PETERS, 2014) to account for the effects of film and corner flow in very dry soils.

In this work, the HYPROP method is used for the wet range of water content but then complemented by measurements acquired by WP4C for the dry range. WP4C is a psychrometer procedure used in the dry water content range by measuring the relative humidity in the atmosphere through the use of two thermometers within a closed chamber. HYPROP evaporation and WP4C psychrometer methods are used in this work to evaluate the relation between volumetric water retention and the pressure head of an Indiana Limestone rock sample. Both apparatuses are commercialized by the METER Group (Munich, Germany).

### 3.3.1 The HYPROP setup

A schematic of the standard HYPROP arrangement adapted for a rock sample having a diameter of 3.81 cm is shown in Figure 22. The system involves pressure head measurements at two depths within a standard 5-cm short sample as water evaporates from the sample surface. Water content and the evaporation flux in time are determined by automated weighing the sample. The water retention and unsaturated hydraulic conductivity functions are estimated from the measured pressure heads and evaporation flow rate (PERTASSEK *et al.*, 2015).

The HYPROP measurement is restricted at the wet range by limitations of the pressure transducers to accurately register very small differences in the pressure head, which provides much justification for measuring the saturated hydraulic conductivity ( $K_s$ ) separately. In the dry range, restrictions are due to water outgassing, bubble formation and subsequent expansion of the bubbles, usually at about -800 cm (W. DURNER, *personal communication*). Improved tensiometers are now being used to allow measurements to pressure heads as low as -3000 cm or more (SCHINDLER *et al.*, 2010). Main advantages of the HYPROP system are its automation once the system is installed, and the fact that pairs of water content as a function of pressure head,  $\theta(h)$ , and hydraulic

conductivity as a function of pressure head,  $K(h)$ , are being generated. The latter means that no functional form of the hydraulic properties (e.g., Brooks & Corey or van Genuchten equations) needs to be selected beforehand.

Pressure heads are recorded at two locations (1.25 cm and 3.75 cm from the evaporating surface) versus time, while the evaporation rate is measured by repeated weighing. After fully saturating the sample, the HYPROP measurements begin and should continue until the upper tensiometer reaches a limiting value (SCHINDLER *et al.*, 2010). The measured tensiometer and sample weight data are then analyzed to provide estimates the average pressure head and water content of the sample, as well as the total head gradient between the two tensiometers, all versus time (PETERS *et al.*, 2015; SCHINDLER *et al.*, 2010). The HYPROP system assumes linear vertical distributions of the pressure head and the water content within the sample. These assumptions have been shown to be very much acceptable (BEZERRA-COELHO *et al.*, 2018; PETERS *et al.*, 2015). The HYPROP manual is available from the METER GROUP, [s.d.].

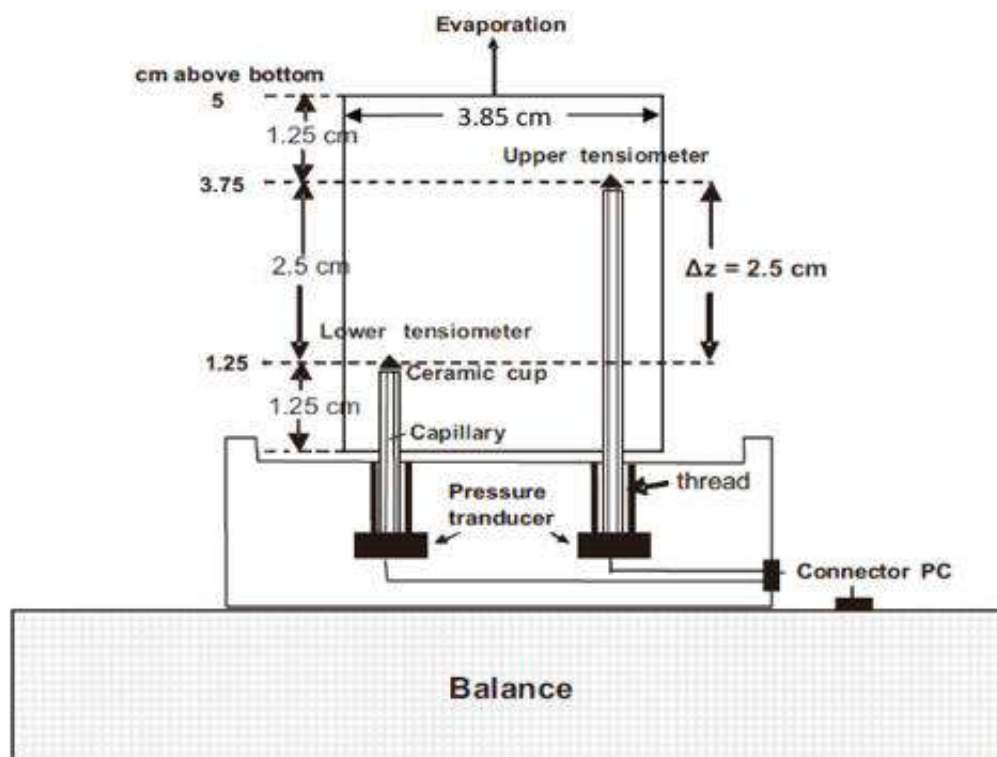


Figure 22 – Schematic of the HYPROP system as applied to the Indiana limestone sample (adapted from Schindler *et al.*, 2010).



For the experiments in this work, a saturated Indiana Limestone sample having a diameter of only 3.85 cm was used. Since the sample's diameter was smaller than the standard HYPROP's inner diameter of 5 cm, an impermeable ring manufactured with a three-dimensional printer was used, as shown by the schematic in Figure 22, and the picture in Figure 23 of the actual sample that was tested. A small rotary saw was used to vertically drill circular holes with a diameter of 0.5 cm through the rock sample to place the tensiometers and a holder pin at the bottom. The tensiometers shafts were placed within the holes such that the middle of the tensiometers cups was located at 1.25 and 3.75 cm from the evaporating surface. Fine- to silt-sized crushed rock particles extracted from the sample were used to ensure good lateral contact between the tensiometer shafts and the rock. The remaining open parts of the two holes above the tensiometers were capped with drilled-out plugs (Figure 23-B) from a neighboring sample of the same overall Indiana Limestone core used. Details concerning other aspects of the equipment and measurement procedure are provided by PERTASSEK *et al.* (2011).

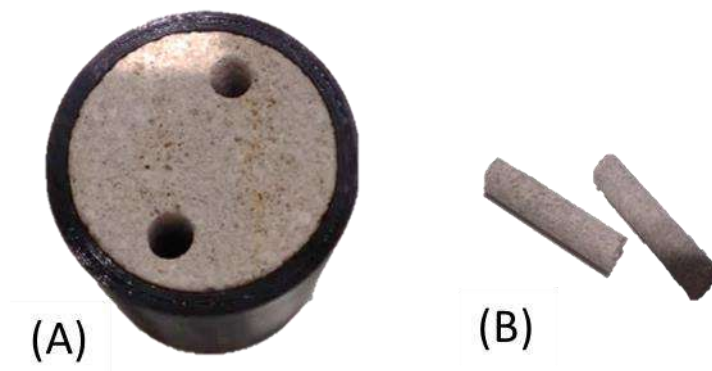


Figure 23 – (A) Actual sample used for the HYPROP measurements; notice the two drilled holes for the tensiometers. (B) Plugs used to cap the holes after installation of the tensiometers.

The HYPROP setup was used for hydraulic measurements down to pressure heads of about -800 cm. For the dryer measurements (above  $pF = -\log|h|$ ) the WP4C chilled-mirror dew point method was used.

### 3.3.2 HYPROP hydraulic measurements

A detailed overview of the HYPROP system, data acquisition and calculations are provided by PERTASSEK *et al.* (2011), and are only briefly summarized here. Again, to acquire the water retention and hydraulic conductivity data with HYPROP, two tensiometers are installed at depths  $z_1$  and  $z_2$  of the initially saturated sample, which is isolated at the bottom and with its laterals surrounded by a ring. The top is left open to the atmosphere to allow evaporation under natural conditions while placing the sample on a scale to measure the weight versus time. The pressure head and hydraulic gradient are calculated with the obtained soil water pressure heads (in kPa or cm). Volumetric water contents and water flow rates are calculated from automated measurements of the weight differences obtained by the scale. Data acquisition stops if either one of the tensiometers dries out or the weight changes become negligible. The remaining water content is determined by oven drying the sample for 24 hours, at  $105^\circ C$ . The initial water content is estimated from the weight of the initial sample, and/or from the weights of the sample at the end of the HYPROP experiment before and after over-drying and the evaporated water during the experiment.

Discrete data for estimating the water retention and conductivity relations are obtained from measurements of the sample weights ( $g^i$ ) and the pressure heads (cm)  $h_1^i$  and  $h_2^i$  at respective depths  $z_1$  and  $z_2$ . Calculations of the hydraulic conductivity assume that between times  $t^{i-1}$  and  $t^i$ , the water flow rate through a cross-section situated exactly between the two tensiometers, at the column center, is  $q^i = \Delta V^i / 2\Delta t^i A$ , where  $\Delta V^i$  is the water loss ( $cm^3$ ) determined from the observed weight changes,  $\Delta t^i$  is the time interval between two measurements and  $A$  is the cross-section area ( $cm^2$ ) of the column. Estimates of the hydraulic conductivity are then determined from the Darcy-Buckingham equation:

$$K^i(\bar{h}^i) = -\frac{q^i}{(\Delta h^i / \Delta z) + 1}, \quad (3.6)$$

where  $K^i$  is the related hydraulic conductivity (in  $cm\ h^{-1}$ )  $\bar{h}^i = 1/4 (h_1^{i-1} + h_2^{i-1} + h_1^i + h_2^i)$  is the average pressure head between the two tensiometers the during time interval,  $\Delta h^i = 1/2 ((h_2^{i-1} - h_1^{i-1}) + (h_2^i - h_1^i))$  is the average difference in the pressure head

between the two tensiometers, and  $\Delta z = z_2 - z_1$  is the distance between the tensiometers (cm).

### 3.3.3 WP4C

The HYPROP measurements can continue until some lower pressure head is reached, generally about -800 cm, unless special tensiometers are employed. When the upper tensiometer starts to fail, the HYPROP water retention data can be augmented with WP4C psychrometer data. WP4C equipment obtained from by the METER Group (Munche, Germany) was used for these measurements. The equipment uses chilled-mirror dewpoint techniques to measure the water potential of a sample (METER, 2020). The WP4C setup consists of a chamber used to equilibrate the sample within a closed-chamber headspace, and a mirror to detect condensation formed on its surface. When at equilibrium, the water potential of the air in the chamber is the same as the water potential of the sample. The temperature of the mirror is controlled very precisely by a thermoelectric cooler. A photoelectric cell is used to determine the dewpoint, the point at which condensation first occurs on the mirror, through the use of a beam of light that is directed to the mirror and reflected into a photodetector cell. The change in reflectance is observed by the photodetector cell when condensation is formed on the mirror. A thermocouple is attached to the mirror and records the temperature at which condensation happens. Hence, the water potential and temperature of the sample are obtained (CARDUCCI *et al.*, 2011) in the dry range to complete the information collected by HYPROP at the wet range. In this study, psychrometer measurements were performed on two 0.5 cm short Indiana Limestone samples having the same lateral dimensions as used for the HYPROP system. Before initiating the WP4C measurements, the rock porous volume was estimated to calculate the amount of water volume to be added to obtain a water content near saturation. Water was added to the sample with a dripper to distribute water evenly over the whole surface. Afterwards, the sample was allowed to equilibrate in a desiccator while variations of the laboratory air temperature were controlled using air conditioning. All WP4C measurements were preceded by equilibrating the temperature of the cup and the sample using a thermal equilibration plate obtained from METER (Munche, Germany). Weights of the sample were recorded immediately after each WP4C measurement, after

which the sample was returned to the desiccator. This procedure was repeated several times over a period of a few days. The WP4C data used for this work started at a pressure head of about -3000 cm (~3.5 pF), and continued until about -27,000 cm (~5.5 pF) when no more weight variations could be detected. After the last WP4C measurements, the samples were dried in an oven to 105°C until constant weight to obtain estimates of the dry mass of the rock sample, as well as of the water content after each WP4C step using the weight data after that step. To the best of the author's knowledge, HYPROP and WPC4 have only been used thus far only for soils; this is the first time a rock sample is tested.

In all retention functions used in this thesis, the water content is expressed in terms of the effective saturation  $S_e$  given by  $S_e = (\theta - \theta_r) / (\theta_s - \theta_r)$ , where  $\theta$  is the volumetric water content and the subscripts  $s$  and  $r$  refer to saturated and residual water contents, respectively. The unimodal water retention model of van Genuchten (VAN GENUCHTEN, 1980) retention function is given by Eq. (2.9), and the bimodal model by Eq. (2.19). In those equations,  $\alpha$  ( $cm^{-1}$ ) is a shape parameter related approximately to the inverse of the air entry pressure  $h_a$  ( $\alpha = -1/h_a$ ), and  $n$  is a dimensionless shape parameter that controls the slope of the retention curve depending upon the pore- or particle-size distribution of the medium. Samples with a narrow pore-size distribution generally have a larger  $n$  value (BEZERRA-COELHO *et al.*, 2018).

The abovementioned retention models are coupled with selected hydraulic conductivity models such as the capillary pore-bundle model of MUALEM (1976) as described in section 2.7.1. The Mualem model predicts the shape of the conductivity function from the shape of the retention function. This means that the shape parameters of the retention function also determine the shape of the relative hydraulic conductivity function,  $K_r(h)$ .

## 3.4 Imaging techniques

### 3.4.1 $\mu$ CT

X-ray microtomography applications aim to address some of the deficiencies of various direct and indirect techniques for measuring the petrophysical properties (REIS NETO *et al.*, 2011), such as mercury porosimetry and basic petrophysics. Micro-computerized tomography ( $\mu$ CT) complements analyses of porous media since it allows observations of the distribution of pores and solids through the use of three-dimensional reconstructed images.

Being able to visualize pores and mineral phases through different X-ray attenuations, which then automatically quantifies volumes in three-dimensional space, makes  $\mu$ CT technique a very attractive tool for characterizing and understanding the void volume of porous media. The basic tomography components are the X-ray source, the detector and a rotation system. In this study, the CoreTOM tomograph equipment, provided by TESCAN (Brno, Czech Republic), is used. The equipment and its basic components are depicted in Figure 24.

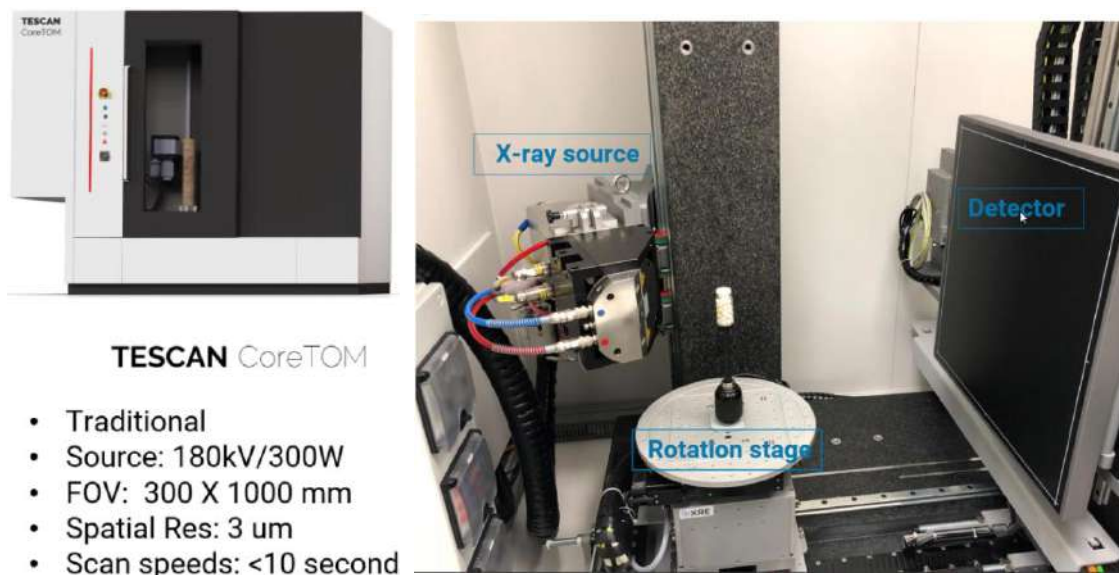
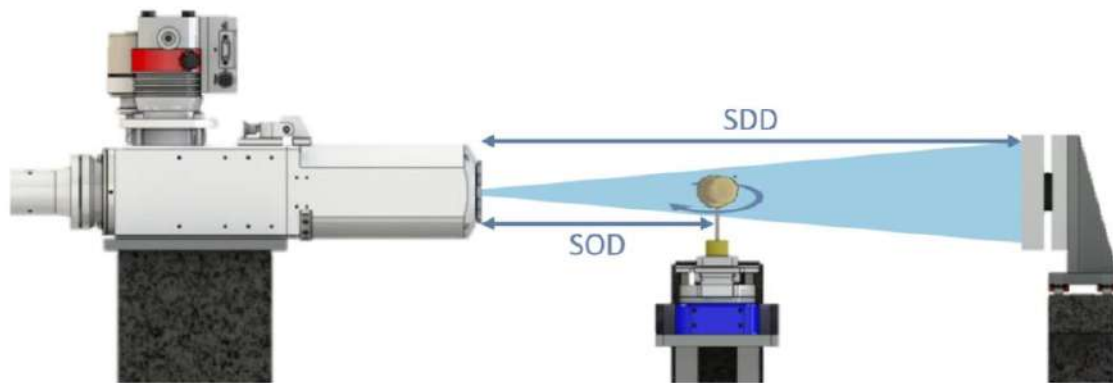


Figure 24 – Pictures of the TESCAN CoreTOM microtomography equipment. FOV stands for field of view, characterizing the area available to scanning (TESCAN, 2020).

The X-ray source used in this research was covered with a 1-mm copper filter to eliminate low energy radiation that usually does not contribute to the analysis of dense samples.

The maximum resolution is a function of the size, shape and position of the sample between the X-ray source and detector, as shown in Figure 25. The spatial resolution cannot exceed the size represented by the pixel. The pixel should ideally be two times smaller than the desired resolution. During three-dimensional reconstructions of the imaged sample, the pixel is mathematically transformed into a voxel representing the radiological depth (REIS NETO *et al.*, 2011). In the current work, a Kocurek Indiana Limestone sample (IH-2) was imaged with a resolution of 8.7  $\mu\text{m}$ . The images were scanned and acquired by CoreTOM, which provided zoomed images from inside the sample with high resolution without cutting or damaging the rock. For this, the cylindrical sample, measuring 5 cm in height and 3.81 cm in diameter, was zoomed-in and submitted to an 8.7  $\mu\text{m}$  resolution, shaped like a cylinder with 1.0 cm in height and 1.0 cm in diameter.



**Resolution:**

Combination of different factors:

- X-ray spot size ( $s$ )
- Detector pixel size ( $d$ )
- Geometric magnification ( $M$ )

$$R = \frac{d}{M} + s\left(1 - \frac{1}{M}\right)$$

$$M = \frac{SDD}{SOD}$$

Figure 25 – Picture showing that the resolution of a sample is a function of geometric magnification ( $M$ ), which is the ratio between SDD (source-detector distance) and SOD (source-object distance), X-ray spot size ( $s$ ) and detector pixel size ( $d$ ). Note that it is possible to obtain larger geometric magnifications of smaller samples as long as the sample fully fits in the X-ray cone generated from the X-ray source that reaches the detector, thus allowing better resolutions (TESCAN, 2020).

The CoreTOM  $\mu$ CT scanned sections were reconstructed using Aquila (acquisition software from TESCAN XRE, Belgium) and treated in Avizo (a data visualization and analysis software from Thermo Fisher Scientific, Waltham, Massachusetts, USA). Hundreds of *.tiff* extension images of the X-ray projections were obtained for each sample and subsequently used for calculating spatial fractal dimensions and three-dimensional pore network models. For this purpose, the images were imported, considering a voxel size of 1  $\mu\text{m}$ . This configuration was used to avoid calculation errors. Posteriorly, the data analyzed in Avizo were converted back to its original pixel size with mathematical codes in Mathematica 11.1<sup>®</sup> (WOLFRAM RESEARCH, 2017).

### **3.4.1.1 $\mu$ CT Image Treatment**

Microtomography was used in this work as input for Pore Network Modeling (PNM) and estimating fractal dimensions by using three-dimensional box-counting techniques. Clean Indiana Limestone samples were submitted to the CoreTOM microtomography. During acquisition, the sample rotated 360 degrees, with 0.5-degree increments, producing 16 bits *.tiff* images per increment at a pre-defined resolution.

The acquired images were treated with the Avizo 9.5 software. The process started by treating the image with a Non-local Means filter that smooths pixels and leads to a better definition of the boundaries between pores and the rock material. The Non-local Mean algorithm was used to filter images and remove noise in the x-y plane by comparison between neighboring voxels. For this, different weights were provided to the voxel under analysis, based on a Gauss kernel, to smooth high-frequency noise without interfering in the detection of borders used to differentiate solid and void regions.

To segment pores from the solid material, it is subsequently necessary to exclude the initially black background surrounding the scanned image. As black is contained in the color range of the porous system, it must be replaced by the 16-bit defined white color. The Volume Edit tool was used for this. The color threshold representing the pores was selected to allow their segmentation from the rest of the image. This procedure allows calculations of the porosity of the sample.

To match the NMR cumulative porosity accounting for pores with radii larger than half of the resolution ( $r > \frac{8.7}{2} \mu m$ ), the Dilate and Erode tools may be used to augment the pore space, leading to a better connection between pores and to exclude the excess of segmentation, respectively, so that only the connections among pores remain. This process forms connections between pore clusters without altering the porosity. It is also possible to determine communicating pores that form clusters by using the Connected Components tool. This procedure is then repeated until the comparison against basic petrophysics is satisfactory, and comparable or smaller than the porosity captured according to the resolution of the imaging process. The treated three-dimensional images can be used for the fractal box-counting technique.

Finally, the pore network was transformed into a skeleton composed of tubes and spheres representing pore throats and bodies, respectively. Pore bodies and throats (i.e., spheres and tubes) are identified through nodes (connections), points (pore bodies) and segments (pore throats). The skeleton data is to be used as input to the PNM software PoreFlow which simulates flow in porous media.

### **3.4.1.2 Pore Network Modeling: Porosity and permeability estimation from $\mu$ CT data**

$\mu$ CT images can be used also to estimate fluid permeabilities based on a tridimensional generated skeleton. For the permeability calculations based on  $\mu$ CT, flow was simulated using the PoreFlow PNM software (RAOOF & HASSANIZADEH, 2010a, 2010b; RAOOF *et al.*, 2010). To analyze the three-dimensional pore network using Avizo, it is necessary to first segment the greyscale images into pores while removing the solid and background. This is done based using NMR and the basic petrophysics data of porosity, as previously explained.

Pore Network Models (PNMs) were constructed using a pore skeleton obtained from the  $\mu$ CT calibrated images. Skeletonization consists of discretizing the pore space into discrete geometries of pores and throats. The voxel skeleton is then converted into a spatial graph object, visually shown by connecting lines in Avizo. The generated skeleton consists of nodes, points and segments, respectively representing voxels, pores and



throats (BULTREYS *et al.*, 2016). The voxel clusters that do not allow percolation across the sample are excluded since they do not interfere in the calculated permeability. An *.xml* extension file table is created, containing information regarding the generated skeleton of nodes (identification, coordinates and coordination number), points (identification, thickness and coordinates), and segments (identification, connecting pair of nodes and connecting points composing the segment). Points do not possess connectivity as opposed to pore bodies. A computational code using Wolfram Mathematica 11.1, developed at the Laboratory of Enhanced Oil Recovery (LRAP/COPPE/UFRJ, Rio de Janeiro, Brazil), may be used to convert the skeleton information from Avizo into input files for the PoreFlow PNM simulator (RAOOF *et al.*, 2013; RAOOF & HASSANIZADEH, 2012, 2010b).

Given the fact that the skeleton from Avizo is composed of spheres representing both pores and throats, it is necessary to create cylinders for representing throats only, thereby allowing more simplified fluid simulation using PoreFlow. The length of a cylinder (throat) connecting two pore bodies is given by the Euclidean distance between the center of the pore bodies:

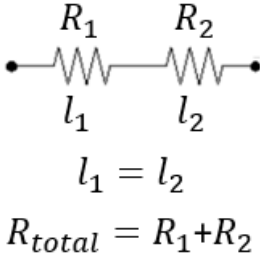
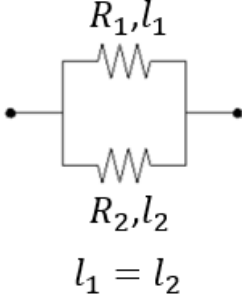
$$d_{P_1P_2} = \sqrt{(x_2 - x_1)^2 + (y_2 - y_1)^2 + (z_2 - z_1)^2} , \quad (3.7)$$

where  $x, y, z$  are the cartesian coordinates of pores 1 and 2.

The thickness (radius) of the cylinder is calculated given the arithmetic, geometric or harmonic averages of the radii of the interconnecting spheres. The averaging method is chosen by comparing calculated results against basic petrophysical measurements of the permeability. This is done since upscaling or calculations of the effective permeability from pore to medium is commonly performed through the use of an average. The three best known mean methods date back to Pythagoras (HUNT *et al.*, 2014): arithmetic, geometric and harmonic means. Each averaging method implies a specific topology or connectivity. The effective permeability or conductivity cannot exceed the arithmetic mean, representing pores in parallel. The effective permeability should not be smaller than the harmonic mean, which assumes that pores are in series. Although, the topologies represented by the arithmetic and harmonic means are rarely present in natural porous

media, which are usually disordered, most natural media are intermediate to these bounding cases. Averaging methods are summarized in Table 3.

Table 3 – Table exemplifying harmonic and arithmetic averages based on resistors (R) with the same length (l). Similar approaches are applicable to pore throat calculation for estimating the permeability. Pore throat radii control permeability and can be interpreted as resisting flow.

| Harmonic Average  | Arithmetic Average  |
|---|---|
|  <p style="text-align: center;"><math>l_1 = l_2</math><br/><math>R_{total} = R_1 + R_2</math></p> |  <p style="text-align: center;"><math>l_1 = l_2</math><br/><math>\frac{1}{R_{total}} = \frac{1}{R_1} + \frac{1}{R_2}</math></p> |

When a pore network is constructed, segments starting and ending at the same pore may form duplicated inverse segments, which may make it necessary to eliminate multiple segments connecting the same two pores. This then will lead to the final input files for the PoreFlow simulations of permeability. In PoreFlow, the pore network is submitted to single-phase fluid flow (water with a viscosity of 1 cP, and a density of 1000 kg/m<sup>3</sup>), such that the PNM calculations mimic the laboratory permeability measurements.

### 3.4.2 Thin Sections

Quantitative data regarding porosity and the pore size distribution can be obtained from direct or indirect petrophysical investigations. Direct investigations are commonly performed using gas or mercury injections, while the indirect studies are performed using

thin sections. Thin section petrographical analyses require careful examination, usually being bi-dimensionally limited.

High-resolution thin section images are obtained from petrographic microscopes that scan thin polished sections or cover slips of rocks. Blue color epoxy dye is typically used to expose pores, thus distinguishing them from the crystal structure of the rock, while the alizarin red color dye is used so that calcite can be differentiated from dolomite (BUONO *et al.*, 2019). Basic petrophysical porosity and permeability data also provide a reference for thin sections, which sometimes produce lower micro- and macro-porosities because of the relatively small area covered by the images (CARNEIRO *et al.*, 2014), resulting in smaller porosity values when compared to those of routine core analysis.

After scanning a rock, the acquired image is segmented to account for pore and porosity using the red-green-blue (RGB) spectrum. A binary image is then generated, where pores are represented in black, and solids in white. For this, the ImageJ (SCHNEIDER *et al.*, 2012) software was used. This process is shown in Figure 26.

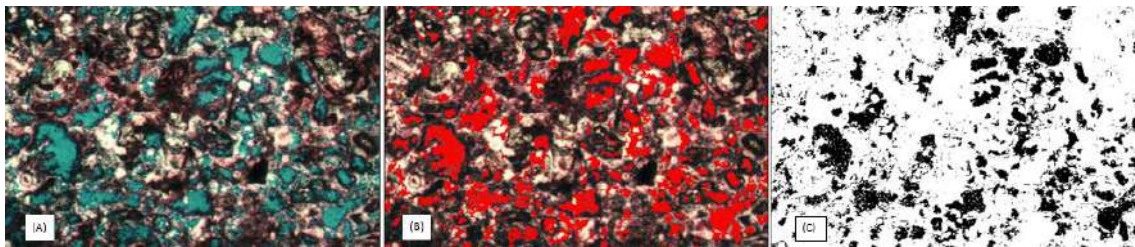


Figure 26 – Illustration of ImageJ processing: (A) Limestone blue-stained thin section, showing pores in blue; (B) segmentation procedure using ImageJ, showing pores in red; (C) binary image generated after segmentation, showing pores in black (Courtesy of World Wide Rock Catalog, by CoreLab).

After generating a binary image, pixels are counted and the porosity and pore size distribution are computed. Feret numbers, aspect ratios, areas, perimeters and circularities are also calculated for the pores. The Feret numbers represent the largest and smallest diameters of the pore. They are measured considering the sides of a rectangular box that encloses each pore within the thin-section, as shown in Figure 27. Feret hence represents the largest side of the rectangle, and FeretMin the smallest side.



Figure 27 – Feret numbers of a pore.

Corrected Feret (CF) and Corrected Feret Minimum (CFM) values are defined as follows:

$$CF = \frac{Area}{Feret * FeretMin} , \quad (3.8)$$

$$CFM = CF * FeretMin , \quad (3.9)$$

where *FeretMin* is the minimum Feret. In petrophysics and rock physics, the Aspect Ratio (AR) is often used for the ratio of the long-axis to the short-axis of the pores. This parameter hence should be close to the Feret length divided by *FeretMin*, and would always be 1 or greater. A few studies define the Aspect Ratio as the short axis divided by long axis, in which case AR is 1 or less.

To find the body to throat ratio (BTR), MICP data are compared against ImageJ data. Since MICP gives pore throat diameters (or radii) and ImageJ gives pore diameters (or radii), it is possible to calculate the BTR as:

$$BTR = \frac{Pore\ Body\ Radius}{Pore\ Throat\ Radius} , \quad (3.10)$$

By multiplying the MICP diameter by an arbitrary BTR, MICP pore throat information is transformed into pore body information:

$$\begin{aligned} BTR * MICPdiam &= \frac{Pore\ Body\ Radius}{Pore\ Throat\ Radius} \\ &= \frac{Pore\ Body\ Radius}{Pore\ Throat\ Radius} * Pore\ Throat\ Radius \\ &= Pore\ Body\ Radius , \end{aligned} \quad (3.11)$$

where  $MICPdiam$  is the MICP distribution of pore throat diameters.

Thin sections can provide valuable information about the recovery factor or other information about a reservoir. For example, the lower the BTR, the higher the recovery factor (RF), defined as the ratio between drained oil saturation and residual oil saturation, or  $(1 - S_{w,irr} - S_{o,r})/(1 - S_{w,irr})$ , where  $S_{w,irr}$  is irreducible water saturation and  $S_{o,r}$  is residual oil saturation (WARDLAW, 1982). This affirmation relies on the fact that recovery depends mainly on the pore throat radius, which is examined first in this work.

### 3.4.3 Box Counting

Box Counting methods involve dividing a given two- or three-dimensional image into squares or boxes, respectively, and accounting for the squares or boxes that comprise parts of the image (AMOSU *et al.*, 2018). An iterative process progressively diminishes the size of the squares or boxes and sums up the parts comprising the image. Through the number of boxes and their lengths, it is possible to calculate the fractal dimension  $D_f$  of the image being analyzed (ANTONIAZZI, 2007):

$$D_f = \frac{\log \left( \frac{N_{i+1}}{N_i} \right)}{\log \left( \frac{1/L_{i+1}}{1/L_i} \right)}, \quad (3.12)$$

where  $N_i$  is the number of boxes or squares and  $L_i$  the integer number of divisions made on the initial square or box, such that:

$$\begin{aligned} N &= L^3 && \text{for 3D images,} \\ N &= L^2 && \text{for 2D images.} \end{aligned} \quad (3.13)$$

In attempts to calculate the fractal dimension, a computational box-counting code was built in C++ to obtain the fractal dimension of bidimensional and tridimensional images, applicable to thin sections (2D) and  $\mu$ CT stacks (3D). In a first iteration, the stack or thin section is not divided but remains as it is. The second iteration is done by dividing the sides of the initial square (or box) into two segments ( $L = 2$ ). Images for the first, second and third iterations for a two-dimensional case are shown in Figure 28, while the

corresponding  $L$  and  $N$  values are given in Table 4. The segments are subsequently divided by 2 in the code that was developed.

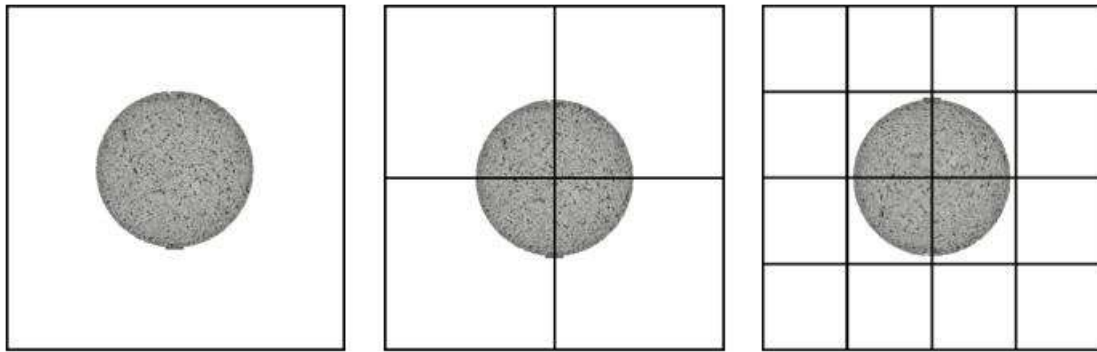


Figure 28 – Schematics showing the process of dividing images, starting from the first iteration, and proceeding to the second and third iterations. The image in the center corresponds to  $\mu$ CT section 10 in the XY plane of Indiana Limestone IH-2. Pores are in black, solid material (rock) is in lighter colors of the grey scale. In this example, the first iteration contains 1 square, and hence only 1 square contains pores. The second iteration has all 4 squares contain pores. The third iteration shows that only 4 out of 16 squares contain pores.

As shown by Eq. (3.13),  $N$  is the total number of squares or boxes comprehending the rock, whether occupied or not by a pore. This work attempts to account for the fractal dimension of the porous medium within a given image. The code reads the images and differentiates pores from solid material and the background through color differentiation. Hence,  $N$  keeps track when a square or box intercepts a pore, as shown in Figure 29. In this figure, pores are represented in black, therefore the squares accounted for  $N$  are shown on the right in solid line black, while the dashed lines in grey define squares that are not accounted for  $N$ . Iterations are done until the square or cube reaches a predetermined side length, e.g., 1 pixel, 2 pixels, 3 pixels, according to the image resolution.

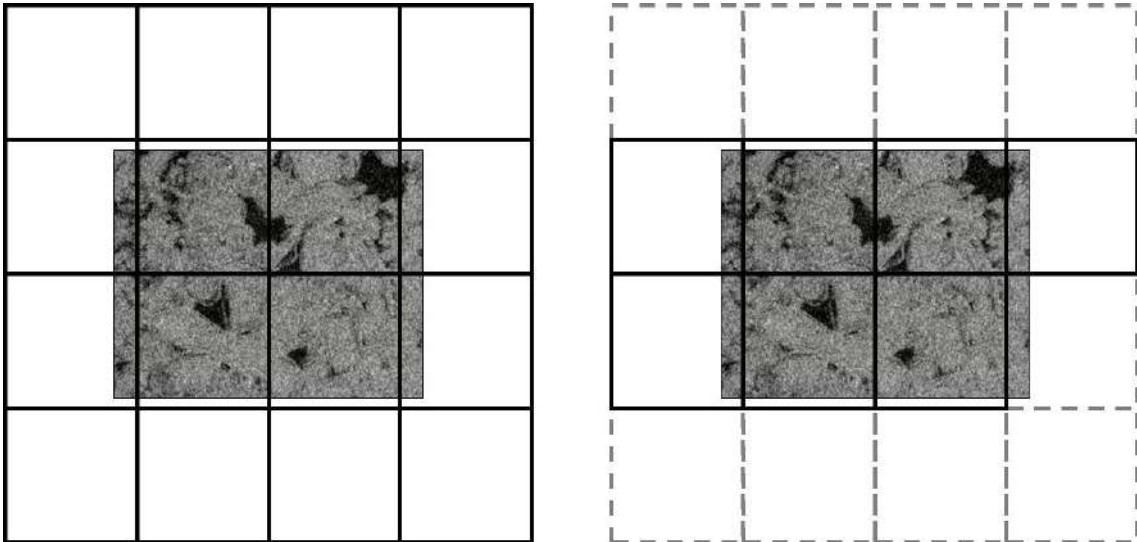


Figure 29 – On the left, a representative zoom showing a division in squares after the  $n^{th}$  iteration (here,  $n=3$ ). The image shows a zoomed shot of slice 1427, in the YZ plane, of an Indiana Limestone IH-2 sample.

Table 4 – Calculations of  $N$  and  $L$  for 2-D (thin section) and 3-D ( $\mu$ CT) images.

|                            | <b>1<sup>st</sup> iteration</b> |         | <b>2<sup>nd</sup> iteration</b> |         | <b>3<sup>rd</sup> iteration</b> |          |
|----------------------------|---------------------------------|---------|---------------------------------|---------|---------------------------------|----------|
| <b>Thin Sections (2-D)</b> | $L = 1$                         | $N = 1$ | $L = 2$                         | $N = 4$ | $L = 4$                         | $N = 16$ |
| <b>MCT Stacks (3-D)</b>    | $L = 1$                         | $N = 1$ | $L = 2$                         | $N = 8$ | $L = 4$                         | $N = 64$ |

For images with different side lengths, such as a rectangle of 10 x 20 units, the first square in the first iteration can be extrapolated such that the short side becomes as large as the largest one (e.g., a 20 x 20 unit rectangle extrapolated from a 10 x 20 unit rectangle). This is possible and does not interfere with calculations since the newly added units do not affect  $N$ . A similar approach can be done for three-dimensional images, which are cubic and have two sides and one height, the latter equal to the number of images composing the stack. The largest length among sides and the height is then used as a basis to extrapolate the others.

Another problem the box counting code can deal with is related to odd image lengths, such as an 11 x 11 unit image (e.g., centimeters) square, as shown in Figure 30. The first iteration then faces no problem since no division is made. But from the second iteration

on it is necessary to add units of squares (or cubes). Assume having a side of 11 units, then the second iteration would account for 2 segments of 5.5 units, a non-integer. If 5-unit segments are chosen, a 1-unit segment is left behind, which requires another 5-unit segment to be added. In this case, the number of squares goes from 4 squares with 5.5 units each, to 9 squares with 5 units each.  $L$  is then hence the rounded-up division of the integer part of the first trial segment (*i.e.*,  $L = \text{round-up of } 11/5 = 3$ ).

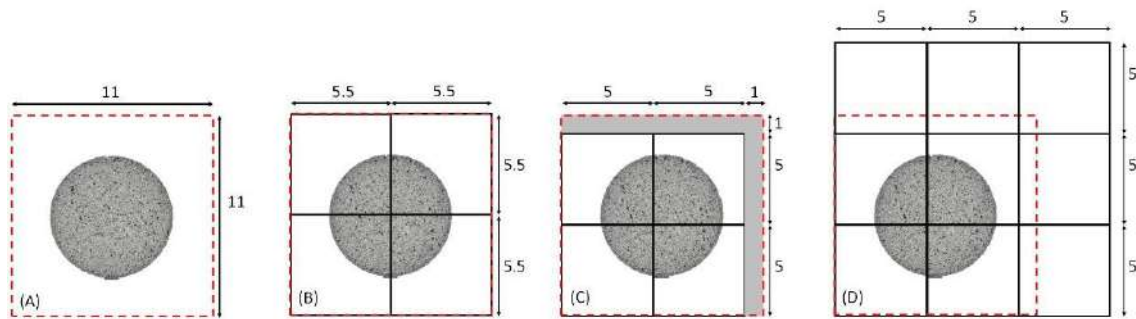


Figure 30 – Box counting iterations for divisions that do not return an integer length: (A) the first iteration (in red) works well since no division is made; (B) the second iteration returns a non-integer length. The squares must be replaced by integer-sided ones, leading to the next step; (C) The closes smallest integer is taken by the squares, leaving the image not covered by the boxes (in shaded grey). Hence, more squares of the same lengths must be added; (D) newly added squares of the same length. A similar approach applies to three-dimensional images.

Finally, it is possible to calculate the fractal dimension of the pore system via box counting. By using linear regression, the fractal dimension is obtained by plotting  $\log(N)$  versus  $\log(1/L)$  of all iterations on a cartesian plot. The slope of the fitted line is the fractal dimension. This is done for thin sections and three-dimensional  $\mu\text{CT}$  images. The fractal dimension obtained from thin-sections, which reflects the tortuosity, is used in the Thomeer-Swanson spreadsheet section to calculate the REV permeability. The fractal dimension from a  $\mu\text{CT}$  image indicates how close the NMR analyzed sample is to the REV.



### 3.5 NMR and NMR Fractal dimension

The NMR derived transversal relaxation time distribution can be used to derive the pore size distribution using Eqs. (2.30) and (2.31). The surface relaxivity value for each sample obtained from the NMR results can be compared with MICP data for Indiana Limestone in the Kocurek and Core Laboratories WWRC database. Pores are then assumed to be cylindrical, with the geometrical factor being equal to 2. NMR is used to estimate the pore size distribution and the fractal dimension of the Indiana Limestone samples.

One of the Critical Path Analysis (CPA) approaches used to parameterize the pore size volumetric probability density function is the fractal description of the pore space, resulting in a power-law distribution. The pore space characterized by a fractal distribution is considered to be self-affine, meaning that each portion of the system can be considered as a reduced-scale image of the whole (MANDELBROT, 1967). HUNT (2001) and HUNT & GEE (2002) have shown that natural porous media show fractal behavior within certain upper and lower boundaries. A derivation (GHANBARIAN-ALAVIJEH & HUNT, 2012b) for the fractal distribution for cylindrical pores is replicated here for a cumulative distribution of pore sizes:

$$N(< r) \sim r^{-D_f}, \quad (3.14)$$

where  $N(< r)$  is the number fraction of pores smaller than size  $r$  and  $D_f$  is the fractal dimension for 3-D systems.

Before calculating the critical radius, it is necessary to calculate the fractal dimension  $D_f$ . A computational routine based on work presented by GHANBARIAN *et al.* (2016a) has been developed to extract the fractal dimension from data of the incremental porosity versus pore radius. Eq. (3.15) defines the incremental porosity (e.g., from NMR data), which is equivalent to the integral in Eq. (3.15), from  $r$  to  $r + dr$ :

$$\Delta \phi = \int_r^{r+dr} s r^3 f(r) dr, \quad (3.15)$$

where  $f(r)$  is the pore size distribution,  $f(r)dr$  is the number of pores with radii between  $r$  and  $r + dr$ , and  $s r^3 f(r)dr$  is the volume occupied by those pores, with  $s$  being a shape

factor. Integrations are carried out between two consecutive radii ( $r_i$  and  $r_{i+1}$ ) available from the NMR data. Each of the integrations gives the porosity for pores between  $r$ , or  $r_i$ , and  $r + \Delta r$ , or  $r_{i+1}$ . Adding up the results of all integrations between  $r_i$  and  $r_{i+1}$  leads to the incremental porosity, from which the total porosity of the sample can be obtained.

Assuming that  $f(r)=r^{-1-D_f}$ , one has:

$$r^3 f(r) = r^3 r^{-1-D_f} = r^{2-D_f} . \quad (3.16)$$

Integrating  $r^{2-D_f}$  over a small interval between radii will result in  $r^{2-D_f} \Delta r$ , which is the incremental porosity  $\emptyset$ :

$$\begin{aligned} \emptyset &= \int_r^{r+\Delta r} r^3 f(r) dr \\ &= \int_r^{r+\Delta r} r^3 r^{-1-D_f} dr = \int_r^{r+\Delta r} r^{2-D_f} dr = r^{2-D_f} \Delta r \end{aligned} \quad (3.17)$$

Hence, it is necessary to take these incremental porosities and divide by the difference in radii ( $\Delta r$ ), and then divide once again by  $r^2$  (an average between the two consecutive radii was used) for normalization purposes.

$$\begin{aligned} \frac{\emptyset}{r^2 \Delta r} &= \frac{r^{2-D_f} \Delta r}{r^2 \Delta r} = r^{-D_f} , \\ \frac{\emptyset}{r^2 \Delta r} &= r^{-D_f} . \end{aligned} \quad (3.18)$$

These two divisions are equivalent to dividing by  $r^3$  (proportional to the volume of a pore), since a pore is represented by a pixel (1D) or voxel (3D). The final result is a plot of pore radius versus incremental porosity divided by pore volume, as shown in Figure 31. The plot shows  $r$  along the horizontal x axis, and  $\frac{\emptyset}{r^2 \Delta r}$  along the vertical axis. By plotting this graph on a log-log scale, a straight line is obtained (Figure 32), from which the fractal dimension ( $D_f$ ) can be obtained as shown by Eq. (3.18).

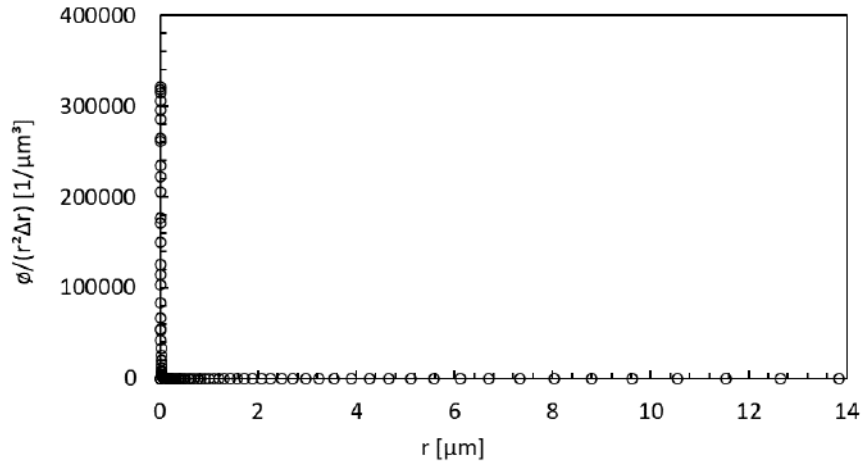


Figure 31 – Plot of  $\frac{\phi}{r^2\Delta r}$  as a function of  $r$ .

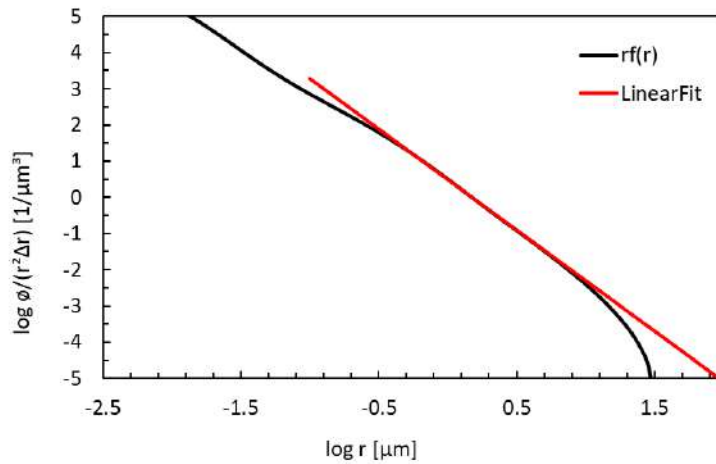


Figure 32 – Log-log plot representing Eq. (3.18). The fractal dimension equals the slope of the straight line (in red).

### 3.6 Permeability computations based on MICP

Mercury porosimetry is used in this work as input to several techniques that estimate the permeability from the pore throat distribution. Porosimetry based on mercury injection capillary pressure is obtained with Eq. (2.6). For the mercury-based experiment, the input is given based on capillary pressure.

### 3.6.1 Thomeer-Swanson spreadsheets

Thomeer-Swanson spreadsheets (CLERKE & MARTIN, 2004) were developed as a way of rock typing the Arab-D formation in Saudi\_Arabia, which was characterized thoroughly by many authors (BUIRING & CLERKE, 2013; CANTRELL & HAGERTY, 1999; CLERKE *et al.*, 2008; SWART *et al.*, 2005, and references therein). A Thomeer-Swanson spreadsheet allows one to analyze the extrapolated displacement pressure  $P_d$  of MICP for unimodal (one pore system, i.e., PS1), bimodal (two pore systems, i.e., PS1 and PS2) and trimodal (pore systems, i.e., PS1, PS2 and PS3) distributions. The porosity group, which contains the largest pore throats (PS1), is expected to dominate the permeability, while the other groups (PS2 and PS3) control oil in place and irreducible water saturation.

The spreadsheet calculations return values of the permeability based either on complete MICP pore-size distributions or on specific pore sizes. In this work, the spreadsheet is modified to facilitate studies of a variety of limestones, while also adding a new feature to allow calculations of the Winland permeability based on the pore throat size at the 35<sup>th</sup> percentile of cumulative pore throat distribution. Firstly, mercury injection capillary pressure data and the corresponding bulk volume, porosity and permeability from basic petrophysics must be entered into the spreadsheet. The bulk volume capillary pressure graph should be continuous and differentiable, thereby forming at least one left-skewed pore throat histogram (LSPTH). Points that are not possible to differentiate are excluded from the histogram by assigning a zero-value weight in the spreadsheet.

Calculations of the G-factor,  $P_d$  and  $(BV)_{P_\infty}$  coefficients were obtained using a code, developed in Mathematica® and the C++ language, which selected each pore system (PS1, PS2 and PS3) separately, with its coefficients calculated as explained in section 2.12.1.1. Closure corrections, tortuosities, fractal dimensions and  $L/L_d$  ratios, as described in section 2.12.1.3, can also be included in the spreadsheet. Interfacial tension, fluid density and the contact angle of the injected fluid can also be provided, or kept at default values. Permeability values are calculated based on methods presented in sections 2.12 and 2.13.

### 3.6.2 Critical Path Analysis

According to critical path analyses, flow or conduction in a highly heterogeneous porous medium with a broad PSD is dominated by pore throats whose radii are slightly larger than a certain critical radius,  $r_c$  (GHANBARIAN *et al.*, 2016a). KATZ & THOMPSON (1986) showed that it is possible to infer the critical pore diameter, and the saturation at which the spanning-cluster first occurs, from the inflection point of the mercury intrusion porosimetry graph.

The critical radius for CPA can be calculated from MICP data using four different approaches according to the methods presented in section 2.14.5: (1) visually, from the modes of  $\Delta S_{Hg}/\Delta \ln(P_{Hg})$  versus radius on a logarithm scale, where  $S_{Hg}$  is the saturation of mercury and  $P_{Hg}$  the capillary pressure of mercury; (2) from the van Genuchten equation fitted to the MICP data, where  $r_c$  is calculated following Dexter's derivation; (3) from the fitted van Genuchten equation, where  $r_c$  is estimated from the van Genuchten  $\alpha$  parameter, and (4) from the fractal dimension as estimated with Eq. (2.64).

The RETC software (VAN GENUCHTEN *et al.*, 1991) was used to fit the van Genuchten equation to the data. For bimodal MICP data, the dual-porosity option within RETC is used. The critical radius of the larger pore-throat size distribution is then selected for the permeability calculations (B. GHANBARIAN, *personal communication*), which is in agreement with the Thomeer approach where permeability is calculated based on a hyperbola fitted to the largest pore system (PS1) for bimodal or trimodal pore systems. Appendix A shows how to convert MICP data into pressure head (cm) and water content data for subsequent analysis using RETC.

With the calculated  $r_c$ , the CPA-based approach by SKAGGS (2011) was used. The approach considers the medium to be independent, with the Skaggs coefficient equal to 53.5, and self-similar ( $l \propto r$ ) with the Skaggs coefficient equal to 72.3, resulting in two different values of the upscaled permeability per critical radius calculated using methods (1) to (4).

For the purpose of checking whether the micro- and macro-porous systems act in parallel, permeability was also estimated separately for both systems. Based on Archie's law, one has:

$$F_{total} = \phi_{total}^{-m_c} \quad (3.19)$$

in which  $F_{total}$  is the total formation factor,  $\phi_{total}$  is the total porosity and  $m_c$  is the cementation exponent, which is equal to  $-\log F_{total} / \log \phi_{total}$ . Using Archie's law, one has:

$$\frac{F_{mic}}{F_{total}} = \left( \frac{\phi_{mic}}{\phi_{total}} \right)^{-m_c} \quad (3.20)$$

$$\frac{F_{mac}}{F_{total}} = \left( \frac{\phi_{mac}}{\phi_{total}} \right)^{-m_c} \quad (3.21)$$

where  $F_{mic}$  and  $F_{mac}$  are the formation factor obtained from the micropores and macropores, respectively,  $\phi_{mic} = (1 - w) \phi_{total}$  is the porosity associated with the micropores, and  $\phi_{mac} = w \phi_{total}$ ,  $\phi_{mac}$  is the porosity associated with the macropores, and  $w$  is one of the van Genuchten parameters for a bimodal distribution, defined as the fraction of macropores within the medium.

Subsequently, the following permeability values are determined for the micropore (mic) and macropore (mac) subsystems:

$$k_{mic} = \frac{r_{c,mic}^2}{c_s F_{mic}} \quad (3.22)$$

$$k_{mac} = \frac{r_{c,mac}^2}{c_s F_{mac}} \quad (3.23)$$

With the total permeability given by:

$$k_{total} = k_{mic} + k_{mac} \quad (3.24)$$

The above tests are all implemented. If the micro- and macro-pores contribute in parallel to the permeability, the  $k_{total}$  value as obtained with Eq. (3.24) should approximate the permeability derived from laboratory tests.

### **3.7 Workflow**

The work developed in this thesis is depicted by the workflow shown in Figure 33, which summarizes the laboratory routines and calculation techniques that were used. Basic petrophysics, mercury intrusion, thin section analysis and electrical resistivity measurements are presented for all 30 limestone samples, while HYPROP, WP4C, mercury extrusion, NMR and  $\mu$ CT measurements were restricted to the Indiana Limestone samples. The white boxes of the workflow show the main parameters and outputs obtained with each technique or study, as well as the purpose and results of the technique, while the pink boxes indicate the calculated or measured permeabilities.

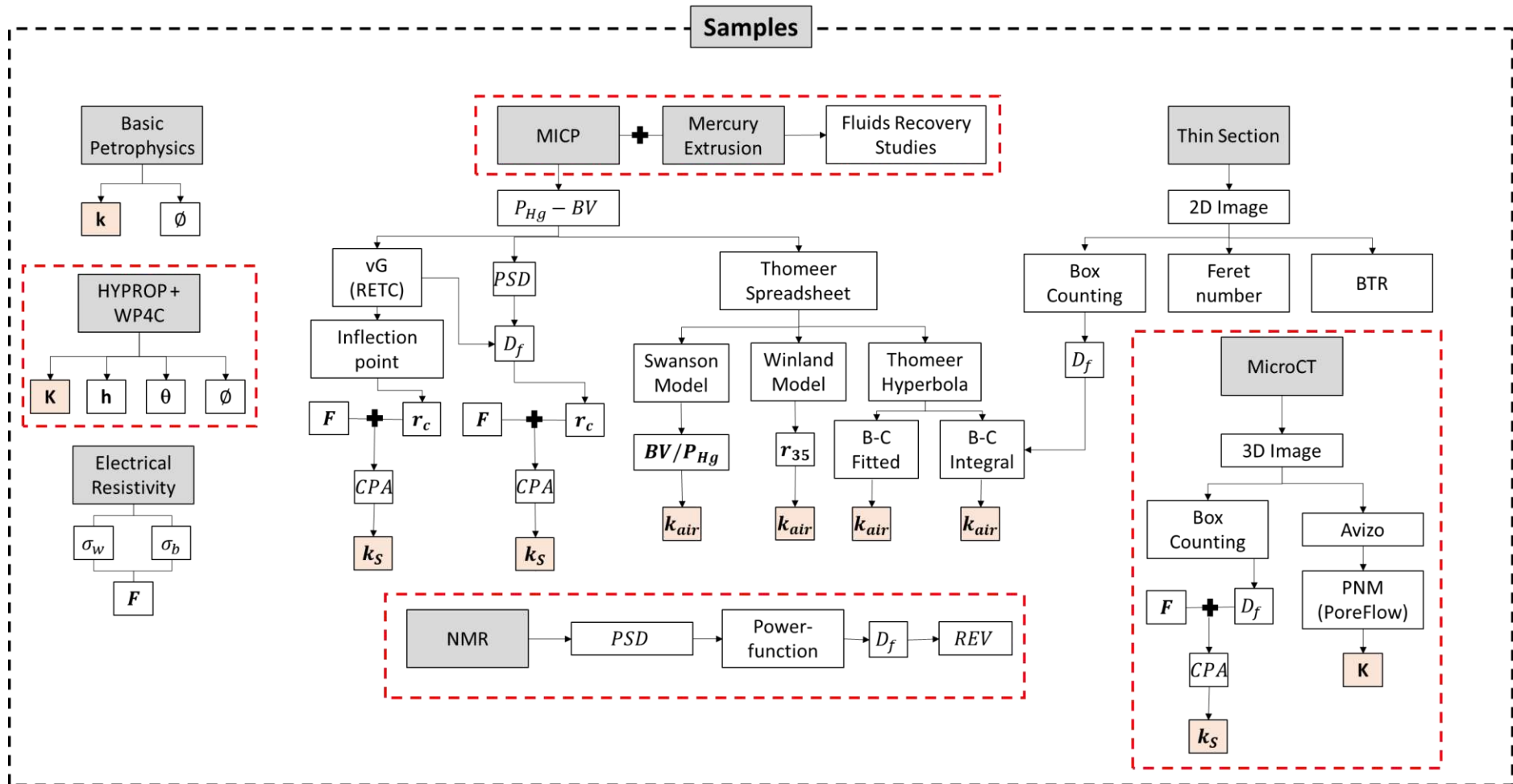


Figure 33 – Thesis workflow. The white boxes show the main parameters and outputs of each step, while the pink boxes indicate calculated or measured permeabilities. The red dashed lines indicate routines performed only on Indiana Limestone.



## 4 Results and Discussion

The results in this thesis cover various analyses performed on 30 limestone samples retrieved from a quarry in Brazil (one sample), and 29 wells worldwide. Results from the routine basic petrophysical measurements are used as the standard values. The objective of all tests was to calculate the REV (upscaled) permeability of the studied carbonate samples, the majority of which showed bimodal pore size distributions. The accuracy of measured versus fitted or calculated data are reflected by several statistical measures, such as  $R$ -squared ( $R^2$ ), and the root mean square error (RMSE). Several measurements involved logarithmic scale data for which the root mean square log-transformed error (RMSLE) are calculated. As an example, the RMSLE parameter comparing the accuracy of the calculated permeability calculated ( $k_{cal}$ ) versus the measured permeability from basic petrophysics ( $k_{meas}$ ) is given by:

$$RMSLE = \sqrt{\frac{1}{N_s} \sum_{i=1}^{N_s} [\log k_{cal} - \log k_{meas}]^2} \quad (4.1)$$

where  $N_s$  represents the number of data.

### 4.1 Routine core analysis and formation factor

Results of the routine core (basic petrophysical) laboratory tests for all samples are presented in Table 5. The data were used as input and benchmarks for the various permeability calculations. The Indiana Limestone High (IH) core from Kocurek Industries was divided into smaller plugs that were subsequently submitted to laboratory tests. The routine core analyses were done twice on IH2 and IH6, and once on plug IH3. Results from the second test on IH2 (IH2\_Test 2) were those used for the critical path analysis: this sample was submitted to mercury intrusion/extrusion and formation factor measurements at Core Laboratories (Houston, USA). Samples IH2 and IH3 were used for the NMR tests. IH3 was tested using the HYPROP evaporation setup, and IH2 using WP4C. Other results for the Indiana Limestone High formation are presented separately

in section 4.4. The limestone plugs from the worldwide wells (L01 to L29) were subjected to routine core, formation factor and MICP analyses.

Table 5 – Basic petrophysical data and the formation factor ( $F$ ) of the tested limestones. Porosities ( $\emptyset$ ) are in percentages and the permeabilities ( $k$ ) in milliDarcies.

| Sample            | $\emptyset$ (%) | $k$ (mD) | $F$  | Sample     | $\emptyset$ (%) | $k$ (mD) | $F$  |
|-------------------|-----------------|----------|------|------------|-----------------|----------|------|
| <b>IH2_Test 1</b> | 21.6            | 400      | 28.9 | <b>L13</b> | 11.9            | 5.55     | 65.9 |
| <b>IH2_Test 2</b> | 18.4            | 236      | 39.8 | <b>L14</b> | 11.6            | 39.5     | 92.4 |
| <b>IH3_Test 1</b> | 18.5            | 311      | 38.3 | <b>L15</b> | 11.2            | 2.49     | 152  |
| <b>IH6_Test 1</b> | 19.5            | 362      | -    | <b>L16</b> | 10.1            | 0.50     | 115  |
| <b>IH6_Test 2</b> | 19.8            | 375      | -    | <b>L17</b> | 3.70            | 0.27     | 434  |
| <b>L01</b>        | 34.7            | 2.13     | 150  | <b>L18</b> | 14.4            | 7.80     | 51.1 |
| <b>L02</b>        | 24.9            | 4430     | 16.9 | <b>L19</b> | 25.1            | 6.65     | 20.9 |
| <b>L03</b>        | 25.0            | 9.48     | 15.1 | <b>L20</b> | 21.4            | 16.1     | 25.2 |
| <b>L04</b>        | 21.7            | 1050     | 22.1 | <b>L21</b> | 20.1            | 217      | 62.9 |
| <b>L05</b>        | 23.5            | 532      | 18.4 | <b>L22</b> | 21.3            | 6.31     | 24.9 |
| <b>L06</b>        | 18.1            | 6.22     | 37.9 | <b>L23</b> | 15.2            | 33.5     | 34.2 |
| <b>L07</b>        | 16.4            | 2.28     | 94.2 | <b>L24</b> | 17.2            | 566      | 65.7 |
| <b>L08</b>        | 18.7            | 368      | 21.9 | <b>L25</b> | 11.3            | 2.07     | 94.6 |
| <b>L09</b>        | 18.1            | 14.8     | 35.1 | <b>L26</b> | 12.5            | 0.09     | 104  |
| <b>L10</b>        | 17.4            | 51.5     | 69.5 | <b>L27</b> | 25.6            | 9.12     | 16.5 |
| <b>L11</b>        | 15.7            | 4.42     | 41.7 | <b>L28</b> | 19.7            | 149      | 30.4 |
| <b>L12</b>        | 8.60            | 211      | 78.9 | <b>L29</b> | 24.5            | 177      | 28.7 |

## 4.2 Thin Sections

Thin sections of the 30 samples were analyzed to obtain BTR (body to throat ratio), AR (aspect ratio) and fractal dimension. The thin section images were acquired with an optical microscope using 32-times zoom-ins, except for samples L05, L20 and L22 that were zoomed in 32 (identified as L05A, L20A and L22A) and 128 times (identified as L05B, L20B and L22B). The images were treated and analyzed with the ImageJ software to generate pores segmented from the solids, as well as MICP pore size diameters. Figure 34 shows a sample before and after segmentation and binarization using ImageJ.

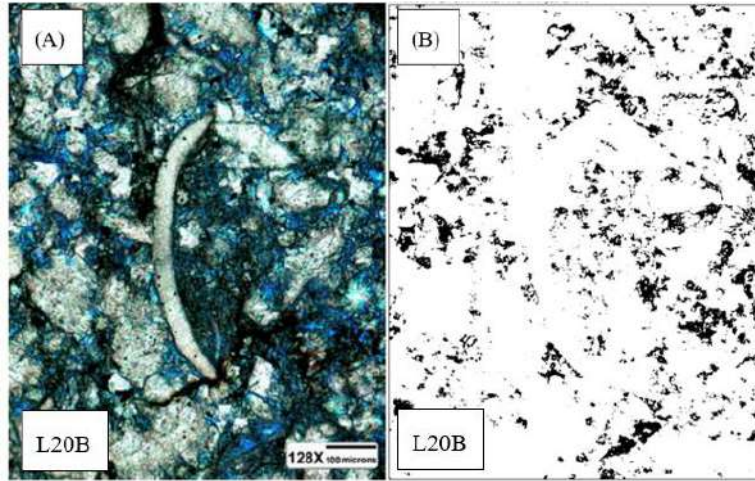


Figure 34 – Thin section of L20B, zoomed in 128 times before segmentation (A), and after segmentation and binarization (B). Pores are shown by the black color.

ImageJ is based on pixel counts to calculate the total area of the thin section as well as the pore system after binarization. Based on the pixel count, the software calculates the circularity of the pores, the Feret number, the Feret minimum (shortest diameter of pore) and the maximum (largest diameter of pore) diameters and porosity. Pore size distributions are obtained according to MICP diameter bins, in micrometers. The pore diameter distributions (histogram) for the thin sections are acquired by counting the frequency of pores per given MICP diameter through the process of binning. Binning consists of grouping pores according to their corrected minimum Feret number to represent the diameter of the pores to be used for the MICP diameter intervals. This is done using the corrected Feret number (CF) given by:

$$CF = \frac{Pore\ Area}{Feret * F_{min}} \quad (4.2)$$

The Minimum Corrected Feret (CFM) number is then obtained as:

$$CFM = CF * F_{min} \quad (4.3)$$

The CFM values are sorted next in ascending order to obtain the CFM frequency at each MICP diameter. This allows the construction of a histogram for comparison against the mercury intrusion pore throat distribution data and subsequent calculations of the average aspect ratio (aveAR) and body to throat ratio (BTR).

Figure 35 shows a comparison of the ImageJ histogram results against the MICP data. The MICP and ImageJ generated PSD curves frequently exhibit a gap between them. The BTR value is obtained by overlaying both curves as shown in Figure 35.

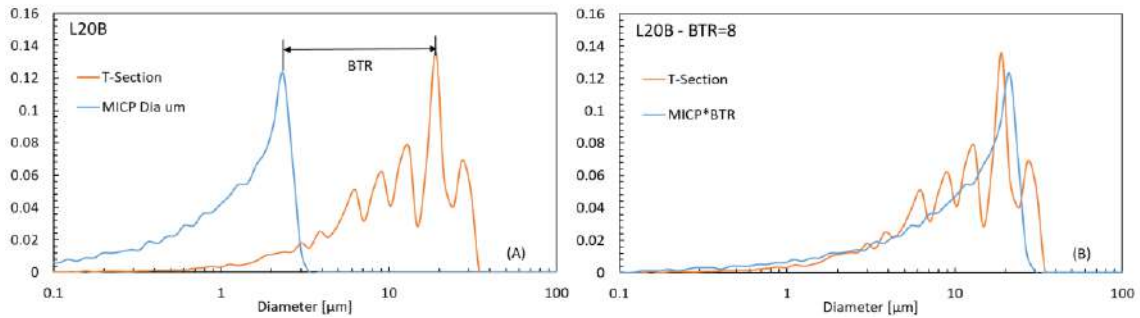


Figure 35 – Pore size distribution curves from a thin section (orange) of L20B (L20 zoomed in 128 times) and MICP (blue) before (A) and after (B) applying the BTR factor to the MICP curve (the BTR, in this case, equals to 8).

The aspect ratio was also obtained using ImageJ. In petrophysics and rock physics, the aspect ratio (AR) is usually the ratio of the long-axis to the short-axis of the pores, leading to values that usually are very similar to the ratio of the Feret maximum and the Feret minimum (equal to or greater than unity). To compute the average aspect ratio of a given thin section, the arithmetic average is used for AR as provided by the software for smooth results that may look scattered due to previous binning. Smoothing (TS51vl) is also applied to the thin section pore diameter distribution, by arithmetically averaging the values of five consecutive measurements. The results in Figure 32 show that AR increases with a decrease in the pore size.

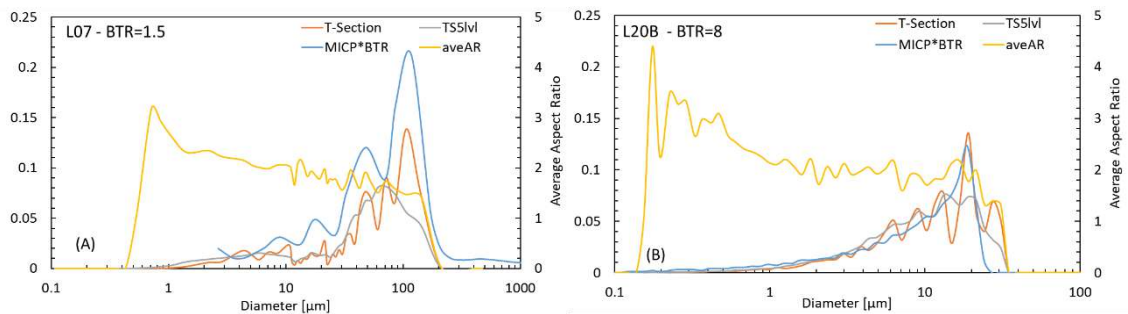


Figure 36 – Results for thin sections L07 (A) and L20B (B) and their contrasts with the MICP data. The pore size distributions (T-Section, in orange) were smoothed (TS51vl, in grey). Average AR values are shown in yellow. The MICP curve multiplied by BTR (8 in this case) is shown in blue.

The box-counting method code was also used to calculate the fractal dimension of the pore system based on binary images of the thin sections as generated with ImageJ. These results were posteriorly used further in the Buiting-Clerke tortuous and relative fractal tubular bundle model (B-C k integral) model to predict the permeability with the Thomeer approach. The procedure leading to values of BTR and the fractal dimension  $D_f$  was applied to all limestone samples. Table 6 summarizes the final results for each thin section.

Table 6 – Summary of the thin section results

| Thin-Section |                    |       |     | Thin-Section |                    |       |     |
|--------------|--------------------|-------|-----|--------------|--------------------|-------|-----|
| Sample       | Box-Counting $D_f$ | Feret | BTR | Sample       | Box-Counting $D_f$ | Feret | BTR |
| <b>IH</b>    | 1.47               | 31.1  | 2   | <b>L15</b>   | 1.44               | 5.18  | 8   |
| <b>L01</b>   | 1.67               | 15.7  | 15  | <b>L16</b>   | 1.34               | 3.34  | 15  |
| <b>L02</b>   | 1.67               | 40.9  | 2   | <b>L17</b>   | 1.49               | 63.3  | 40  |
| <b>L03</b>   | 1.6                | 21.5  | 9   | <b>L18</b>   | 1.48               | 23.2  | 12  |
| <b>L04</b>   | 1.57               | 92.7  | 4   | <b>L19</b>   | 1.57               | 28.8  | 50  |
| <b>L05</b>   | 1.64               | 37.6  | 4   | <b>L20</b>   | 1.57               | 14.9  | 10  |
| <b>L06</b>   | 1.54               | 16.6  | 28  | <b>L21</b>   | 1.72               | 47.2  | 5   |
| <b>L07</b>   | 1.75               | 14.3  | 25  | <b>L22</b>   | 1.21               | 7.84  | 2   |
| <b>L08</b>   | 1.61               | 35.1  | 8   | <b>L23</b>   | 1.61               | 27.9  | 30  |
| <b>L09</b>   | 1.57               | 14.4  | 6   | <b>L24</b>   | 1.65               | 7.94  | 10  |
| <b>L10</b>   | 1.64               | 3.81  | 10  | <b>L25</b>   | 1.49               | 16.7  | 10  |
| <b>L11</b>   | 1.49               | 10.9  | 35  | <b>L26</b>   | 1.22               | 19.2  | 70  |
| <b>L12</b>   | 1.54               | 23.1  | 3   | <b>L27</b>   | 1.29               | 18.5  | 8   |
| <b>L13</b>   | 1.39               | 23.3  | 10  | <b>L28</b>   | 1.56               | 23.4  | 3   |
| <b>L14</b>   | 1.56               | 50.6  | 6   | <b>L29</b>   | 1.55               | 27.6  | 10  |

## 4.3 REV Permeability Calculations

### 4.3.1 Thomeer-Swanson spreadsheet permeability

The Thomeer-Swanson spreadsheet was first developed by Ed Clerke, a Saudi Aramco researcher, to devise a way of rock typing the Arab-D formation (CANTRELL & HAGERTY, 2003) using MICP data. The analysis consists of finding the values of  $(BV)_{P_{\infty}}$  and  $P_d$ , which represent the bulk volume occupied by mercury at infinite pressure and the extrapolated displacement pressure, respectively, with the parameters of the Thomeer curve fitted to the MICP data. The Thomeer curve (a left-skewed pore throat histogram), whose parameters dictate the geometry and position of the curve, are then used to calculate the permeability. This approach was used here for every pore system of the samples in terms of three different systems, i.e., unimodal (PS1), bimodal (PS1, PS2) and trimodal (PS1, PS2 and PS3). PS1 is the pore system composed of larger pores while PS2 and PS3 represent the finer pore systems within a sample. For estimating the permeability, PD1 is probably the most important, but for estimating oil in place and irreducible water saturation, PD2 and PD3 are equally or more important, as shown later. The Thomeer parameters of G-factor,  $(BV)_{P_{\infty}}$  and  $P_d$  were used in three different approaches for the permeability: The Thomeer hyperbola monomodal approach (monomodal fit), the Buiting-Clerke tortuous and relative fractal tubular bundle approach (B-C Integral), and the Thomeer-based Buiting-Clerke permeability approach fitted Thomeer curve ((B-C Fit).

To proceed with the Thomeer-based calculations, MICP data of capillary pressure and bulk volume of the 30 limestone samples must be entered in the Thomeer-Swanson spreadsheet. A weight (0 or 1) is assigned to the pairs of data. Data to be excluded from the analysis are given a weight of 0. Next, closure corrections may need to be used when the increment of pressure indicates pore mercury entry, as shown in Figure 37.

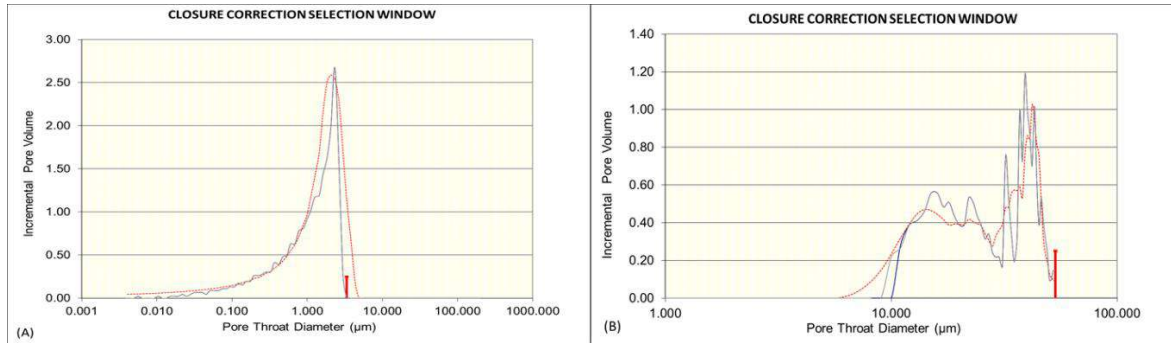


Figure 37 – Plots showing closure corrections (red vertical bars) of zero for sample L20 (A) and 0.20 for sample L05 (B).

Values of the G-factor,  $(BV)_{P_{\infty}}$  and  $P_d$  were calculated for each pore system of the samples using the computational code developed for this research, based on Thomeer's pore throat distribution hyperbola. The Thomeer hyperbola was then fitted to the MICP data, as shown in Figure 38. Capillary pressure curves were also generated with the Thomeer-Swanson spreadsheet, as shown by the results in Figure 39.

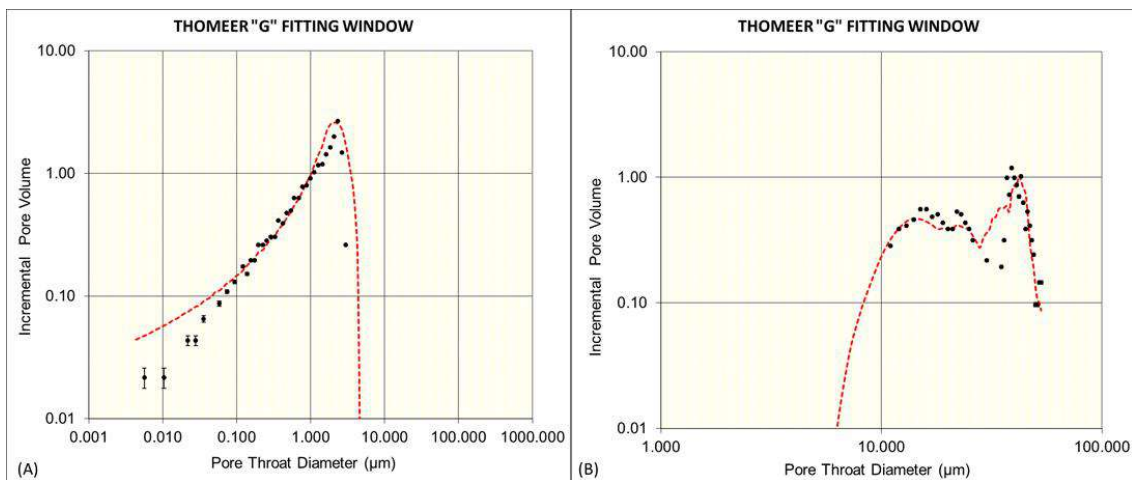


Figure 38 – Thomeer hyperbola (red dashed lines) fitted to MICP data (black dots) of (A) unimodal sample L20 having G-factor,  $(BV)_{P_{\infty}}$  and  $P_d$  values equal to 0.23, 60 and 32, respectively, and (B) bimodal sample L05 having G-factor,  $(BV)_{P_{\infty}}$  and  $P_d$  values equal to 0.73, 20.30 and 3.06, respectively for PS1, and 0.10, 5.0 and 233, respectively, for PS2.

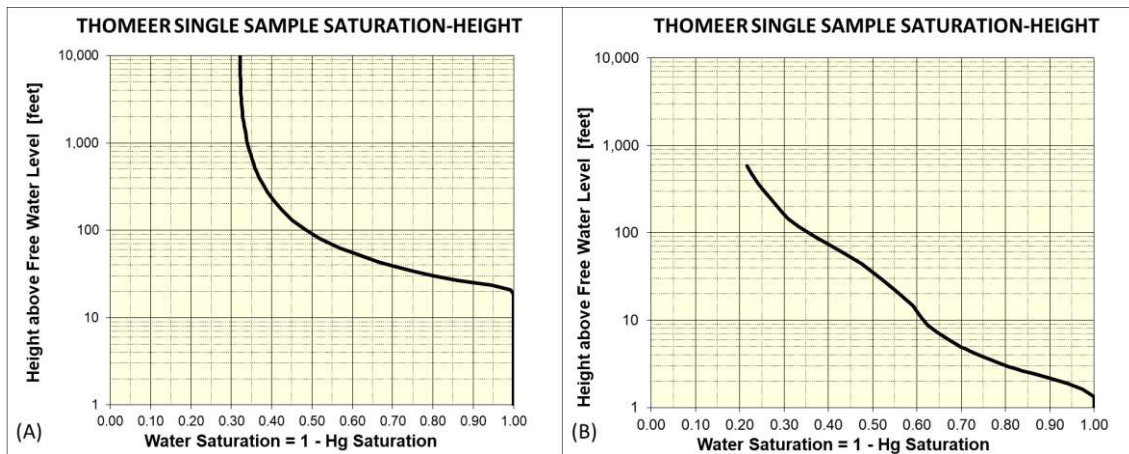


Figure 39 – Capillary pressure curves of unimodal sample L20 (A) and bimodal sample L05 (B), showing water saturation values versus water pressure head in feet.

The estimated values of G-factor,  $(BV)_{P_{\infty}}$ ,  $P_d$  in Figure 34, as well as the left-skewed pore throat size distribution histogram, were used next as input for the Thomeer-based approaches to predict the permeability. Results are summarized in Table 7 and Figure 40, the latter showing a plot of the logarithm of the calculated permeability versus the logarithm of the measured permeabilities of the various limestone samples. The figure shows different models in different colors: the Thomeer hyperbola monomodal approach (monomodal fit, in orange), the Buiting-Clerke tortuous and relative fractal tubular bundle model (B-C Integral, in grey) and the Thomeer-based Buiting-Clerke permeability methodology (B-C Fit, in green). Dashed lines in the plot show a very conservative variation of  $\pm 20\%$  in the permeability (a factor of  $\pm 1.2$ ). Usually, a factor of 3 for permeability estimation is considered to be satisfactory and representative of samples in the oil industry (KENYON (1997) and references therein).



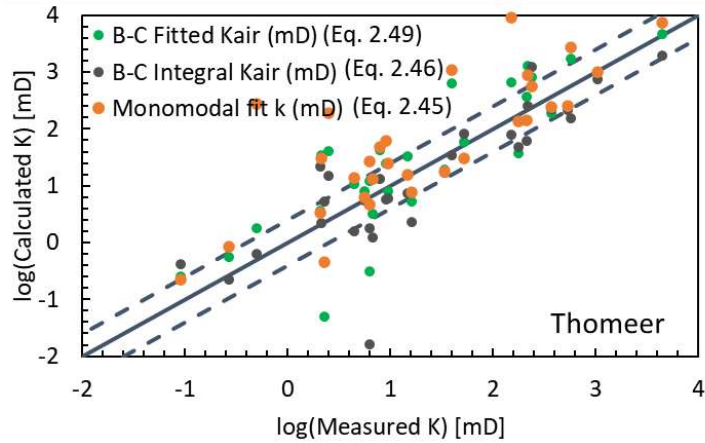


Figure 40 – The logarithms of the calculated permeabilities are plotted against the logarithms of the measured permeabilities for the full-histogram Thomeer-based approaches discussed above, for the 30 limestone samples. Dashed lines indicate theoretical predictions within a 20% range of precision.

For the purpose of dividing the obtained permeability results according to the pore system (unimodal versus bimodal) in the Thomeer approach, the graphs shown in Figure 40 were split among the two pore systems for rock typing, again using the best fit of the Thomeer hyperbolae. Results are shown in Figure 41.

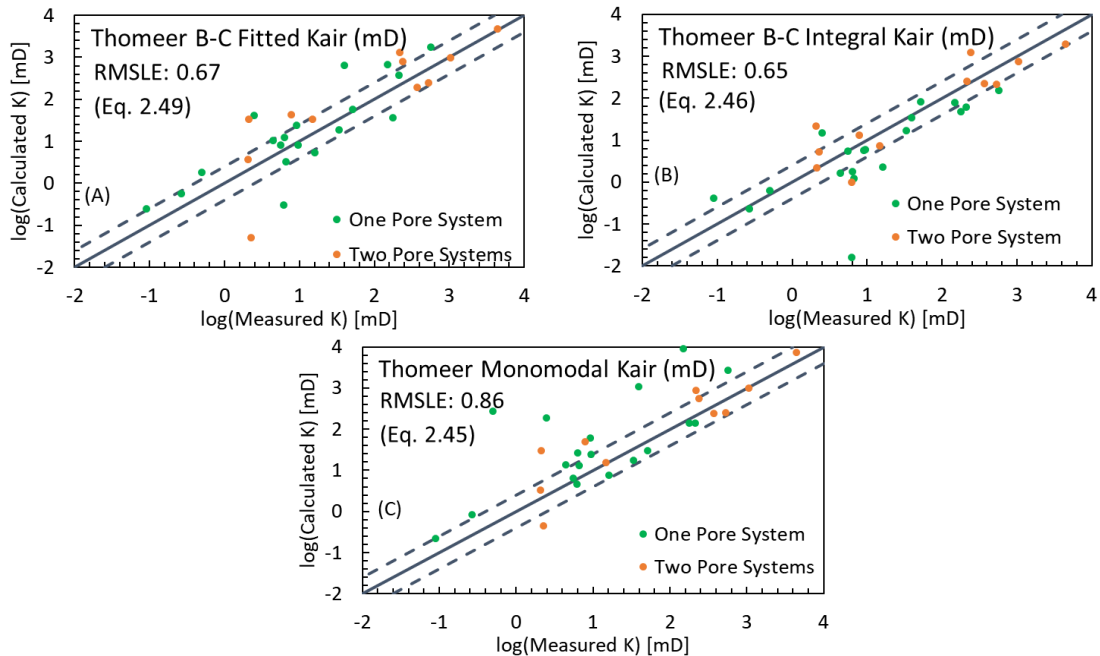


Figure 41 – Plots showing calculated versus measured permeability values of 30 limestones, assuming the presence of one or two pore systems. Results are for (A) the Thomeer Buiting-Clerke model, (B) the Thomeer Buiting-Clerke integral model and (C) the Thomeer monomodal model. Dashed lines indicate theoretical predictions within a 20% range of precision.

Another method for permeability calculations based on MICP data, also included in the Thomeer-Swanson spreadsheet, is the Swanson approach. Differently from the others mentioned earlier, the analysis consists of finding the unique pair of values of  $(BV)_{P_c}$  and  $P_c$  from the MICP data that returns the largest  $(BV)_{P_c}/P_c$  ratio. This method does not require any pore size distribution hyperbola. The Swanson point producing the largest  $((BV)_{P_c}/P_c)$  value is then used for the permeability calculations based on Eq. (2.50).

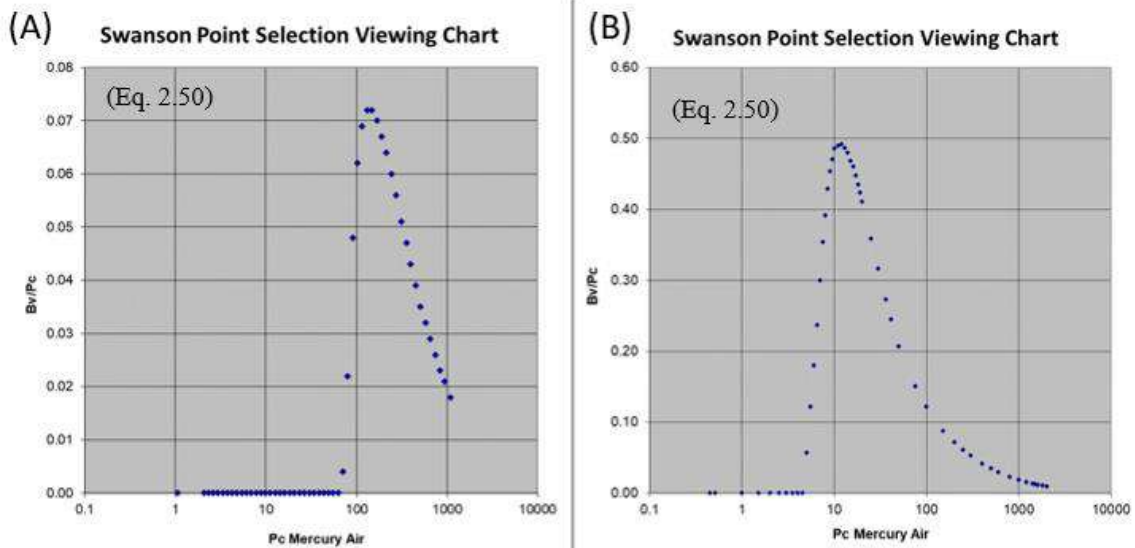


Figure 42 shows the viewing chart from which the maximum Swanson point was selected.

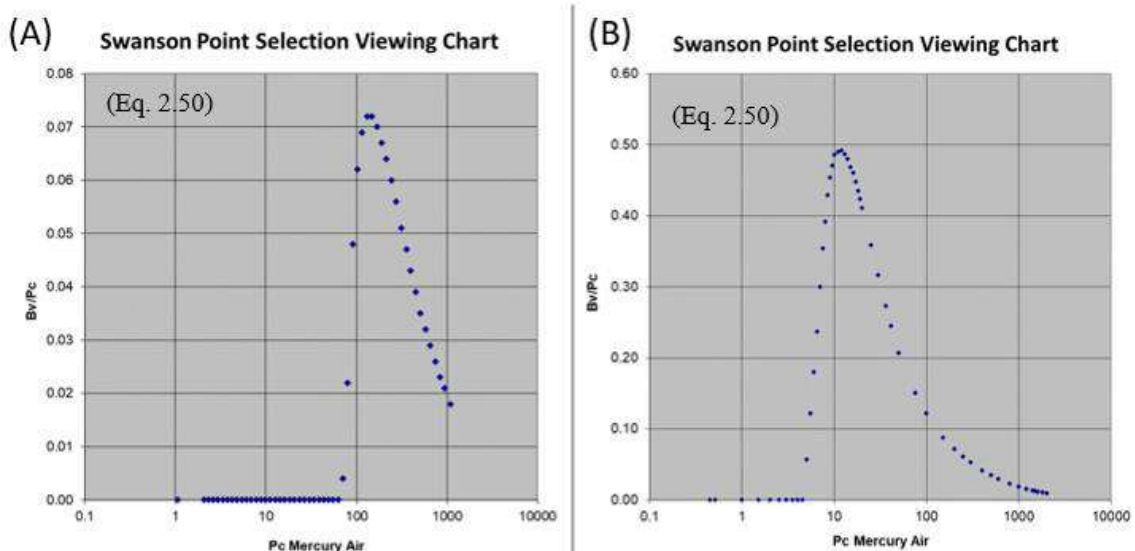


Figure 42 – Swanson point selection view window for samples L20 (A) and L05 (B). The Swanson point is the highest value of the  $(BV)_{P_c}/P_c$  ratio, located at the peak of the curve.

The permeability values obtained using the Swanson approach are shown in Figure 43. The plot shows that the Swanson approach performs very well for both unimodal and bimodal rock types.

The Thomeer spreadsheet additionally generated summary plots of the raw and closure-corrected Pc data, as well as results of the Thomeer optimizations. Figure 44 shows the resulting windows for the same samples as before (L20 and L05).

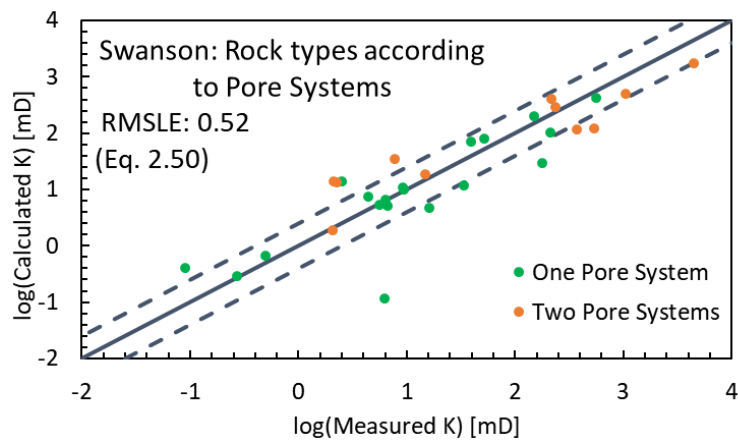


Figure 43 – Plot showing Swanson calculated permeabilities of the 30 limestone samples. The number of pore systems (unimodal or bimodal) per sample was obtained according to the best fit of the Thomeer hyperbolae. Dashed lines indicate theoretical predictions within a 20% range of precision.

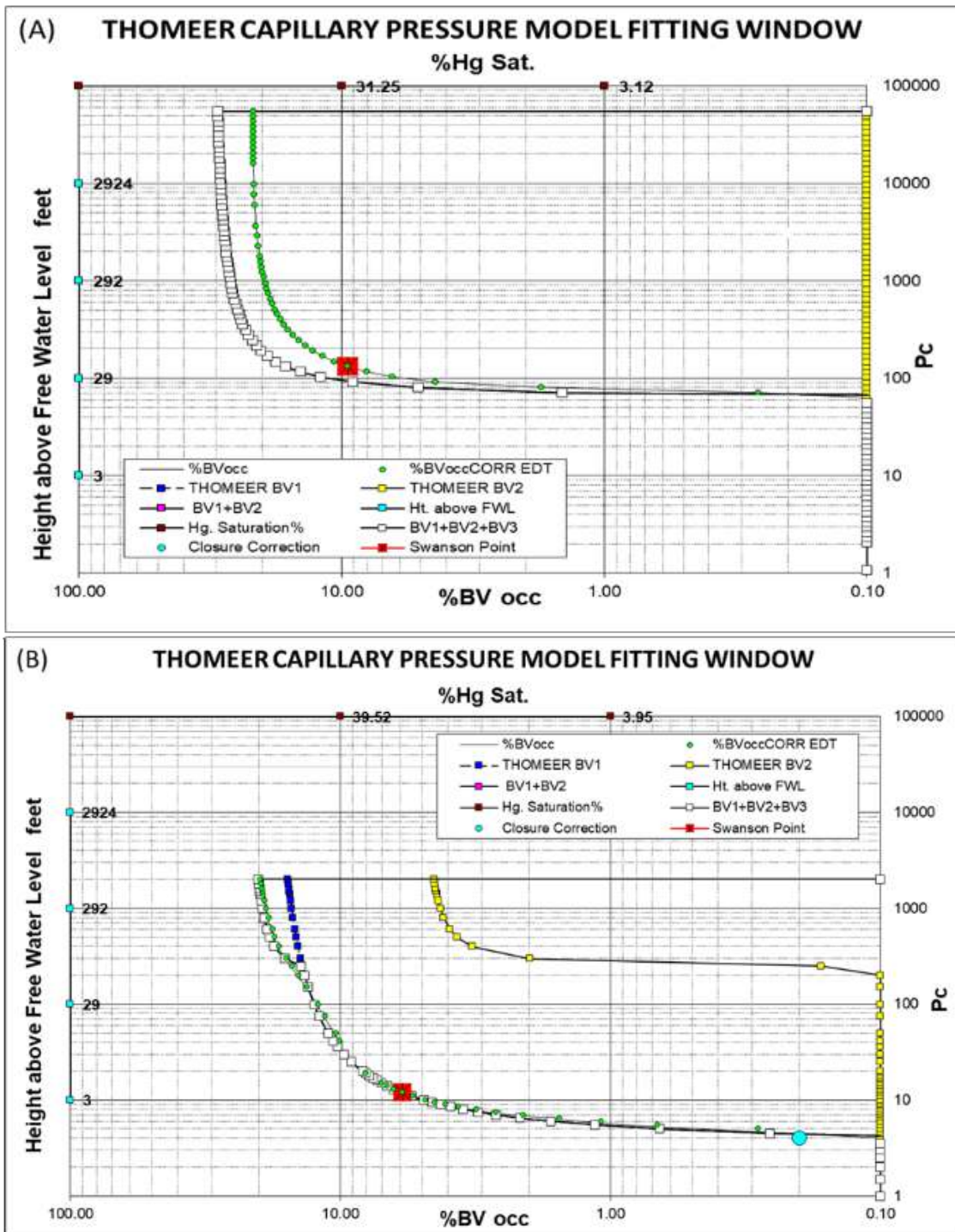


Figure 44 – View of the raw and closure corrected Pc data, and results of the Thomeer fits using up to three pore systems for sample L20 (A) and sample L05 (B). The left axis shows equivalent pressure heads (in feet), the right axis the capillary pressure (in psi), the bottom axis the injected bulk volume, and the top axis mercury saturation.

Finally, the Winland approach, corresponding to Eq. (2.51), was added to the Thomeer-Swanson spreadsheet for this work. The Winland calculations assume that the pore throat radius corresponding to the 35<sup>th</sup> percentile of injected mercury bulk volume designates the permeability correctly, even if the distribution is bimodal or trimodal. This approach was also included here, even though several (e.g., GUNTER *et al.*, 2014) found relatively poor results using the Winland method for some moldic and vuggy porosity systems. Figure 45 shows a plot of calculated Winland permeabilities versus measured values for all samples (unimodal and bimodal). The results indicate good agreement for the unimodal samples, but slightly less so for the bimodal media, as compared to the Swanson data in Figure 46.

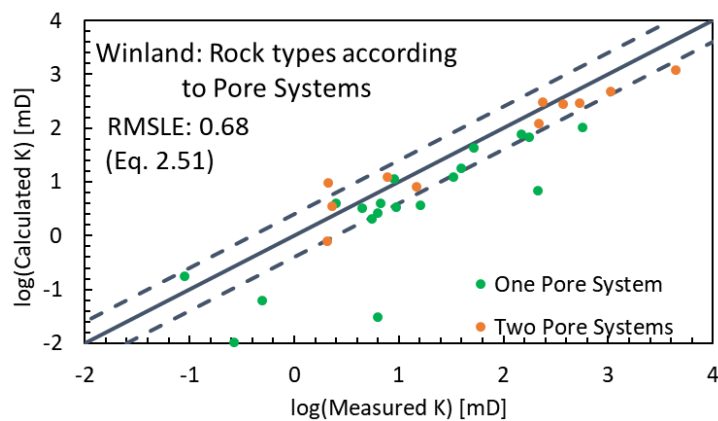


Figure 45 – Plot showing Winland calculated permeabilities for the 30 samples. The number of pore systems per sample was obtained according to the best fit of the Thomeer hyperbolae. Dashed lines indicate theoretical predictions within a 20% range of precision.

The Swanson and the Winland approaches are based on single points of the MICP data. The radius corresponding to the 35<sup>th</sup> percentile of the injected bulk volume of mercury was compared against the Swanson parameter (injected bulk volume divided by capillary pressure) in Figure 46. Results show no clear mathematical relationship between the minimum radius dictating permeability in both approaches, although both approaches presented relatively good results.

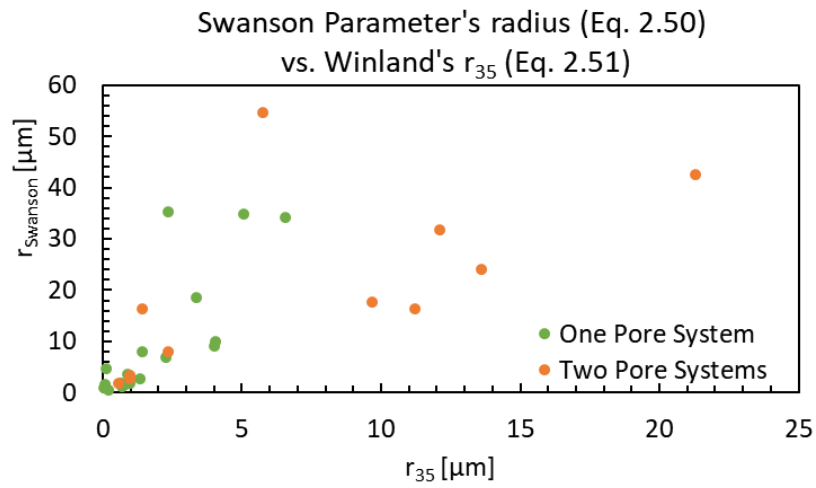


Figure 46 – Plot comparing radii corresponding to the Swanson parameter versus Winland radii at the 35<sup>th</sup> percentile for samples with one pore system (unimodal) and two pore systems (bimodal).

Table 7 – Calculated permeabilities\* and main parameters of the Thomeer-Swanson and Thomeer-Winland approaches. The number of pore systems was defined according to the Thomeer fitting function which produced the best results for each sample.

| <b>Thomeer-based approaches</b> |                     |                    |             |                  |                 |                  |                             |                               |                             |
|---------------------------------|---------------------|--------------------|-------------|------------------|-----------------|------------------|-----------------------------|-------------------------------|-----------------------------|
| <b>Sample</b>                   | <b>Pore Systems</b> | <b>Swanson</b>     |             |                  | <b>Winland</b>  |                  | <b>Thomeer Hyperbola</b>    |                               |                             |
|                                 |                     | <b>BV/P radius</b> | <b>BV/P</b> | <b>Kair (mD)</b> | <b>r35 (um)</b> | <b>Kair (mD)</b> | <b>B-C Fitted Kair (mD)</b> | <b>B-C Integral Kair (mD)</b> | <b>Monomodal fit k (mD)</b> |
| <b>IH</b>                       | 2                   | 31.9               | 0.83        | 290              | 12.1            | 299              | 800                         | 1230                          | 557                         |
| <b>L01</b>                      | 2                   | 2.83               | 0.14        | 13.7             | 0.96            | 9.69             | 34.2                        | 2.22                          | 30.1                        |
| <b>L02</b>                      | 2                   | 42.6               | 2.42        | 1770             | 21.3            | 1226             | 4735                        | 1920                          | 7309                        |
| <b>L03</b>                      | 1                   | 1.92               | 0.11        | 9.87             | 0.66            | 3.36             | 8.02                        | 5.98                          | 24.7                        |
| <b>L04</b>                      | 2                   | 24.1               | 1.15        | 502              | 13.6            | 472              | 959                         | 750                           | 985                         |
| <b>L05</b>                      | 2                   | 17.8               | 0.49        | 120              | 9.68            | 292              | 247                         | 213                           | 253                         |
| <b>L06</b>                      | 1                   | 1.06               | 0.01        | 0.11             | 0.05            | 0.03             | 0.31                        | 0.02                          | 4.67                        |
| <b>L07</b>                      | 2                   | 3.5                | 0.14        | 13.5             | 0.96            | 3.53             | 0.05                        | 5.31                          | 0.44                        |
| <b>L08</b>                      | 2                   | 16.4               | 0.49        | 117              | 11.2            | 276              | 190                         | 222                           | 239                         |
| <b>L09</b>                      | 2                   | 16.4               | 0.16        | 18.4             | 1.41            | 7.97             | 33.4                        | 7.24                          | 15.4                        |
| <b>L10</b>                      | 1                   | 10.0               | 0.39        | 80.2             | 4.05            | 43.6             | 58.3                        | 81.2                          | 29.9                        |
| <b>L11</b>                      | 1                   | 1.92               | 0.10        | 7.47             | 0.96            | 3.32             | 10.6                        | 1.61                          | 13.8                        |
| <b>L12</b>                      | 1                   | 35.3               | 0.45        | 101              | 2.37            | 6.94             | 369                         | 60.7                          | 142                         |
| <b>L13</b>                      | 1                   | 3.56               | 0.08        | 5.35             | 0.89            | 2.04             | 7.99                        | 5.47                          | 6.36                        |
| <b>L14</b>                      | 1                   | 18.5               | 0.36        | 69.3             | 3.38            | 17.8             | 647                         | 34.6                          | 1073                        |
| <b>L15</b>                      | 1                   | 8.07               | 0.14        | 14.2             | 1.41            | 3.99             | 41.4                        | 15.1                          | 186                         |
| <b>L16</b>                      | 1                   | 4.73               | 0.02        | 0.68             | 0.13            | 0.06             | 1.80                        | 0.63                          | 272                         |
| <b>L17</b>                      | 1                   | 1.53               | 0.01        | 0.29             | 0.10            | 0.01             | 0.56                        | 0.23                          | 0.83                        |

| Sample | Pore Systems | Swanson     |      |           | Winland  |           | Thomeer Hyperbola    |                        |                      |
|--------|--------------|-------------|------|-----------|----------|-----------|----------------------|------------------------|----------------------|
|        |              | BV/P radius | BV/P | Kair (mD) | r35 (um) | Kair (mD) | B-C Fitted Kair (mD) | B-C Integral Kair (mD) | Monomodal fit k (mD) |
| L18    | 2            | 8.04        | 0.24 | 34.5      | 2.34     | 12.6      | 42.7                 | 13.1                   | 48.9                 |
| L19    | 1            | 1.12        | 0.08 | 5.24      | 0.71     | 4.03      | 3.20                 | 1.22                   | 13.1                 |
| L20    | 1            | 1.61        | 0.07 | 4.68      | 0.81     | 3.64      | 5.37                 | 2.27                   | 7.7                  |
| L21    | 2            | 54.6        | 1.01 | 405       | 5.76     | 122       | 1310                 | 254                    | 873                  |
| L22    | 1            | 1.92        | 0.09 | 6.56      | 0.66     | 2.65      | 12.3                 | 1.77                   | 26.7                 |
| L23    | 1            | 6.87        | 0.13 | 12.0      | 2.27     | 12.4      | 19.1                 | 17.2                   | 17.5                 |
| L24    | 1            | 34.3        | 1.04 | 428       | 6.58     | 104       | 1759                 | 152                    | 2704                 |
| L25    | 2            | 1.78        | 0.04 | 1.88      | 0.56     | 0.80      | 3.64                 | 21.5                   | 3.34                 |
| L26    | 1            | 0.47        | 0.02 | 0.41      | 0.21     | 0.17      | 0.25                 | 0.41                   | 0.22                 |
| L27    | 1            | 2.65        | 0.12 | 10.9      | 1.32     | 11.3      | 24.3                 | 5.64                   | 62.1                 |
| L28    | 1            | 34.9        | 0.67 | 201       | 5.05     | 77.8      | 672                  | 77.7                   | 9115                 |
| L29    | 1            | 9.02        | 0.22 | 29.9      | 4.00     | 67.1      | 37.2                 | 48.6                   | 137                  |

\*Because permeability is often plotted on a logarithmic scale, some discrepancies are not visually well represented in the plots showing the of calculated versus measured permeability.



### 4.3.2 Critical Path Analysis Permeability

A Critical Path Analysis (CPA) was performed on all limestone samples. The formation factor, porosity and the Skaggs coefficients for self-similar and independent media were used in conjunction with the calculated critical radius from the MICP inflection point to calculate permeability at the REV.

The first proposed approach considered here determined the critical radius visually from the peaks of the graphs of  $\Delta S_{Hg}/\Delta \ln(P_{Hg})$ . An example of how the peak of  $\Delta S_{Hg}/\Delta \ln(P_{Hg})$  was selected visually is given below. With the largest critical radius (from the macropore system's peak), the Skaggs CPA equation is used for both self-similar and independent media, leading to two different values of the permeability for each limestone sample. Figure 47 shows a bimodal pore size distribution involving two peaks corresponding to two different inflection points on a MICP plot indicating the critical radii. The largest critical radius is used for calculations of the permeability since permeability is governed by the largest pores within multimodal samples.

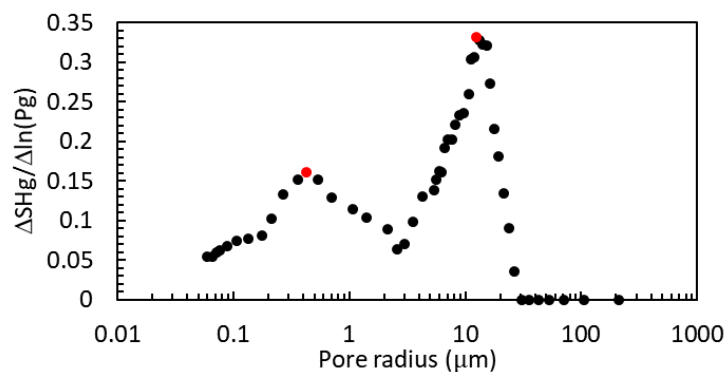


Figure 47 – Critical radii per pore system (red dots) for sample L05. The values of 0.43  $\mu\text{m}$  and 12.55  $\mu\text{m}$  for this case were chosen visually from the peaks of the MICP derived pore size distribution.

MICP data of mercury saturation versus mercury capillary pressure were also transformed into water retention versus pressure head data, which were fitted with the original and bimodal van Genuchten equations, leading to estimates of the van Genuchten parameters. As noted earlier, one should be able to estimate the critical radius (a) from the inverse of the van Genuchten  $\alpha$  parameter when his equation is fitted to the water retention data, or (b) from the inflection point of the fitted curve using Dexter's equation. The MICP

pressure data (in psi) data were for this purpose converted into radii (m) and then pressure heads (cm) using Eq. (2.6), while saturation was converted into water content with equation (2.8). Figure 48 depicts the MICP data of sample L05, previously shown in Figure 47, transformed into water content versus  $pF = -\log|h|$ , where  $h$  is the pressure head (cm). The resulting curve was posteriorly fitted with van Genuchten's equation for bimodal data.

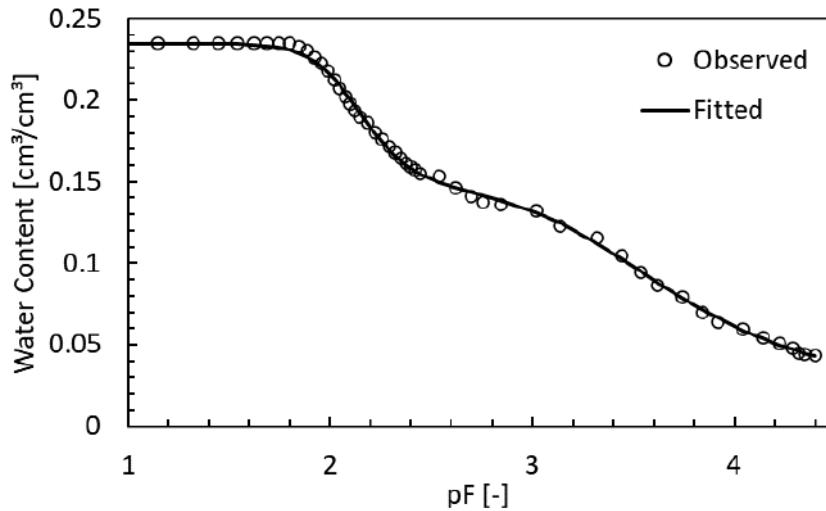


Figure 48 – L05 MICP data as input for RETC (circles), and the fitted van Genuchten equation. The fitted equation enables two different methods for calculating the critical radius: (a) from the inflection point based on Dexter's equation, and (b) from the fitted  $\alpha$  van Genuchten parameter.

Another method of calculating the critical radius used in this work comprises the fractal approach, without a need to fit the van Genuchten curve to the measured data nor selecting the peaks on a graph corresponding to the MICP inflection point. The calculations for the fractal critical radius and the critical radius based on Dexter's equation were demonstrated in section 2.14.5. All acquired critical radii were used in the Skaggs equations for self-similar and independent media. Results are shown below.

One scenario for calculating the critical radius is based on the inflection point of the MICP cumulative graph, corresponding to the peak on the MICP incremental graph. Critical radii for macro and microporous systems were obtained visually (as shown in Figure 47) from the peaks corresponding to curve. The largest critical radius was used for the calculations using the Skaggs CPA approach, which considers the medium to be both self-similar and independent. Results for the limestones are shown in Figure 49.

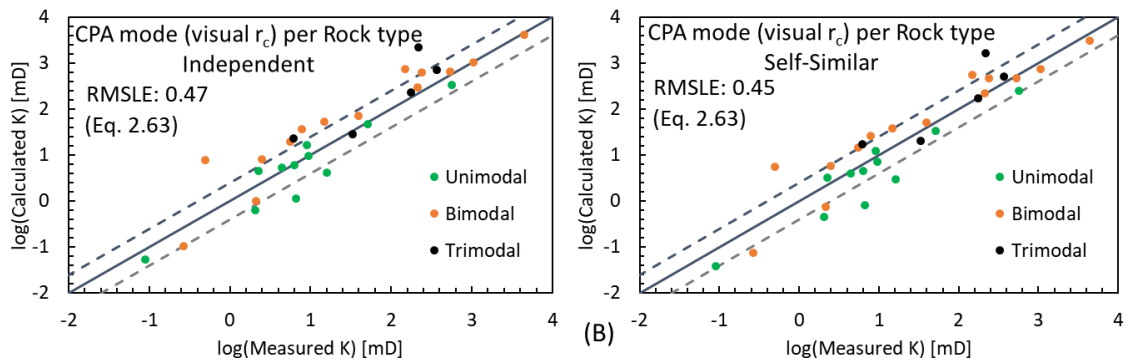


Figure 49 – Results for (A) independent and (B) self-similar porous systems via the Skaggs CPA calculations, with the critical radius chosen visually from the graph. Dashed lines indicate theoretical predictions within a 20% range of precision.

The second scenario uses the bimodal van Genuchten equation fitted to the measured MICP data, transformed into water retention data (water contents versus pressure heads). The critical radius is then assumed to be the inverse of the van Genuchten  $\alpha$  value. Results are shown in Figure 50.

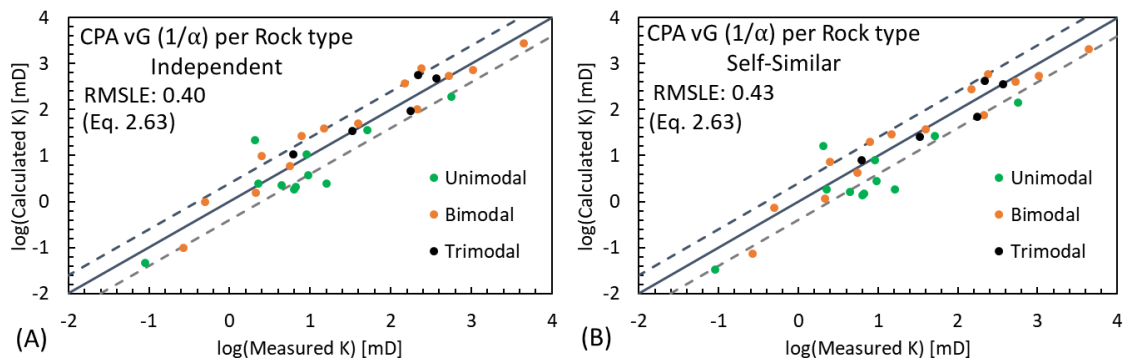


Figure 50 - Results for independent (A) and self-similar (B) pore systems via the Skaggs CPA calculations, with the critical radius being equated to the inverse of the van Genuchten  $\alpha$  value. Dashed lines indicate theoretical predictions within a 20% range of precision.

The third scenario uses the bimodal van Genuchten equation fitted to the measured MICP data, transformed into water retention data (water contents versus pressure heads), with the critical radius based on the inflection point of the MICP derived water retention curve using Dexter's equation. Results are shown in Figure 51.

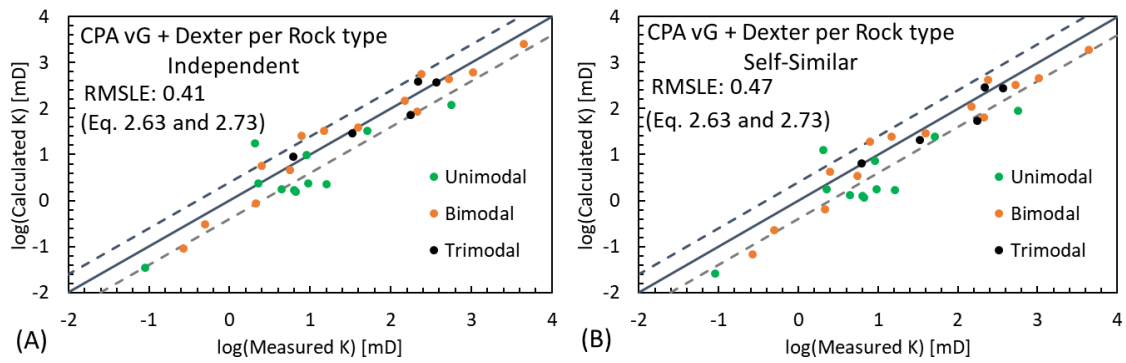


Figure 51 - Results for independent (A) and self-similar (B) pore systems via the Skaggs CPA calculations, with the critical radius estimated using Dexter's equation. Dashed lines indicate theoretical predictions within a 20% range of precision.

The fourth CPA scenario assumes that the critical radius can be estimated from the fractal dimension of the system while using again permeabilities calculated via the Skaggs methodologies for independent and self-similar media. Results are shown in Figure 52.

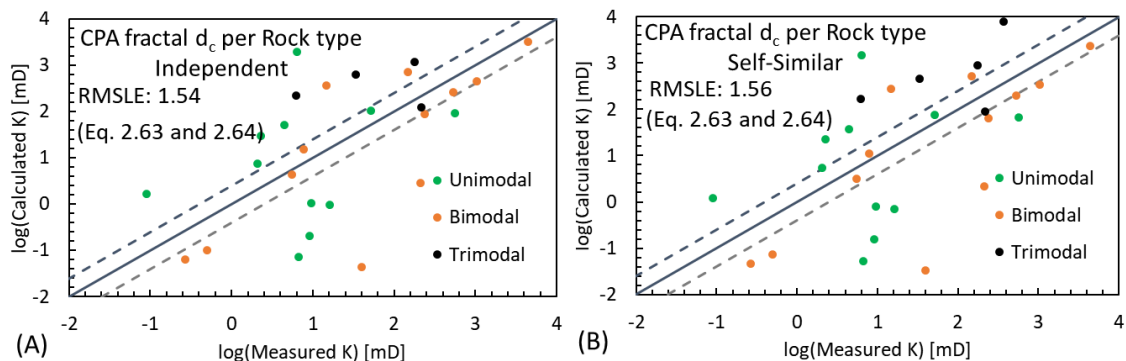


Figure 52 - Results for independent (A) and self-similar (B) porous systems via the Skaggs CPA calculations, with the critical radius calculated using a fractal approach formula. Dashed lines indicate theoretical predictions within a 20% range of precision.

Finally, to test whether the micropore and macropore systems contribute in parallel to the permeability, a test for parallelism was conducted on the results. The formation factor, the porosity and the permeability were estimated based on Archie's law for micro- and macro-pore systems, each having their proportion defined by the van Genuchten weighting parameter  $w$ . Water retention curves of the micropore and macropore systems are demonstrated in Figure 53, along with the overall curve.

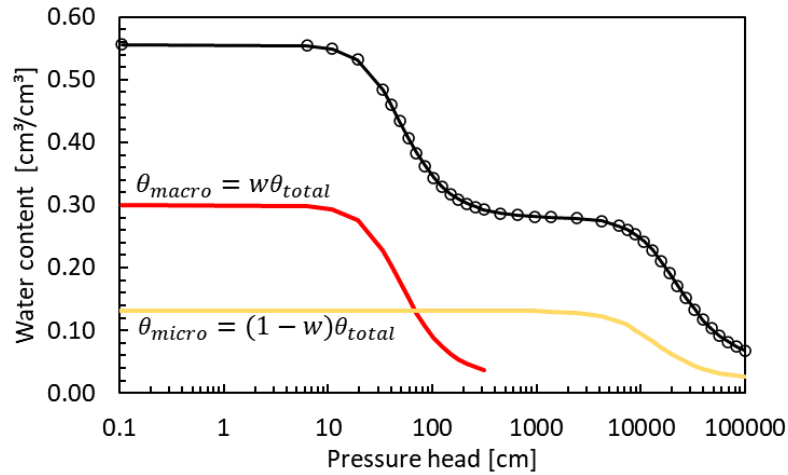


Figure 53 – Black circles show the measured data of the water content as a function of the pressure head of a bimodal sample. The black line is the bimodal van Genuchten equation fitted to the data. The bimodal van Genuchten fitted curve is the sum of contributions from the microporosity system and the macroporosity system. Figure was obtained using the RETC software (VAN GENUCHTEN *et al.*, 1991).

The results of the total permeability of the systems considered to be in parallel should be compared against the measured permeability. In Figure 54, the graph on the left (Test A) shows calculations considering parallel systems (macro and micropores), each of them having their formation factor and porosity. The graph on the right (Test B) shows calculations considering parallel systems with the total formation factor for both systems, corresponding to the overall porosity, but accounting for permeability as if they were still in parallel. Permeability was calculated using the Skaggs approach for self-similar and independent cases. Test considerations are summarized in Table 8.

Table 8 – Summary of parallelism tests that resulted in the plots of Figure 54.

| Parallelism – Test A                        | Parallelism – Test B                          |
|---|---|
| $\Phi_{mic}, \Phi_{mac}$                    | $\Phi_{mic}, \Phi_{mac}$                      |
| $F_{mic}, F_{mac}$                          | $F_{mic} = F_{mac} = F_{total}$               |
| $k_{mic} = \frac{r_{c,mic}^2}{c_s F_{mic}}$ | $k_{mic} = \frac{r_{c,mic}^2}{c_s F_{total}}$ |
| $k_{mac} = \frac{r_{c,mac}^2}{c_s F_{mac}}$ | $k_{mac} = \frac{r_{c,mac}^2}{c_s F_{total}}$ |
| $k_{total} = k_{mic} + k_{mac}$             | $k_{total} = k_{mic} + k_{mac}$               |

Comparison between the assumptions and resulting plots allows one to conclude that the macropore system does not conduct fluids independently from the micropore system (i.e., the macro and microporous systems are not parallel, but somehow communicate). This can be seen especially in the Test B plot (Figure 54), which used the system’s overall formation factor. The resulting permeabilities calculated using the Skaggs methods were much more similar to the approaches above, except for one that uses the fractal critical radius. The second plot also shows plot that, even though the pore systems do not act in parallel, the micropore system has a major impact on the permeability calculations.

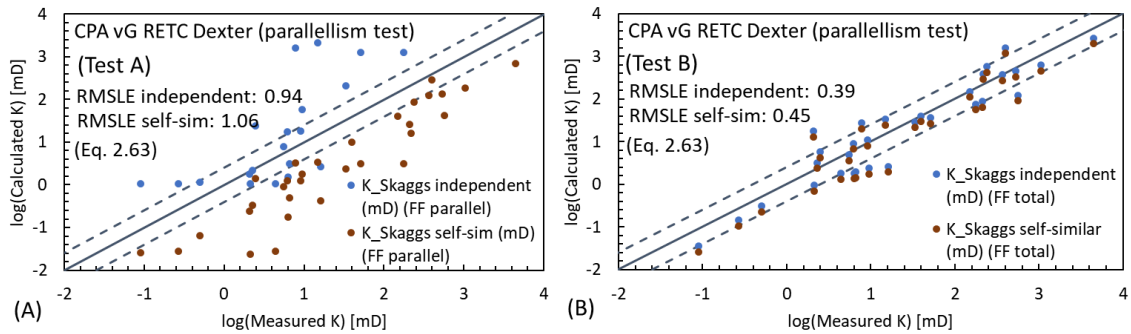


Figure 54 - Results for self-similar and independent porous systems via the Skaggs CPA calculations, considering the micro- and macro-pore parts in parallel according to the formation factor defined as in Test A (plot A) and Test B (plot B). Dashed lines indicate theoretical predictions within a 20% range of precision.

Table 9 shows the critical radius of the micropore system and resulting permeability calculated using Skaggs CPA-based approaches for independent and self-similar media.

Table 9 – Results of CPA-based approaches using the independent and self-similar equations of Skaggs

| CPA-based approaches |   |                          |                                  |   |                                   |                                  |   |                            |                                  |   |                                |                                  |   |   |   |   |   |
|----------------------|---|--------------------------|----------------------------------|---|-----------------------------------|----------------------------------|---|----------------------------|----------------------------------|---|--------------------------------|----------------------------------|---|---|---|---|---|
| Sam<br>ple           | Number<br>of<br>Modes<br>$\frac{\Delta S_{Hg}}{\Delta \ln(P_{Hg})}$ | CPA mode (visual $r_c$ ) |                                  |   | CPA vG RETC air entry<br>pressure |                                  |   | CPA vG RETC Dexter         |                                  |   | CPA fractal approach for $d_c$ |                                  |   | CPA vG RETC Dexter (Parallelism test)               |   |   |   |
|                      |   | $r_c$ macro<br>porosity  | K Skaggs<br>independ<br>ent (mD) | K<br>Skaggs<br>self-<br>similar<br>(mD) | $r_c$<br>macro<br>porosity        | K Skaggs<br>independ<br>ent (mD) | K<br>Skaggs<br>self-<br>similar<br>(mD) | $r_c$<br>macro<br>porosity | K Skaggs<br>independ<br>ent (mD) | K<br>Skaggs<br>self-<br>similar<br>(mD) | $r_c$<br>macro<br>porosity     | K Skaggs<br>independ<br>ent (mD) | K<br>Skaggs<br>self-<br>similar<br>(mD) | K Skaggs<br>independ<br>ent (mD)<br>(F<br>parallel) | K<br>Skaggs<br>self-<br>sim<br>(mD)<br>(F<br>paral-<br>lel) | K Skaggs<br>independ<br>ent (mD)<br>(F total) | K<br>Skaggs<br>self-<br>similar<br>(mD)<br>(F<br>total) |
| <b>IH</b>            | 2   | 18.3                     | 629                              | 459                                     | 20.5                              | 786                              | 582                                     | 17.3                       | 564                              | 418                                     | 6.77                           | 86                               | 63.73                                   | 115   | 85.3  | 565   | 418   |
| <b>L01</b>           | 2   | 1.42                     | 1.00                             | 0.73                                    | 1.78                              | 1.58                             | 1.17                                    | 1.32                       | 0.87                             | 0.64                                    | 0.03                           | ~0                               | ~0                                      | 0.03  | 0.02  | 0.94  | 0.70  |
| <b>L02</b>           | 2   | 30.5                     | 4107                             | 3002                                    | 25.1                              | 2781                             | 2061                                    | 24.1                       | 2566                             | 1901                                    | 26.9                           | 3206                             | 2376                                    | 916   | 679   | 2646  | 1961  |
| <b>L03</b>           | 1   | 1.40                     | 9.7                              | 7.09                                    | 0.88                              | 3.79                             | 2.81                                    | 0.69                       | 2.39                             | 1.77                                    | 0.46                           | 1.05                             | 0.78                                    | 2.39  | 1.77  | 2.39  | 1.77  |
| <b>L04</b>           | 2   | 17.4                     | 1022                             | 747                                     | 14.7                              | 734                              | 544                                     | 13.5                       | 620                              | 459                                     | 11.6                           | 456                              | 338                                     | 248   | 184   | 620   | 459   |
| <b>L05</b>           | 2   | 12.6                     | 639                              | 467                                     | 11.6                              | 545                              | 404                                     | 10.5                       | 448                              | 332                                     | 8.04                           | 262                              | 194                                     | 180   | 133   | 449   | 332   |
| <b>L06</b>           | 3   | 3.44                     | 23.3                             | 17                                      | 2.33                              | 10.7                             | 7.91                                    | 2.12                       | 8.87                             | 6.57                                    | 10.7                           | 224                              | 166                                     | 1.67  | 1.24  | 9.12  | 6.76  |
| <b>L07</b>           | 1   | 2.36                     | 4.42                             | 3.23                                    | 1.78                              | 2.52                             | 1.86                                    | 1.74                       | 2.39                             | 1.77                                    | 6.16                           | 30.1                             | 22.3                                    | 0.45  | 0.33  | 3.21  | 2.38  |
| <b>L08</b>           | 3   | 14.2                     | 690                              | 504                                     | 11.8                              | 478                              | 354                                     | 10.4                       | 367                              | 272                                     | 56.2                           | 10788                            | 7994                                    | 165   | 122   | 368   | 272   |
| <b>L09</b>           | 2   | 4.96                     | 52.4                             | 38.3                                    | 4.29                              | 39.2                             | 29                                      | 3.95                       | 33.2                             | 24.6                                    | 13.1                           | 366                              | 271                                     | 4.48  | 3.32  | 33.2  | 24.6  |
| <b>L10</b>           | 1   | 6.54                     | 45.9                             | 33.6                                    | 5.80                              | 36.2                             | 26.8                                    | 5.51                       | 32.6                             | 24.2                                    | 9.83                           | 103                              | 76.9                                    | 4.18  | 3.1   | 35.9  | 26.6  |
| <b>L11</b>           | 1   | 1.73                     | 5.37                             | 3.92                                    | 1.11                              | 2.22                             | 1.65                                    | 0.99                       | 1.75                             | 1.3                                     | 5.34                           | 51.1                             | 37.9                                    | 0.04  | 0.03  | 1.78  | 1.32  |
| <b>L12</b>           | 2   | 17.7                     | 295                              | 216                                     | 10.5                              | 103                              | 76.9                                    | 9.58                       | 86.9                             | 64.4                                    | 1.75                           | 2.89                             | 2.14                                    | 34.5  | 25.6  | 87.1  | 64.5  |
| <b>L13</b>           | 2   | 4.13                     | 19.4                             | 14.1                                    | 2.27                              | 5.85                             | 4.33                                    | 2.04                       | 4.71                             | 3.49                                    | 1.94                           | 4.28                             | 3.17                                    | 1.20  | 0.89  | 4.83  | 3.6   |
| <b>L14</b>           | 2   | 9.27                     | 69.6                             | 50.8                                    | 7.86                              | 50.1                             | 37.1                                    | 6.98                       | 39.5                             | 29.2                                    | 0.23                           | 0.04                             | 0.03                                    | 13.5  | 10  | 39.5  | 29.3  |
| <b>L15</b>           | 2   | 4.04                     | 8.04                             | 5.88                                    | 4.47                              | 9.82                             | 7.28                                    | 3.39                       | 5.66                             | 4.2                                     | 0.03                           | ~0                               | ~0                                      | 1.86  | 1.38  | 5.5   | 4.22  |

| Sam<br>ple | Number<br>of<br>Modes<br>$\frac{\Delta S_{Hg}}{\Delta \ln(P_{Hg})}$ | CPA mode (visual $r_c$ ) |                                  |   | CPA vG RETC air entry<br>pressure |                                  |   | CPA vG RETC Dexter              |                                  |   | CPA fractal approach for $d_c$  |                                  |   | CPA vG RETC Dexter (Parallelism test)               |   |   |   |
|------------|---|--------------------------|----------------------------------|---|-----------------------------------|----------------------------------|---|---------------------------------|----------------------------------|---|---------------------------------|----------------------------------|---|---|---|---|---|
|            |   | $r_c$ macro<br>porosity  | K Skaggs<br>independ<br>ent (mD) | K<br>Skaggs<br>self-<br>similar<br>(mD) | $r_c$<br>macro<br>poro-<br>sity   | K Skaggs<br>independ<br>ent (mD) | K<br>Skaggs<br>self-<br>similar<br>(mD) | $r_c$<br>macro<br>poro-<br>sity | K Skaggs<br>independ<br>ent (mD) | K<br>Skaggs<br>self-<br>similar<br>(mD) | $r_c$<br>macro<br>poro-<br>sity | K Skaggs<br>independ<br>ent (mD) | K<br>Skaggs<br>self-<br>similar<br>(mD) | K Skaggs<br>independ<br>ent (mD)<br>(F<br>parallel) | K<br>Skaggs<br>self-<br>sim<br>(mD)<br>(F<br>paral-<br>lel) | K Skaggs<br>independ<br>ent (mD)<br>(F total) | K<br>Skaggs<br>self-<br>similar<br>(mD)<br>(F<br>total) |
| <b>L16</b> | 2   | 3.44                     | 7.69                             | 5.62                                    | 1.23                              | 0.99                             | 0.73                                    | 0.68                            | 0.30                             | 0.22                                    | 0.39                            | 0.1                              | 0.07                                    | 0.09  | 0.06  | 0.31  | 0.23  |
| <b>L17</b> | 2   | 0.77                     | 0.10                             | 0.07                                    | 0.76                              | 0.1                              | 0.07                                    | 0.73                            | 0.09                             | 0.07                                    | 0.61                            | 0.06                             | 0.05                                    | 0.04  | 0.03  | 0.14  | 0.11  |
| <b>L18</b> | 2   | 4.96                     | 36                               | 26.3                                    | 4.26                              | 26.5                             | 19.7                                    | 4.16                            | 25.3                             | 18.8                                    | 3.22                            | 15.2                             | 11.3                                    | 4.32  | 3.20  | 27.2  | 20.2  |
| <b>L19</b> | 1   | 0.56                     | 1.12                             | 0.82                                    | 0.76                              | 2.05                             | 1.52                                    | 0.66                            | 1.58                             | 1.17                                    | 0.14                            | 0.07                             | 0.05                                    | 0.66  | 0.49  | 1.95  | 1.45  |
| <b>L20</b> | 1   | 1.17                     | 4.06                             | 2.97                                    | 0.92                              | 2.51                             | 1.86                                    | 0.88                            | 2.30                             | 1.71                                    | 0.56                            | 0.94                             | 0.70                                    | 0.57  | 0.42  | 2.62  | 1.94  |
| <b>L21</b> | 3   | 43.2                     | 2216                             | 1619                                    | 21.9                              | 569                              | 421                                     | 18.03                           | 386                              | 286                                     | 10.1                            | 120                              | 89                                      | 21.93   | 16.3  | 386   | 286   |
| <b>L22</b> | 1   | 1.42                     | 6.04                             | 4.41                                    | 0.79                              | 1.85                             | 1.37                                    | 0.75                            | 1.67                             | 1.24                                    | 25.6                            | 1962                             | 1454                                    | 0.24  | 0.18  | 1.84  | 1.36  |
| <b>L23</b> | 3   | 3.56                     | 27.7                             | 20.3                                    | 3.9                               | 34.6                             | 25.6                                    | 3.62                            | 28.6                             | 21.2                                    | 16.8                            | 617                              | 457                                     | 3.14  | 2.33  | 29.1  | 21.6  |
| <b>L24</b> | 1   | 17.2                     | 334                              | 244                                     | 12.9                              | 189                              | 140                                     | 10.4                            | 121                              | 90.4                                    | 8.9                             | 89.8                             | 66.6                                    | 57.7  | 42.7  | 122   | 90.43   |
| <b>L25</b> | 1   | 0.89                     | 0.63                             | 0.46                                    | 5.25                              | 21.8                             | 16.2                                    | 4.68                            | 17.3                             | 12.8                                    | 3.1                             | 7.49                             | 5.55                                    | 0.33  | 0.25  | 17.6  | 13.04   |
| <b>L26</b> | 1   | 0.27                     | 0.05                             | 0.04                                    | 0.25                              | 0.05                             | 0.03                                    | 0.22                            | 0.04                             | 0.03                                    | 1.51                            | 1.63                             | 1.21                                    | 0.04  | 0.03  | 0.04  | 0.03  |
| <b>L27</b> | 1   | 1.91                     | 16.5                             | 12.1                                    | 1.54                              | 10.8                             | 7.99                                    | 1.47                            | 9.84                             | 7.29                                    | 0.21                            | 0.21                             | 0.15                                    | 1.71  | 1.26  | 10.8  | 8.01  |
| <b>L28</b> | 2   | 17.5                     | 749                              | 548                                     | 12.4                              | 378                              | 280                                     | 7.81                            | 149                              | 111                                     | 16.9                            | 702                              | 520                                     | 55  | 40.8  | 149   | 111   |
| <b>L29</b> | 3   | 9.35                     | 228                              | 166                                     | 6.04                              | 95.1                             | 70.5                                    | 5.3                             | 73.3                             | 54.3                                    | 21.3                            | 1184                             | 877                                     | 4.19  | 3.11  | 74.9  | 55.6  |



### 4.3.3 Summary tables

The RMSLE (root mean square log-transformed error) parameter was calculated in order to compare statistically the accuracy of the Thomeer-based and Winland methods for estimating the permeability. Measured permeabilities are compared against calculated permeabilities.

Table 10 – RMSLE values obtained using the implemented Thomeer spreadsheet.

| <b>Method</b> | <b>MICP</b> | <b>RMSLE</b> |
|---------------|-------------|--------------|
| B-C Fitted    |             | 0.67         |
| B-C Integral  | Full PSD    | 0.66         |
| Monomodal     |             | 0.86         |
| Swanson       | Single      | 0.52         |
| Winland       | point       | 0.68         |

RMSLE were also obtained for the CPA-based Skaggs self-similar and independent models using different methods of obtention of critical radius. Results are shown in Table 11.

Table 11 – RMSLE calculations for the implemented CPA-based methods.

| <b>Method</b>                           | <b>MICP</b> | <b>RMSLE</b>       |                     |
|---|-------------|--------------------|---------------------|
|   |             | <b>Independent</b> | <b>Self-Similar</b> |
| CPA mode (visual $r_c$ )                |             | 0.47               | 0.45                |
| CPA vG RETC air entry pressure          |             | 0.40               | 0.43                |
| CPA vG RETC Dexter                      | Single      | 0.41               | 0.47                |
| CPA fractal approach for $d_c$          | Point       | 1.54               | 1.56                |
| CPA vG RETC Dexter (parallelism test A) |             | 0.94               | 1.06                |
| CPA vG RETC Dexter (parallelism test B) |             | 0.39               | 0.45                |

Table 12 and 13 further present differences (in percentages) between the average measured permeability and the average permeability estimated with the Thomeer and CPA methods, respectively.

Table 12 – Average permeability error calculations for the implemented Thomeer spreadsheet.

| <b>Method</b> | <b>MICP</b> | <b>Average Error [%]</b> |
|---------------|-------------|--------------------------|
| B-C Fitted    |             | 48                       |
| B-C Integral  | Full        | -37                      |
| Monomodal     | PSD         | 196                      |
| Swanson       | Single      | -48                      |
| Winland       | point       | -62                      |

Table 13 – Average permeability error calculations for the implemented CPA-based methods.

| <b>Method</b>                           | <b>MICP</b> | <b>Average Error [%]</b> |                     |
|---|-------------|--------------------------|---------------------|
|   |             | <b>Independent</b>       | <b>Self-Similar</b> |
| CPA mode (visual rc)                    |             | 34                       | -2                  |
| CPA vG RETC air entry pressure          |             | 4                        | -23                 |
| CPA vG RETC Dexter                      | Single      | -17                      | -38                 |
| CPA fractal approach for dc             | Point       | 141                      | 79                  |
| CPA vG RETC Dexter (parallelism test A) |             | -74                      | -81                 |
| CPA vG RETC Dexter (parallelism test B) |             | -16                      | -37                 |

The entries in Table 10 through Table 13 that the best results for estimating the permeability using the MICP data for carbonate limestones (which frequently show multimodal distributions), were obtained with the CPA-based approach using the Skaggs equation for an independent medium, with the critical radius obtained from van Genuchten's air entry pressure. Important graphs are shown in Appendix B.

## 4.4 Indiana Limestone High

Of the various limestone samples studied up to this point, Indiana Limestone High samples was chosen to be special by subjecting them to a wide range and diversity of tests, thus allowing supplementary analysis and investigation of the various techniques that are possible. Additional results hence are presented here for these specific samples, which are similar to those found in Brazilian Pre-salt reservoirs.

### 4.4.1 Basic Petrophysics for IH

The Indiana Limestone plugs used in this study are well behaved cylindrical samples, with good porosity (~20% range) and permeability (300 – 400 mD range), as shown by the laboratory measurements provided earlier. The samples are 1.5-inch thick (diameter) and 3 inches high. IH stands for “Indiana High”. It is possible to find Indiana limestones with low, medium and high permeabilities; this study used the higher-permeability samples.

Routine core analyses were performed on samples IH2, IH3 and IH6 of Indiana Limestone. Samples are shown in Figure 55. The obtained results are summarized in Table 14. Basic petrophysical measurements were carried out three times per sample. The results in Table 14 represent arithmetic average of the three measurements.

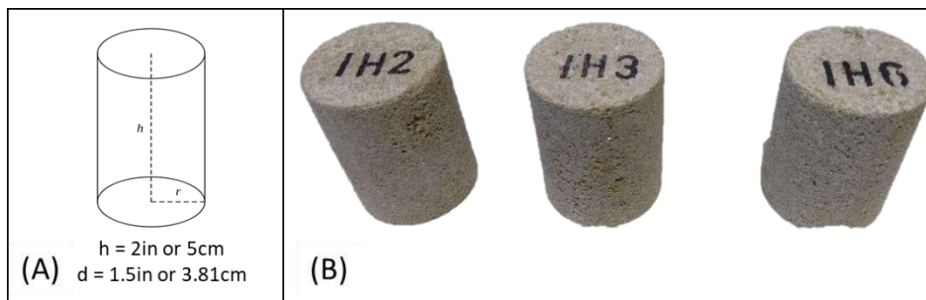


Figure 55 – (A) Dimension of the IH2, IH3 and IH6 plugs. (B) Pictures of the Indiana Limestone plugs.

Table 14 – Poropermeameter data obtained for Indiana Limestone High (IH) cylindrical samples IH2, IH3 and IH6. Permeability tests were performed under a pressure of 500 psi.

| Sample | Grain Density | Ø (%) | k <sub>air</sub> (mD) | k <sub>Klink</sub> (mD) | Dry weight (g) | Length (cm) | Diam. (cm) |
|--------|---------------|-------|-----------------------|-------------------------|----------------|-------------|------------|
| IH2    | 2.68          | 18.5  | 311                   | 287                     | 125            | 5.00        | 3.86       |
| IH3    | 2.68          | 20.1  | 400                   | 372                     | 123            | 5.00        | 3.86       |
| IH6    | 2.68          | 19.8  | 374                   | 347                     | 123            | 4.99        | 3.86       |

#### 4.4.2 Formation Factors for IH

Formation factors were measured using a saline solution of KCl at 30 Kppm with a conductivity of 59.86 mS/cm at 21.4°C. Results of the formation factor and cementation factors for 30Kppm brine are shown in Table 15. The resistivities for IH2 were measured a second time, as indicated in

Table 16, for use in the critical path analysis approaches.

Table 15 – Formation and cementation factors of Indiana limestone samples IH2 and IH3

| IH2            |                  |                    | IH3            |                  |                    |
|----------------|------------------|--------------------|----------------|------------------|--------------------|
| Pressure       | Formation Factor | Cementation Factor | Pressure       | Formation Factor | Cementation Factor |
| 500            | 37.6             | 2.17               | 500            | 29.1             | 2.17               |
| 1000           | 38.1             | 2.18               | 1000           | 28.8             | 2.16               |
| 1500           | 39.2             | 2.20               | 1500           | 28.7             | 2.16               |
| 2000           | 38.4             | 2.19               |                |                  |                    |
| 2500           | 38.4             | 2.19               |                |                  |                    |
| 3000           | 38.3             | 2.19               |                |                  |                    |
| <b>Average</b> | <b>38.3</b>      | <b>2.19</b>        | <b>Average</b> | <b>28.87</b>     | <b>2.16</b>        |

Table 16 – Formation and cementation factor of Indiana limestone sample IH2 used for the CPA-based approach.

| IH2 - CPA      |                  |                    |
|----------------|------------------|--------------------|
| Pressure       | Formation Factor | Cementation Factor |
| 500            | 38.3             | 2.17               |
| 1000           | 39.8             | 2.18               |
| 1500           | 40.4             | 2.18               |
| 2000           | 41.4             | 2.18               |
| <b>Average</b> | <b>40</b>        | <b>2.18</b>        |

The results of both resistivity tests performed on IH2 agreed closely, indicating consistency in the laboratory routine. Next, mercury injection and extrusion experiments were carried out, to be used in conjunction with the formation factors for the CPA permeability calculations.

#### **4.4.3 Mercury Porosimetry: pore throat distributions for IH**

Mercury intrusion and extrusion tests were performed on Indiana Limestone sample IH2. The intrusion results were used in the CPA analysis and in the Thomeer-Swanson spreadsheet. Mercury extrusion is an extension of mercury injection by step-wise decreasing the applied pressures. While the intrusion process provides information regarding pore throat size and volume, the information determined by the extrusion process is rarely used because of numerous still largely unresolved questions. Extrusion can be required when the intrusion experiment takes too long, or there is knowledge missing about data interpretation or the measured parameters (VOIGT *et al.*, 2020). Hysteresis between intrusion and extrusion, as shown in

Figure 56, can be due to the pore shapes and the irregular sequence of larger and smaller pores. The larger pores drain more quickly, while the smaller ones recharge more quickly. During extrusion, the pore throat causes breakage of the mercury network at the throats, resulting in trapped mercury remaining in the sample. The amount of trapped mercury is dependent on the contact angle hysteresis and pore network properties, *e.g.*, the ratio between pore entry openings and the cavity of the pore body versus the ratio between pore lengths and pore openings (GIESCHE, [s.d.]). Therefore, mercury extrusion for this example is considered to be important by providing key information about oil recovery during water injection as occurs using WAG EOR (Water-alternating-gas enhanced oil recovery) methods, to compare BTR values and aspect ratios with obtained PSDs from mercury extrusion.

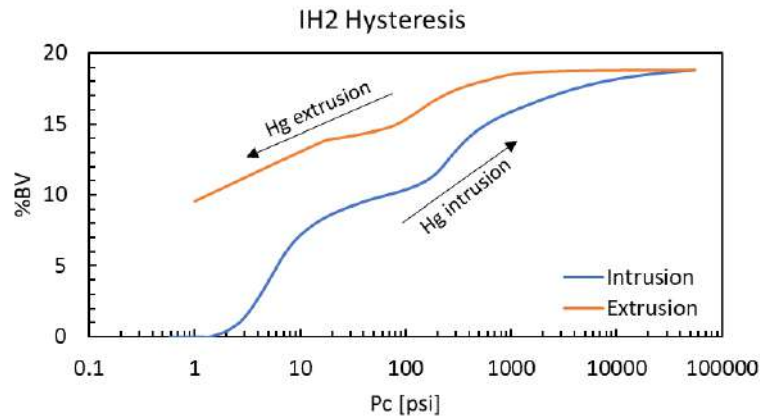


Figure 56 – Results of mercury (Hg) intrusion and extrusion experiments using the IH2 sample. The graph shows the mercury bulk volume (%) versus injection pressure for intrusion and extrusion.

During mercury injection in an initially vacuumed sample, the injection pressure is dictated by the pore openings (throats), which are the main obstacles to mercury entrance in the pores. The initially empty pore is then gradually occupied by mercury, which expels part of the air in the pore body, but leaving a residual air saturation which may form a film on the walls of the pores. Afterwards, mercury is drained by decreasing the pressure. As mercury is extruded, air occupies the pore bodies, with residual mercury remaining entrapped. In other words, assuming “ink bottle shape pores”, *i.e.*, pores consisting of a large, cylindrical pore body sandwiched between two smaller, co-axial pore necks (RIGBY, 2020), mercury intrusion reflects pore throat sizes, while extrusion yields pore body sizes. Hence, at a given value of saturation, it is possible to estimate the pore-body to pore-throat ratio. This process is depicted in Figure 57. Data of this type make it possible to estimate mercury recovery factors, which correlated to oil recovery factors, by calculating the difference in mercury (or water) saturation prior to injection and posterior to extrusion. Figure 57 also provides a means for estimating BTR (body to throat ratio) values, which are on the order of 8-10 for the smallest pores where extrusion saturations overlap the intrusion data.

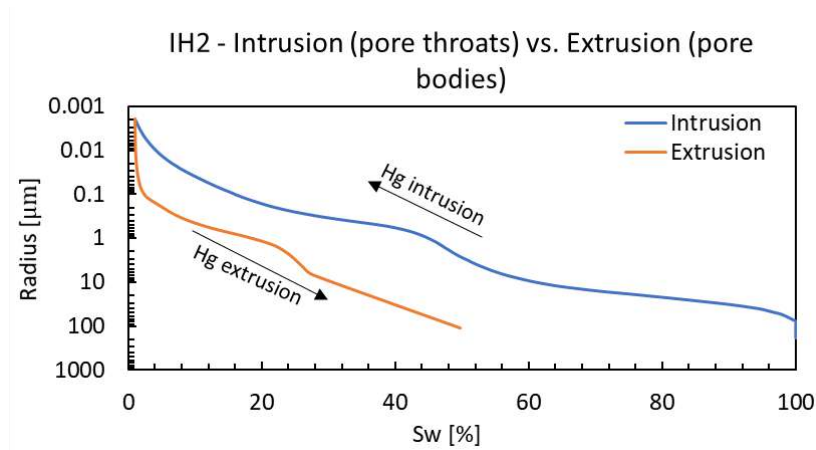


Figure 57 – Wetting fluid saturation versus pore throat radius for mercury intrusion and pore body radius from mercury extrusion. During intrusion, the wetting fluid saturation decreases as mercury saturation increases in the pore throats. Afterwards, during extrusion, mercury saturation decreases as water saturation increases in pore bodies.

Mercury extrusion commonly does not cover the same interval or pore size distribution range as mercury intrusion due to entrapment in the larger pores during extrusion. Although there is not enough data at the larger pores range, it is possible to infer a BTR of 2 when comparing the modes from the small pores of the intrusion and extrusion data (Figure 58), estimated by shifting the intrusion curve towards the extrusion curve until both match for the smaller pores. Oil recovery factors are inversely proportional to BTR values, which hence is a property related to the mercury recovery efficiency, which was found to be a mid-range value, equal to 50% in this case as seen in Figure 57. Usually, the mercury recovery factor is found to be between ~30% (low recovery factor) to ~70% (high recovery factor).

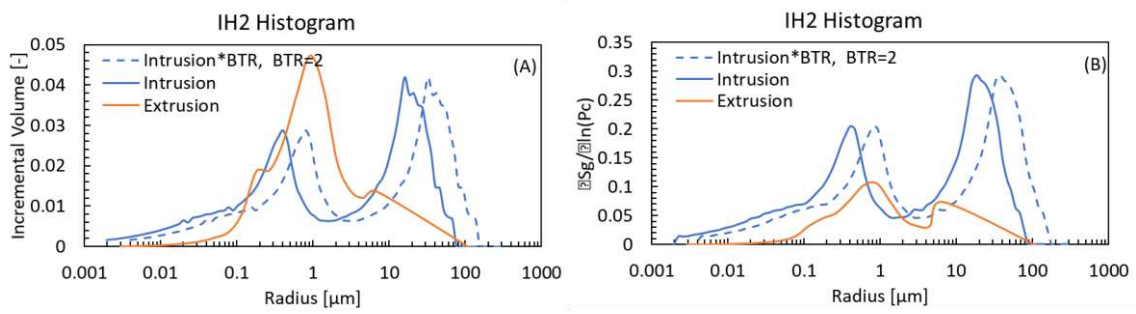


Figure 58 – Pore Throat Size Distribution obtained from intrusion and extrusion of mercury in the IH2 sample. (A) shows incremental volume and (B) shows differential saturation per natural logarithm of differential of pressure. Plot shows mercury intrusion in blue, representing pore throats, and mercury extrusion in orange, representing pore bodies. BTR is given by the ratio between pore body and throat radii from mercury porosimetry tests, equal to 2 for IH2. Dashed line shows intrusion data corrected using a BTR of 2.

Another method to determine the BTR is through an analysis of thin sections compared against MICP data. Thin section analyses were performed on sample IH1 with three different augmentations and locations. Figure 59 shows the thin sections of Indiana Limestone High samples IH1-A (with scale in red of 500 μm), IH1-B (with scale in red of 0.5 mm) and IH1-C (with scale in red of 0.5 mm). The resulting pore size distributions for these thin sections are shown Figure 60. Estimates of the BTR value is obtained by comparing the thin sections with the MICP intrusion histograms.

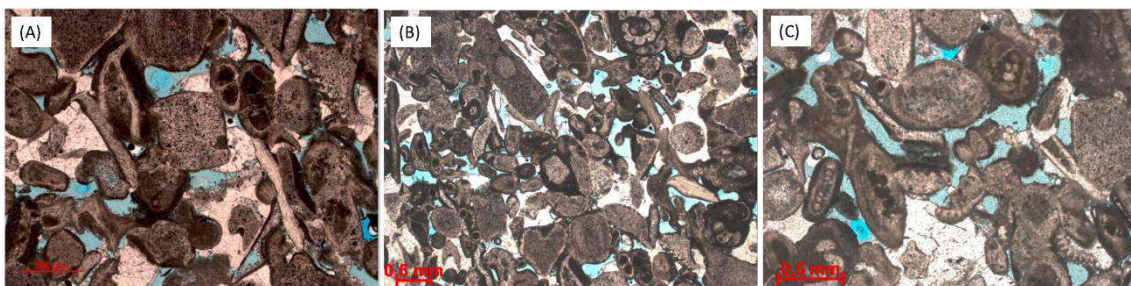


Figure 59 – Indiana Limestone High thin section. Pores are dyed in blue. Scales represent (A) IH1-A with scale in red of 500 μm, (B) IH1-B with scale in red of 0.5 mm and (C) IH1-C with scale in red of 0.5 mm.



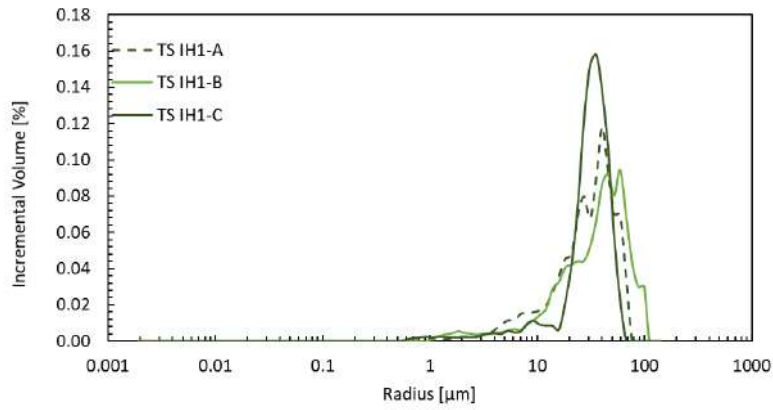


Figure 60 – Thin Section Histograms for IH1-A, IH1-B and IH1-C.

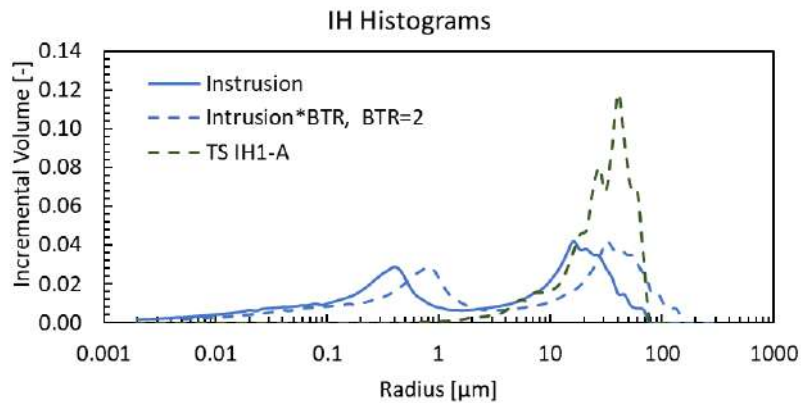


Figure 61 – Histogram of intruded mercury and thin section analysis (green dashed line) obtained for Indiana High. To match the thin section distributions, intrusion data were multiplied by a factor of 2, equal to the BTR.

The BTR value of 8-10 obtained from Figure 57 found for mercury intrusion and extrusion differs from the BTR value of 2 obtained from Figure 61 by comparing the MICP data and the Thin Section. However, when comparing the modes of the small pores from intrusion and extrusion, a BTR of 2 seems reasonable. The limited overlap between the intrusion and extrusion data over this pore size range implies a BTR ranging from 2-10 if one considers all of the intrusion and extrusion data. The BTR correlation between MICP and the Thin Section is more relevant for the larger pores, while the BTR correlation between intrusion and extrusion MICP is more relevant for the smaller pores. KENYON *et al.* (2002) showed that BTR typically varies over the range of pores bodies and throats, which most likely is the case here also. Still, the analysis of the mercury distributions and the thin sections highlights the loss of sensitivity in the overlapped zone

by impeding the distributions to merge well in this zone to enable a more complete evaluation of BTR over the full pore size distribution.

The aspect ratio (AR) for this sample was also obtained from the thin section analysis done with ImageJ. The closer the AR is to unity, the closer the shape of the pore is to a circle. For IH1-A, for example, the average aspect ratio per pore diameter is around 2.5. The thin section histogram's incremental volume (in green and blue in Figure 62) is also averaged. This is shown in Figure 62.

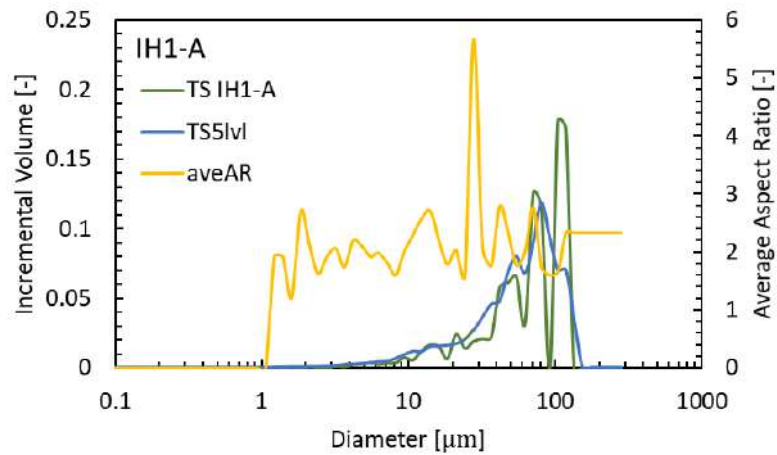


Figure 62 – IH1-A thin section analysis. The green curve shows the histogram (incremental volume distribution) from the image analysis, the blue curve is the 5-level average of the incremental volume distribution, and the yellow curve shows the average aspect ratio per pore diameter.

#### 4.4.4 Mercury injection for IH permeability estimations

##### 4.4.4.1 Permeability distribution from MICP

When performing mercury intrusion porosimetry tests, it is possible to classify the obtained pore throat radii into micro, meso and macro scales according to their throat radii, as shown in Figure 63.

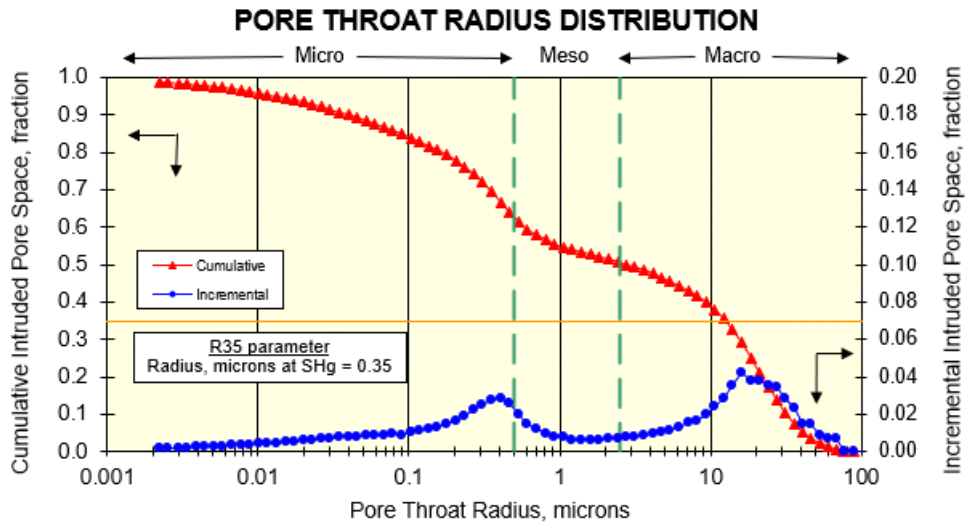


Figure 63 – IH2 MICP results for the incremental and cumulative intruded pore space, classified according to the pore scale. Graphs provided by Core Laboratories.

The incremental permeability distribution per pore throat radius is also provided. This distribution was first analyzed by PURCELL (1949), who proposed a “bundle of tubes” permeability model. Purcell’s model was extended by BURDINE *et al.* (1950). In Burdine’s model, the absolute permeability of a particular rock is a function of the pore entry radii and the mercury-filled pore volume. The resulting graph of the permeability distribution as a function of pore throat, based on the models by Purcell and Burdine, is given in Figure 64.

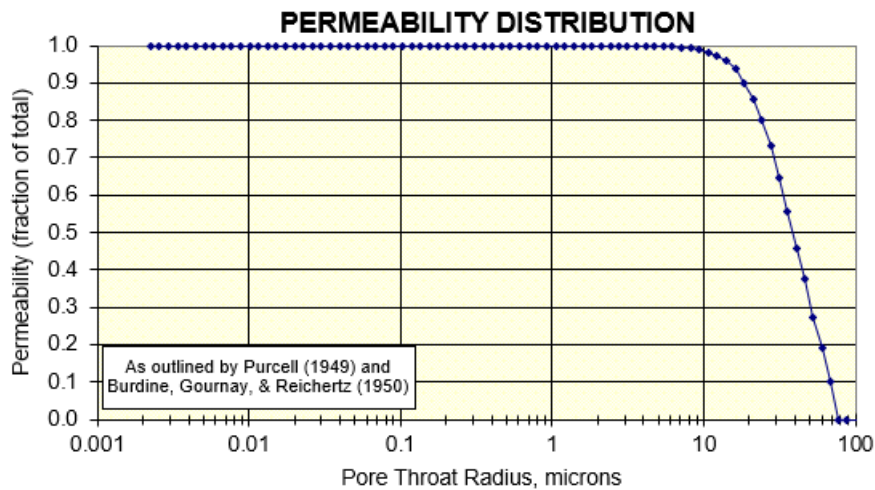


Figure 64 – IH2 permeability distribution according to the mercury injection experiment. Graph provided by Core Laboratories.

#### 4.4.4.2 Thomeer-Swanson and Winland approaches for IH

Having done the mercury data analysis, it is possible to use the results for the Thomeer-Swanson spreadsheet, Winland calculation and the Critical Path Analysis approaches. The Thomeer-Swanson spreadsheet has been used for the purpose of rock typing the Indiana Limestone (IH, plug IH2) formation through an analysis of the MICP data. Prior to proceeding, the mercury injection data were split between pore systems and examined with the computational code developed for this research using Mathematica® that characterizes the geometry of the hyperbola function fitted to the data, to obtain estimates of the related G-factor,  $(BV)_{P_{\infty}}$  and  $P_d$ . Two pore systems were identified in the IH sample, leading to two Thomeer hyperbolae with geometric factors as listed in Table 17.

Table 17 – Calculated geometric factors per pore system from MICP performed on Indiana Limestone High using the developed Mathematica® code.

| Pore system                     | G-factor | $(BV)_{P_{\infty}}$ (%) | $P_d$ (psi) |
|---------------------------------|----------|-------------------------|-------------|
| <b>PS1 (large pores system)</b> | 0.5      | 2.10                    | 16          |
| <b>PS2 (fine pores system)</b>  | 0.5      | 120                     | 7           |

The obtained geometric parameters were used next in the Thomeer-Swanson spreadsheet to calculate air permeability after inserting mercury injection pressure and bulk volume information. The parameters can be verified in Figure 65, where the left-skewed Thomeer hyperbola was fitted to the experimental data.

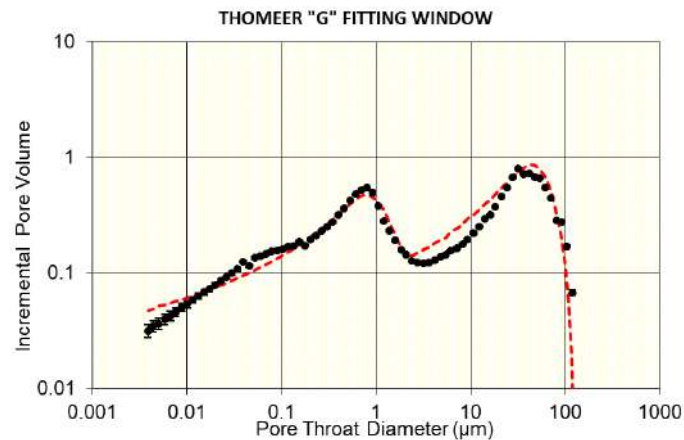


Figure 65 – Incremental bulk volume data versus pore throat diameter for IH2. The graph allows correction and verification of calculated geometric factors. These factors define the shape of the left-skewed Thomeer hyperbola (red dashed line) fitted to the measured data (black dots). Two hyperbolae are apparent, one per pore system.

A closure correction as provided by the calculations was implemented on the data, as shown in Figure 66. The closure correction was found to be 0.2.

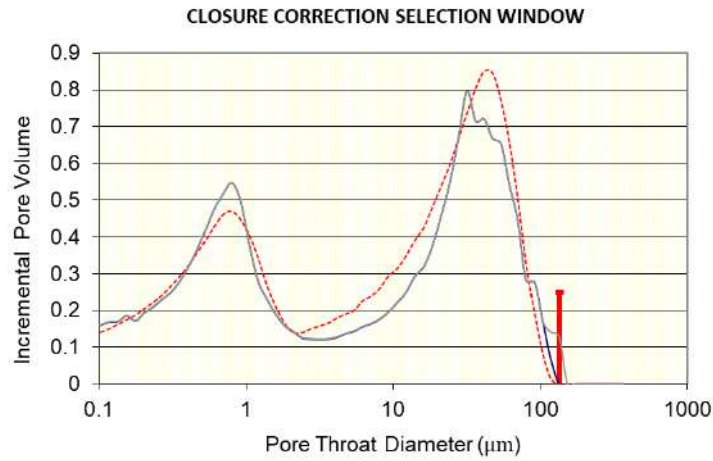


Figure 66 – Closure correction indicated by the vertical red line. The blue line represents experimental data of IH2. The red dashed line is the left-skewed Thomeer hyperbola fitted to the experimental data.

The Thomeer-Swanson spreadsheet also provides a saturation-height graph (Figure 67) in terms of water saturation and height in feet above the water table.

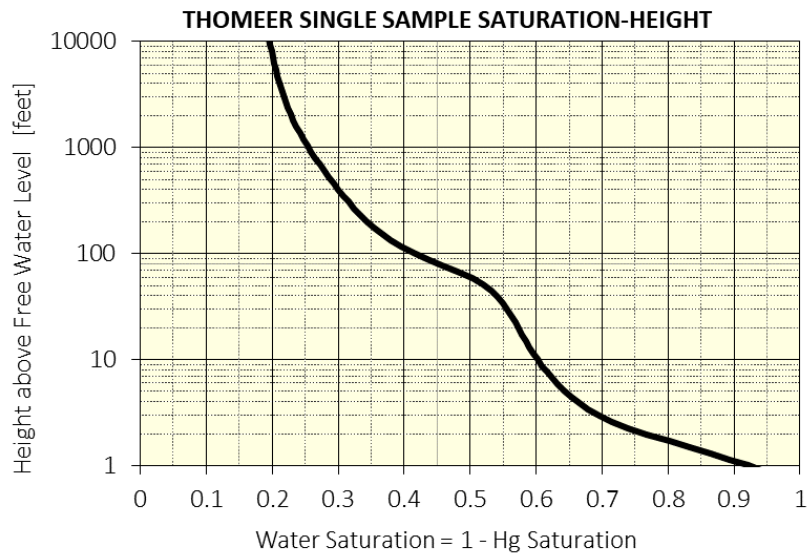


Figure 67 – Plots of the IH2 capillary pressure, represented in terms of height above a free water level, versus water saturation.

To proceed with the calculations for permeability presented in sections 2.12 and 2.13, the bulk volume and capillary pressure data were used to generate input data to the methods, such as  $B_v^Q$  and  $e^{-2D_f Q}$  used in the Buiting-Clerke tortuous and relative fractal tubular bundle integral method, following Eq. (2.47) and represented in Figure 68, and the Swanson Point used in the Swanson Model's Eq. (2.50). The Swanson Point was obtained by calculating the maximum value of the ratio  $\left| \frac{BV(P_c)}{P_c} \right|$ . The maximum was obtained from the peak of the graph presented in Figure 69.

For the Indiana Limestone integrations, a fractal dimension ( $D_f$ ) equal to 1.47, was calculated using the computational code developed in C++ for this work. The code may be used to analyze the thin section binary images using a bidimensional Box-Counting methodology. Figure 69 shows the summarized Thomeer data before and after fitting the equations.

The Winland Model was also added to the Thomeer-Swanson spreadsheet for this work, to facilitate permeability calculations based on the 35<sup>th</sup> percentile of the pore throat cumulative bulk volume distribution. Results found for the air permeability based on the Thomeer-Swanson spreadsheet with geometric factors of the Thomeer hyperbola and the fractal dimension calculated with the computational codes developed during this research, as well as by the Winland models, are summarized in Table 18.

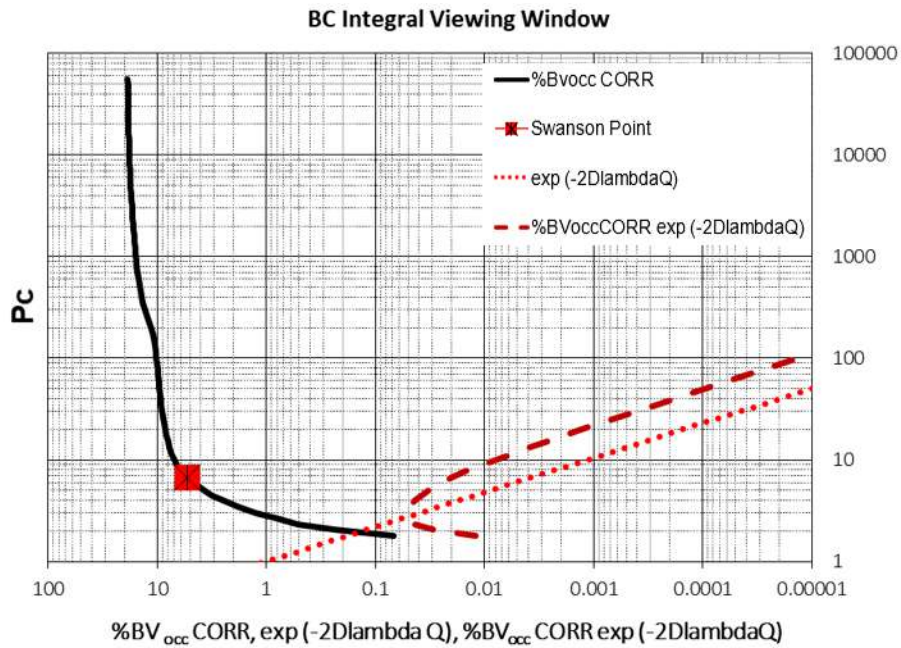


Figure 68 – Plots of  $B_v^Q$  (%BV<sub>occ</sub> CORR) and  $e^{-2DfQ}$  (exp(-2Dlambda Q)) used for the Buiting-Clerke tortuous and relative fractal tubular bundle integral. The Swanson point is also indicated in this graph.

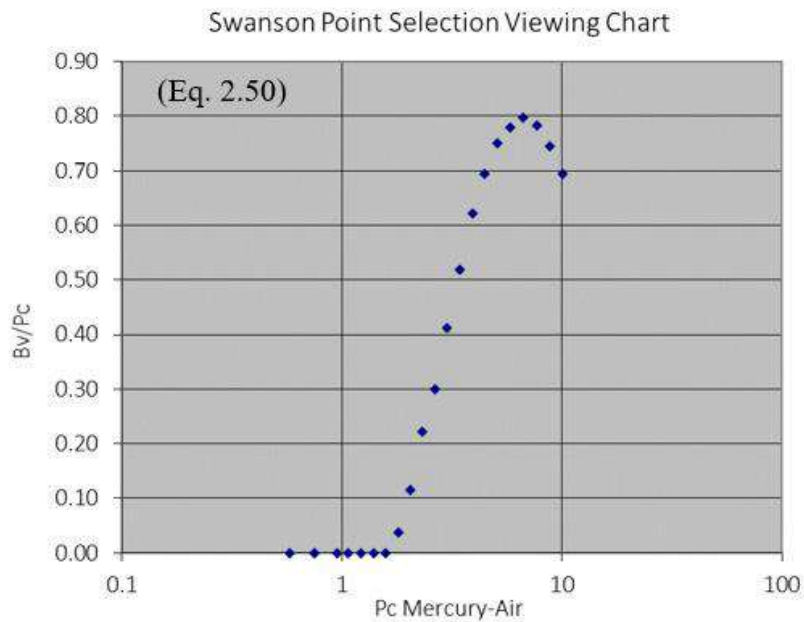


Figure 69 – Plot showing that the Swanson point of IH2 can be obtained by finding the coordinates that have the largest  $BV/P_c$  ratio.



The Thomeer spreadsheet additionally generated summary plots of the raw and closure-corrected Pc data, as well as results of the Thomeer optimizations, are shown in Figure 70 for the IH sample.

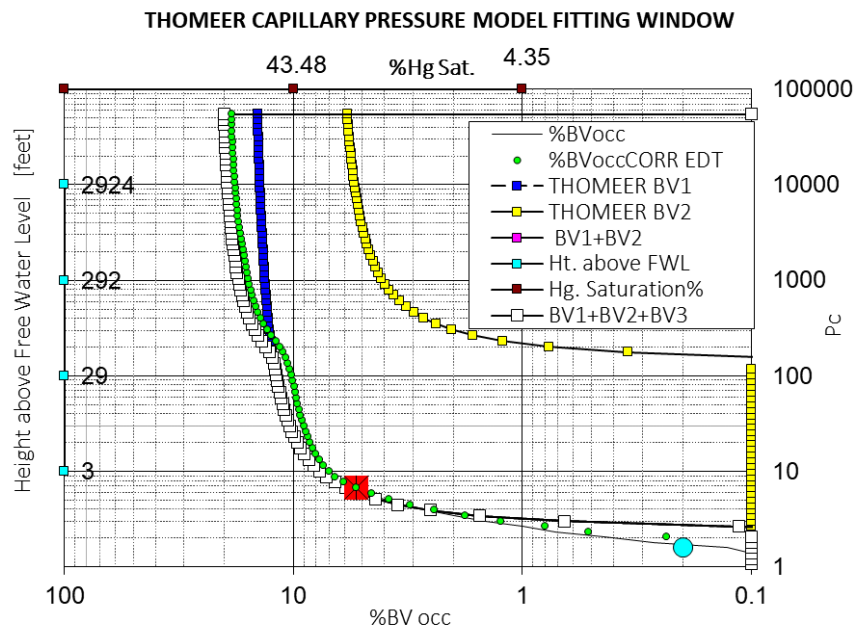


Figure 70 – View of the raw, and closure-corrected Pc data and results for the Thomeer fits using up to three pore systems for IH2. The left axis shows the equivalent pressure head (feet), the right axis the capillary pressure (psi), the bottom axis the injected bulk volume and the top axis mercury saturation.

The Winland Model was also added to the Thomeer-Swanson spreadsheet for this work, to facilitate permeability calculations based on the 35<sup>th</sup> percentile of the pore throat cumulative bulk volume distribution. Results found for the air permeability based on the Thomeer-Swanson spreadsheet with geometric factors of the Thomeer hyperbola and the fractal dimension calculated with the computational codes developed during this research, as well as by the Winland models, are summarized in Table 18.

Table 18 also includes calculated errors relative to the measured air permeabilities. Samples IH2, IH3 and IH6 had dimensions equivalent to 5 cm in length and 3.85 cm in diameter for the basic petrophysical measurements, and an average permeability of 362 mD (reference to Error B in Table 18). IH2 was posteriorly submitted again to basic petrophysics, using a new length of 2.62 cm and a measured permeability of 240 mD (reference to Error A in Table 18).



Table 18 – Obtained results for the air permeability based on the Thomeer-Swanson and Winland spreadsheet and comparison against permeabilities measured using basic petrophysics done immediately prior to the mercury intrusion experiments.

| <b>Approach used for air permeability estimation</b>               | <b>Calculated k</b> | <b>Error A [%]</b> | <b>Error B [%]</b> |
|--|---------------------|--------------------|--------------------|
| <b>Basic Petrophysics Permeability</b>                             | -                   | 240 mD             | 362 mD             |
| <b>Thomeer monomodal fitting method</b>                            | 577 mD              | 140                | 59                 |
| <b>Buiting-Clerke using fractal tubular bundle integral method</b> | 921 mD              | 284                | 154                |
| <b>Buiting-Clerke using fitted Thomeer hyperbola method</b>        | 800 mD              | 233                | 121                |
| <b>Swanson point-based method</b>                                  | 273 mD              | 13                 | 25                 |
| <b>Winland's 35<sup>th</sup> percentile method</b>                 | 299 mD              | 24                 | 17                 |

#### 4.4.4.3 Critical Path Analysis on Indiana Limestone

A Critical Path Analysis was also applied to the Indiana limestone sample IH2 mercury data, as presented in section 4.3.2. The formation factor, porosity and permeability were also measured immediately before mercury injection and extrusion. CPA was applied using the Skaggs coefficients for self-similar and independent media.

##### 4.4.4.3.1 Visual choice of critical radius

IH2 was tested for both mercury intrusion and extrusion. The inflection point on the mercury porosimetry curve, if measured accurately by increasing the mercury pressure slowly and gradually, indicates the percolation threshold for single phase. Inflection points on the mercury porosimetry curve are located at the peak on  $\Delta S_{Hg}/\Delta \ln(P_{Hg})$  plots.

To visually choose the critical radius, mercury data must be plotted as  $\Delta S_{Hg}/\Delta \ln(P_{Hg})$ , where  $P_{Hg}$  is the mercury pressure or capillary pressure  $P_c$ , as seen in Figure 71. This technique is applicable to both mercury intrusion and extrusion.

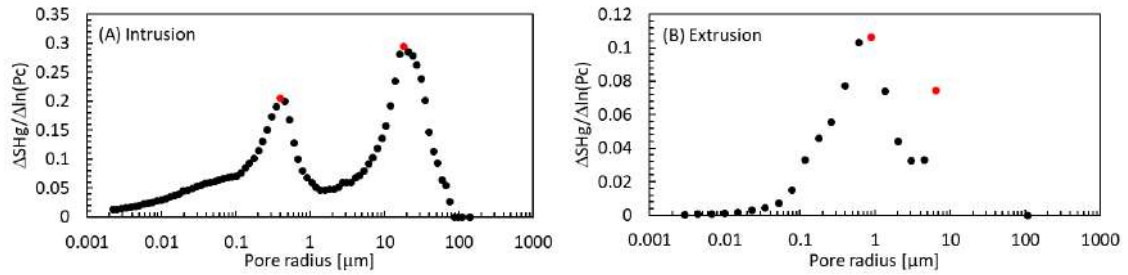


Figure 71 – Mercury (A) intrusion and (B) extrusion derivative data. Red points at the peaks correspond to inflection points on the porosimetry curves.

The intrusion and extrusion plots of the Indiana Limestone High (IH) sample has a clear bimodal (or dual-porosity) pore size distribution. In agreement to the literature reviewed in this work, the critical radius was chosen from the peak with the largest radius. Results from the CPA analysis using the visual method for the critical radius is presented in Table 19 for the intrusion and extrusion experiments. Two types of porous media were considered: independent and self-similar media, resulting in permeability calculations of  $k_{Skaggs}^{indep}$  and  $k_{Skaggs}^{self-sim}$ , respectively. The difference between the independent and self-similar approaches by Skaggs is the constant multiplying the formation factor.

Table 19 – Summary of Skaggs-CPA air permeability results for the intrusion and extrusion experiments, with the critical radius extracted from differential graph as described in the text.

| Experiment | $r_c$ [ $\mu\text{m}$ ] | $k_{Skaggs}^{indep}$ [mD] | $k_{Skaggs}^{self-sim}$ [mD] |
|------------|-------------------------|---------------------------|------------------------------|
| Intrusion  | 18.3                    | 629                       | 459                          |
| Extrusion  | 6.62                    | 82.3                      | 60.2                         |

Errors in the air permeability were again estimated relative to the measured air permeability values using basic petrophysics. Samples IH2, IH3 and IH6 had dimensions equivalent to 5 cm in length and 3.85 cm in diameter during the basic petrophysics experiments. IH2 was posteriorly submitted again to basic petrophysics, with a new length of 2.62 cm (IH2B). Results are presented in Table 20.

Table 20 – Summary of Skaggs-CPA air permeability results for the intrusion and extrusion experiments, with the critical radius extracted from the differential graph as described above. Results are compared against previous permeability measurements in terms of percentual error.

| Experiment       | Sample | $k_{air}$ [mD] | $k_{Skaggs}^{indep}$ | Error [%] | $k_{Skaggs}^{self-sim}$ | Error [%] |
|------------------|--------|----------------|----------------------|-----------|-------------------------|-----------|
| <b>Intrusion</b> | IH2    | 311            |                      | 102       |                         | 48        |
|                  | IH2 B  | 240            |                      | 162       |                         | 92        |
|                  | IH3    | 400            |                      | 57        |                         | 15        |
|                  | IH6    | 375            |                      | 68        |                         | 23        |
| <b>Extrusion</b> | IH2    | 311            |                      | 74        |                         | 81        |
|                  | IH2 B  | 240            |                      | 66        |                         | 75        |
|                  | IH3    | 400            |                      | 79        |                         | 85        |
|                  | IH6    | 375            |                      | 78        |                         | 84        |

Average values of the measured permeability using basic petrophysics applied to equally cut samples were again compared against calculated Skaggs-CPA results for independent and self-similar media. IH2, IH3 and IH6 measured permeability values were averaged and compared against the calculated values in terms of percentage error. Results are shown in Table 21.

Table 21 –The Skaggs-CPA results are compared against the average of permeability measurements from samples IH2, IH3 and IH6 in terms of percentual error.

| Experiment       | $k_{air}$ [mD] | $k_{Skaggs}^{indep}$ | Error [%] | $k_{Skaggs}^{self-sim}$ [mD] | Error [%] |
|------------------|----------------|----------------------|-----------|------------------------------|-----------|
| <b>Intrusion</b> | 362            |                      | 74        |                              | 27        |
| <b>Extrusion</b> |                |                      | 77        |                              | 83        |

Table 22 provides a summary of the best approach for calculating the air permeability of each sample when estimating the critical radius visually from the intrusion and extrusion graphs in Figure 71. The summary indicates that the best method for estimating the permeability from the critical radii is the self-similar medium approach for intrusion data, and the independent medium approach for extrusion data.

Table 22 – Summary of best Skaggs-CPA calculation method, based on errors presented, for critical radii ( $r_c$ ) obtained visually from the graphs in Figure 71.

| Sample       | Best Skaggs-CPA Method for visually chosen |             |
|--------------|--|-------------|
|              | $r_c$                                      |             |
|              | Intrusion                                  | Extrusion   |
| <b>IH2</b>   | Self-Similar                               | Independent |
| <b>IH2 B</b> | Self-Similar                               | Independent |
| <b>IH3</b>   | Self-Similar                               | Independent |
| <b>IH6</b>   | Self-Similar                               | Independent |

It is reasonable to expect that permeabilities estimated from the extrusion experiments are lower than those from intrusion, which agrees with the mid-range value of residual mercury saturation of 50% obtained in section 4.4.3. This confirms the fact that mercury gets trapped in pores during pressure release and wetting-fluid entrance in the system due to hysteresis.

#### 4.4.4.3.2 Critical radius from air entry pressure

The van Genuchten equation was used in two different manners for obtaining the critical radius from mercury injection observations. The first method reported here is estimating the critical radius from an analysis of the van Genuchten  $\alpha$  parameter, which is approximately equal to the inverse of air entry pressure head in centimeters. For this analysis, water retention data were calculated based on provided mercury saturations per given pressure step. The air entry pressure is located at the inflection point of the water retention curve and can be calculated as the pressure head (in centimeters) for later estimation of the critical radius.

The bimodal equation of van Genuchten was used in the RETC software, returning two  $\alpha$  values, one per pore system. The larger value of  $\alpha$  relates to the macropore system, and the smaller value to the smaller pores. From the value of  $\alpha$ , it is possible to calculate the air entry pressure and related pore radius. The larger value of  $\alpha$ , and consequently the smaller value of pressure head, gives the CPA critical radius. Table 23 lists the van Genuchten parameters that estimated from the Indiana Limestone mercury injection data.

Table 23 – Estimated values of the van Genuchten parameter  $\alpha$  (inverse of the pressure head) and  $h$  (the pressure head) for a bimodal distribution of pore sizes and the equivalent pore radii ( $r$ ).

| Pore system | $\alpha$ [1/cm] | $h$ [cm] | $r$ [ $\mu\text{m}$ ] |
|-------------|-----------------|----------|-----------------------|
| Micropores  | 0.00039         | 2564     | 0.58                  |
| Macropores  | 0.0138          | 72.5     | 20.5                  |

The largest radius as estimated from van Genuchten’s air entry pressure value was used for the Skaggs-CPA permeability calculation. Results are shown in Table 24. All errors were calculated relative to the average Indiana Limestone permeability of 362 mD.

Table 24 – Estimated permeabilities and corresponding errors for the critical radiuses estimated from the air entry pressure, considering the medium to be independent and self-similar.

| $r_c$ [ $\mu\text{m}$ ] | $k_{Skaggs}^{indep}$ [mD] | Error [%] | $k_{Skaggs}^{self-sim}$ [mD] | Error [%] |
|-------------------------|---------------------------|-----------|------------------------------|-----------|
| 20.46                   | 786                       | 117       | 582                          | 61        |

#### 4.4.4.3.3 Critical radius from Dexter’s derivation

The second possible approach using the van Genuchten equation for estimating the critical radii from MICP injection data involves the inflection points as proposed by Dexter (Eq. 2.74). From the inflection points, the corresponding radii can be calculated. Permeability values were obtained for independent and self-similar media according to the Skaggs-CPA approach. For the Dexter equation, it was necessary to analyze the MICP data in terms of the bimodal van Genuchten hydraulic equation using RETC. The values of  $m$  and  $n$  obtained with the optimization were used in Dexter’s equation for the inflection point and correspondent radii. Results are given in Table 25.

Table 25 – van Genuchten parameters used for estimating radii at the inflection points and radii based on Dexter’s equation for the macropore and micropore systems.

| Pore system | $\alpha$ [1/cm] | $m$  | $n$  | $r$ [ $\mu\text{m}$ ] |
|-------------|-----------------|------|------|-----------------------|
| Micropores  | 0.0004          | 0.38 | 1.61 | 0.31                  |
| Macropores  | 0.014           | 0.65 | 2.88 | 17.3                  |

Based on the definition of CPA, the largest radius calculated from Dexter's equation was used to calculate the system's air permeability. Table 26 shows the errors relative to the average Indiana Limestone permeability that was measured (362 mD).

Table 26 – Estimated permeability values and corresponding errors of the critical radius calculated with Dexter's equation, considering the medium to be independent and self-similar.

| $r_c$ [ $\mu\text{m}$ ] | $k_{Skaggs}^{indep}$ [mD] | Error [%] | $k_{Skaggs}^{self-sim}$ [mD] | Error [%] |
|-------------------------|---------------------------|-----------|------------------------------|-----------|
| 17.3                    | 564                       | 56        | 418                          | 15        |

Dexter's equation (2.74) was also used to analyze the existence of parallelism between the pore systems. For this, the van Genuchten dual-porosity equation (was fitted to the mercury intrusion data transformed into a water retention curve. The obtained coefficient  $w$  that divides the medium into micro- and macro-pores was used to calculate the porosity, the formation factor and and permeability for each porous system. The obtained results for IH are given in Table 27.

Table 27 – Variables used for the parallelism test based on van Genuchten's bimodal equation fitted to the IH water retention data.  $\emptyset$  is the porosity,  $F$  is the formation factor,  $w$  and  $m$  are van Genuchten parameters, and the subscripts mic and mac represent the micropore and macropore subsystems, respectively.

| Parameter         | Value |
|-------------------|-------|
| $w$               | 0.52  |
| $m$               | 2.17  |
| $\emptyset_{mic}$ | 0.09  |
| $\emptyset_{mac}$ | 0.09  |
| $F_{mic}$         | 165   |
| $F_{mac}$         | 195   |

For each pore system (micro and macro), a critical radius was calculated and the permeability then estimated using formation factors ( $F_{mic}$  and  $F_{mac}$ ) for the micro and microporous systems, based on Archie's law, respectively (Test A). All errors (Table 28) were calculated with respect to the average Indiana Limestone permeability of 362 mD.

Table 28 – Parallelism test’s estimated permeability values and corresponding errors for critical radius calculated from Dexter’s derivation, for Test A, considering the medium to be independent and self-similar.  $F_{mic}$  and  $F_{mac}$  were used instead of  $F_{total}$ .

| <b>Porous system</b> | $r_c$ [ $\mu\text{m}$ ] | $k_{Skaggs}^{indep}$ [mD] | Error [%] | $k_{Skaggs}^{self-sim}$ [mD] | Error [%] |
|----------------------|-------------------------|---------------------------|-----------|------------------------------|-----------|
| <b>Micropores</b>    | 0.31                    | 0.04                      | -         | 0.03                         | -         |
| <b>Macropores</b>    | 17.3                    | 115                       | -         | 85.2                         | -         |
| <b>Sum</b>           | -                       | 115                       | 68        | 85.3                         | 76        |

The test B of parallelism consisted of still using the  $w$  coefficient for dividing the medium into micro and macropores, but now assuming that  $F_{mic} = F_{mac} = F_{total}$ . All errors were calculated with respect to the average Indiana Limestone permeability of 362 mD. Results are presented in Table 29.

Table 29 – Parallelism test’s estimated permeability values and corresponding errors for critical radius calculated using Dexter’s equation for Test B, considering the medium to be independent and self-similar.  $F_{total}$  were used instead of  $F_{mic}$  and  $F_{mac}$ .

| <b>Porous system</b> | $r_c$ [ $\mu\text{m}$ ] | $k_{Skaggs}^{indep}$ [mD] | Error [%] | $k_{Skaggs}^{self-sim}$ [mD] | Error [%] |
|----------------------|-------------------------|---------------------------|-----------|------------------------------|-----------|
| <b>Micropores</b>    | 0.3104                  | 0.18                      | -         | 0.13                         | -         |
| <b>Macropores</b>    | 17.3                    | 564                       | -         | 418                          | -         |
| <b>Sum</b>           | -                       | 565                       | 56        | 418                          | 15        |

The parallelism tests show that the Test B results are very similar to those obtained with Skaggs-CPA using Dexter’s equation, and also show smaller percent errors based on the average measured permeability of 362 mD. Nevertheless, Test A results demonstrate a smaller percent error in comparison to the measured permeability of 240 mD of sample “IH2 B”, which was subjected to mercury porosimetry, giving errors of 52 % and 64 % for independent and self-similar media, respectively.

#### 4.4.4.3.4 Critical radius from the fractal dimension approach

Based on the description presented in section 2.14.5, the critical radius was calculated using the fractal dimension ( $D_f$ ) of porous media. Using a value of  $D_f$  equal to 2.5, a

minimum radius of 0.17  $\mu\text{m}$  and a maximum radius of 142.21  $\mu\text{m}$ , the obtained critical radius was equal to 156.41  $\mu\text{m}$ . Henceforth, the Skaggs-CPA permeabilities for independent and self-similar media were 45,590 mD and 34,056 mD, respectively. These results compared to the averaged measured permeability of 362 mD lead to the extremely high errors of more than 12,596 % and 9,307 %, respectively.

#### 4.4.5 NMR Pore Size Distributions

Nuclear Magnetic Resonance (NMR) techniques are a great tool for studying petroleum reservoirs and fluids within it, being applicable to petrophysics and fluid characterization (LACERDA JR., 2018). This work uses NMR applied to petrophysics for direct estimation of porosity and the pore size distribution (PSD), that encompass the whole interligated medium, including pore bodies and throats.

NMR data were available for samples IH2 and IH3. Measurements were acquired using three different scenarios for each sample. The scenarios listed in chronological order were:

- After water saturation, in 2015,
- After water saturation and confinement stress, in 2015,
- After water saturation, in 2017.

The acquired data (amplitudes and relaxation times) are shown in Figure 72 for both samples. The amplitude (a.u. or amplitude units) can be transformed into incremental porosity (p.u. or pore units), while relaxation time (s, seconds) can be transformed into pore radius ( $\mu\text{m}$ ). For the tested Indiana Limestone samples, the surface relaxivity ( $\rho$ ,  $\mu\text{m/s}$ ) parameter to translate relaxation time into radii was found to be equal to 24  $\mu\text{m/s}$ , based on fitting the MICP and NMR  $T_2$  data, with no allowance made for body to throat ratio, as shown in Figure 72. Other studies (SOUZA *et al.*, 2013; SOUZA, 2012) employed different methods for calculating the surface relaxivity for the Indiana Limestone rock sample, which led to a value of 8  $\mu\text{m/s}$ . The method by Souza (2012, 2013) weighted more toward the smaller pores which then usually gives a smaller value of the surface relaxivity. Since the larger pores are the most important for estimating



permeability, surface relaxivity was recalculated here using the correlation between NMR and MICP for the larger pores. This produced higher surface relaxivity values.

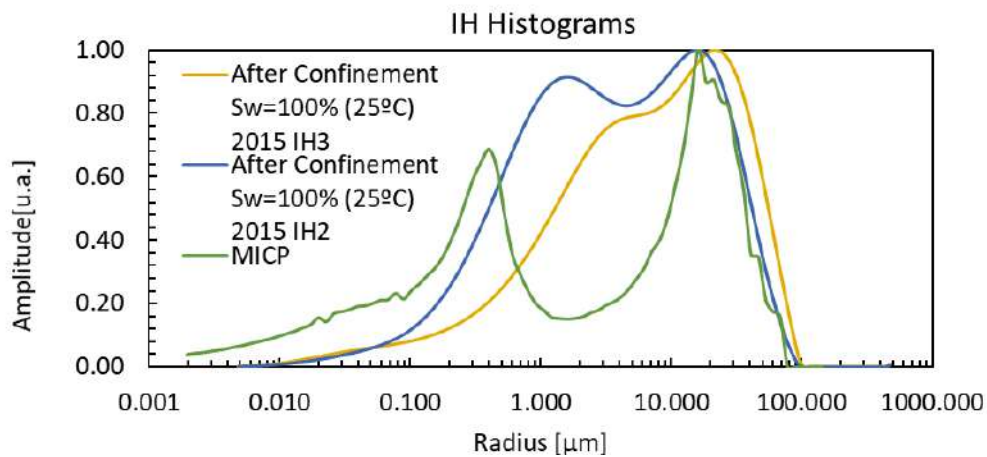


Figure 72 – MICP results for IH2 compared with NMR data for IH2 and IH3. The curves show normalized values. By matching the MICP and NMR peaks, it was possible to obtain a NMR surface relaxivity,  $\rho$ , of 24  $\mu\text{m/s}$  needed to translate relaxation times into radii.

The NMR results show bimodal distributions for both IH2 and IH3, with IH2 showing more distinction between the two modes, as seen also by the NMR distributions in Figure 73. Additional information regarding the NMR acquisition of the present samples are provided by LIMA (2016), CARNEIRO *et al.* (2014) and SOUZA, (2012).

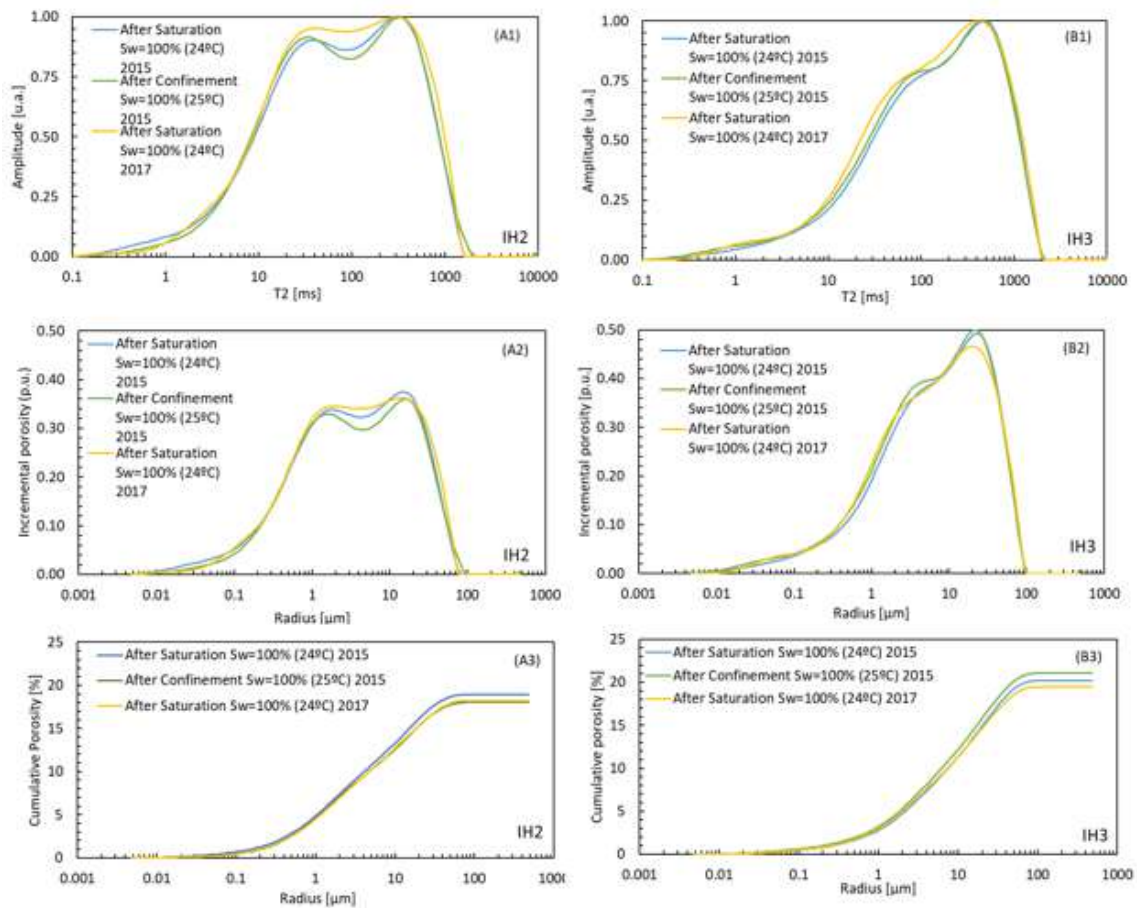


Figure 73 – Plots on the left show NMR results of IH2, and plots on the right show NMR results of IH3. A1 and B1: NMR data of amplitude (units of amplitude) versus relaxation time (milliseconds). A2 and B2: NMR data for the incremental porosity (pore units) versus radii (micrometers). A3 and B3: NMR data for the cumulative porosity (%) versus radii (micrometers). The surface relaxivity  $\rho$  was 24  $\mu\text{m/s}$  for both IH2 and IH3.

When a bimodal distribution shows up in NMR data, the area under the short time feature of the  $T_2$  distribution can be considered to be related mainly to the pore throats (smaller openings), mainly, while the peak at the largest values of  $T_2$  is associated more with the pore bodies (larger openings). When comparing NMR and MICP, the NMR curve shows a slightly bimodal distribution dominated by macroporosity, while the MICP curve clearly shows a bimodal pore system. Plotting the Thin Section distribution as having a porosity of 5.2% (related to macropores), NMR porosity as 21% (IH3) and 18% (IH2) and the MICP as having 18.2% porosities, Figure 74 is generated, prior to any corrections, with the NMR surface relaxivity ( $\rho$ ) equal to 24  $\mu\text{m/s}$  matching the larger pore distribution in MICP.

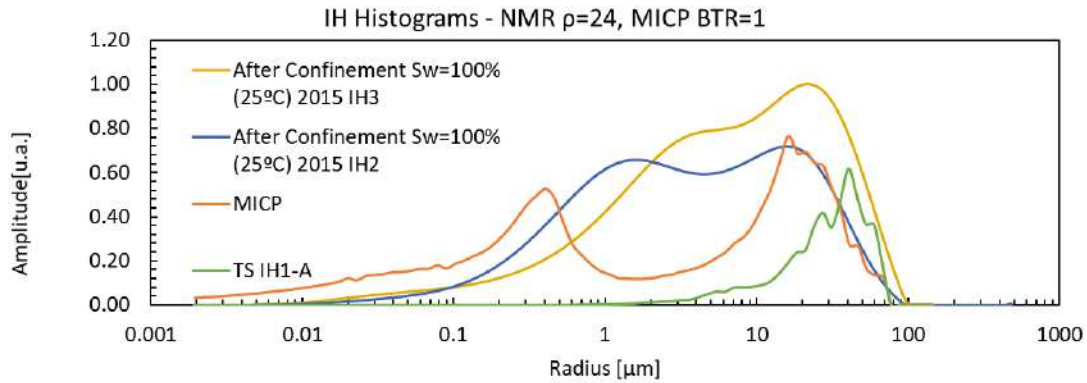


Figure 74 – Distribution of pore sizes from tests performed on Indiana Limestone. The MICP curve shows a PSD associated more with the throats. All curves are corrected to the experiment’s porosity, accordingly. NMR has been adjusted according to MICP, with no allowance from BTR ( $\rho = 24 \mu\text{m/s}$ ).

To obtain better results for the surface relaxivity, the MICP distribution can be transformed from throats to bodies by applying a BTR value of 2, thus allowing the larger pore distribution from MICP to match the Thin Section distribution. This is shown in Figure 75.

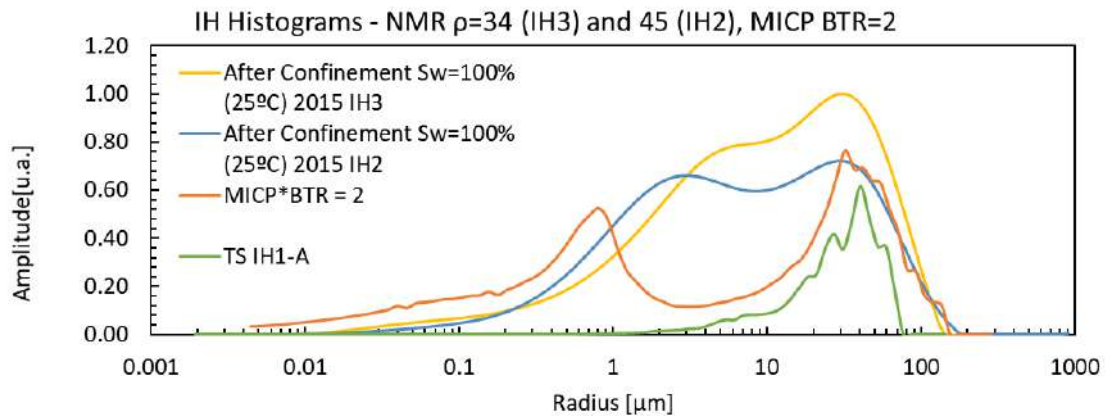


Figure 75 – MICP, NMR and Thin Section histograms as a function of pore body radius. The MICP curve was adjusted to show pore bodies with a BTR of 2, and with NMR surface relaxivity ( $\rho$ ) values equal to  $24 \mu\text{m/s}$  for IH3 and  $45 \mu\text{m/s}$  for IH2. All curves were corrected to the experiment’s porosity.

It can be seen from Figure 75 that the NMR distribution of IH2 overlaps the MICP and Thin Section distributions at the larger radii with a surface relaxivity ( $\rho$ ) equal to  $45 \mu\text{m/s}$ , while the NMR results of IH3 better overlap those two distributions when using a surface

relaxivity ( $\rho$ ) equal to 34  $\mu\text{m/s}$ . The resulting NMR plots for the newly calculated surface relaxivity values are shown in Figure 76.

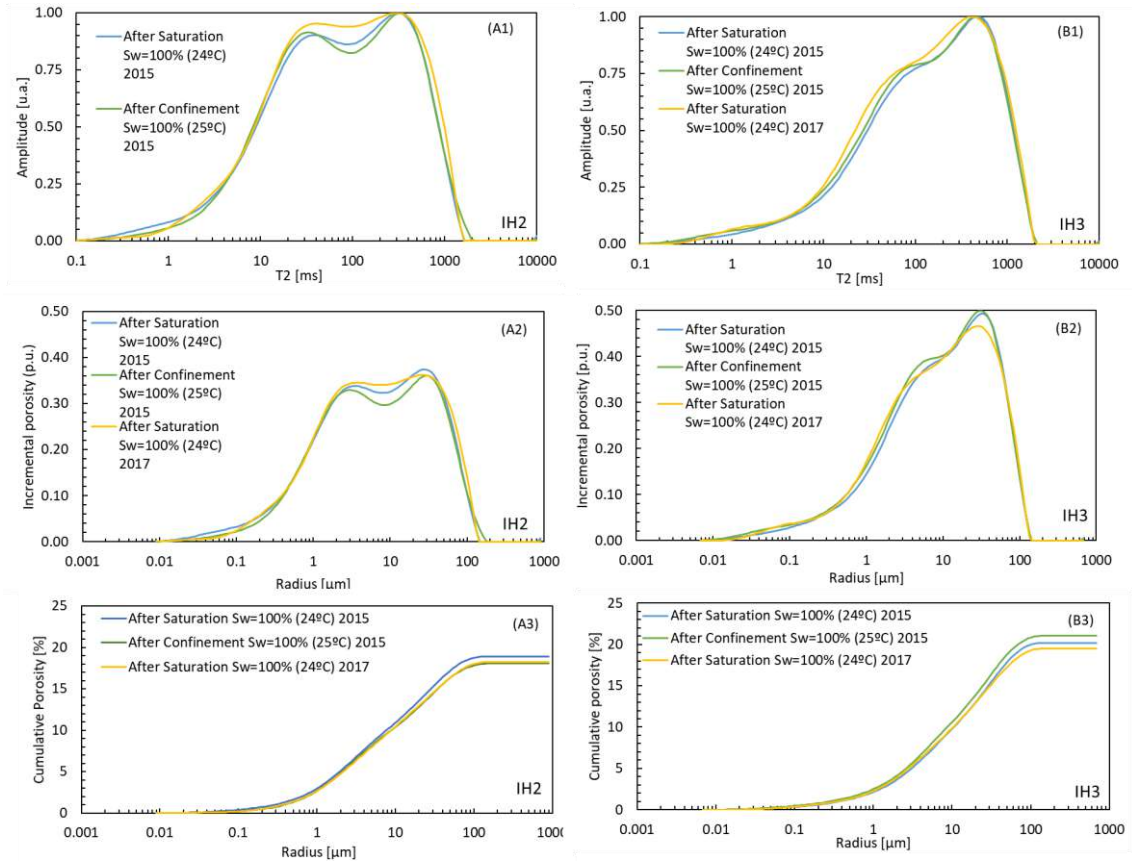


Figure 76 – Plots on the left show NMR results of IH2, and plots on the right show NMR results of IH3. A1 and B1: NMR data of amplitude (units of amplitude) versus relaxation time (milliseconds). A2 and B2: NMR data for incremental porosity (pore units) versus radii (micrometers). A3 and B3: NMR data for cumulative porosity (%) versus radii (micrometers). Surface relaxivity  $\rho$  of 45  $\mu\text{m/s}$  for IH2 and 34  $\mu\text{m/s}$  IH3.

It is important to note that for the transversal relaxation time calculations, the bulk transversal relaxation time,  $T_{2(\text{bulk})}$ , for water was fixed at 2500 ms for all required calculations. Another component of the diffusion transversal relaxation time that can be considered is  $T_{2(\text{diffusion})}$ , due to diffusive coupling. The diffusive coupling phenomenon may happen in nuclear magnetic resonance experiments when macropores are attached to micropores, leading to a migration of hydrogen spins present in the macropores to the surrounding micropores. Mixed wettability also make is more difficult to interpret NMR data because of diffusional exchange of signal with an individual fluid phase that is partially in contact with the solid phase of the rock, and partially isolated by a non-wetting

surface or fluid boundary (SAYEDAKRAM *et al.*, 2016). As a result, multimodality may be masked, giving place to a more broader unimodal pore size distribution. This behavior is commonly found in carbonaceous samples, which frequently have multimodal pore size distributions, but show NMR results with unimodal or only very slight bimodal PSD behavior. Diffusive coupling between pores may complicate the interpretation of NMR data and lead to inaccurate PSD data of the sample. A positive aspect of diffuse coupling, on the other hand, is that it can provide information about connectivity within the pore space, such as knowing whether the macropores directly connect to each other, or if they are connected to each other through micropores (CARNEIRO *et al.*, 2014). Such an analysis aids in permeability studies and their interpretation.

As presented earlier in this work, routine core analysis results showed porosity values of 18.5% and 20.2% for IH2 and IH3, respectively. The area under the short time feature of  $T_2$  distributions (related to the smaller pores) is considerably smaller, with equivalent porosities of roughly less than 8% for IH2 and 7% for IH3 (fairly close to half of the total porosity). It is possible to see clear evidence of diffusive coupling between the micro and macropores during the NMR experiment. This conclusion is reached by comparing the area under the micro-porosity part of the NMR distribution, with the porosity found using basic petrophysics and the van Genuchten model fitted to the HYPROP+WP4C and MICP data corrected by BTR. This since all experiments deliver through the van Genuchten model a fraction of micropores in the sample occupying roughly half of the porosity, while NMR does not show such clear bimodality.

As pointed out by CARNEIRO *et al.* (2014), NMR has been used to evaluate rocks based on  $T_1$ ,  $T_2$  and  $D(t)$  (the diffusion coefficient). Relaxation time distributions can be related to pore sizes and to the free and bound fluid fractions. Diffusion in time,  $D(t)$ , is related to the pore volume to surface area ratio at short times, and to pore tortuosity at long times. Diffusive coupling between pores complicates the interpretation of NMR data because the relaxation time distribution is then no longer an accurate representation of the pore size distribution. Numerical simulations by CARNEIRO *et al.* (2014) did incorporate the effects of diffusive coupling between micro- and macro-porosities, and thus support the interpretation of our measurements. The experimental results show clear evidence of interpore diffusion. They tested the Kocurek's Indiana Limestone High sample and used their numerical simulations to isolate the micro and macropores in order to eliminate

diffusion between them. Hence it was possible to see that the areas under the micro and macroporosity peaks in the NMR distribution were roughly equal, in contrast to the NMR distributions with evidence of diffusive coupling (Figure 77). In addition, the position of the macro-peak did shift to longer times, which would lead to a lower surface relaxivity value compared to MICP. By contrast, the position of the micro-peak did not essentially change, meaning that most of the relaxation in the micropores is within the large microporous grain and unaffected by the barrier. This shift implies that estimating pore sizes directly from the NMR  $T_2$  distribution can be difficult because diffusive coupling shifts the position of the peak that represents the larger pores. This point is reinforced if one compares the  $T_2$  distribution with MICP data. The MICP measurements clearly indicate that the  $T_2$  distributions at the larger pores are shifted to smaller lengths. These considerations are especially relevant because it are the large pores that are most important in estimating permeability.

Another explanation for the shift to lower  $T_2$  values for the macroporosity has been proposed by EL-HUSSEINY & KNIGHT (2017) who examined the effect of rough surfaces in the macropores, which would increase their surface to volume ratio. This implies that the geometrical shape factor  $n$  in Eq. (2.31) is much larger than 2 (for cylindrical pores) or 3 (spherical pores) for the macropores. SEM photos from Indiana Limestone samples in CHURCHER *et al.* (1991) (reproduced in this work in Figure 1) clearly show the macropores are lined by calcite crystals, which result in higher than expected surface area values. Since the presence of calcite crystals lining the walls of the macropores can result in both increased surface area and diffusive coupling, converting a  $T_2$  distribution into a pore size distribution for carbonates should be complimented with both MICP and thin section analyses for analyzing macro-porosity, and if feasible HYPROP analyses also.

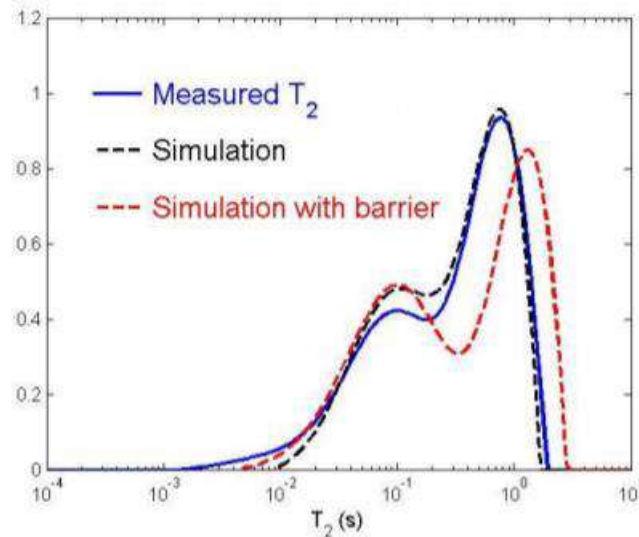


Figure 77 – Indiana Limestone NMR experimental data showing diffusive coupling (e.g., diffusion between large and small pores) for two different simulated NMR results, one of which eliminated diffusive coupling. The vertical axis is the NMR amplitude. This graph was extracted from the work by CARNEIRO *et al.* (2014). Differently from the study presented in this work, surface relaxivity in their study was equal to 8  $\mu\text{m/s}$ , based on the works by Souza (SOUZA *et al.*, 2013; SOUZA, 2012).

#### 4.4.6 IH Fractal Dimension from NMR

A relatively new method for rock typing is to use the fractal dimension of a rock. The fractal dimension of porosity informs how much of a porous medium is occupied by pores. It is possible to see if a cumulative NMR graph plotted on a log-log plot of the pore system will show linear behavior following a power law (fractal property), such as Figure 32. The fractal dimension,  $D_f$ , of the pore system is most easily found by fitting a linear function to the data of the log-log plot of  $r$  along the horizontal x axis and  $\frac{\phi}{r^2 \Delta r}$  along the vertical axis, based on Eq. (3.18). The angular coefficient is then equal to  $-D_f$ .

Table 30 compares results obtained of the fractal dimension calculated from the IH2 and IH3 NMR data using a Mathematica program. Data are shown chronologically from left to right. NMR measurements were obtained after saturation in 2015, after confinement stress in 2017, and after saturation in 2017. No relation was found between the NMR porosity and the fractal dimension, as shown graphically by the data in Figure 78.



Table 30 – Comparison tables of IH2 and IH3 NMR data and corresponding calculated fractal dimensions obtained using Mathematica. Data are shown chronologically from left to right. NMR measurements were obtained (A) after saturation in 2015, (B) after confinement stress in 2017 and (C) after saturation in 2017.

| IH2                   |      |       |       |                 |       |
|-----------------------|------|-------|-------|-----------------|-------|
| Property              | A    | B     | C     | Dimensions [mm] |       |
| NMR Porosity [%]      | 18.9 | 18.1  | 18.2  | Diameter        | 38.4  |
| Fractal Dimension [-] | 2.72 | 2.79  | 2.87  | Height          | 49.9  |
| IH3                   |      |       |       |                 |       |
| Property              | A    | B     | C     | Dimensions [mm] |       |
| NMR Porosity [%]      | 20.2 | 21.03 | 19.46 | Diameter        | 38.34 |
| Fractal Dimension [-] | 2.44 | 2.46  | 2.64  | Height          | 49.92 |

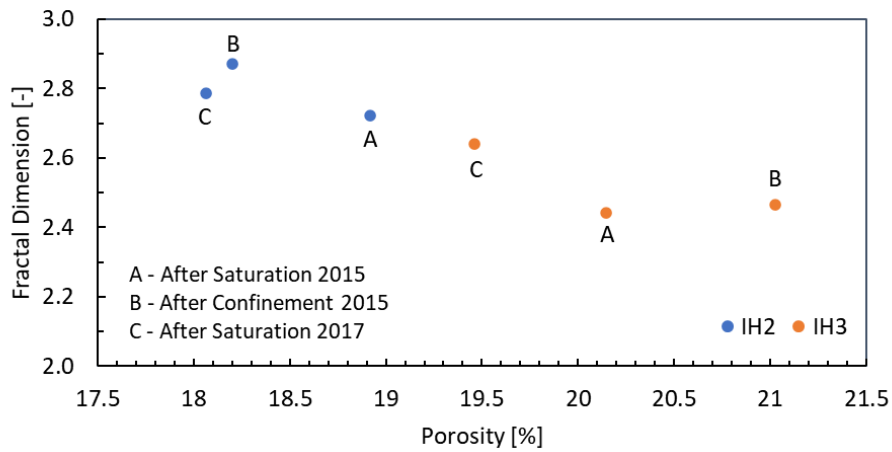


Figure 78 - Graphical comparison between NMR porosity and corresponding calculated fractal dimension.

NMR data of the IH2 and IH3 samples at saturated conditions were found to have bimodal behavior when plotted in terms of incremental porosity (pore units, p.u.) versus pore radii ( $\mu\text{m}$ ), as shown in Figure 73. Thus, two linear fittings using the cumulative porosity data were performed to estimate the fractal dimension: before and after the local minima of the PSD in Figure 73 A2 and B2. As before  $r$  was plotted in the x-axis, and  $\frac{\phi}{r^2 \Delta r}$  in the y-axis in log-log scale, leading to the results in Figure 79. The plots in the figure show that the larger pores have a larger fractal dimension, close to 3, while the smaller pores have a fractal dimension closer to 2. This could indicate that the sample examined is larger than the representative elementary volume (REV) by covering the complete range of pore sizes necessary for upscaling the permeability.



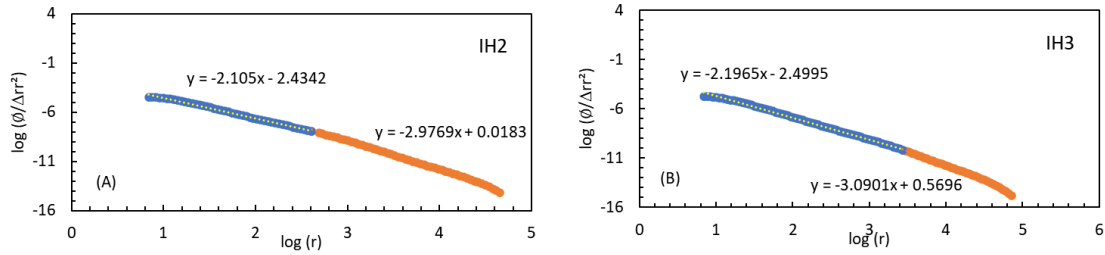


Figure 79 – Plots used to estimate the fractal dimension of the micropore and macropore systems of (A) IH2 and (B) IH3. Results do not vary substantially between NMR measurements, which were obtained after saturation in 2015, after confinement stress in 2017 and after saturation in 2017.

#### 4.4.7 Water retention curve: HYPROP-WP4C

The unsaturated hydraulic properties (constitutive relationships) of natural porous formations provide important data for theoretical and/or practical studies of multiphase fluid flow. HYPROP and WP4C were used in this study to estimate the water retention and unsaturated hydraulic conductivity relationships, alternatively referred to as the capillary pressure-saturation ( $P_c$ - $S$ ) and relative permeability curves, respectively. Water retention curve obtained by measuring a series of water content ( $\theta$ ) and pressure head ( $h$ ) pairs, and then by fitting a particular function to the data, such as the van Genuchten model.

Once the pressure heads and actual evaporation rates (obtained from the monitored sample weights) were obtained, the HYPROP-FIT software ((PERTASSEK *et al.*, 2015; METER, Munchen) was used to analyze with the measured data. HYPROP-FIT uses the root mean square error (RMSE) to quantify differences between the measured ( $y_i$ ) and calculated ( $y_i^c$ ) water retention and hydraulic conductivity data:

$$\text{RMSE} = \sqrt{\sum_{i=1}^{n_p} \frac{1}{N} (y_i^c - y_i)^2} \quad (4.4)$$

where  $N$  is the number of data points, and  $y_i$  refers to either water content,  $\theta_i$ , or the logarithm of the unsaturated hydraulic conductivity, i.e.,  $\log(K_i)$ . The HYPROP-FIT analysis also provides values of the corrected Akaike Information Criterion (AICc),

usually a negative value. The larger the absolute AICc number, the more appropriate the model.

Figure 80 shows the water retention data obtained using HYPROP and WP4C, and the HYPROP-FIT derived hydraulic conductivity data, the latter plotted versus volumetric water content as well as the pF ( $pF = -\log|h|$ , where  $h$  is the pressure head in centimeters). The experiments were done on Indiana Limestone samples IH3 and IH2, using HYPROP and WP4C, respectively. The obtained retention data reflect a relatively bimodal pore size distribution, presumably in part due to fine calcite crystals lining the pores and creating microporosity, and in part possibly due to intra-particle microporosity in some of the fossil fragments and oolites. As compared to the water retention data, the hydraulic conductivity data did not show a similar clear bimodal behavior, mostly because they are outside of the micropore range identified with the WP4C data. The dual-porosity nature of the Indiana Limestone samples is consistent with several previous studies showing the bimodal nature of Indiana Limestone rocks. For example, Mercury Injection Capillary Pressure (MICP) tests by CHURCHER *et al.* (1991) on Indiana Limestone samples showed very clear bimodal pore-size distributions, similarly to the mercury injection test performed and presented in this study. An NMR study by DUNN *et al.* (1994) similarly showed bimodality in the relaxation time and associated pore-size distributions, with the peak of the smaller pores being associated with irreducible saturation.

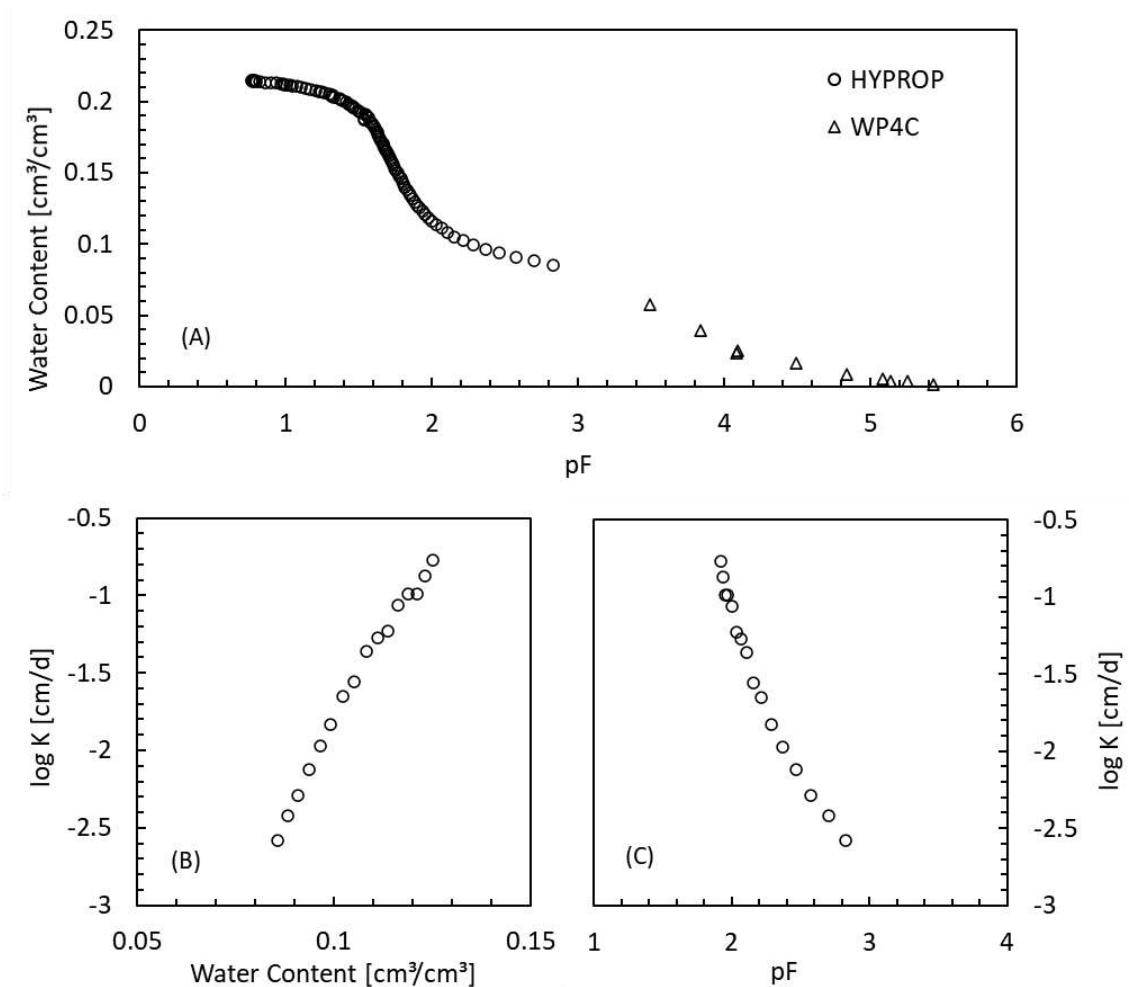


Figure 80 – Observed HYPROP evaporation (circles) and WP4C (triangles) water retention (A) and hydraulic conductivity data as a function of volumetric water content (B) and pF (C).

The observed water retention and conductivity data were analyzed next in terms of the various unsaturated hydraulic functions. Figure 81 shows results for the water retention curve. Clearly, the traditional unimodal van Genuchten model given by Eq. (2.9), as well as the van Genuchten model with variable  $m$  and  $n$  parameters, did not match the data well due to the bimodal nature of the curves, while the bimodal equivalents given by Eq. (2.19) provided excellent fits to the data. Fitted parameter values of the various models that were used are listed in

Table 31, while Table 32 compares the statistical results of the various optimizations. The PDI model (IDEN *et al.*, 2014), also available in HYPROP-FIT, allows an extension of the van Genuchten equations, accounting for film and corner flow as well as vapor phase

contribution to flow. The PDI model was also tested for the Indiana Limestone samples, but only slightly improved the unimodal and bimodal van Genuchten equations. For these reasons, this study focuses only on the standard uni- and bi-modal van Genuchten functions assuming  $m=1-1/n$ . The PDI and van Genuchten scenarios assuming variable  $m, n$  parameters are hence not further shown.

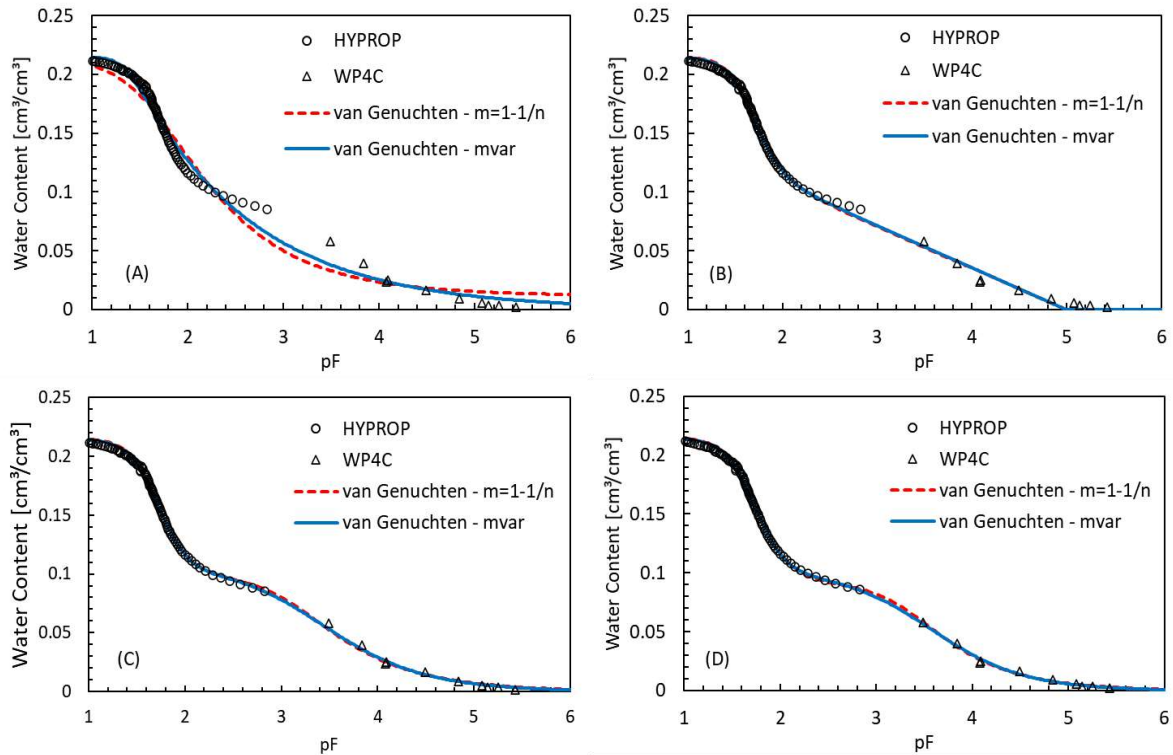


Figure 81 – Observed HYPROP (circles) and WP4C (triangles) volumetric water retention data fitted with the standard ( $m=1-1/n$ ) and variable (independent  $m$  and  $n$ ) van Genuchten and PDI hydraulic functions. The plots show results for (A) the unimodal van Genuchten functions, (B) the unimodal PDI functions, (C) the bimodal van Genuchten functions and (D) the bimodal PDI functions.

The van Genuchten parameter  $n$  is related to the broadness of pore size distribution or size of grains. When analyzing the pressure head as a function of volumetric water content curve, the higher the value of  $n$ , the steeper the curve near the inflection point, and hence the narrower the water retention curve becomes between full saturation and the dry part of the curve. By analyzing the van Genuchten parameter  $n$  within the perspective of a PSD, one notices that the higher values of  $n$  represent narrower pore- and particle-size distributions. Under the perspective of grain types, smaller  $n$  values are common to fine-textured media, while larger  $n$  values are common to coarser media (VAN GENUCHTEN

& NIELSEN, 1985; CARSEL & PARRISH, 1988). Usually, sands have higher  $n$  values (around 2 – 3), which are higher than the  $n$  values for clays, for example. The low value of  $n$  in clays is due to their capacity to retain water longer when drying out. When  $n$  gets close to its lower limit of 1.0, the curve is very smooth. The  $\alpha$  parameter is related to the texture of the formation, the average size of pores and is the inverse of air entry pressure  $h_a$  (cm). Fine-textured media (like clays) generally have lower  $\alpha$  value, due to its high capillary pressure.

Table 31 – Fitted parameter values for the van Genuchten (VG) and PDI unimodal and bimodal hydraulic formulations assuming the VG constraint that  $m=1-1/n$ . Fixed values are indicated by an asterisk (\*).

| Parameter<br>(unit)                            | Unimodal<br>VG model | Bimodal<br>VG model | Unimodal<br>PDI model | Bimodal<br>PDI model |
|--|----------------------|---------------------|-----------------------|----------------------|
| $\alpha$ [1/cm]                                | 0.0270               | -                   | 0.0236                | -                    |
| $n$ [-]  | 1.449                | -                   | 3.286                 | -                    |
| $\theta_r$ [cm <sup>3</sup> /cm <sup>3</sup> ] | 0.008                | 0.0                 | 0.119                 | 0.0                  |
| $\theta_s$ [cm <sup>3</sup> /cm <sup>3</sup> ] | 0.215*               | 0.215*              | 0.215*                | 0.215*               |
| $K_s$ [cm/day]                                 | 30.9*                | 30.9*               | 30.9*                 | 30.9*                |
| $L$ [-]  | -0.611               | 0.159               | 0.251                 | 2.430                |
| $w_1, w_2$ [-]                                 | -                    | 0.445; 0.555        | -                     | 0.427; 0.573         |
| $\alpha_1, \alpha_2$ [1/cm]                    | -                    | 0.00048; 0.0221     | -                     | 0.00048;<br>0.0217   |
| $n_1, n_2$ [-]                                 | -                    | 1.712; 3.146        | -                     | 1.645; 2.938         |
| $\theta_r$ [cm <sup>3</sup> /cm <sup>3</sup> ] | 0.008                | 0.0                 | 0.119                 | 0.0                  |
| $\theta_s$ [cm <sup>3</sup> /cm <sup>3</sup> ] | 0.215                | 0.215               | 0.215                 | 0.215                |
| $pF_{dry}$                                     | -                    | -                   | 5.0                   | 6.01                 |
| $\omega$ [-]                                   | -                    | -                   | 0.00730               | 0.00508              |
| $A$ [-]  | -                    | -                   | -1.721                | -1.681               |

Table 32 – Statistical analysis of the fitted water retention and hydraulic conductivity models.

| Statistical<br>Criterion                          | Unimodal<br>VG model | Bimodal<br>VG model | Unimodal<br>PDI model | Bimodal<br>PDI model |
|---|----------------------|---------------------|-----------------------|----------------------|
| <b><math>m=1-1/n</math> restriction</b>           |                      |                     |                       |                      |
| <b>RMSE<sub>θ</sub></b>                           | 0.0099               | 0.0024              | 0.0030                | 0.0020               |
| <b>RMSE<sub>logK</sub></b>                        | 0.3803               | 0.1678              | 0.0460                | 0.0412               |
| <b>AICc</b>                                       | -1156                | -1466               | -1478                 | -1563                |
| <b>variable <math>m</math> and <math>n</math></b> |                      |                     |                       |                      |
| <b>RMSE<sub>θ</sub></b>                           | 0.0068               | 0.0018              | 0.0027                | 0.0019               |

|                            |        |        |        |        |
|----------------------------|--------|--------|--------|--------|
| <b>RMSE<sub>logK</sub></b> | 0.5419 | 0.0571 | 0.0944 | 0.0515 |
| <b>AICc</b>                | -1189  | -1585  | -1487  | -1572  |

Bimodal hydraulic functions were found to produce better results than the standard unimodal van Genuchten functions. For this particular sample, essentially no improvement was obtained using the PDI model to account for film and corner flow at low water contents.

Figure 82 compares the water retention with the mercury intrusion and extrusion data. Assuming that results from the evaporation experiments indicate pore body distributions, and the mercury intrusion reflect the distribution of pore throats, a BTR of 2 was found when shifting the mercury intrusion towards the HYPROP+WP4C curve. Figure 82 includes the thin section distribution from IH1-A. The curves show that the BTR from mercury intrusion and the thin section coincides with the estimate from the mercury intrusion and water retention pore size distribution. From this figure, it is also possible to see good agreement between the thin section pore size distribution and the water retention data for the largest pores, while for the smaller pores the best agreement occurs between mercury injection and the water retention curve.

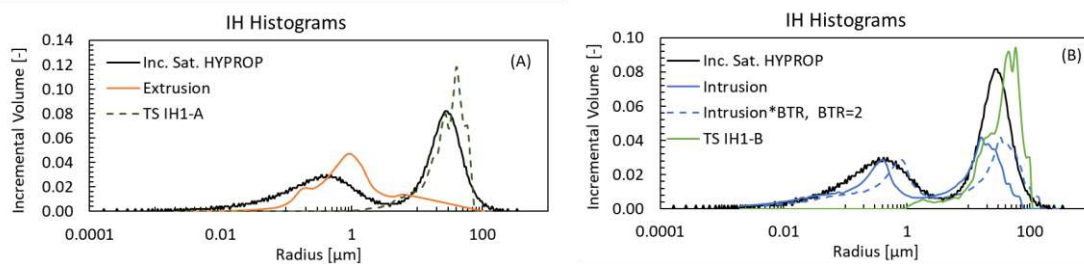


Figure 82 – Comparison between distributions of the HYPROP and WP4C data (black lines), thin section (dark green dashed lines) and (A) mercury extrusion (orange lines) and (B) mercury intrusion (blue lines).

Figure 83 shows results for the standard unimodal and bimodal van Genuchten hydraulic conductivity functions, assuming  $m=1-1/n$ , plotted versus volumetric water content as well as pressure head (the latter in terms of pF values, or logarithm of pressure head in cm). Results for the variable  $m,n$  functions were only marginally better, which was the case also for the PDI functions compared to the bimodal van Genuchten functions. The various optimizations were carried out assuming a fixed value of the saturated water

content ( $\theta_s$ ) and the saturated hydraulic conductivity ( $K_s$ ) of the Indiana Limestone sample. These values were obtained by means of poropermeameter measurements (routine core analysis) on samples IH2 and IH3, as well as by pressure-saturating the sample and carrying out constant head infiltration measurements just before the HYPROP experiments. The values obtained for IH2 were 311 mD (or 25.9 cm/d) for air, and 287 mD (or 23.9 cm/d) for water. IH3 presented values of 400 mD (33.3 cm/d) for air, and 372 mD (30.9 cm/d) for water. IH2 and IH3 further showed helium porosities of 0.185 and 0.201, respectively. The IH3 data of porosity and permeability in the HYPROP-FIT optimizations were assumed to be fixed values.

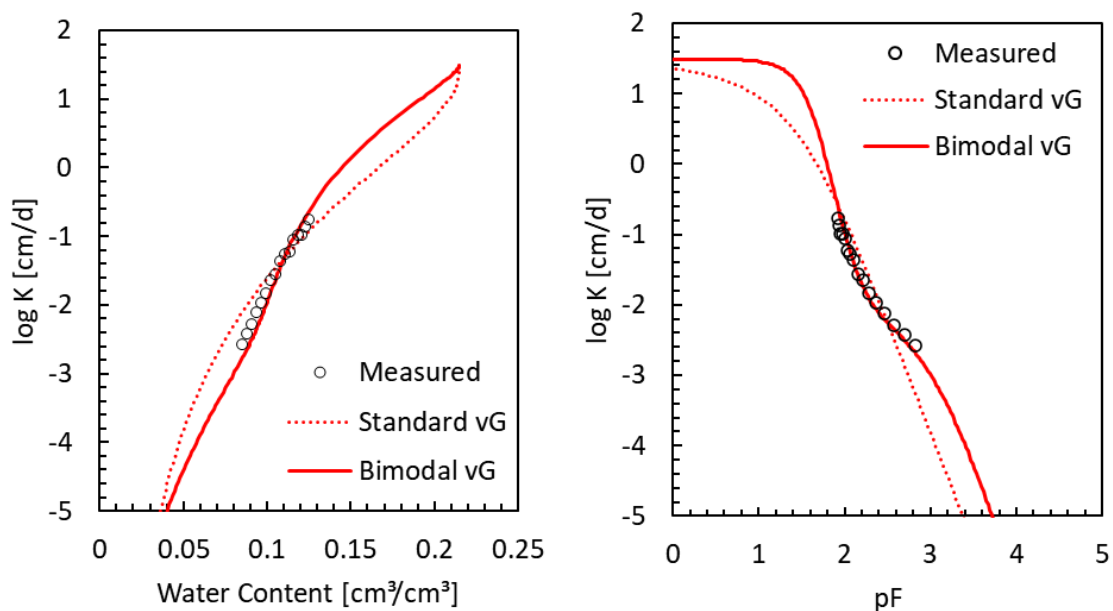


Figure 83 – Observed HYPROP hydraulic conductivity curves fitted with the unimodal and bimodal van Genuchten equations assuming  $m=1-1/n$ .

The relative accuracy of the different formulations is best demonstrated by comparing RMSE values of the fitted water content ( $RMSE_{\theta}$ ) and the hydraulic conductivity ( $RMSE_{\log K}$ ) data, as well as the AICc values. Results for all scenarios are shown in Table 32. The data do not indicate much improvement when adopting variable  $m$  and  $n$  values in the van Genuchten and PDI models for the tested Indiana Limestone sample. This is the main reason why these approaches were no further investigated since they are far more complicated numerically by leading to incomplete beta functions or hypergeometric functions (DOURADO NETO *et al.*, 2011; VAN GENUCHTEN & NIELSEN, 1985).

#### 4.4.8 $\mu$ CT Permeability

Indiana Limestone sample IH2 was scanned using the CoreTOM micro-tomograph. The resolution used was  $8.7\ \mu\text{m}$ , thus allowing one to account for pores with radii of  $4.35\ \mu\text{m}$  or larger. To reach such a high resolution, CoreTOM uses a zoom-in procedure, which allows scans of a cubic region with 1 cm sides in the interior of the sample at high resolutions with no need for destructive measurements, as depicted in Figure 84. The scanned sections were reconstructed using the Aquila software by TESCAN and posteriorly treated using Avizo software 9.5 by Thermo Fischer Scientific.

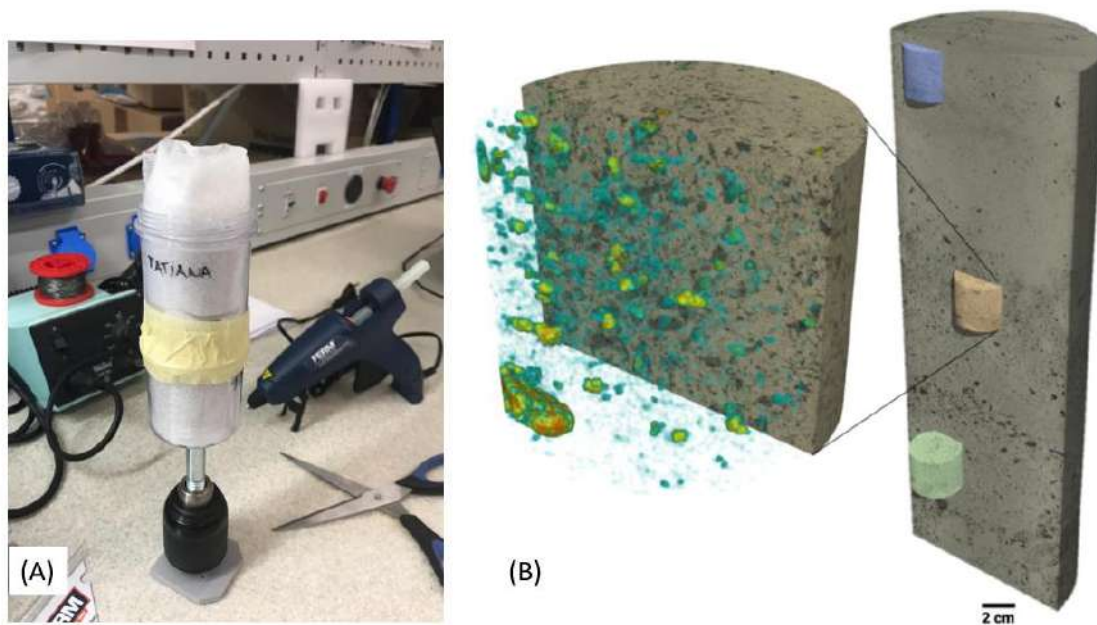


Figure 84 – (A) Sample being prepared for image acquisition using CoreTOM, carried out in Brno, Czech Republic. (B) Image provided by TESCAN during an online seminar held in May 2020, showing how the zoom is done without damaging the sample.

Segmentation of the pores is shown in Figure 85. The obtained porosity of 10.5% closely matched the cumulative porosity given by NMR for pores with radii larger than  $4.35\ \mu\text{m}$  (9.1% for IH2, 12.5% for IH3, which together result in an average value of 10.8%).



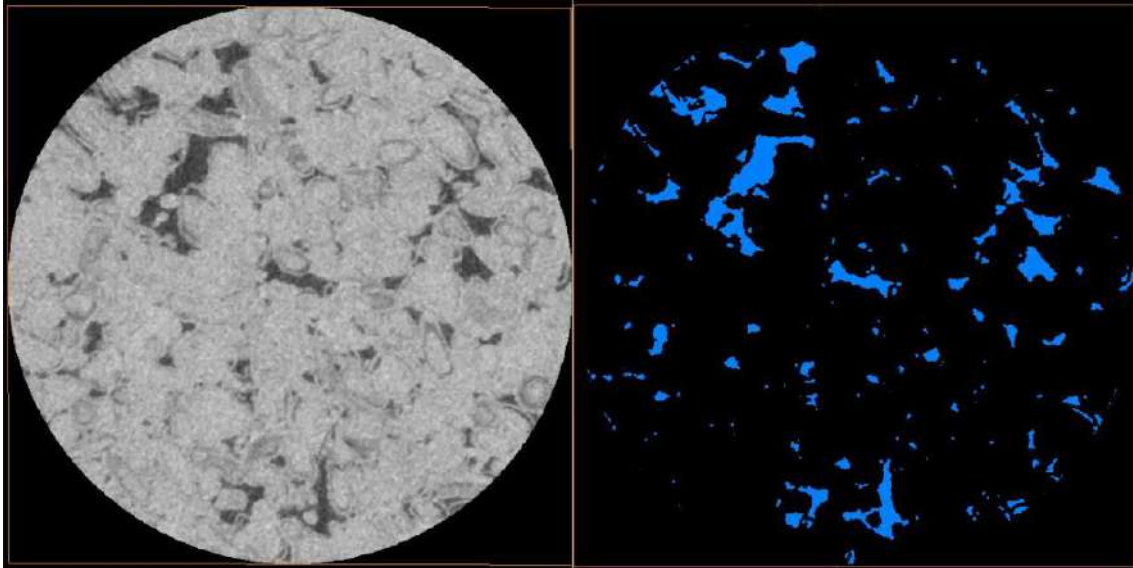


Figure 85 – Segmentation process using the Avizo software. Left image shows a random slice of the IH2 zoom (solid material is in grey color, and pores in black). Right image shows the resulted segmentation (pores are represented in blue).

After segmentation, the skeleton consisting of tubes (pore throats) and spheres (pore bodies) was built and used as input to the PoreFlow PNM software to numerically estimate permeability. Since the numerical mesh was irregular in terms of positioning of the pores, porous layers for fluid entry and exit were defined. Modelling was done in the vertical ( $z$ ) direction. Pores contained along the vertical edges within a ring of 4% of the total height of the sample were considered to be part of the boundary conditions facilitating fluid entry and exit, as shown in Figure 86. No tortuosity was considered for this simulation.

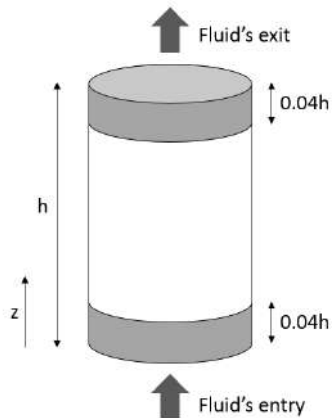


Figure 86 – Illustration of the implementation of boundary condition in POREFLOW to define pores destined for fluid entry and for fluid exit.

PoreFlow simulations produced a permeability of 211 mD, while basic petrophysics returned a porosity of 18.5%, an air permeability of 311 mD, and a permeability of 287 mD after correcting for the Klinkenberg effect. MICP routine core analysis performed on IH2 returned a porosity of 18.7%, an air permeability of 240 mD, and a Klinkenberg corrected permeability of 227 mD. When comparing the digital porosity obtained with Avizo with those from the other techniques, one may conclude that approximately 45% of porosity was lost in the imaging process. The lost porosity may be due to the presence of pores with diameters smaller than the resolution ( $8.7 \mu\text{m}$ ). The simulation with PoreFlow was visualized using the ParaView software (AHRENS *et al.*, 2005). Results are shown in Figure 87.

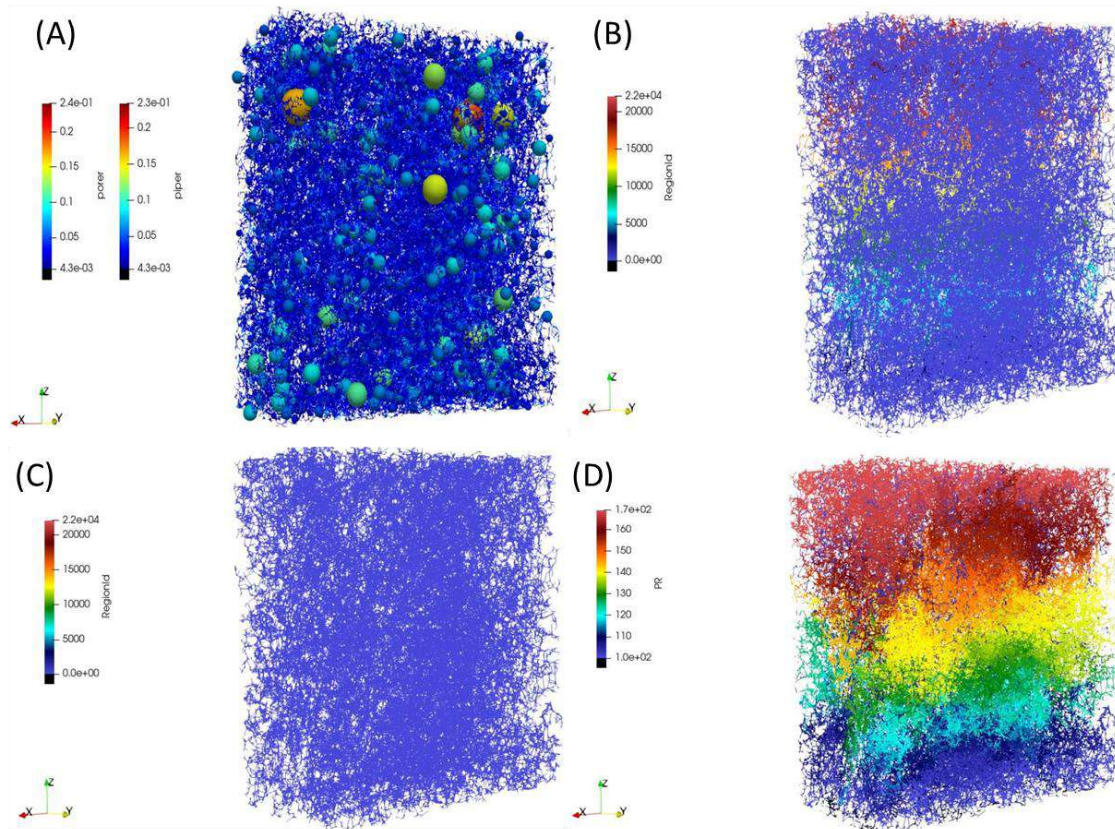


Figure 87 – ParaView visualization of (A) Representation of pore bodies (spherical pores) and pore throats (cylinders) of the examined cube, with the scale in millimeters (pore radii varied from 4.3  $\mu\text{m}$  to 240  $\mu\text{m}$ , and throat radii from 4.3  $\mu\text{m}$  to 230  $\mu\text{m}$ .) (B) All clusters of connected pores, (C) Largest cluster of connected pores, (D) Pressure distribution, which varied from 100 psi (blue) to 170 psi (red).

#### 4.4.9 $\mu\text{CT } D_f$

Micro-tomography *.tiff* images acquired using CoreTOM were binarized and used to estimate the fractal dimension from the IH2 three-dimensional stack. The stack was iteratively divided into blocks (or boxes) with half of the volume of the previous block, until a predetermined side length. Through the use of linear regression, the fractal dimension  $D_f$  was obtained by plotting  $\log(N)$  versus  $\log\left(\frac{1}{L}\right)$  at every iteration using Cartesian coordinates. The slope of the line fitted through the data equals then the fractal dimension.

The image used for the fractal dimension estimation was the same as the one used in PoreFlow, acquired through a zoom-in process with CoreTOM using a 8.7  $\mu\text{m}$  resolution, shaped like a cylinder 1.0 cm in height and 1.0 cm in diameter. The obtained fractal

dimension for the non-destructive zoom made for the IH2 sample was equal to 2.79. To compare the obtained result, the zoom was virtually cut (Figure 88) to reduce the dimensions of the sample to 750 x 750 x 1200  $\mu\text{m}$ . Recalculation of the fractal dimension of the virtual cut made from IH2 zoom was found to be equal to 2.68.

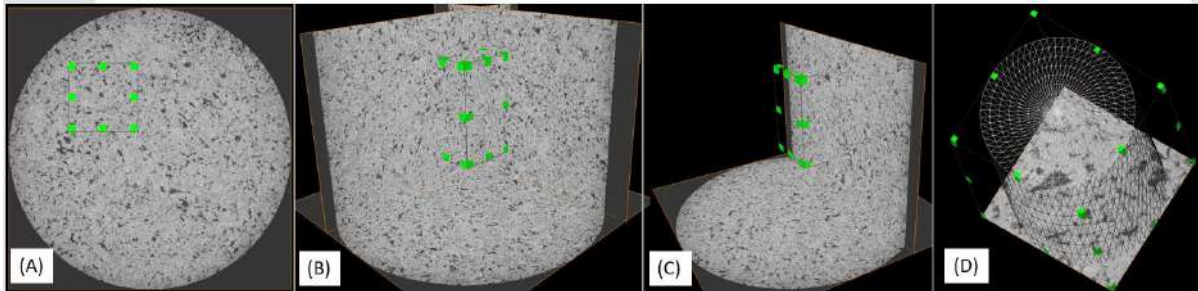


Figure 88 – Virtual cut (limited by the green marks) inside of the IH2 zoom stack for posterior calculation of the fractal dimension. (A) superior view, (B) interior view on 3-D perspective, (C) interior view showing orthogonal slices in the Y plane, (D) cylinder within the cut at the end of the procedure.

Figure 89 shows the linear fittings used to obtain the fractal dimension of the zoom and the cut zoom. The plot indicates that the fractal dimension from the larger stack (Zoom) is closer to 3 than the one from the virtual cut, which was to be expected since the larger sample was closer to being an REV.

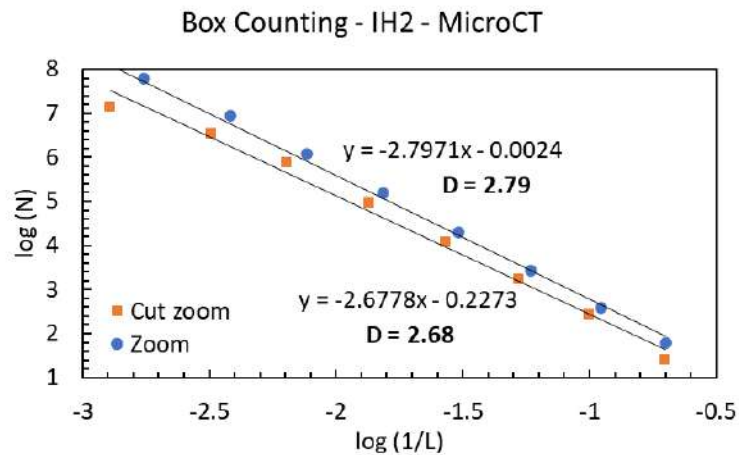


Figure 89 – Fractal dimension calculations using linear fitting.  $N$  is the number of cycles (iterations) and  $L$  the division between the size of the image and the edge of the cube.

## 5 Conclusions and Considerations

Upscaling techniques require comprehensive and solid knowledge regarding the extent and limitations of the invoked methods from input to the resulting output. Redundancy is desired when possible, to allow better results. Taken this into account, this work proposed the use of several techniques of petrophysical characterizations for rock typing and permeability estimation of 30 limestone carbonate samples similar to those found in the Brazilian Pre-salt formations. The samples were retrieved from 29 unidentified wells around the globe, as well as one from a particular quarry in the state of Indiana, USA. The main objective of the presented research was to provide insight into permeability and fluid recovery given petrophysical characterizations of carbonate formations.

Boyle's Law porosimetry with helium is the industry-standard for estimating porosities since helium gas molecules, because of their small size, can enter pore bodies through any pore throat larger than a few molecular diameters. Compared to other techniques such as capillary pressure, NMR and imaging techniques, helium porosimetry provides the largest values of porosity, and hence are popularly used to calibrate results obtained with the other methods.

Permeability in basic petrophysics is related to porosity in the simplest way by establishing a pressure gradient from one end of a plug to the other end, with the outside cylindrical surface sealed and measuring gaseous flow. The permeability is the effective two-dimensional cross-sectional area available for gas flow as established by the arrangement of the three-dimensional pore system with previously known porosity. The basic petrophysics results of air permeability, Klinkenberg permeability and porosity are then generally used as standard values for comparison against other techniques.

Mainly composed of multi-modal samples, the studied carbonates may have particularities and difficulties in terms of petrophysical characterization and rock typing, which consequently may cause porosity and permeability to diverge from their originally measured routine values. This work explores alternatives methods for estimating permeabilities at pertinent REV values.

The Thomeer-Swanson spreadsheet, also used for the Winland calculations, provides a method for rock typing through the analysis of MICP data. Up to three pore systems within a sample can be analyzed in the calculations. This includes the pore system

corresponding to the largest pores dictating permeability, as well as very small pores responsible mostly for estimating oil in place and irreducible water saturation. Four major approaches were used in the Thomeer-Swanson spreadsheet: The Thomeer hyperbola monomodal approach (monomodal fit), the Buiting-Clerke tortuous and relative fractal tubular bundle model (B-C Integral) approach, the Thomeer-based Buiting-Clerke permeability estimation method (B-C Fit), and the Swanson method. In this work, the Winland approach was included also in the spreadsheet, thus adding one more method for permeability estimation. The first three methods are based on full MICP distributions, while Winland and Swanson are based on single-points from MICP. No correlation between the Swanson parameter's radius and Winland's radius at the 35<sup>th</sup> percentile was found. The Winland method produced RMSLE value close to the RMSLE of those two methods which consider full MICP distributions. The smallest RMSLE value in the Thomeer-Swanson-Winland proposed spreadsheet was obtained using Swanson's approach, while the largest RMSLE value was obtained with the Thomeer monomodal hyperbola approach.

Considered to be among the most effective techniques for upscaling, CPA-based methods use the concept of percolation theory, which aims to predict permeability and the electrical conductivity of porous media with a broad pore-size distribution. The advantage of CPA methods is due to the relationship between the macroscopic hydraulic and electrical conductances, which is assumed to be the same as at the pore-scale, with ratios proportional to the square of the critical radius ( $r_c^2$ ), thereby allowing the estimation of permeability over 4 to 6 orders of magnitude in the spatial scale. The Skaggs method for Critical Path Analysis allows one to opt between a self-similar and independent pore system, uses the formation factor and single mercury capillary pressure points characterizing the critical radius  $r_c$  that dominates percolation. The critical radius used in Skaggs's equation was obtained in 4 different manners: visually from the peak of graphs of  $\Delta S_{Hg} / \Delta \ln (P_{Hg})$ , from the inverse of van Genuchten's  $\alpha$  parameter, from the inflection point of the van Genuchten curve using Dexter's equation, and from a fractal approach. The lowest RMSLE values were found for the Skaggs approach assuming independent media with  $r_c$  calculated from both van Genuchten's air entry pressure and the inflection point (RMSLE = 0.41), followed by the  $r_c$  obtained from the peak in the graph. The

highest RMSLE (1.54 – 1.56) values were obtained using the CPA fractal approach for  $r_c$ .

Different coordination numbers as a result of heterogeneity may have provided ill-defined (noisy) MICP curves that were difficult to analyze in terms of estimating the inflection point leading to the critical radius. However, analysis using the Skaggs approach was greatly aided by first fitting van Genuchten's equation to the data. Unlike the Brooks-Corey equation, commonly used in the petroleum industry, the van Genuchten equations were found to describe bimodal data very well. Parallelism tests were also performed using CPA, with results indicating that the pore systems act in conjunction, not independently.

The fractal analysis of Thin Sections provided the fractal dimensions used in the Thomeer-Swanson spreadsheet, representing tortuosity. The fractal dimensions calculated from NMR pore size distributions and  $\mu$ CT three-dimensional images provided means to assure that the data were REV-representative. This was confirmed by the  $\mu$ CT images that were used in the PoreFlow software for estimating the permeability. Permeabilities estimated from  $\mu$ CT images were quite accurate, especially considering the limited resolution of this technique.

Body to throat ratio's (BTRs), inversely proportional to the recovery factor, were estimated for all samples. Aside from aiding in studies related to capillary pressure and permeability, results obtained from the MICP experiments allow one to generate a range of factors decisive to oil recovery, prior and post-EOR. The analysis of BTRs also guide studies of diffusive coupling of larger and smaller pores, meaning that there is a difference between the pore systems regarding their body to throat ratios. The average aspect ratio was provided further in this analysis, which allows the interpreter to infer the circularity of pores.

Results of the PSDs from most experiments showed the presence of more-or-less dual-porosity pore systems, with each of the invoked techniques having certain advantages and limitations. A remarkable achievement concerns the use of the combined HYPROP + WP4C experimental setup and application of the original and bimodal van Genuchten equations to characterize rock formations. The approach proved to be an attractive alternative to existing capillary pressure experiments by bringing a new approach to the



oil and gas industry. While the HYPROP experiment was carried out on a sample with the same size as the NMR plugs, MICP was done using much smaller samples, far from realistic REV. Additionally, fractal analysis may aid in the selection of proper sample sizes for the experiments and their interpretation regarding pore size distribution and permeability. The results are summarized in Figure 90.

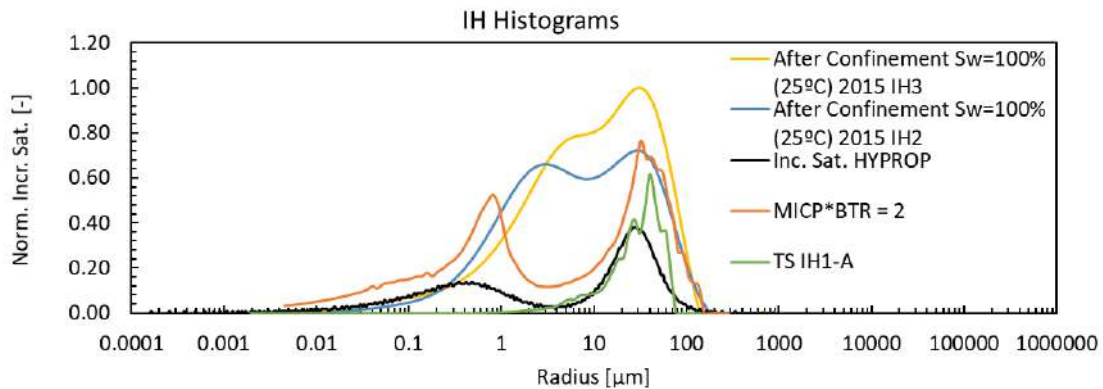


Figure 90 – Normalized incremental saturations or porosities versus pore radius for NMR (yellow and blue) with their respective values of the relaxation time, MICP corrected using BTR (orange), thin section A (green) and HYPROP + WP4C (black).

Taken into account the characteristics of the samples and used techniques for permeability estimation, the author of this work considers the CPA method for independent media combined with the van Genuchten equation fitted to MICP data to be the best approach. The van Genuchten equation was used in two different manners for the calculation of the critical radius, both leading to very close final results. The most preeminent technique uses the van Genuchten’s  $\alpha$  parameter from MICP data to obtain the critical radius for CPA. To the best of the author’s knowledge, the technique is innovative for CPA critical radii estimation and provided the best results for permeability estimations based on RMSLE results, being suitable for PSDs from both water retention and MICP data. The CPA method combined with the van Genuchten equation and Dexter’s derivation for critical radius based on MICP data also provided very good estimatives. The CPA method where the critical radius was chosen from the macroporosity mode ranks in third place, although very straight forward and necessary for the understanding of the choice of critical radii. The Swanson technique is also a very consolidated single-point method in the industry and have provided reliable permeability estimations, ranking fourth place. The Buiting-Clerke spreadsheet and Winland method worked well for permeability estimations, but worse than those of CPA and Swanson. The results from  $\mu\text{CT}$  data used



for permeability estimation were satisfactory when considering the resolution of the acquisition process. The CPA using fractal estimation for the critical radius resulted in the less suitable method for this kind of problem according to the presented analyses.

## 5.1 Future work

The studies presented here should be expanded to a larger set of sedimentary rocks. The different BTR values of the microporosity and macroporosity subsystems may cause diffusive coupling and its impact on the recovery factor because of the use of different techniques and the presence of dominant shapes of the pores within each subsystem.

Interesting future work would be to use NMR and HYPROP pore-size distribution data into the upscaling techniques. It is also suggested to incorporate where possible pores below the invoked resolution, *i.e.*, those that are not detected using  $\mu$ CT, NMR or MICP, to obtain better porosity and permeability estimates. The confirmation of REV may be done using a fractal analysis to estimate the fractal dimension from box-counting techniques applied to images. or from power-law definitions applied to pore size and/or NMR  $T_2$  distributions.

Thin-sections can also be used for fractal analysis and related assessments of the fractal dimension. High-resolution thin section images will produce larger pore surface areas, and low-resolution images lower surface areas, which will directly impact the fractal dimension and the desired representativeness of the medium.

## Bibliography

- ACHARYA, R. C.; VAN DER ZEE, S. E. A. T. M.; LEIJNSE, A. Transport modeling of nonlinearly adsorbing solutes in physically heterogeneous pore networks. *Water Resources Research*, v. 41, n. 2, 2005. <<http://doi.wiley.com/10.1029/2004WR003500>>
- ADAMS, A. J. Relationships Between Observed Pore and Pore-Throat Geometries, Measured Porosity and Permeability, and Indirect Measures of Pore Volume by Nuclear Magnetic Resonance. 2005. Texas A&M University, 2005.
- AHRENS, J.; GEVECI, B.; LAW, C. ParaView: An End-User Tool for Large Data Visualization, *Visualization Handbook*.: Elsevier, 2005.
- AKIN, S.; KOVSCEK, A. R. Computed tomography in petroleum engineering research. *Geological Society, London, Special Publications*, v. 215, n. 1, p. 23–38, 2003. <<http://sp.lyellcollection.org/lookup/doi/10.1144/GSL.SP.2003.215.01.03>>
- ALLAIRE, S. E.; ROULIER, S.; CESSNA, A. J. Quantifying preferential flow in soils: A review of different techniques. *Journal of Hydrology*, v. 378, n. 1–2, p. 179–204, 2009. <<https://linkinghub.elsevier.com/retrieve/pii/S0022169409004776>>
- AMBEGAOKAR, V. N.; HALPERIN, B. I.; LANGER, J. S. Hopping conductivity in disordered systems. *Phys. Rev. B*, v. 4, p. 2612–2621, 1971.
- AMOSU, A.; MAMOOD, H.; OFOCHE, P.; IMSALEM, M. Interactive Estimation of the Fractal Properties of Carbonate Rocks., p. 1–11, 2018. <<http://arxiv.org/abs/1802.06276>>
- ANTON, H.; RORRES, C. *Álgebra Linear com Aplicações*. Porto Alegre: Bookman, 2001.
- ANTONIAZZI, R. L. Aplicação do método box counting para a estimativa da dimensão fractal de figuras planas digitalizadas. 2007. Universidade Federal de Santa Maria, 2007.
- ARCHIE, G. E. The electrical resistivity log as an aid in determining some reservoir characteristics. *Trans. Metall. Soc. AIME*, v. 146, p. 54–61, 1942.

ARYA, L. M. Wind and hot-air methods. In: DANE, J. H.; TOPP, D. G. C. (Eds.). *Methods of soil analysis: Physical methods*. Madison: Soil Science Society of America, 2002. p. 916–920.

BANAVAR, J. R.; JOHNSON, D. L.. Characteristic pore sizes and transport in porous media. *Physical Review B*, v. 35, n. 13, p. 7283–7286, 1987. <<https://link.aps.org/doi/10.1103/PhysRevB.35.7283>>

BARENBLATT, G. I.; ZHELTOV, Y. P. Fundamental equations of filtration of homogeneous liquids in fissured rocks, v. 13, p. 545–548, 1960.

BEAR, J. *Dynamics of Fluids in Porous Media*. New York: Dover Publications, 1972.

BERKOWITZ, B.; BALBERG, I. Percolation theory and its application to groundwater hydrology. *Water Resources Research*, v. 29, n. 4, p. 775–794, 1993. <<http://doi.wiley.com/10.1029/92WR02707>>

BERKOWITZ, B.; EWING, R. P. Percolation theory and network modeling applications in soil physics. *Surveys in Geophysics*, v. 19, n. 1, p. 23–72, 1998.

BEZERRA-COELHO, C. R.; ZHUANG, L; BARBOSA, M. C.; SOTO, M. A.; VAN GENUCHTEN, M. Th. Further tests of the HYPROP evaporation method for estimating the unsaturated soil hydraulic properties. *Journal of Hydrology and Hydromechanics*, v. 66, n. 2, p. 161–169, 2018.

BITTELLI, M.; FLURY, M. Errors in Water Retention Curves Determined with Pressure Plates. *Soil Science Society of America Journal*, v. 73, n. 5, p. 1453–1460, 2009. <<http://doi.wiley.com/10.2136/sssaj2008.0082>>

BOGGS JR., S. *Principles of Sedimentology and Stratigraphy*. 4. ed. New Jersey: Pearson Prentice Hall, 2006.

BROOKS, R. H.; COREY, A. T. *Hydraulic properties of porous media.*: Colorado State University, Hydrology and Water Resources Program, Fort Collins, 1964.

BUITING, J. J. M.; CLERKE, E. A. Permeability from porosimetry measurements: Derivation for a tortuous and fractal tubular bundle. *Journal of Petroleum Science and Engineering*, v. 108, p. 267–278, 2013. <<http://dx.doi.org/10.1016/j.petrol.2013.04.016>>

BULTREYS, T.; DE BOEVER, W.; CNUUDE, V. Imaging and image-based fluid transport modeling at the pore scale in geological materials: A practical introduction to the current state-of-the-art. *Earth-Science Reviews*, v. 155, p. 93–128, 2016.

BUONO, A. FULLMER, S.; LUCK, K.; PETERSON, K.; HUBERT, K.; MORE, P. J.; LEBLANC, S. Quantitative digital petrography: Full thin section quantification of pore space and grains. *SPE Middle East Oil and Gas Show and Conference, MEOS, Proceedings*, v. 2019- March, 2019.

BURDINE, N. T. Relative Permeability Calculations From Pore Size Distribution Data. *Journal of Petroleum Technology*, v. 5, n. 03, p. 71–78, 1953. <<http://www.onepetro.org/doi/10.2118/225-G>>

BURDINE, N. T.; GOURNAY, L. S.; REICHERTZ, P. P. Pore Size Distribution of Petroleum Reservoir Rocks. *Journal of Petroleum Technology*, v. 2, n. 07, p. 195–204, 1950. <<http://www.onepetro.org/doi/10.2118/950195-G>>

CANTRELL, D. L.; HAGERTY, R. M. P. Microporosity in Arab Formation Carbonates, Saudi Arabia. *GeoArabia*, v. 4, n. 2, p. 129–154, 1999.

CANTRELL, D. M.; HAGERTY, R. M. Reservoir rock classification, Arab-D reservoir, Ghawar field, Saudi Arabia. *GeoArabia*, v. 8, n. 3, p. 453–462, 2003.

CARDUCCI, C. E.; OLIVEIRA, G. C.; SEVERIANO, E. C.; ZEVIANI, W. M. Modelagem da curva de retenção de água de latossolos utilizando a equação duplo van genuchten. *Revista Brasileira de Ciencia do Solo*, v. 35, n. 1, p. 77–86, 2011.

CARMAN, P. C. Fluid flow through granular beds. *Transactions, Institution of Chemical Engineers*, v. 15, p. 150–166, 1937.

CARMAN, P. C. Flow of gases through porous media.

CARNEIRO, G.; SOUZA, A.; BOYD, A.; SCHWARTZ, L.; SONG, Y. Q.; AZEREDO, R.; TREVIZAN, W.; SANTOS, B.; RIOS, E.; MACHADO, V. Evaluating pore space connectivity by NMR diffusive coupling. *SPWLA 55th Annual Logging Symposium*, 2014.

CHURCHER, P. L.; FRENCH, P.R.; SHAW, J.C.; SCHRAMM, L.L. Rock Properties of Berea Sandstone, Baker Dolomite, and Indiana Limestone. In: *SPE INTERNATIONAL*

SYMPOSIUM ON OILFIELD CHEMISTRY 1991, Anais... : Society of Petroleum Engineers, 1991. <<http://www.onepetro.org/doi/10.2118/21044-MS>>

CLERKE, E. A.; MARTIN, P. R. Thomeer Swanson excel spreadsheet and FAQ's and user comments NoordwijkSPWLA 2004 Carbonate Workshop, , 2004.

CLERKE, E. A.; MUELLER III, H. M.; PHILLIPS, E. C.; EYVAZZADEH, R. Y.; JONES, D.H.; RAMAMOORTHY, R.; SRIVASTAVA, A. Application of Thomeer Hyperbolas to decode the pore systems, facies and reservoir properties of the Upper Jurassic Arab D Limestone, Ghawar field, Saudi Arabia: A “Rosetta Stone” approach. *GeoArabia*, v. 13, n. 4, p. 113–160, 2008.

CNUUDE, V.; MASSCHAELE, B.; DIERICK, M.; VLASSEN BROECK, J.; VAN HOOREBEKE, L.; JACOBS, P. Recent progress in X-ray CT as a geosciences tool. *Applied Geochemistry*, v. 21, n. 5, p. 826–832, 2006. <<https://linkinghub.elsevier.com/retrieve/pii/S0883292706000503>>

CNUUDE, V.; BOONE, M. N. High-resolution X-ray computed tomography in geosciences: A review of the current technology and applications. *Earth-Science Reviews*, v. 123, p. 1–17, 2013. <<https://linkinghub.elsevier.com/retrieve/pii/S001282521300069X>>

COATES, G. R.; XIAO, L.; PRAMMER, M. G. *NMR Logging: Principles and Applications.*: USA: Halliburton Energy Services, 1993.

CORBETT, P.; HAYASHI, F. Y.; ALVES, M. S.; JIANG, Z.; WANG, H.; DEMYANOV, V.; MACHADO, A.; BORGHI, L.; SRIVASTAVA, N. Microbial carbonates: a sampling and measurement challenge for petrophysics addressed by capturing the bioarchitectural components. *Geological Society, London, Special Publications*, v. 418, n. 1, p. 69–85, 2015. <<http://sp.lyellcollection.org/lookup/doi/10.1144/SP418.9>>

DA SILVA, M. D. Study of the representative elementary volume of carbonate rocks and pore network simulation. 2019. Federal University of Rio de Janeiro, 2019.

DAIGLE, H. Application of critical path analysis for permeability prediction in natural porous media. *Advances in Water Resources*, v. 96, p. 43–54, 2016. <<https://linkinghub.elsevier.com/retrieve/pii/S0309170816301968>>

- DAL FERRO, N.; CHARRIER, P.; MORARI, F. Dual-scale micro-CT assessment of soil structure in a long-term fertilization experiment. *Geoderma*, v. 204–205, p. 84–93, 2013. <<https://linkinghub.elsevier.com/retrieve/pii/S0016706113001225>>
- DANE, J. H.; HOPMANS, J. W. Methods of soil analysis: Part 4 – physical methods. In: DANE, J. ..; TOPP, G. C. (Eds.). *Water retention and storage*. Madison: American Society of America, 2002. p. 671–720.
- DE VRIES, E. T.; RAOOF, A.; VAN GENUCHTEN, M. Th. Multiscale modelling of dual-porosity porous media; a computational pore-scale study for flow and solute transport. *Advances in Water Resources*, v. 105, p. 82–95, 2017.
- DEXTER, A. R. Soil physical quality Part III: Unsaturated hydraulic conductivity and general conclusions about S-theory. *Geoderma*, v. 120, n. 3–4, p. 201–214, 2004.
- DOURADO NETO, D.; VAN LIER, Q. J.; VAN GENUCHTEN, M.TH.; REICHARDT, K.; METSELAAR, K.; NIELSEN, D.R. Alternative Analytical Expressions for the General van Genuchten-Mualem and van Genuchten-Burdine Hydraulic Conductivity Models. *Vadose Zone Journal*, v. 10, n. 2, p. 618–623, 2011. <<http://doi.wiley.com/10.2136/vzj2009.0191>>
- DULLIEN, F. *Porous Media Fluid Transport and Pore Structure*.: Academic Press, 1979.
- DUNN, K. J.; BERGMAN, D. J.; LATORRACA, G. A. *Nuclear Magnetic Resonance: Petrophysical and Logging Applications*. England: Elsevier Science, 2002.
- DUNN, K. J.; LATORRACA, G. A.; WARNER, J. L.; BERGMAN, D. J. On the calculation and interpretation of NMR relaxation time distributions. *Proceedings - SPE Annual Technical Conference and Exhibition*, v. Omega, p. 45–54, 1994.
- DURNER, W. Hydraulic conductivity estimation for soils with heterogeneous pore structure. *Water Resour Res*, v. 30, p. 211–223, 1994.
- DURNER, W.; LIPSIUS, K. Determining Soil Hydraulic Properties. In: *Encyclopedia of Hydrological Sciences*. Chichester, UK: John Wiley & Sons, Ltd, 2005.
- EL-HUSSEINY, A.; KNIGHT, R. A laboratory study of the link between NMR relaxation data and pore size in carbonate skeletal grains and micrite. *Petrophysics*, v. 58, n. 2, p. 116–125, 2017.

- EWING, R. P.; GUPTA, S. C. Modeling percolation properties of random media using a domain network. *Water Resources Research*, v. 29, n. 9, p. 3169–3178, 1993. a. <<http://doi.wiley.com/10.1029/93WR01496>>
- EWING, R. P.; GUPTA, S. C. Percolation and permeability in partially structured networks. *Water Resources Research*, v. 29, n. 9, p. 3179–3188, 1993. b. <<http://doi.wiley.com/10.1029/93WR01497>>
- FERRAND, L. A.; CELIA, M. A. The effect of heterogeneity on the drainage capillary pressure-saturation relation. *Water Resources Research*, v. 28, n. 3, p. 859–870, 1992. <<http://doi.wiley.com/10.1029/91WR02679>>
- FRIEDMAN, S. P.; SEATON, N. A. Critical path analysis of the relationship between permeability and electrical conductivity of three-dimensional pore networks. *Water Resources Research*, v. 34, n. 7, p. 1703–1710, 1998. <<http://doi.wiley.com/10.1029/98WR00939>>
- GARDNER, W. F.; MIKLICH, F. J. Unsaturated conductivity and diffusivity measurements by a constant flux method. *Soil Science*, v. 93, n. 4, p. 271–274, 1962.
- GHANBARIAN-ALAVIJEH, B.; HUNT, A. G. Unsaturated hydraulic conductivity in porous media: Percolation theory. *Geoderma*, v. 187–188, p. 77–84, 2012. a. <<https://linkinghub.elsevier.com/retrieve/pii/S001670611200170X>>
- GHANBARIAN-ALAVIJEH, B.; HUNT, A. G. Unsaturated hydraulic conductivity in porous media: Percolation theory. *Geoderma*, v. 187–188, p. 77–84, 2012. b. <<http://dx.doi.org/10.1016/j.geoderma.2012.04.007>>
- GHANBARIAN, B.; IOANNIDIS, M. A.; HUNT, A. G. Theoretical Insight Into the Empirical Tortuosity-Connectivity Factor in the Burdine-Brooks-Corey Water Relative Permeability Model. *Water Resources Research*, v. 53, n. 12, p. 10395–10410, 2017.
- GHANBARIAN, B.; SAHIMI, M.; DAIGLE, H. Modeling relative permeability of water in soil: Application of effective-medium approximation and percolation theory. *Water Resources Research*, v. 52, n. 7, p. 5025–5040, 2016.
- GHANBARIAN, B.; TORRES-VERDÍN, C.; SKAGGS, T. H. Quantifying tight-gas sandstone permeability via critical path analysis. *Advances in Water Resources*, v. 92, p. 316–322, 2016.

GIESCHE, H. Mercury Porosimetry. In: Handbook of Porous Solids. Weinheim, Germany: Wiley-VCH Verlag GmbH. p. 309–351.

GONG, M. Mechanical and Hydraulic Behavior of Acid Fractures—Experimental Studies and Mathematical Modeling. 1997. U. of Texas at Austin, 1997.

GREGG, SJ; SING, KSW. Adsorption. Surface area and porosity. Academic Press, London., 1982.

GRINSTEAD, C. M.; SNELL, J. L. Introduction to Probability.: Orange Grove Texts, 2009.

<[https://www.dartmouth.edu/~chance/teaching\\_aids/books\\_articles/probability\\_book/Chapter4.pdf](https://www.dartmouth.edu/~chance/teaching_aids/books_articles/probability_book/Chapter4.pdf)>. Access: 5 aug. 2019.

GUNTER, G. W.; SPAIN, D. R.; VIRO, E. J.; THOMAS, J. B.; POTTER, G.; WILLIAMS, J. Winland pore throat prediction method - a proper retrospect: New examples from carbonates and complex systems. SPWLA 55th Annual Logging Symposium 2014, n. 1980, p. 1–12, 2014.

HAGHI, A. H.; TALMAN, S.; CHALATURNYK, R. Consecutive Experimental Determination of Stress-Dependent Fluid Flow Properties of Berea Sandstone and Implications for Two-Phase Flow Modeling. Water Resources Research, v. 56, n. 1, 2020. <<https://onlinelibrary.wiley.com/doi/abs/10.1029/2018WR024245>>

HALPERIN, B. I. Remarks on percolation and transport in networks with a wide range of bond strengths. Physica D: Nonlinear Phenomena, v. 38, n. 1–3, p. 179–183, 1989. <<https://linkinghub.elsevier.com/retrieve/pii/0167278989901887>>

HOPMANS, J. W.; ŠIMŮNEK, J.; ROMANO, N.; DURNER, W. Inverse modeling of transient water flow. In: SSSA (Ed.). Methods of Soil Analysis. Part 4. Physical Methods. Madison. p. 963–1008.

HOUNSFIELD, G. N. Method of and apparatus for examining a body by radiation such as x or gamma radiation, US 3919552, 1975.

HUNT, A. G. Applications of percolation theory to porous media with distributed local conductances. Advances in Water Resources, v. 24, n. 3–4, p. 279–307, 2001.



HUNT, A. G.; GEE, G. W. Application of critical path analysis to fractal porous media: comparison with examples from the Hanford Site. *Adv. Water Resour.*, v. 25, p. 129–146, 2002.

HUNT, A.; EWING, R.; GHANBARIAN, B. *Percolation Theory for Flow in Porous Media*. Lecture Notes in Earth and Planetary System Science. Cham: Springer International Publishing, 2014. v. 880 <<http://link.springer.com/10.1007/978-3-319-03771-4>>

HUNT, A. G.; SAHIMI, M.. *Flow, Transport, and Reaction in Porous Media: Percolation Scaling, Critical-Path Analysis, and Effective Medium Approximation*. *Reviews of Geophysics*, v. 55, n. 4, p. 993–1078, 2017.

IDEN, S. C.; DURNER, W. Free-Form estimation of soil hydraulic properties using Wind's method. *European Journal of Soil Science*, v. 59, n. 6, p. 1228–1240, 2008. <<http://doi.wiley.com/10.1111/j.1365-2389.2008.01068.x>>

IDEN, S.; DURNER, W. Comment to "Simple consistent models for water retention and hydraulic conductivity in the complete moisture range" by A. Peters. *Water Resour. Res.*, v. 50, p. 7530–7534, 2014.

IDEN, S. C.; BLÖCHER, J. R.; DIAMANTOPOULOS, E.; PETERS, A.; DURNER, W. Numerical test of the laboratory evaporation method using coupled water, vapor and heat flow modelling. *Journal of Hydrology*, v. 570, p. 574–583, 2019. <<https://linkinghub.elsevier.com/retrieve/pii/S0022169419300204>>

Indiana Limestone Handbook. v4: Indiana Limestone Institute of America, 1975. <<http://www.iliai.com>>

J. KOZENY. Ueber kapillare Leitung des Wassers im Boden. *Sitzungsber Akad. Wiss*, v. 136, n. 2a, p. 271–306, 1927.

JING, X. *Advances and Challenges in EOR Implementation*. In: 2018, Rio de Janeiro. Anais... Rio de Janeiro

JOEKAR-NIASAR, V.; HASSANIZADEH, S. M.; DAHLE, H. K. Non-equilibrium effects in capillarity and interfacial area in two-phase flow: dynamic pore-network modelling. *Journal of Fluid Mechanics*, v. 655, p. 38–71, 2010. <[https://www.cambridge.org/core/product/identifier/S0022112010000704/type/journal\\_article](https://www.cambridge.org/core/product/identifier/S0022112010000704/type/journal_article)>

KATZ, A. J.; THOMPSON, A. H. Quantitative prediction of permeability in porous rock. *Physical Review B*, v. 34, n. 11, p. 8179–8181, 1986. <<https://link.aps.org/doi/10.1103/PhysRevB.34.8179>>

KATZ, A. J.; THOMPSON, A. H. Prediction of rock electrical conductivity from mercury injection measurements. *Journal of Geophysical Research*, v. 92, n. B1, p. 599, 1987. <<http://doi.wiley.com/10.1029/JB092iB01p00599>>

KENYON, W. E. Petrophysical principles of applications of NMR logging. *Log Analyst*, v. 38, n. 2, p. 21–40, 1997.

KENYON, W. E.; ALLEN, D. F.; LISITZA, N. V.; SONG, Y. Q. Better pore-size distributions from stimulated-echo NMR lab measurements using magnetic susceptibility contrast and small encoding angles. *SPWLA 43rd Annual Logging Symposium 2002*, 2002.

KLINKENBERG, L. J. The permeability of porous media to liquids and gases. “Proceedings” of “OilGasScientificResearchProjects” Institute, SOCAR, [s. l.], n. 2, p. 57–73, 1941. <[http://proceedings.socar.az/uploads/pdf/11/57-73\\_Klinker.pdf](http://proceedings.socar.az/uploads/pdf/11/57-73_Klinker.pdf)>

KLUTE, A.; DIRKSEN, C. *Hydraulic Conductivity and Diffusivity: Laboratory Methods*. 1986. <<https://dl.sciencesocieties.org/publications/books/abstracts/sssabookseries/methodsofsolan1/687>>

KÖHNE, J. M.; SCHLÜTER, S.; VOGEL, H.-J.. Predicting Solute Transport in Structured Soil Using Pore Network Models. *Vadose Zone Journal*, v. 10, n. 3, p. 1082, 2011. <<https://www.soils.org/publications/vzj/abstracts/10/3/1082>>

KOLODZIE, S. Analysis of pore throat size and use of the Waxman-Smits equation to determine OOIP in spindle field, Colorado. *SPE annual technical conference and exhibition*, p. 150–155, 1980.

KOSUGI, K.. Lognormal distribution model for unsaturated soil hydraulic properties. *Water Resour. Res.*, v. 32, p. 2697–2703, 1996.

LACERDA JR., V. *Fundamentos de Espectrometria e Aplicações*. 1. ed. Rio de Janeiro: Atheneu, 2018.

- LE DOUSSAL, P. Permeability versus conductivity for porous media with wide distribution of pore sizes. *Physical Review B*, v. 39, n. 7, p. 4816–4819, 1989. <<https://link.aps.org/doi/10.1103/PhysRevB.39.4816>>
- LEVITT, M. H. *Spin Dynamics: Basics of Nuclear Magnetic Resonance.*: EUA: Wiley, 2001.
- LIMA, M. C. O. Estimativa de porosidade utilizando diferentes técnicas laboratoriais em rochas reservatórias petrolíferas. 2016. Universidade Federal Fluminense, 2016.
- LIMA, M. C. O.; PONTEDEIRO, E. M.; RAMIREZ, M.; BOYD, A.; VAN GENUCHTEN, M. TH; BORGHI, L.; COUTO, P.; RAOOF, A. Petrophysical Correlations for the Permeability of Coquinas (Carbonate Rocks). *Transport in Porous Media*, v. 135, n. 2, p. 287–308, 2020. <<https://doi.org/10.1007/s11242-020-01474-1>>
- LIU, P.; YUAN, Z.; LI, K. An improved capillary pressure model using fractal geometry for coal rock. *Journal of Petroleum Science and Engineering*, v. 145, p. 473–481, 2016. <<http://dx.doi.org/10.1016/j.petrol.2016.05.047>>
- LOONEY, B. B.; FALTA, R. W. *Vadose Zone: Science and Technology Solutions (2 Volume Set)*. Battelle Press, 2000.
- MANDELBROT, B. How Long Is the Coast of Britain? Statistical Self-Similarity and Fractional Dimension. *Science*, v. 156, n. 3775, p. 636–638, 1967. <<http://www.sciencemag.org/cgi/doi/10.1126/science.156.3775.636>>
- MANGALASSERY, S.; SJÖGERSTEN, S.; SPARKES, D.L.; STURROCK, C.J.; MOONEY, S.J. The effect of soil aggregate size on pore structure and its consequence on emission of greenhouse gases. *Soil and Tillage Research*, v. 132, p. 39–46, 2013. <<https://linkinghub.elsevier.com/retrieve/pii/S0167198713000901>>
- MASALMEH, S. K.; WEI, L.; BLOM, C.; JING, X. *EOR Options for Heterogeneous Carbonate Reservoirs Currently Under Waterflooding*. 2014.
- MASALMEH, S. K.; JING, X.; ROTH, S.; WANG, C.; DONG, H.; BLUNT, M. *Towards Predicting Multi-Phase Flow in Porous Media Using Digital Rock Physics: Workflow to Test the Predictive Capability of Pore-Scale Modeling*. 2015.

MESQUITA, P. V. Melhoria da estimativa de permeabilidade através da integração de dados de RMN e MICP em rochas análogas a reservatórios de hidrocarbonetos. 2017. Universidade Federal Fluminense, 2017.

METER GROUP. Soil moisture release curves. <<https://www.metergroup.com/environment/products/hyprop-2/>>. Access: 21 sep. 2020.

MUALEM, Y. A new model for prediction the hydraulic conductivity of unsaturated porous media. *Water Resources Research*, v. 12, p. 513–522, 1976.

NIMMO, J. R.; PERKINS, K. S.; LEWIS, A. M. Steady-state centrifuge. In: DANE, J. H.; TOPP, G. C. (Eds.). *Methods of Soil Analysis, part 4, Physical Methods*. Madison: Soil Sci. Soc. of Am., 2002. p. 903–916.

NISHIYAMA, N.; YOKOYAMA, T. Estimation of permeability of sedimentary rocks by applying water-expulsion porosimetry to Katz and Thompson model. *Engineering Geology*, v. 177, p. 75–82, 2014. <<https://linkinghub.elsevier.com/retrieve/pii/S0013795214001240>>

ODDONE, D. A Retomada do Setor de Petróleo e Gás. Rio de Janeiro. 2017. <[http://www.sindigas.org.br/novosite/wp-content/uploads/2017/09/A\\_Retomada\\_do\\_Setor\\_de\\_Petroleo\\_e\\_Gas.pdf](http://www.sindigas.org.br/novosite/wp-content/uploads/2017/09/A_Retomada_do_Setor_de_Petroleo_e_Gas.pdf)>

ODDONE, D. Brazilian O&G Market Revival. Houston. 2018. <[http://www.anp.gov.br/images/Palestras/PPT\\_ANP\\_Decio\\_Oddone\\_Brazilian\\_O&G\\_Market\\_Revival\\_02\\_05\\_2018.pdf](http://www.anp.gov.br/images/Palestras/PPT_ANP_Decio_Oddone_Brazilian_O&G_Market_Revival_02_05_2018.pdf)>

PERTASSEK, T.; PETERS, A.; DURNER, W. HYPROP-FIT Software User's Manual, München METER Group AG, 2015. <<https://www.metergroup.com>>

PERTASSEK, T.; PETERS, A.; DURNER, W. HYPROP Data Evaluation Software, 2011.

PETERS, A. Simple consistent models for water retention and hydraulic conductivity in the complete moisture range. *Water Resources Research*, v. 49, n. 10, p. 6765–6780, 2013. <<http://doi.wiley.com/10.1002/wrcr.20548>>

PETERS, A. Reply to comment by S. Iden and W. Durner on “Simple consistent models for water retention and hydraulic conductivity in the complete moisture range.” *Water*

Resources Research, v. 50, n. 9, p. 7535–7539, 2014.  
<<http://doi.wiley.com/10.1002/2014WR016107>>

PETERS, A.; DURNER, W. A simple model for describing hydraulic conductivity in unsaturated porous media accounting for film and capillary flow. *Water Resources Research*, v. 44, n. 11, 2008. <<http://doi.wiley.com/10.1029/2008WR007136>>

PETERS, A.; IDEN, S. C.; DURNER, W. Revisiting the simplified evaporation method: Identification of hydraulic functions considering vapor, film and corner flow. *Journal of Hydrology*, v. 527, p. 531–542, 2015.  
<<https://linkinghub.elsevier.com/retrieve/pii/S0022169415003704>>

PETROBRAS. Petrobras: Pre-salt. 2019. <<http://www.petrobras.com.br/en/our-activities/performance-areas/oil-and-gas-exploration-and-production/pre-salt/>>. Access: 17 sep. 2019.

PFINGSTEN, W. Experimental and Modeling Indications for Self-Sealing of a Cementitious Low- and Intermediate-Level Waste Repository by Calcite Precipitation. *Nuclear Technology*, v. 140, n. 1, p. 63–82, 2002.  
<<https://www.tandfonline.com/doi/full/10.13182/NT02-A3324>>

PITTMAN, E. D. Relationship of porosity and permeability to various parameters derived from mercury injection capillary pressure curves for sandstones. *AAPG Bulletin*, v. 76, n. 2, p. 191–198, 1992.

PRIESACK, E.; DURNER, W. Closed-form expression for the multi-modal unsaturated conductivity function. *Vadose Zone Journal*, v. 5, p. 121–124, 2006.

PURCELL, W. R. Capillary Pressures - Their Measurement Using Mercury and the Calculation of Permeability Therefrom. *Journal of Petroleum Technology*, v. 1, n. 02, p. 39–48, 1949. <<http://www.onepetro.org/doi/10.2118/949039-G>>

RAOOF, A.; NICK, H. M.; WOLTERBEEK, T. K.T.; SPIERS, C. J. Pore-scale modeling of reactive transport in wellbore cement under CO<sub>2</sub> storage conditions. *International Journal of Greenhouse Gas Control*, v. 11, n. SUPPL, p. S67–S77, 2012.  
<<http://dx.doi.org/10.1016/j.ijggc.2012.09.012>>

RAOOF, A.; NICK, H. M.; HASSANIZADEH, S. M.; SPIERS, C. J. PoreFlow: A complex pore-network model for simulation of reactive transport in variably saturated

porous media. *Computers and Geosciences*, v. 61, p. 160–174, 2013. <<http://dx.doi.org/10.1016/j.cageo.2013.08.005>>

RAOOF, A.; HASSANIZADEH, S. M. A new formulation for pore-network modeling of two-phase flow. *Water Resources Research*, v. 48, n. 1, p. 1–13, 2012.

RAOOF, A.; HASSANIZADEH, S. M. Saturation-dependent solute dispersivity in porous media: Pore-scale processes. *Water Resources Research*, v. 49, n. 4, p. 1943–1951, 2013. <<http://doi.wiley.com/10.1002/wrcr.20152>>

RAOOF, A.; HASSANIZADEH, S. M.. Upscaling transport of adsorbing solutes in porous media. *Journal of Porous Media*, v. 13, n. 5, p. 395–408, 2010. a.

RAOOF, A.; HASSANIZADEH, S. M.. A New Method for Generating Pore-Network Models of Porous Media. *Transport in Porous Media*, v. 81, n. 3, p. 391–407, 2010. b. <<http://link.springer.com/10.1007/s11242-009-9412-3>>

RAOOF, A.; HASSANIZADEH, S. M.; LEIJNSE, A. Upscaling Transport of Adsorbing Solutes in Porous Media: Pore-Network Modeling. *Vadose Zone Journal*, v. 9, n. 3, p. 624, 2010. <<https://www.soils.org/publications/vzj/abstracts/9/3/624>>

REEVES, P. C.; CELIA, M. A. A functional relationship between capillary pressure, saturation, and interfacial area as revealed by a pore-scale network model. *Water Resources Research*, v. 32, n. 8, p. S 2345–2358, 1996.

REIS NETO, J. M., FIORI, A. P.; LOPES, A. P.; MARCHESE, C.; PINTO-COELHO, C. V.; VASCONCELLOS, E. M. G.; DA SILVA, G. F.; SECCHI, R. A microtomografia computadorizada de raios x integrada à petrografia no estudo tridimensional de porosidade em rochas. *Revista Brasileira de Geociencias*, v. 41, n. 3, p. 498–508, 2011.

RIGBY, S. P. *Structural Characterisation of Natural and Industrial Porous Materials: A Manual*. Cham: Springer International Publishing, 2020. <<http://link.springer.com/10.1007/978-3-030-47418-8>>

RUDIYANTO; MINASNY, B.; SHAH, R. M.; SETIAWAN, B. I.; VAN GENUCHTEN, M. Th. Simple functions for describing soil water retention and the unsaturated hydraulic conductivity from saturation to complete dryness. *Journal of Hydrology*, v. 588, p. 125041, 2020. <<https://linkinghub.elsevier.com/retrieve/pii/S0022169420305011>>

SAHIMI, M. Flow and transport in porous media and fractured rock: from classical methods to modern approaches. 2nd Ed. ed. Weinheim, Germany: Wiley-VCH, 2011.

SAN JOSÉ MARTÍNEZ, F.; MUÑOZ ORTEGA, F.J.; CANIEGO MONREAL, F.J.; KRAVCHENKO, A.N.; WANG, W. Soil aggregate geometry: Measurements and morphology. *Geoderma*, v. 237–238, p. 36–48, 2015. <<https://linkinghub.elsevier.com/retrieve/pii/S0016706114003048>>

SAYEDAKRAM, N. I.; SHIKHOV, I.; ARNS, J. Y.; ARNS, C. H. MICRO-CT assisted interpretation of NMR responses of heterogeneous mixed-wet carbonate rock. SPWLA 57th Annual Logging Symposium 2016, p. 1–20, 2016.

SCANLON, B. R.; ANDRASKI, B. J.; BILSKIE, J. Miscellaneous Methods for Measuring Matric or Water Potential. In: DANE, Jacob H.; TOPP, Clarke G. (Eds.). *Methods of Soil Analysis: Part 4 Physical Methods*. Madison: Soil Science Society of America, 2002. p. 643–670.

SCHELLE, H.; IDEN, S.C.; PETERS, A.; DURNER, W. Analysis of the Agreement of Soil Hydraulic Properties Obtained from Multistep-Outflow and Evaporation Methods. *Vadose Zone Journal*, v. 9, n. 4, p. 1080–1091, 2010. <<http://doi.wiley.com/10.2136/vzj2010.0050>>

SCHINDLER, U.; VON UNOLD, G.; DURNER, W.; MÜLLER, L. Evaporation method for measuring unsaturated hydraulic properties of soils: extending the range. *Soil Sci. Soc. Am. J.*, v. 74, p. 1071–1083, 2010.

SCHNEIDER, C. A.; RASBAND, W. S.; ELICEIRI, K. W. NIH Image to ImageJ: 25 years of image analysis. *Nature methods*, v. 9, n. 7, p. 671–5, 2012. <<https://imagej.nih.gov/ij/docs/guide/>>

SHAFER, J.; NEASHAM, J.. Mercury porosimetry protocol for rapid determination of petrophysical and reservoir quality properties. <[https://www.researchgate.net/publication/265526344\\_Mercury\\_porosimetry\\_protocol\\_for\\_rapid\\_determination\\_of\\_petrophysical\\_and\\_reservoir\\_quality\\_properties](https://www.researchgate.net/publication/265526344_Mercury_porosimetry_protocol_for_rapid_determination_of_petrophysical_and_reservoir_quality_properties)>.

SILVA, W. G. A. L.; RIOS, E. H.; HOERLLE, F. O.; PONTEDEIRO, E. M. B. D.; BORGHI, L.; ALVES, J. L. D.; COUTO, P. Representative elementary volume of a region of interest of a heterogeneous carbonate rock using X-ray computed

microtomography and numerical simulation. *Revista Brasileira de Geofísica*, v. 36, n. 4, p. 519–526, 2018.

ŠIMŮNEK, J.; SEJNA, M.; VAN GENUCHTEN, M. Th. The HYDRUS-1D software package for simulating the movement of water, heat, and multiple solutes in variably-saturated media. Golden International Ground Water Modeling Center, Colorado School of Mines, 1998.

SKAGGS, T. H. Effects of finite system-size and finite inhomogeneity on the conductivity of broadly distributed resistor networks. *Physica B: Condensed Matter*, v. 338, n. 1–4, p. 266–269, 2003. <<https://linkinghub.elsevier.com/retrieve/pii/S092145260300509X>>

SKAGGS, T. H. Assessment of critical path analyses of the relationship between permeability and electrical conductivity of pore networks. *Advances in Water Resources*, v. 34, n. 10, p. 1335–1342, 2011. <<https://linkinghub.elsevier.com/retrieve/pii/S0309170811001229>>

SOUZA, A.; CARNEIRO, G.; ZIELINSKI, L.; POLINSKI, R.; SCHWARTZ, L.; HÜRLIMANN, M. D.; BOYD, A.; RIOS, E. H.; COUTINHO, B.; TREVIZAN, W. A.; MACHADO, V. F.; BAGUEIRA, R. A. V. Permeability Prediction Improvement Using 2D NMR Diffusion-T2 Maps. p. 1–16, 2013.

SOUZA, A. A. Estudo de propriedades petrofísicas de rochas sedimentares por Ressonância Magnética Nuclear. 2012. Universidade de São Paulo, 2012.

STEIGERWALD, D. G. Economics 245A – Introduction to Measure Theory.: University of California, Santa Barbara. <<http://econ.ucsb.edu/~doug/245a/Lectures/Measure Theory.pdf>>. Access: 5 aug. 2019.

STEVENSON, D. L. Salem Limestone oil and gas production in the Keenville Field, Wayne County, Illinois. *Indiana State Geological Survey Series - Illinois Petroleum*, v. 114, p. 16, 1978.

SWANSON, B. F. Simple Correlation Between Permeabilities and Mercury Capillary Pressures. *JPT, Journal of Petroleum Technology*, v. 33, n. 12, p. 2498–2504, 1981.

SWART, P. K. CANTRELL, D. L.; WESTPHAL, H.; HANDFORD, C. R.; KENDALL, C. G. Origin of Dolomite in the Arab-D Reservoir from the Ghawar Field, Saudi Arabia:



Evidence from Petrographic and Geochemical Constraints. *Journal of Sedimentary Research*, v. 75, n. 3, p. 476–491, 2005.

Utilizing True Dynamic CT Imaging for 3D non-destructive in situ Experimentation. Direction: TESCAN. Brno: TESCAN ORSAY HOLDING, 2020.

THOMEER, J. H. Air Permeability As a Function of Three Pore-Network Parameters. *JPT, Journal of Petroleum Technology*, v. 35, n. 4, p. 809–814, 1983.

THOMEER, J. H. M. Introduction of a Pore Geometrical Factor Defined by the Capillary Pressure Curve. *Journal of Petroleum Technology*, v. 12, n. 03, p. 73–77, 1960.

TIAB, D.; DONALDSON, E. C. *Petrophysics: Theory and Practice of Measuring Reservoir Rock and Fluid Transport Properties*. 2. ed.: Gulf Professional Publishing, 2003.

VAN GENUCHTEN, M. Th. Closed-Form Equation for Predicting the Hydraulic Conductivity of Unsaturated Soils. *Soil Science Society of America Journal*, v. 44, n. 5, p. 892–898, 1980.

VAN GENUCHTEN, M. Th. *Non-equilibrium transport parameters from miscible displacement experiments*. Riverside, CA.

VAN GENUCHTEN, M. Th.; LEIJI, F. J.; YATES, S. R. *The RETC Code for Quantifying the Hydraulic Functions of Unsaturated Soils* Environmental Protection, Ada, Oklahoma, 1991.  
<[http://afsrweb.usda.gov/SP2UserFiles/Place/53102000/pdf\\_pubs/P1228.pdf](http://afsrweb.usda.gov/SP2UserFiles/Place/53102000/pdf_pubs/P1228.pdf)>

VAN GENUCHTEN, M. Th.; NIELSEN, D. R. On Describing and Predicting the Hydraulic Properties of Unsaturated Soils. *Annales Geophysicae*, v. 3, n. 5, p. 615–628, 1985.

VIK, B.; BASTESEN, E.; SKAUGE, A. Evaluation of representative elementary volume for a vuggy carbonate rock-Part: Porosity, permeability, and dispersivity. *Journal of Petroleum Science and Engineering*, v. 112, p. 36–47, 2013.  
<<http://dx.doi.org/10.1016/j.petrol.2013.03.029>>

VIK, B.; SYLTA, K. E.; SKAUGE, A. Evaluation of representative elementary volume for a vuggy carbonate rock - Part II: Two-phase flow. *Journal of Petroleum Science and Engineering*, v. 112, p. 48–60, 2013. <<http://dx.doi.org/10.1016/j.petrol.2013.10.023>>

VINEGAR, H. J.; WELLINGTON, S. L. Tomographic imaging of three-phase flow experiments. *Review of Scientific Instruments*, v. 58, n. 1, p. 96–107, 1987. <<http://aip.scitation.org/doi/10.1063/1.1139522>>

VOIGT, C.; HUBÁLKOVÁ, J.; GIESCHE, H.; ANEZIRIS, C. G. Intrusion and extrusion mercury porosimetry measurements at Al<sub>2</sub>O<sub>3</sub>-C - Influence of measuring parameter. *Microporous and Mesoporous Materials*, v. 299, p. 110125, 2020. <<https://linkinghub.elsevier.com/retrieve/pii/S1387181120301281>>

WANG, Z.; FEYEN, J.; NIELSEN, D. R.; VAN GENUCHTEN, M. T. Two-phase flow infiltration equations accounting for Air Entrapment Effects. *Water Resources*, v. 33, n. 12, p. 2759–2767, 1997.

WARDLAW, N. C. The Effects of Geometry , Wettability, Viscosity and Interfacial Tension on Trapping in Single Pore-Throat Pairs. *JCPT*, 1982.

WARDLAW, N. C.; LI, Y.; FORBES, D. Pore-throat size correlation from capillary pressure curves. *Transport in Porous Media*, v. 2, n. 6, 1987. <<http://link.springer.com/10.1007/BF00192157>>

WARDLAW, N. C.; TAYLOR, R. P. Mercury capillary pressure curves and the interpretation of pore structures and capillary behavior in reservoir rocks. *Bulletin of Canadian Petroleum Geology*, v. 24, p. 225–262, 1976.

WEATHERFORD LABORATORIES. Gas Permeameter - Helium Porosimeter System Operation Manual DV-4000Houston, 2017.

WENDROTH, O.; EHLERS, W.; HOPMANS, J.W.; KLAGE, H.; HALBERTSMA, J.; WÖSTEN, J.H.M. Reevaluation of the evaporation method for determining hydraulic functions in unsaturated soils. *Soil Sci. Soc. Am. J.*, v. 57, p. 1436–1443, 1993.

WILDENSCHILD, D.; SHEPPARD, A. P. X-ray imaging and analysis techniques for quantifying pore-scale structure and processes in subsurface porous medium systems. *Advances in Water Resources*, v. 51, p. 217–246, 2013. <<https://linkinghub.elsevier.com/retrieve/pii/S0309170812002060>>

WIND, G. P. Capillary conductivity data estimated by a simple method. In: RIJTEMA, P. E.; WASSINK, H. (Eds.). *Water in the Unsaturated Zone*, vol. 1. Proceedings of the

Wageningen Symposium. Gentbrugge, The Netherlands and UNESCO, Paris: Int. Assoc. Sci. Hydrol. Publ. (IASH), 1968.

WINSAUER, W. O.; SHEARIN, H. M.; MASSON, P. H.; WILLIAM, M. Resistivity of Brine-Saturated Sands in Relation to Pore Geometry. American Association of Petroleum Geologists Bulletin, v. 36, p. 253–277, 1952.

WOLFRAM RESEARCH, Inc. MathematicaChampaign, IllinoisWolfram Research, Inc., 2017.

ZHOU, H.; PENG, X.; PERFECT, E.; XIAO, T.; PENG, G. Effects of organic and inorganic fertilization on soil aggregation in an Ultisol as characterized by synchrotron based X-ray micro-computed tomography. Geoderma. Geoderma, v. 195, p. 23–30, 2013.

ZHUANG, L.; HASSANIZADEH, S. M.; KLEINGELD, P. J.; VAN GENUCHTEN, M. TH. Revisiting the horizontal redistribution of water in soils: Experiments and numerical modeling. Water Resources Research, v. 53, n. 9, p. 7576–7589, 2017. <<http://doi.wiley.com/10.1002/2017WR020410>>

ZINSZNER, B.; PELLERIN, F.-M.. A Geoscientist's Guide to Petrophysics - Edition en langue anglaise.

## Appendix A

### Transforming NMR radii into pressure head using Excel

- 1) **Column A:** insert NMR radii (um)
- 2) **Column B:** transform radii in column A into meters

$$r[m] = 10^{-6}r[\mu m]$$

- 3) **Column C:** use Young-Laplace to transform radii into equivalent pressure (N/m<sup>2</sup>)

$$P = \frac{2\sigma\cos(\theta)}{r}$$

$$P = \frac{2 * 0.07275 [N/m] * \cos(0)}{r [m]}$$

where:

$\sigma$  is the surface tension of water, equal to 0.07275 J/m<sup>2</sup> or 0.07275 N/m or 72.75 mN/m,

$\theta$  is the contact angle between water and air in radians ( $\frac{\theta\pi}{180}$ , where  $\theta = 0$ ), and

$r$  is radius from column B, in meters.

- 4) **Column D:** transform pressure (N/m<sup>2</sup>) into equivalent pressure head (cmH<sub>2</sub>O):  
Multiply column C by 0.0101972. Explanation as follows:

$$1 \frac{N}{m^2} = 0.0101972 \text{ cmH}_2\text{O}$$

N/m<sup>2</sup> is a unit that shows how the pascal unit is derived from other SI units. The pressure is defined as Force/Area, the SI unit for Force is newtons (N) and the SI unit for Area is Square Meters (m<sup>2</sup>). 1 newton per square metre equals 1 pascal.

The N/m<sup>2</sup> pressure unit is one of the few units that clearly describes what pressure represents in its name symbol. Although it is not generally used to describe a pressure reading, it can be useful for calculating the force required to generate a certain pressure. For example, if one knows the cross-sectional area of the inside of a hydraulic ram cylinder (m<sup>2</sup>), one can then calculate the required force (N) to generate a particular pressure in pascals (Pa) by multiplying the two together.

Alternatively, one can calculate the hydraulic ram area size (m<sup>2</sup>) needed by dividing the available Force (N) by the Pressure (Pa), or determine the pressure (N/m<sup>2</sup>) produced by the hydraulic system by dividing the Force (N) by the Hydraulic ram area (m<sup>2</sup>).

Centimeters of Water Column is a manometric unit used to relate a pressure reading to the height of fresh water at a temperature of 4 °C. 1.0 centimeter of water gauge equals 98.0665 pascals. The cm H<sub>2</sub>O pressure unit is mostly used to measure breathing in respirators and ventilators, which are used in medical and physiological applications such as controlling respiratory conditions or monitoring athletic performance.

There are many ways of writing centimeters of water, but the main causes of confusion are Water Column (WC) and Water Gauge (WG), which both mean exactly the same ..

- 5) **Column E:** calculate pF: calculate the logarithm of the values in column D:

$$pF = \log (cmH_2O)$$

- 6) **Columns F and G:** turn capillary pressure into bar and MPa:

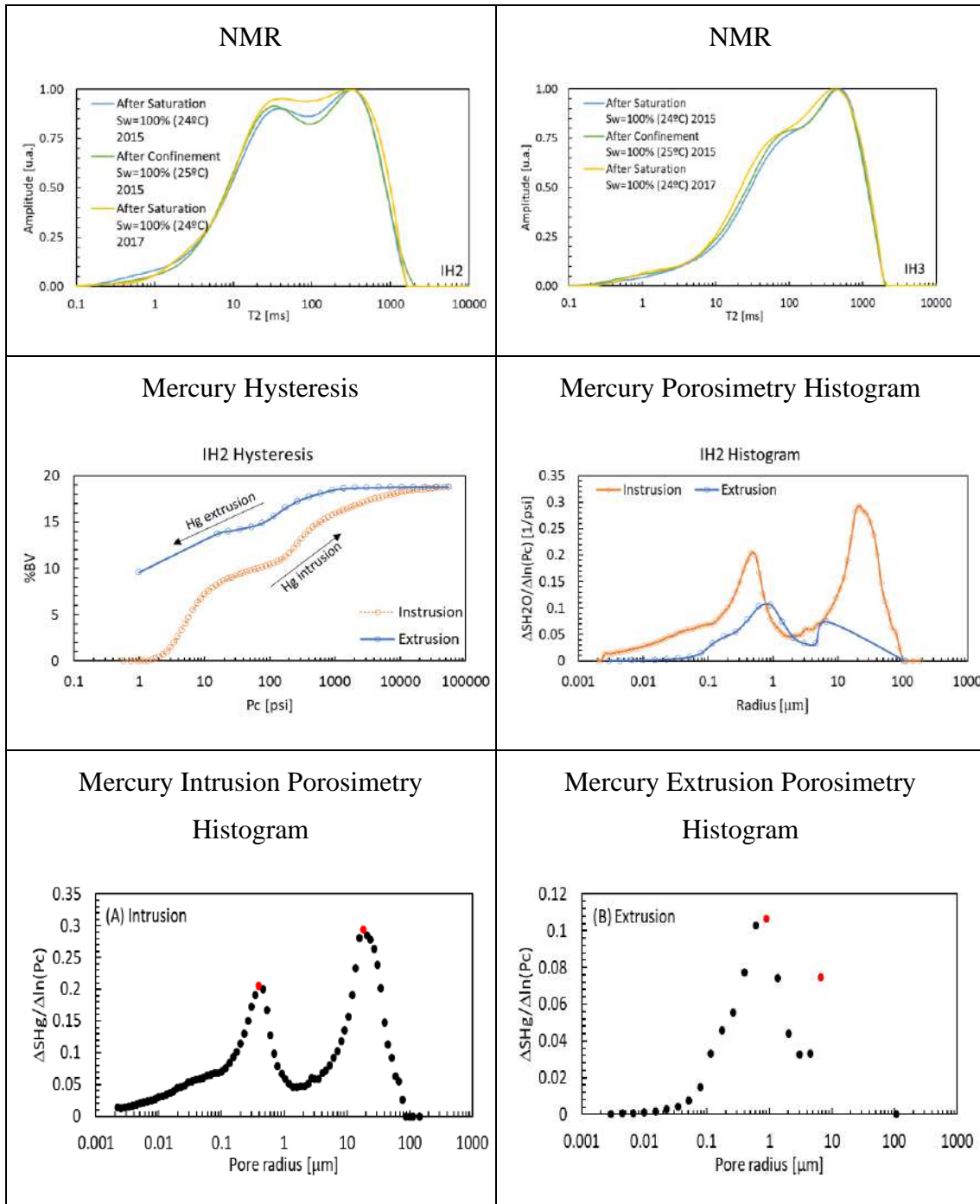
$$P [bar] = \frac{P[cmH_2O]}{1020}$$

$$P [MPa] = \frac{P[bar]}{9.81}$$

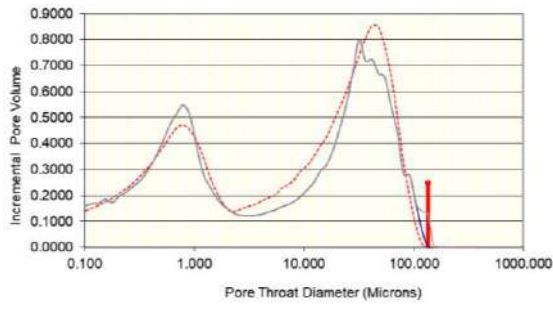
# Appendix B

## Graphs for each studied sample

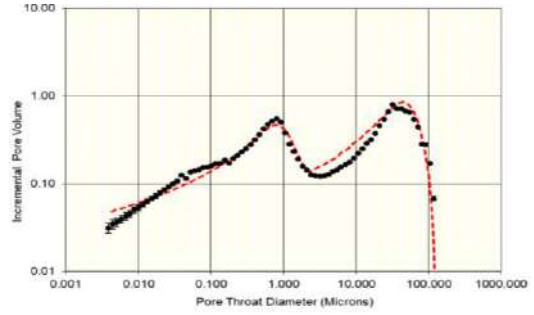
### Sample: Indiana Limestone High



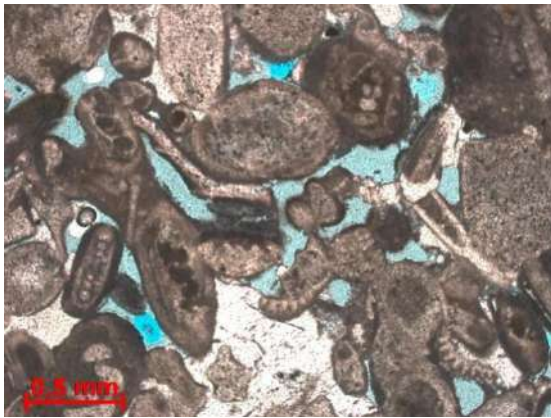
Thomeer Hyperbola



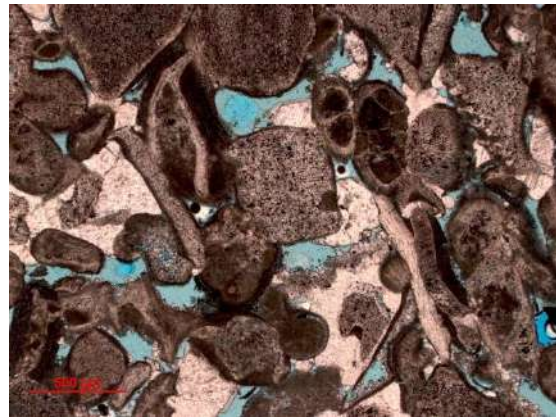
Thomeer G-Fitting Window



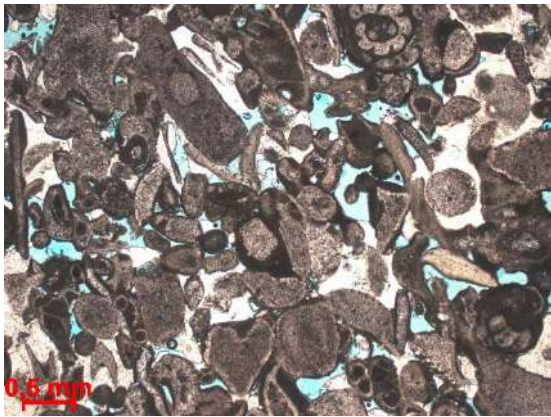
Thin-Section



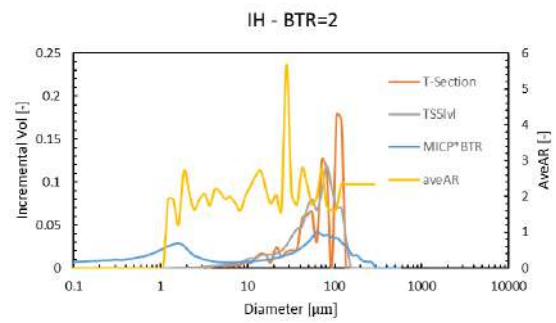
Thin-Section



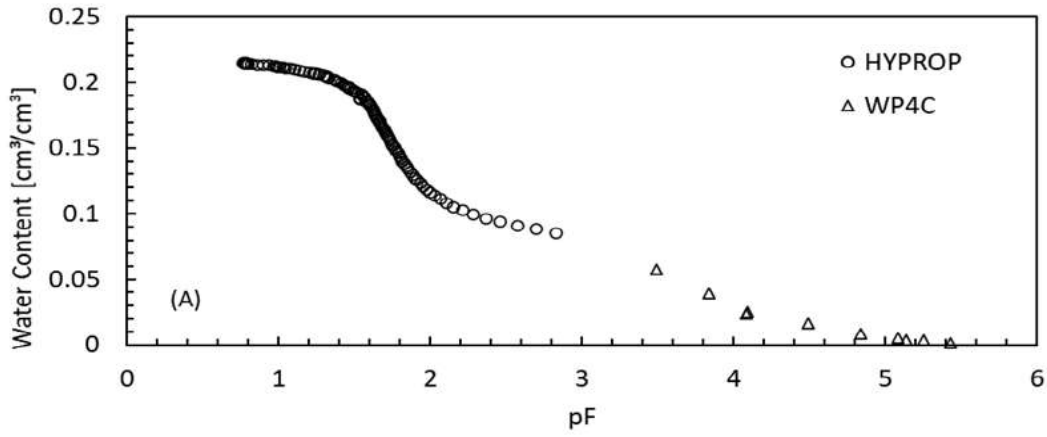
Thin-Section



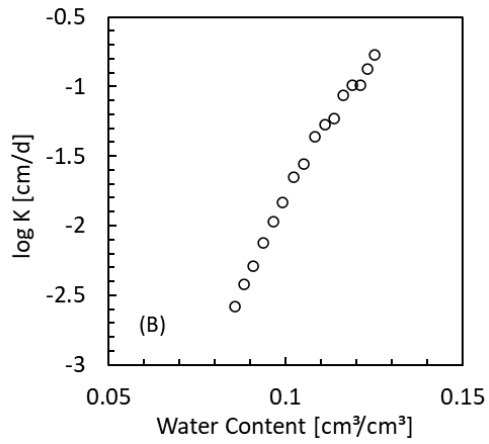
BTR



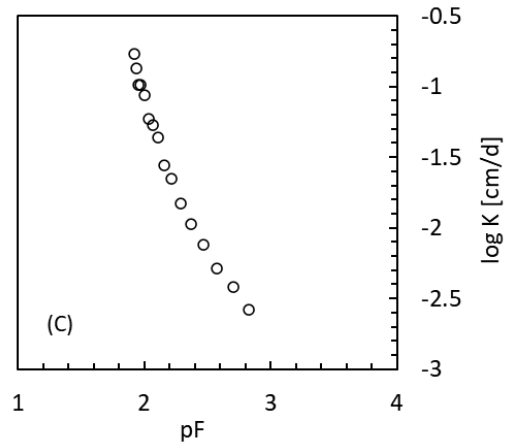
Water retention vs. hydraulic conductivity



Water retention vs. water content

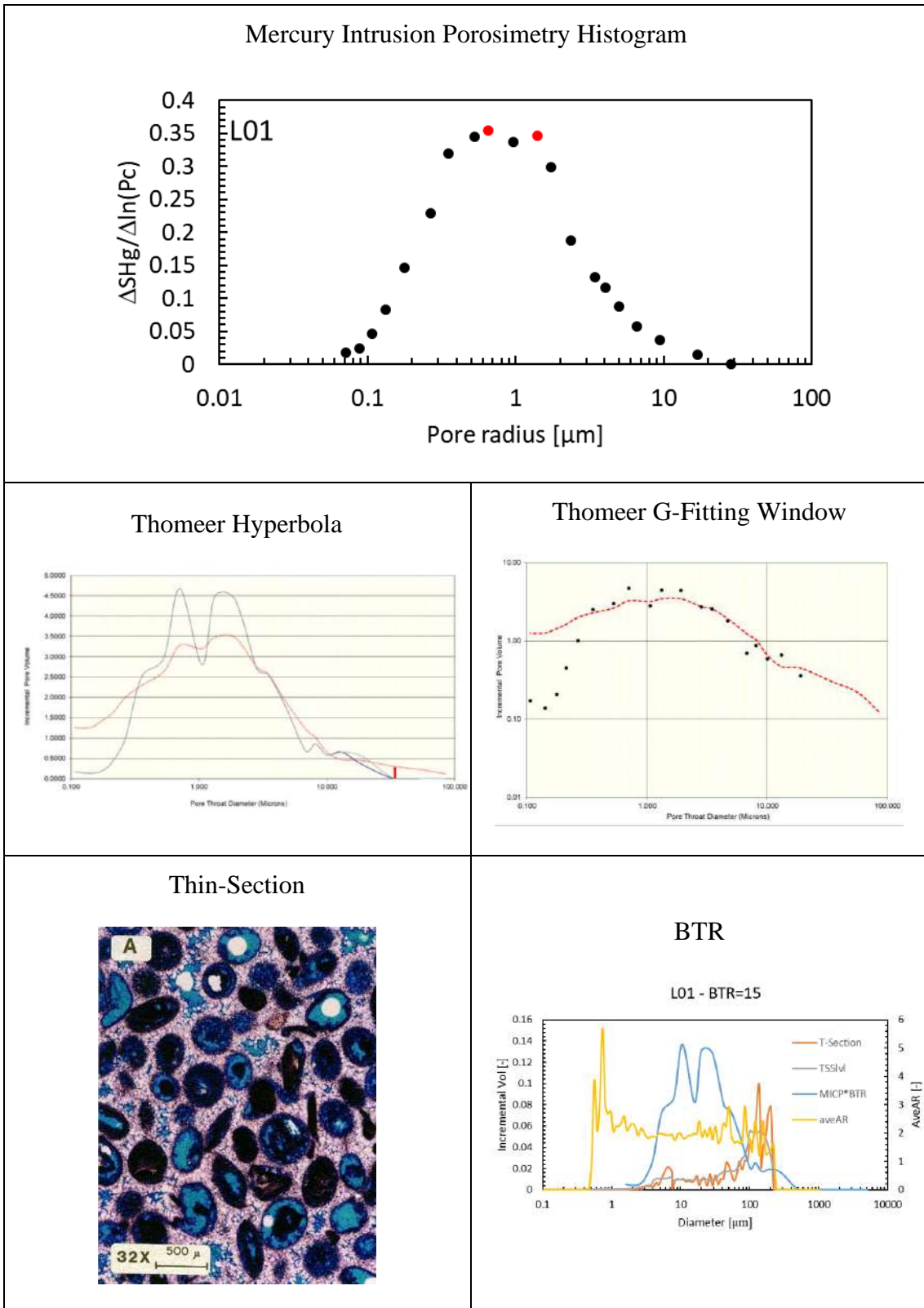


Water retention vs. pF

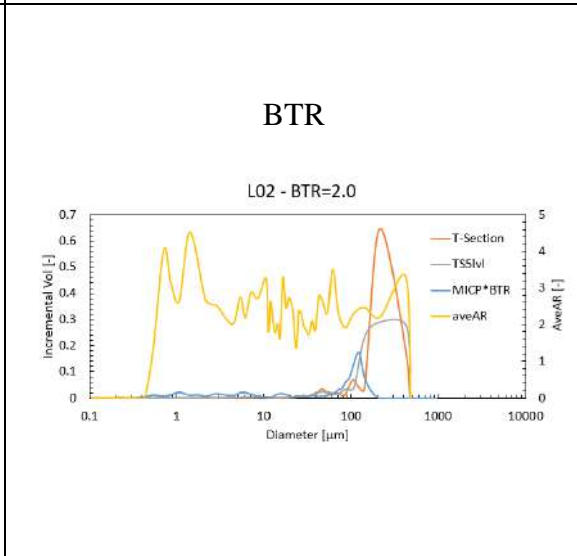
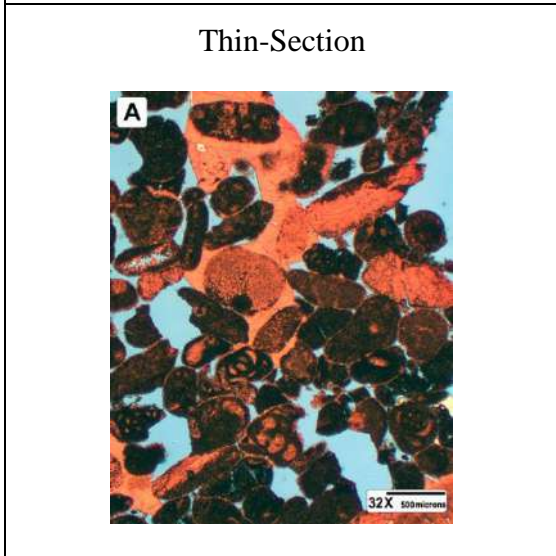
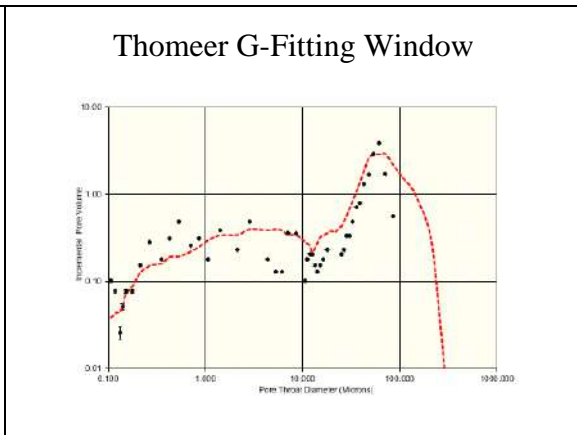
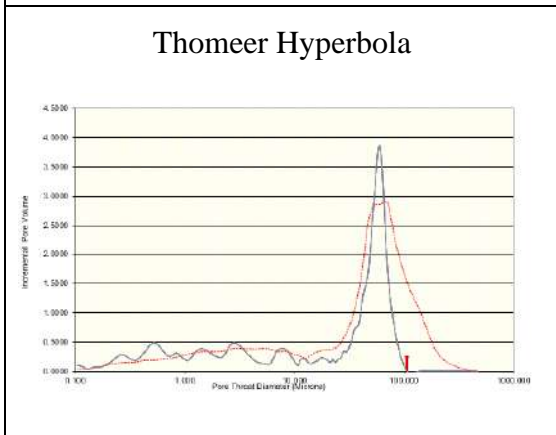
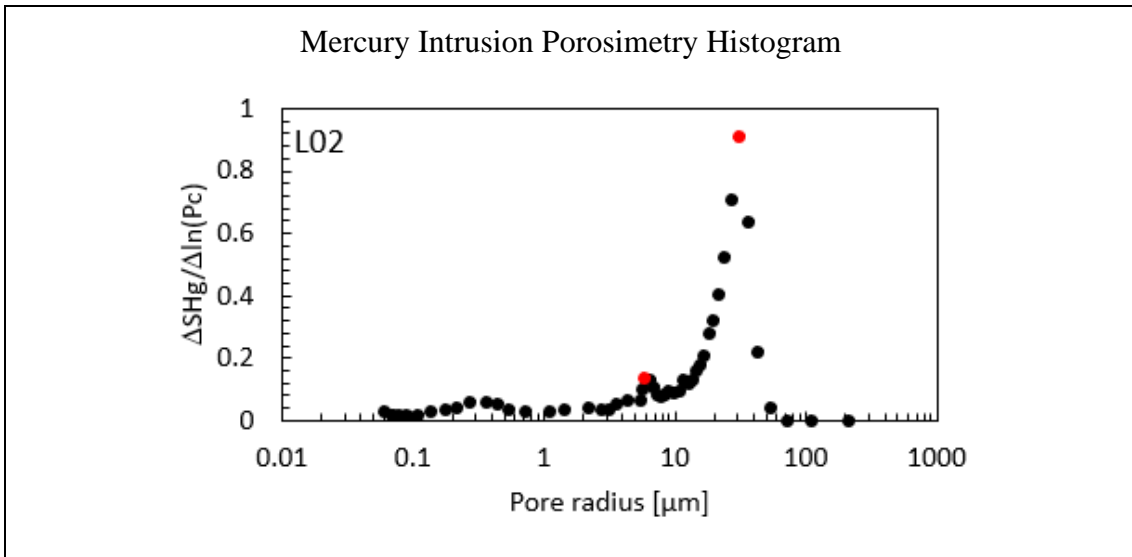




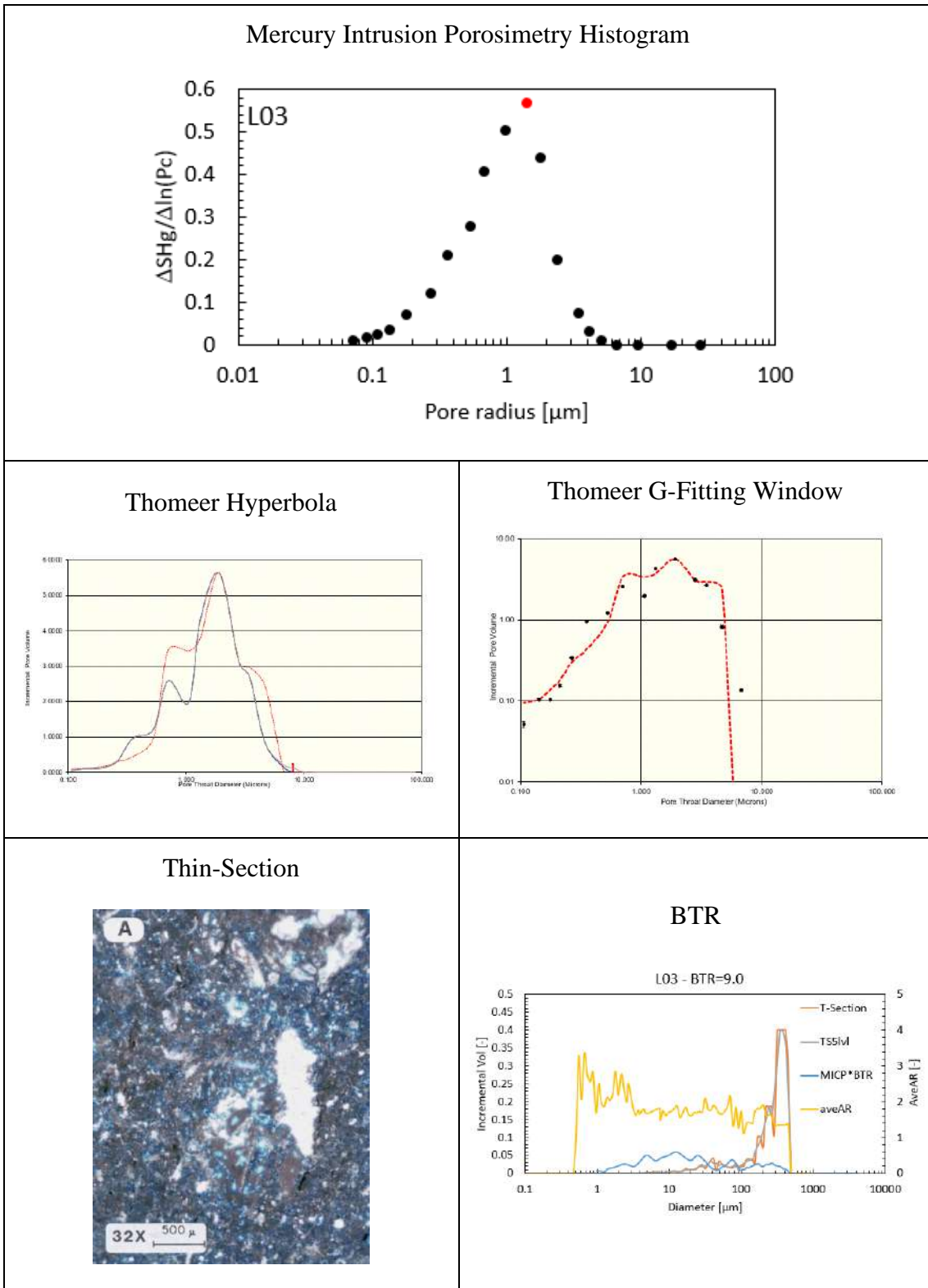
**Sample: L01**



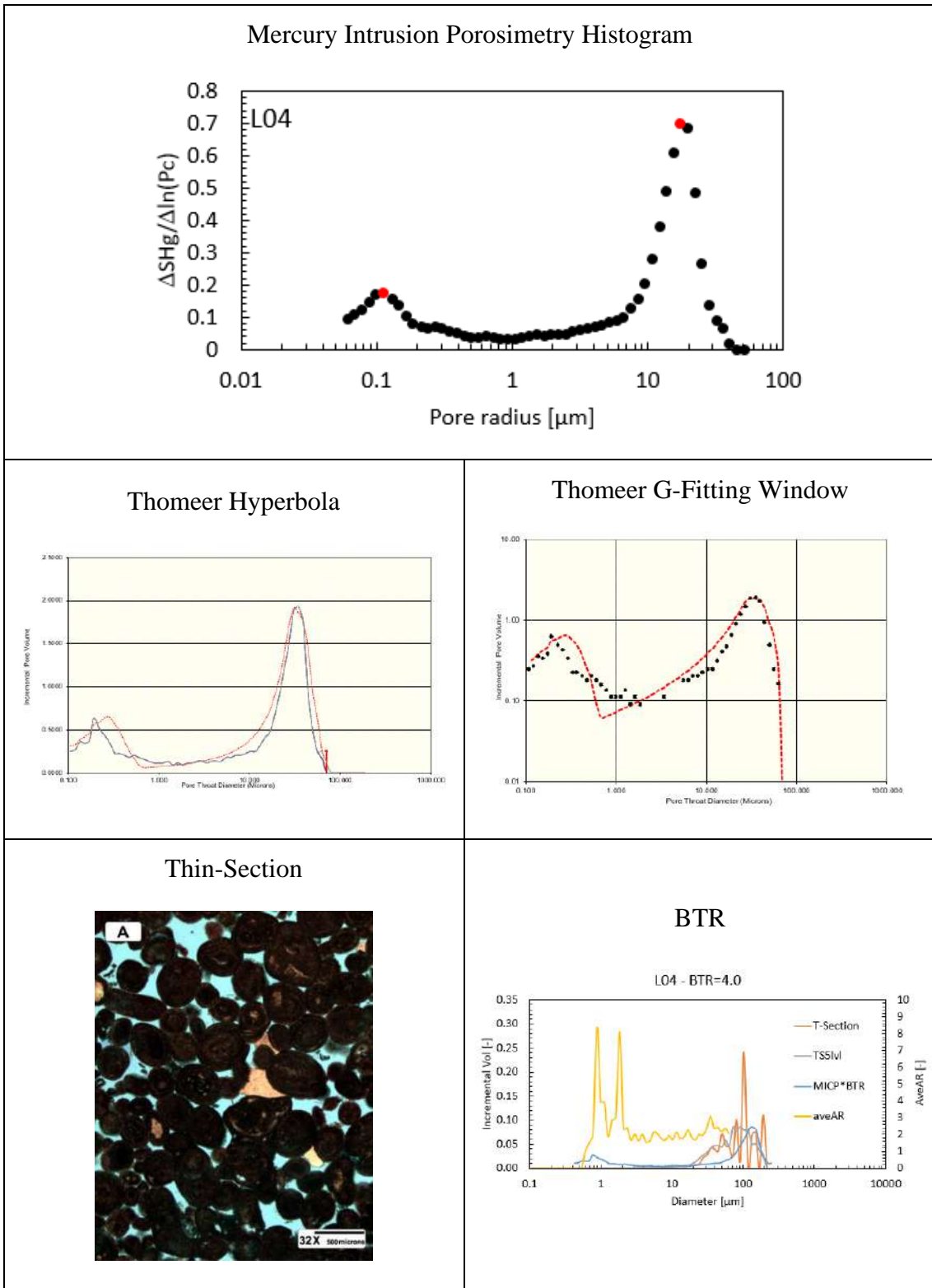
# Sample: L02



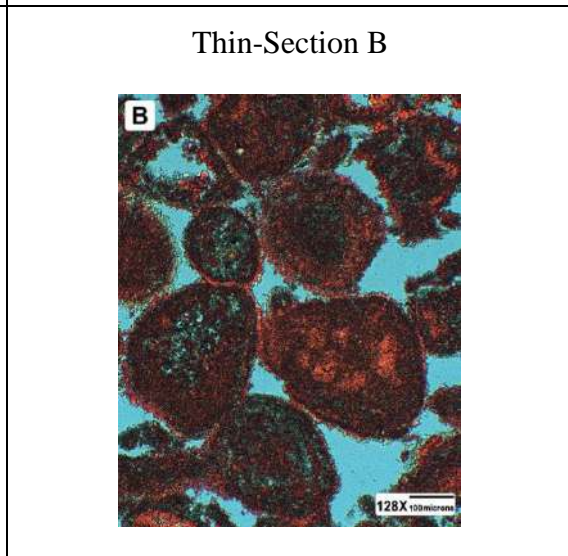
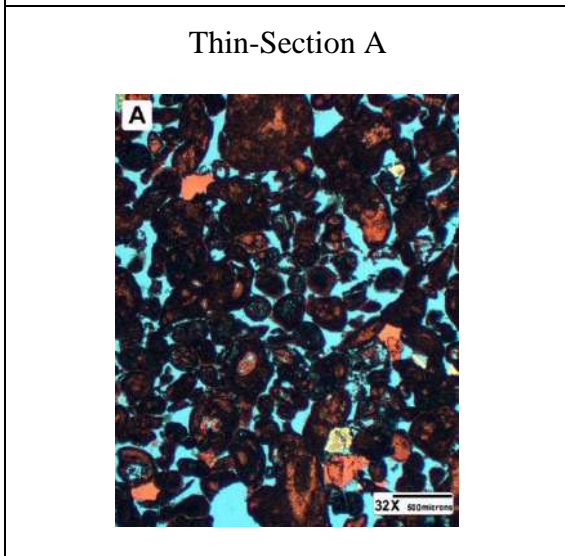
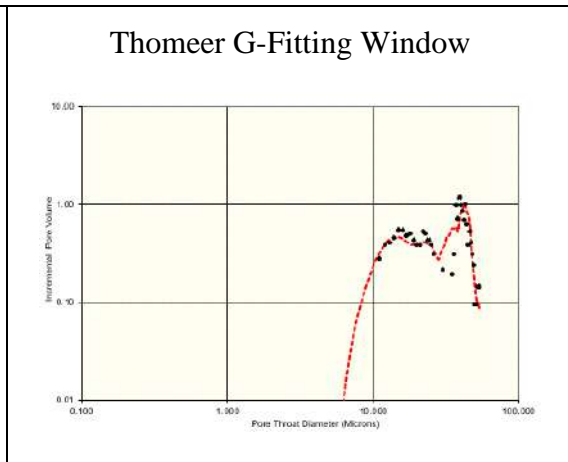
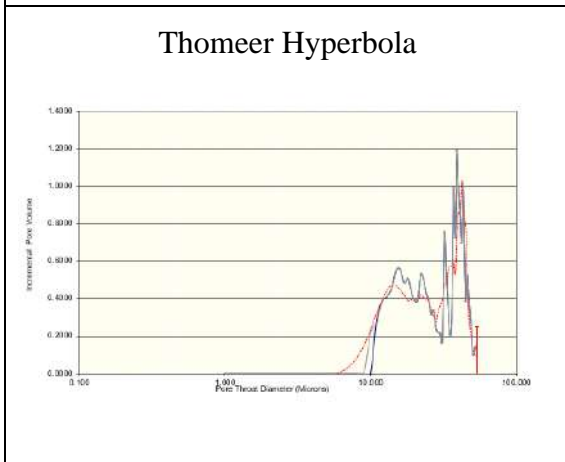
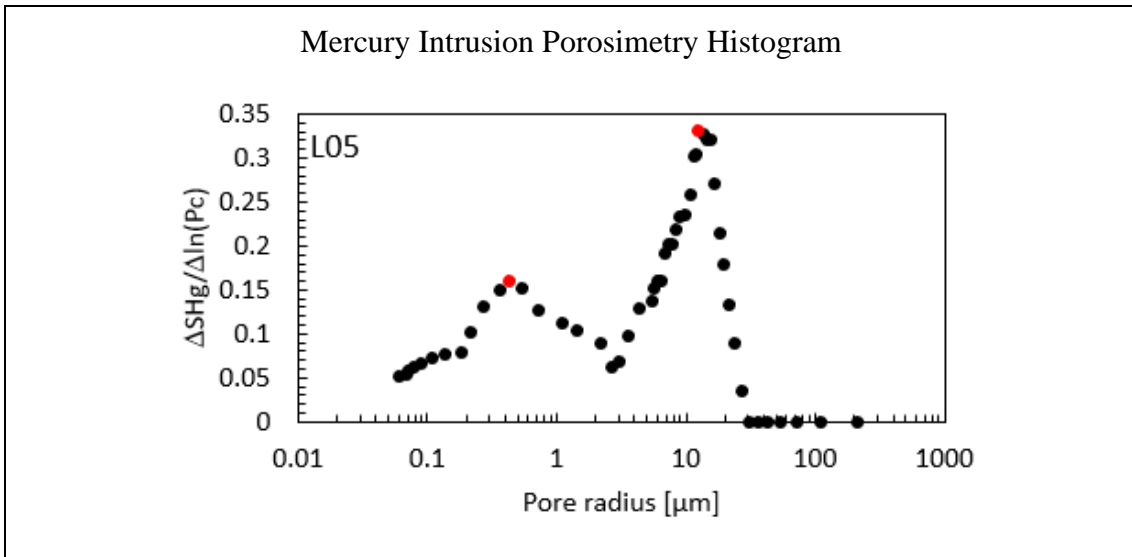
### Sample: L03

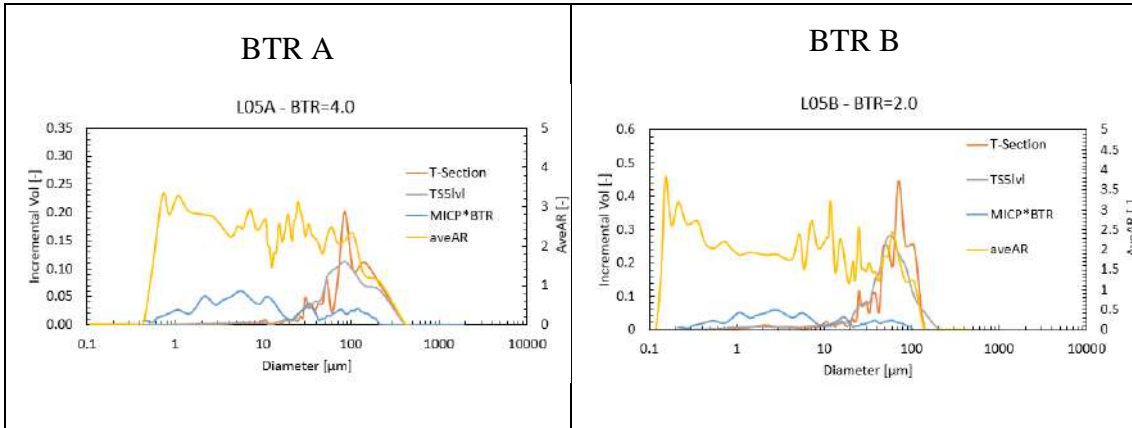


# Sample: L04

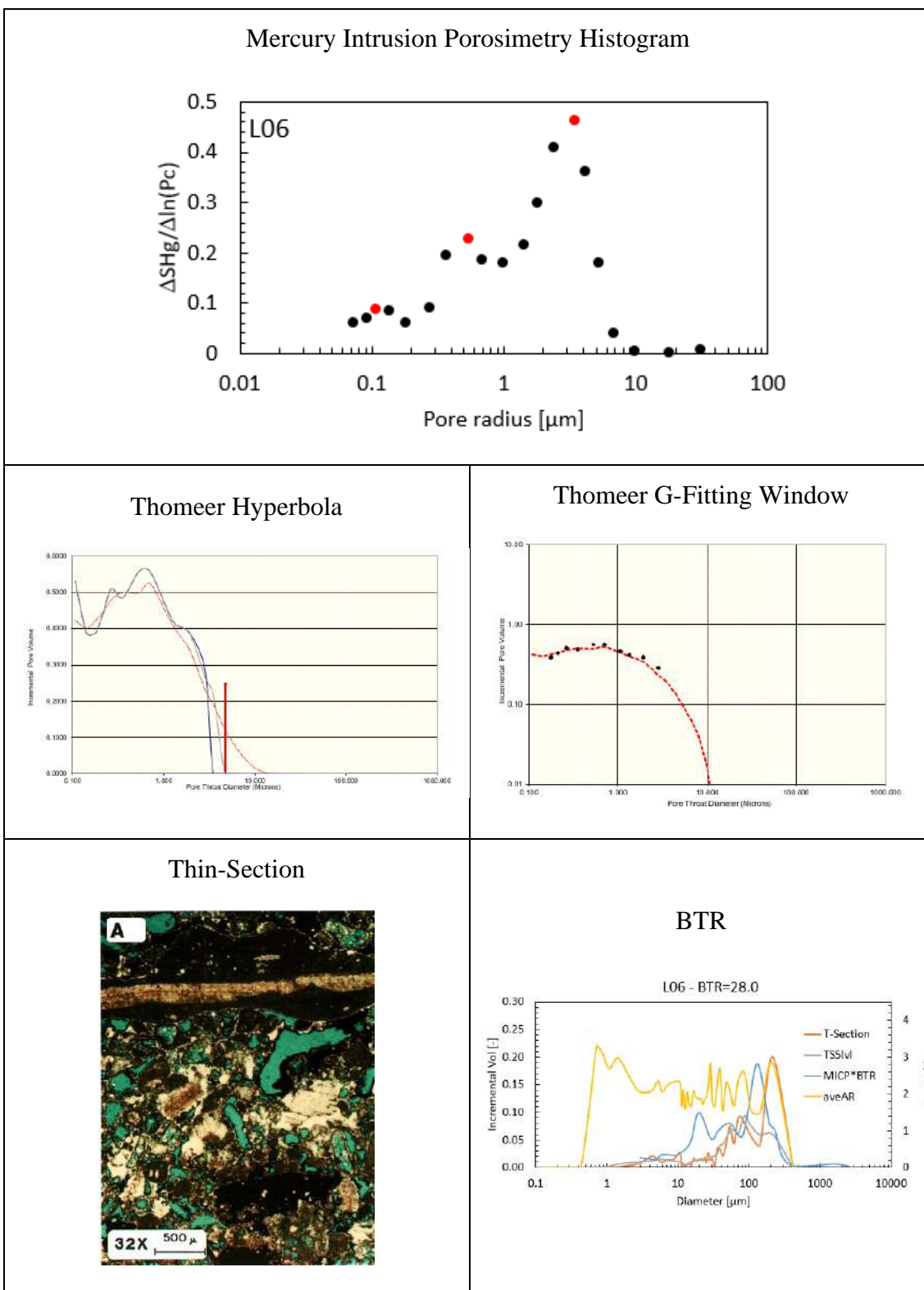


### Sample: L05



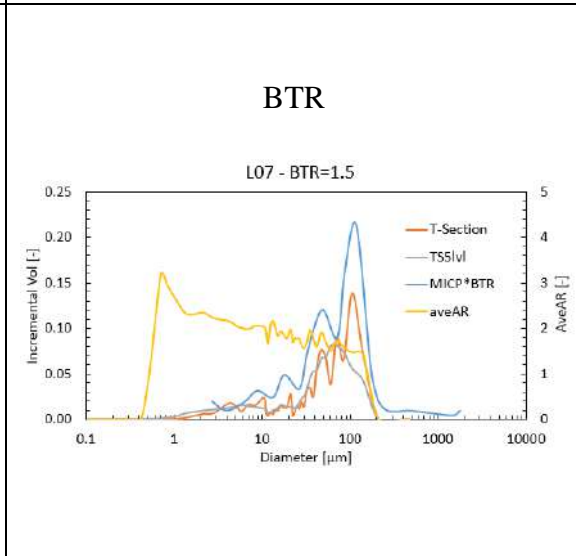
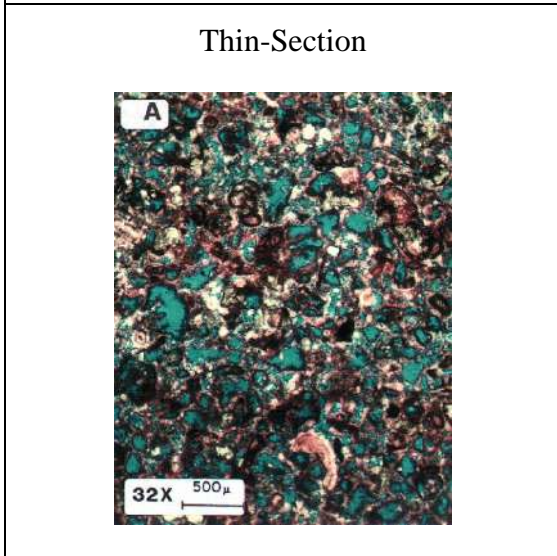
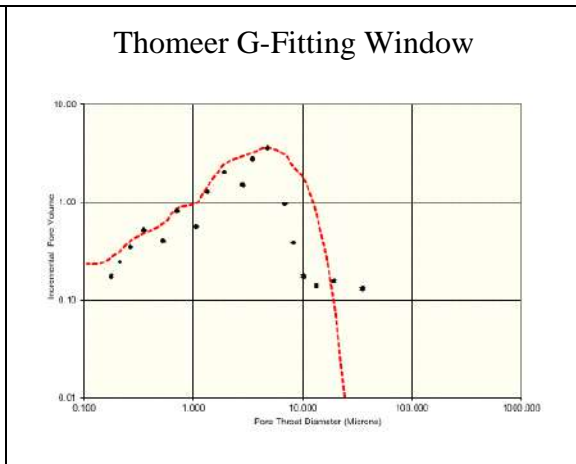
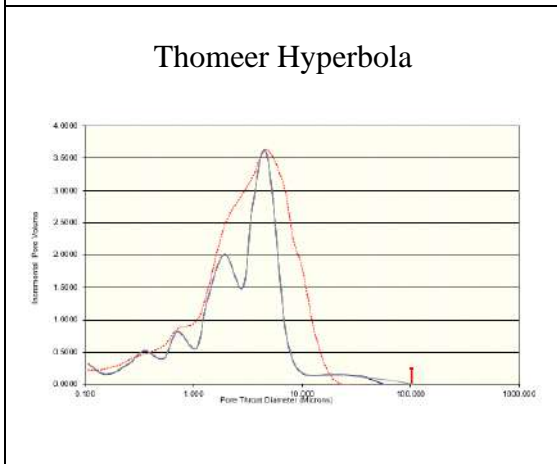
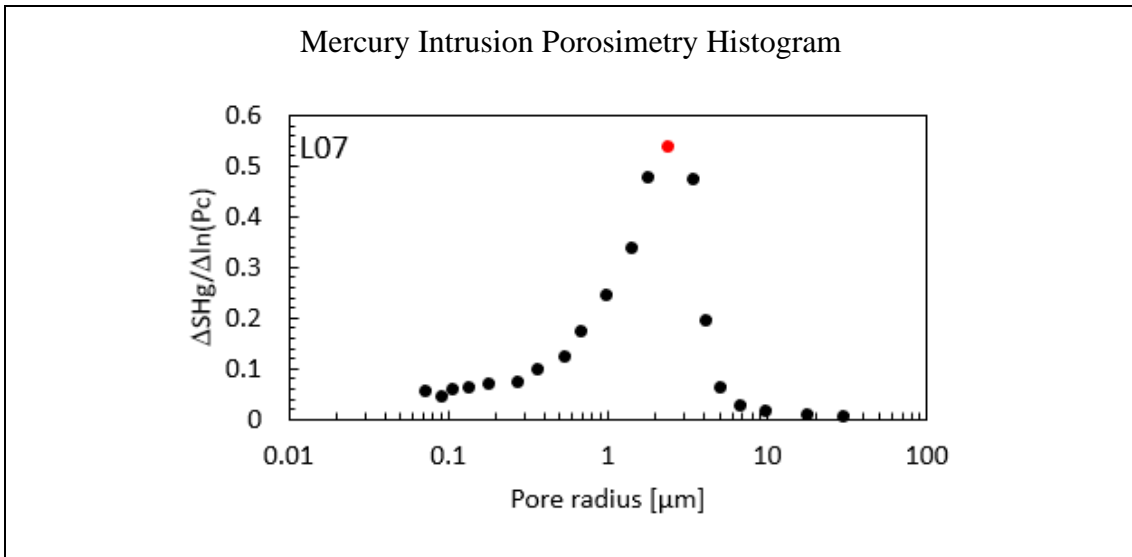


### Sample: L06



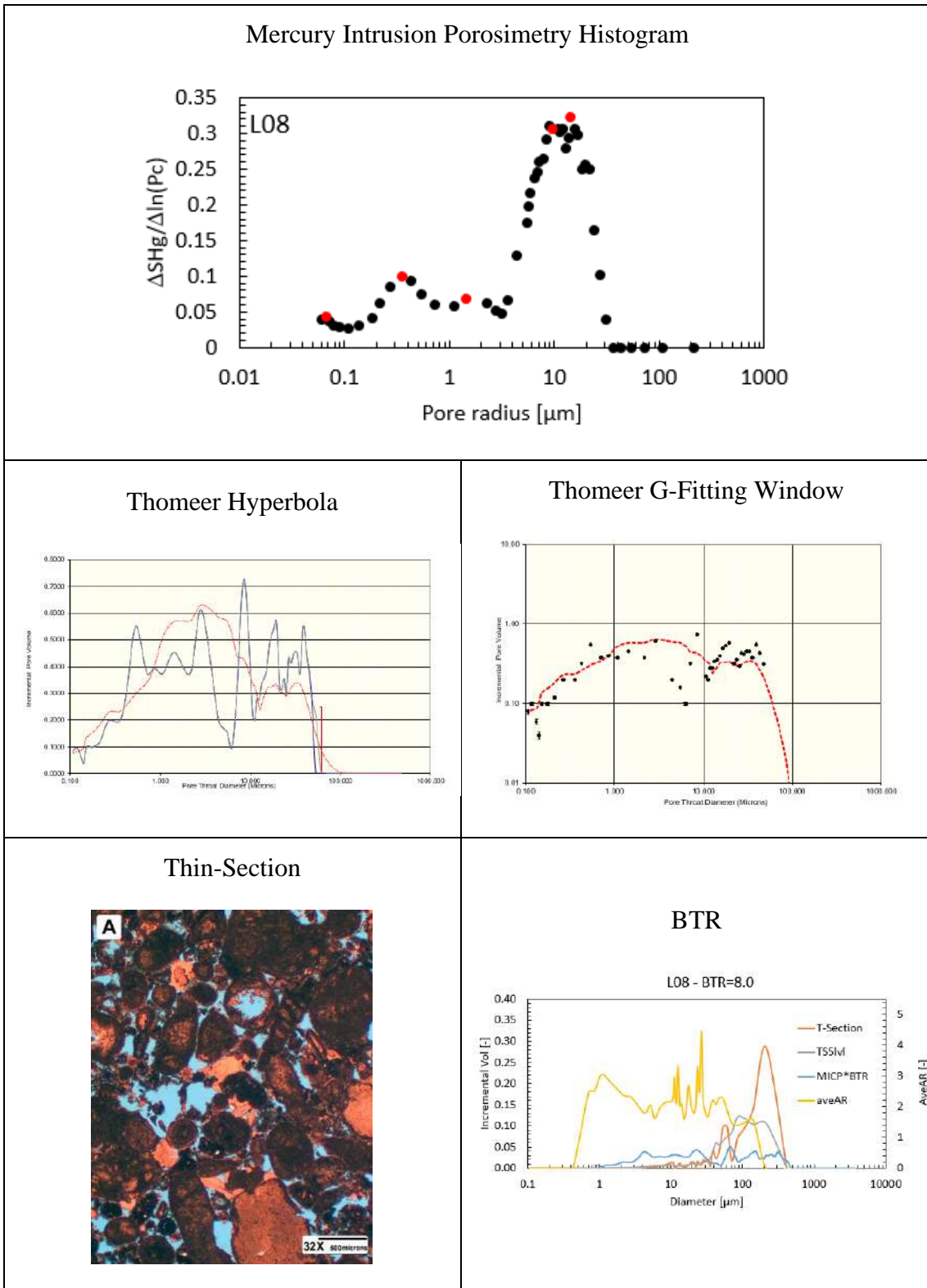


### Sample: L07

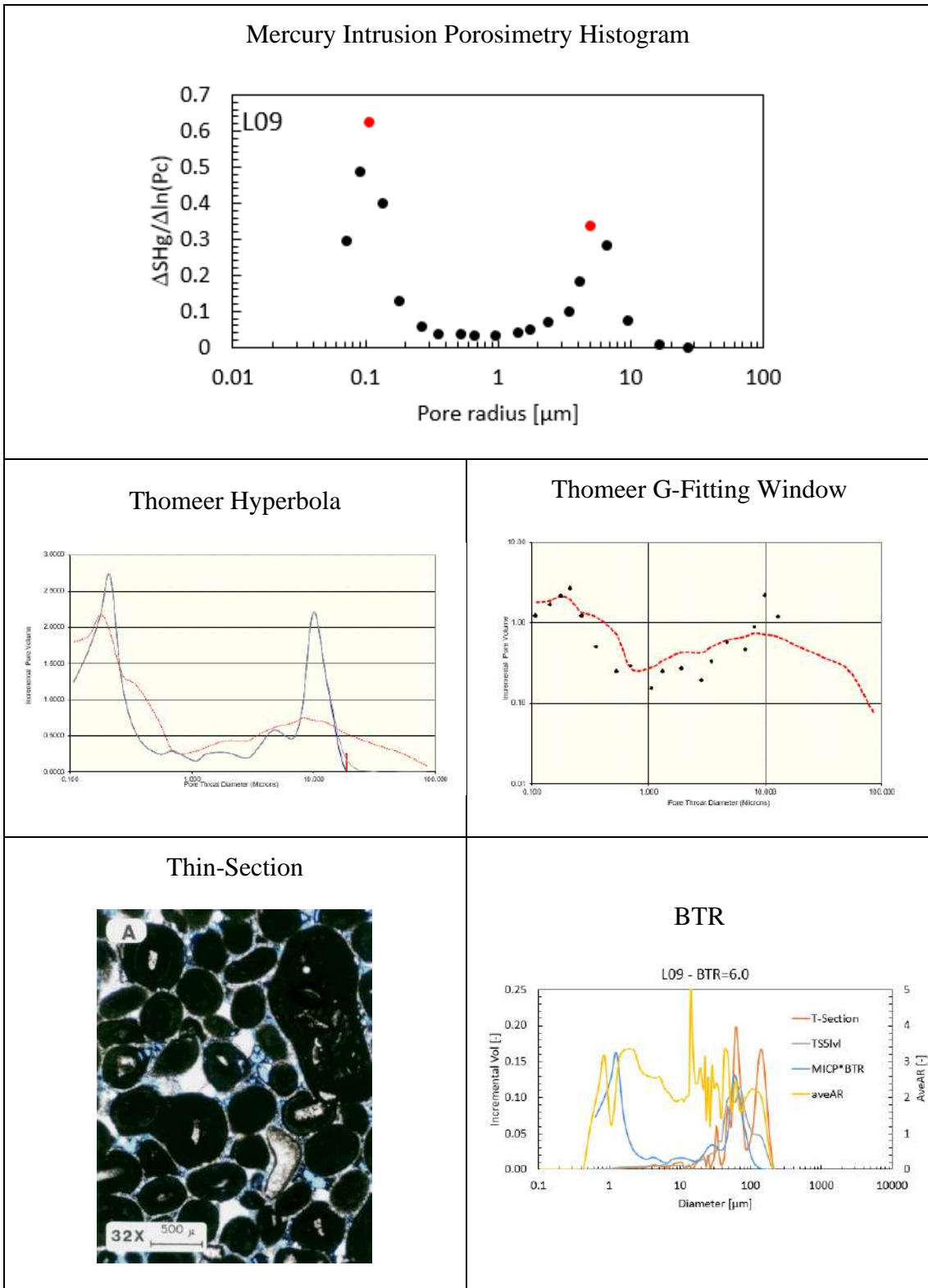




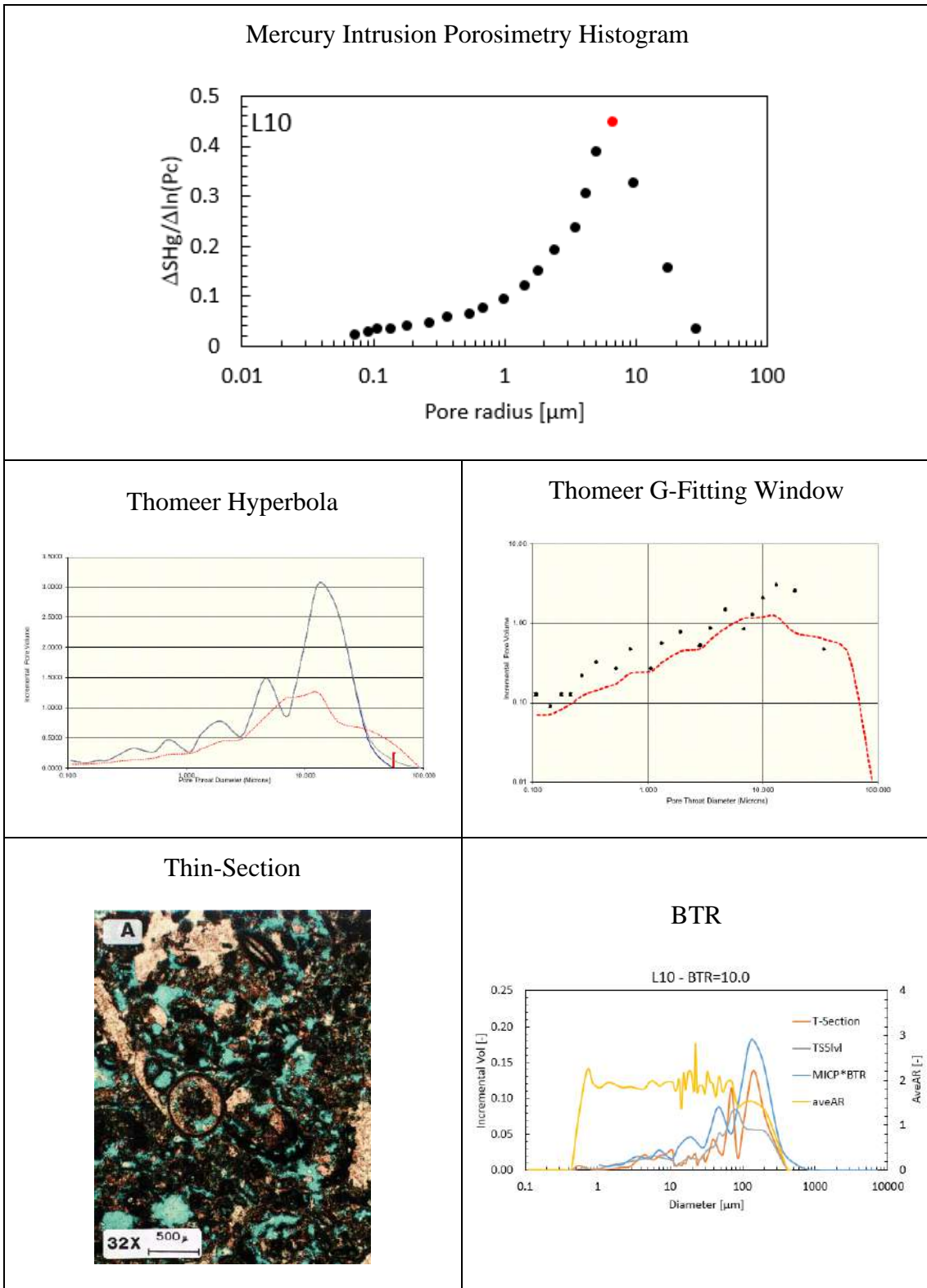
# Sample: L08



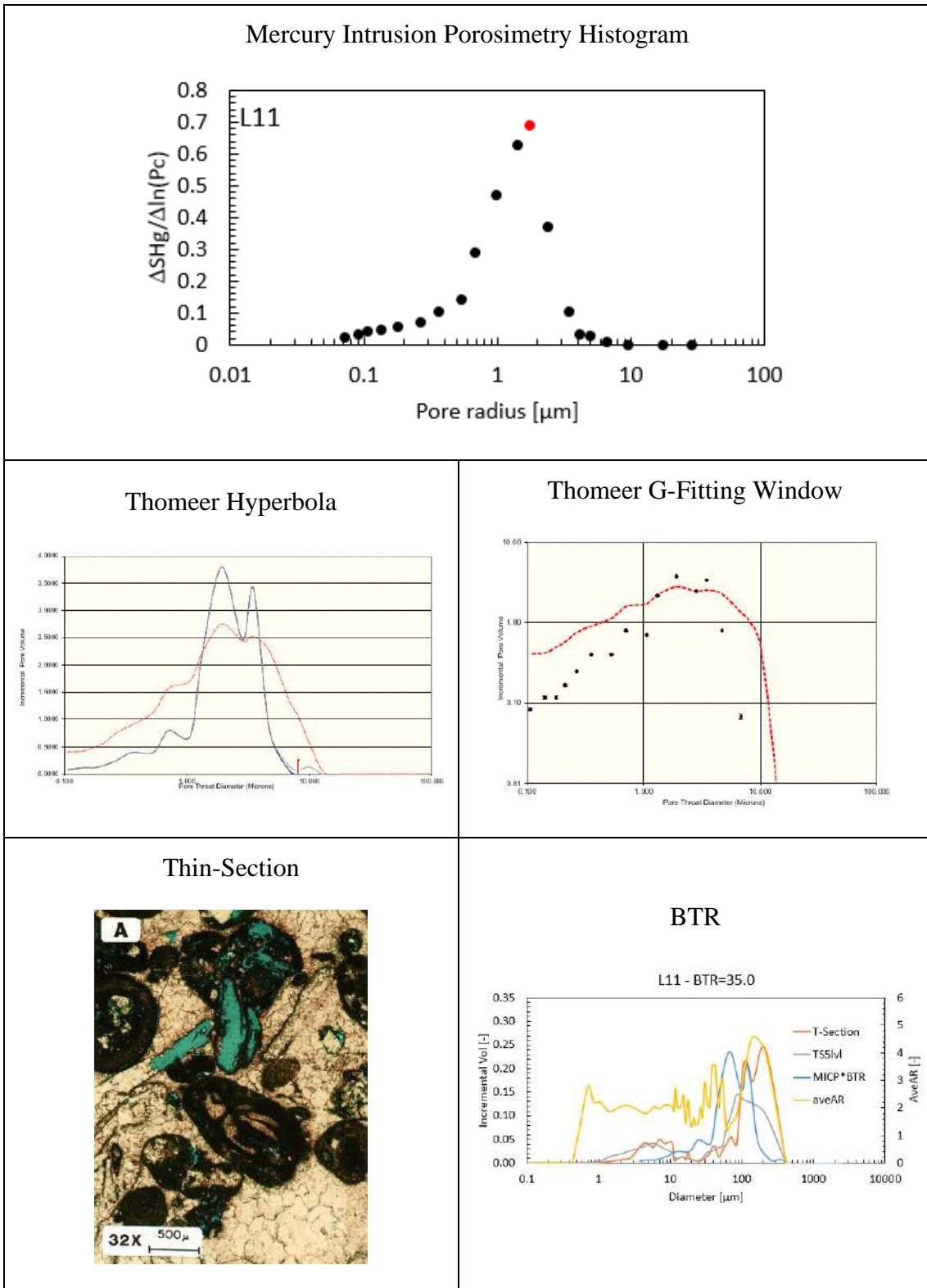
**Sample: L09**



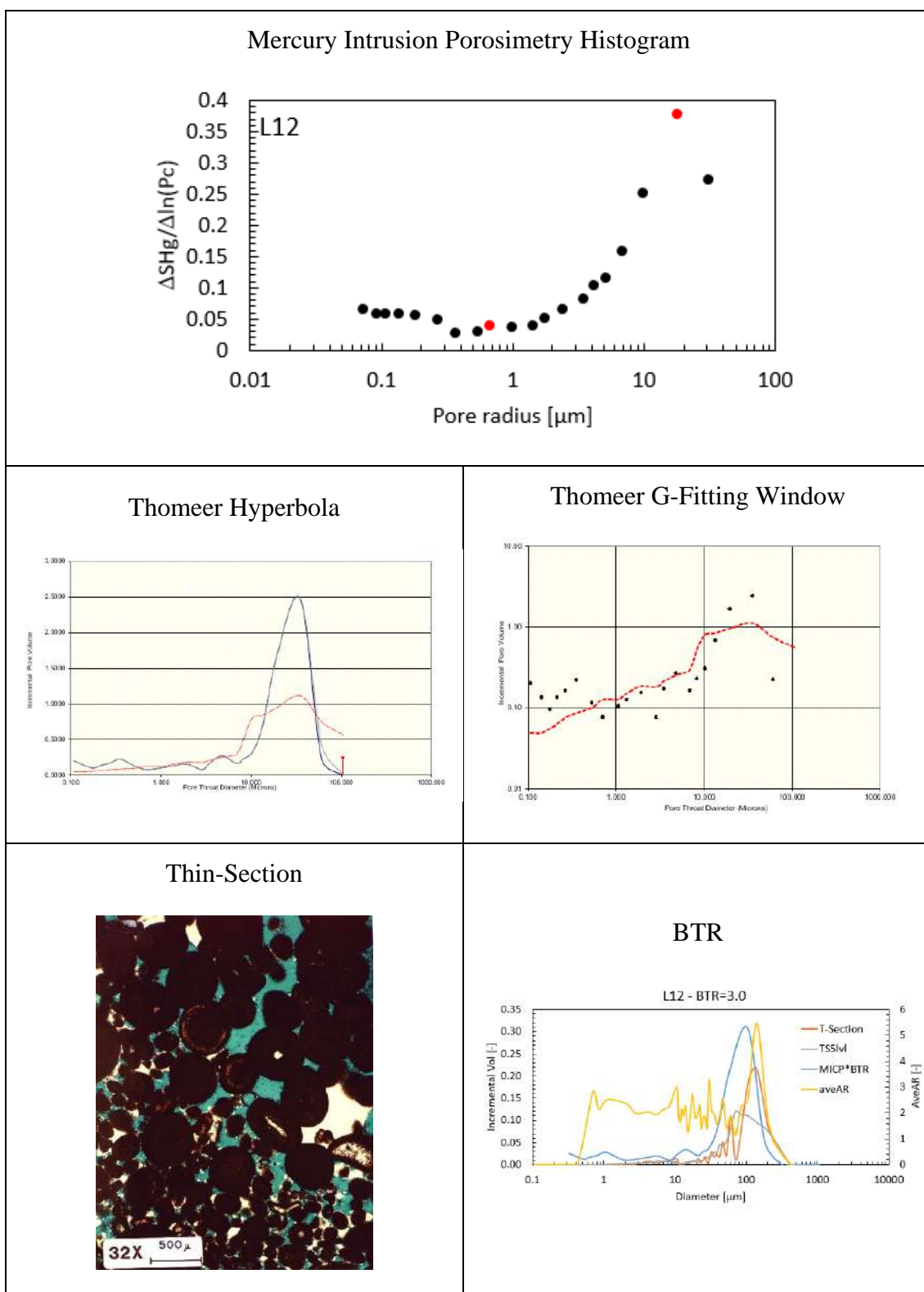
## Sample: L10



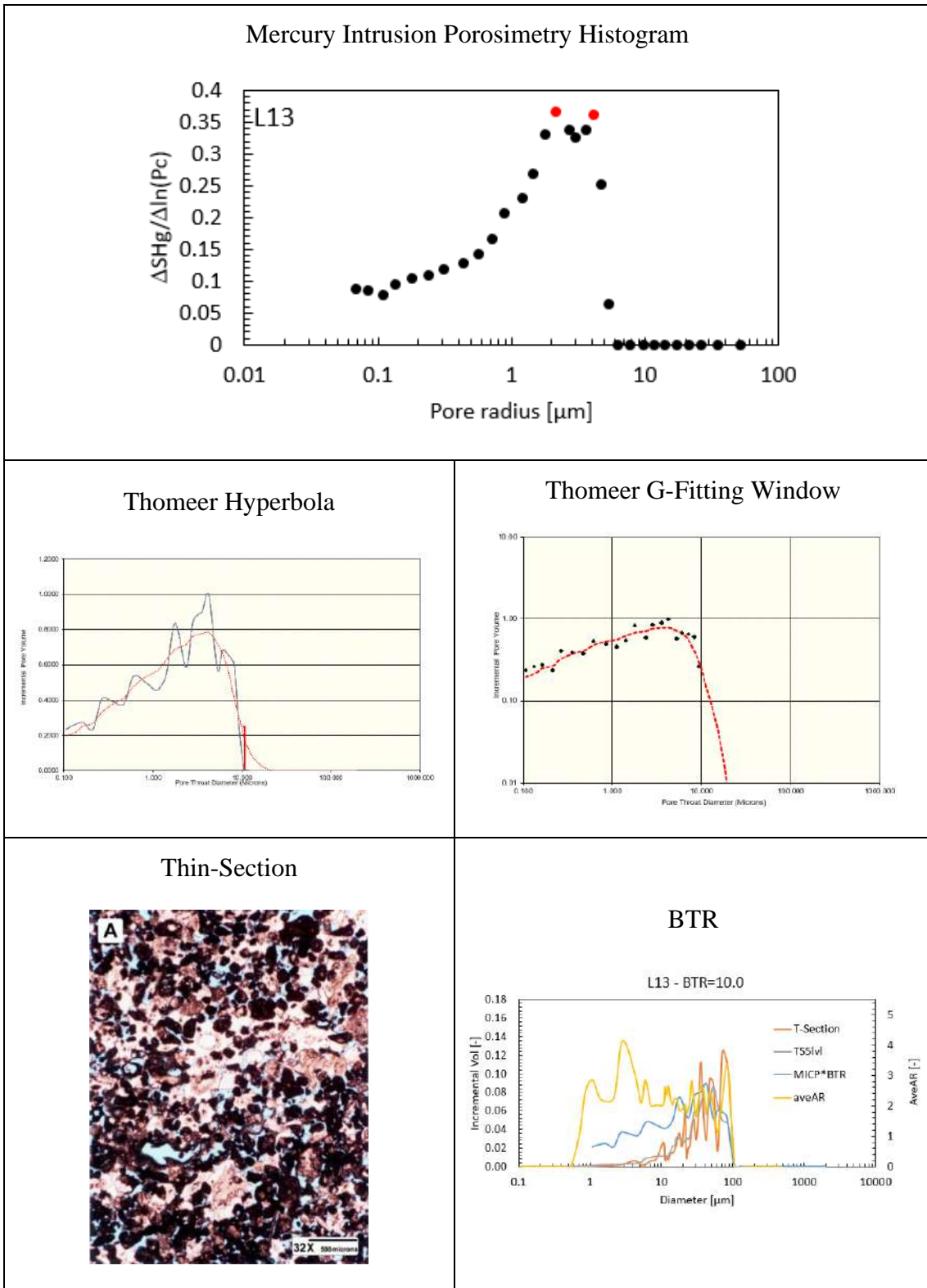
## Sample: L11



## Sample: L12

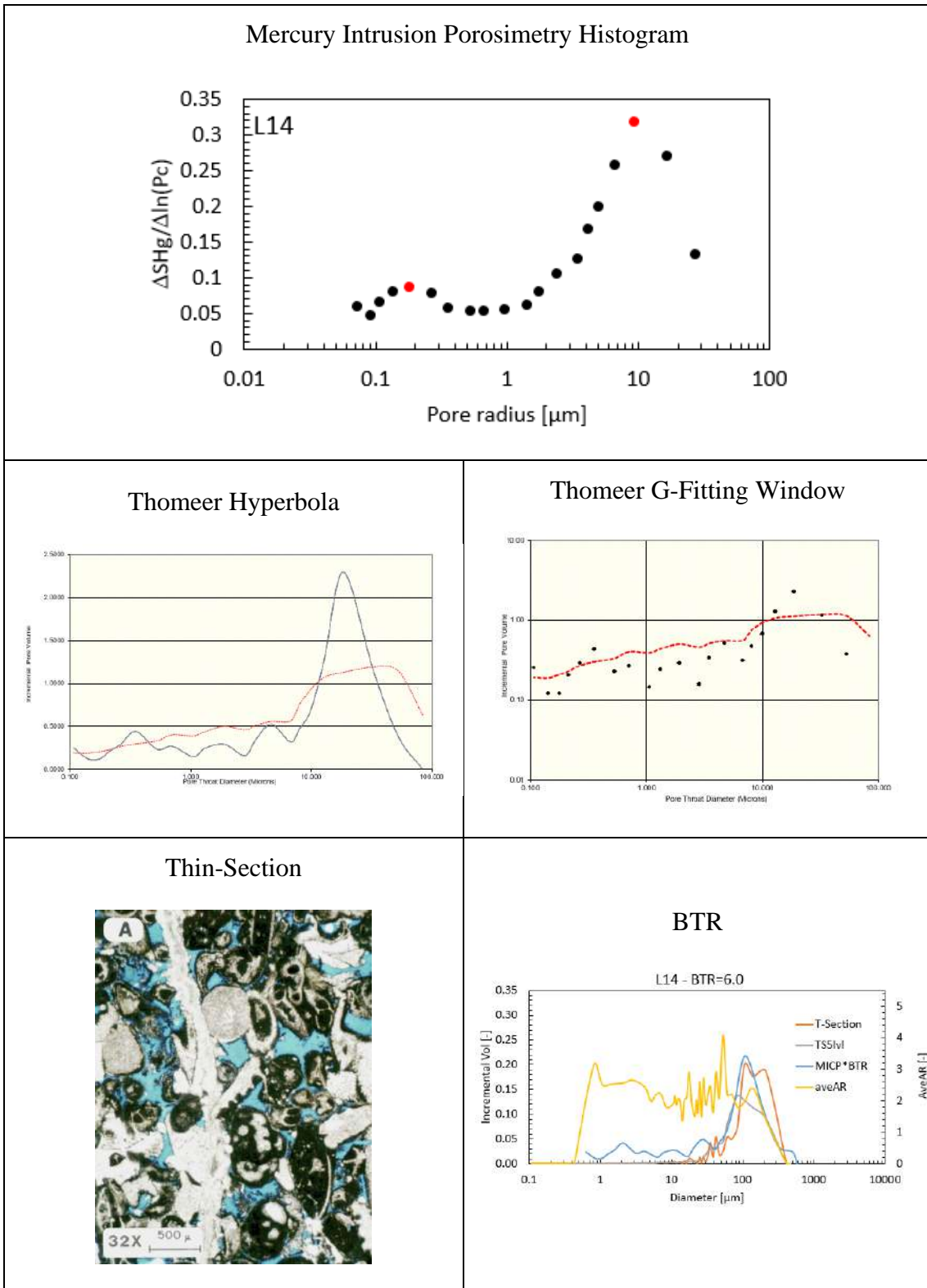


### Sample: L13

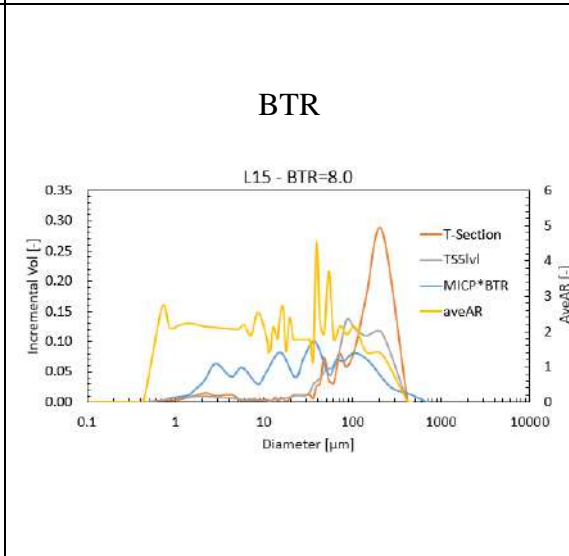
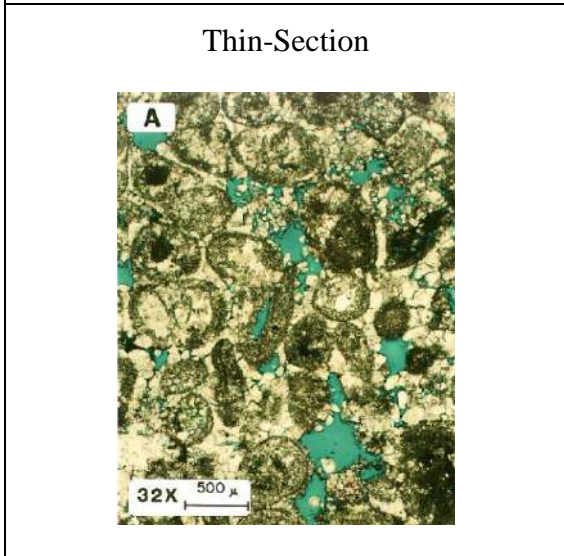
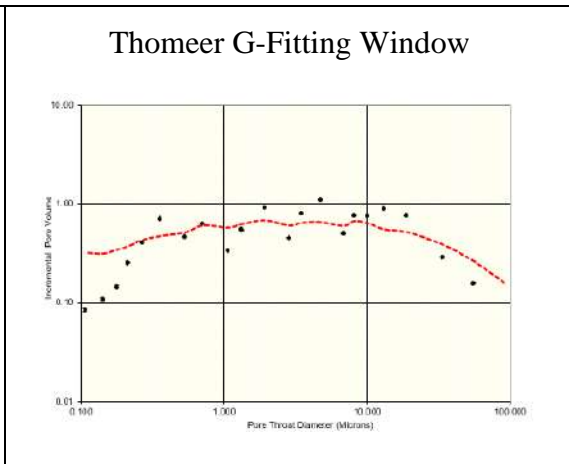
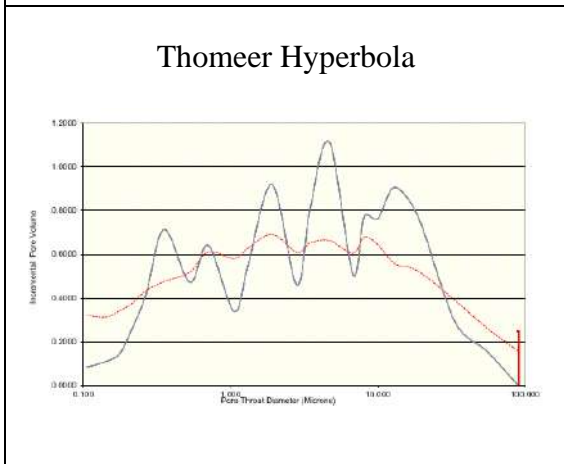
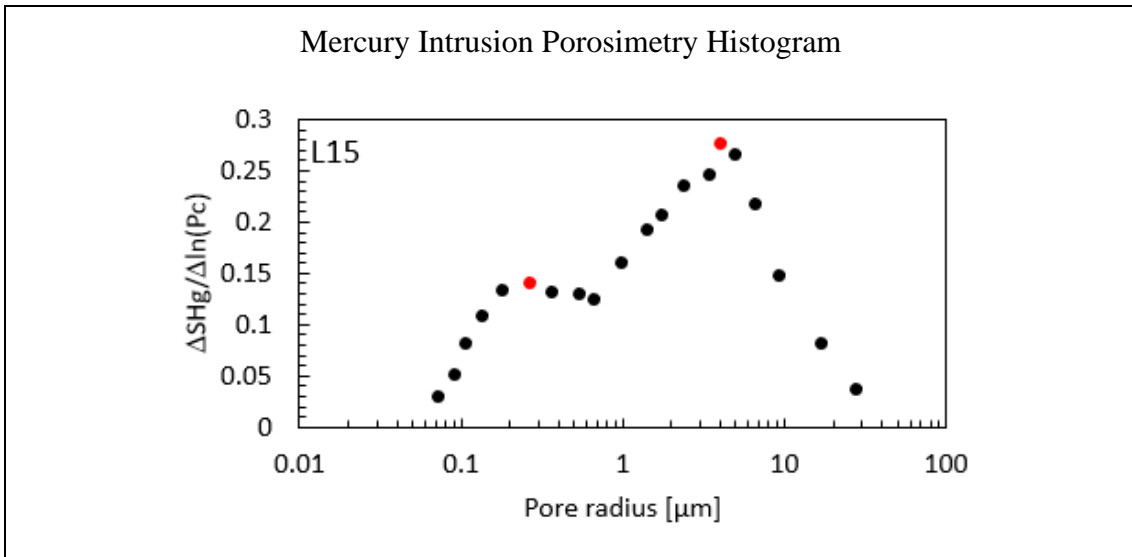




## Sample: L14

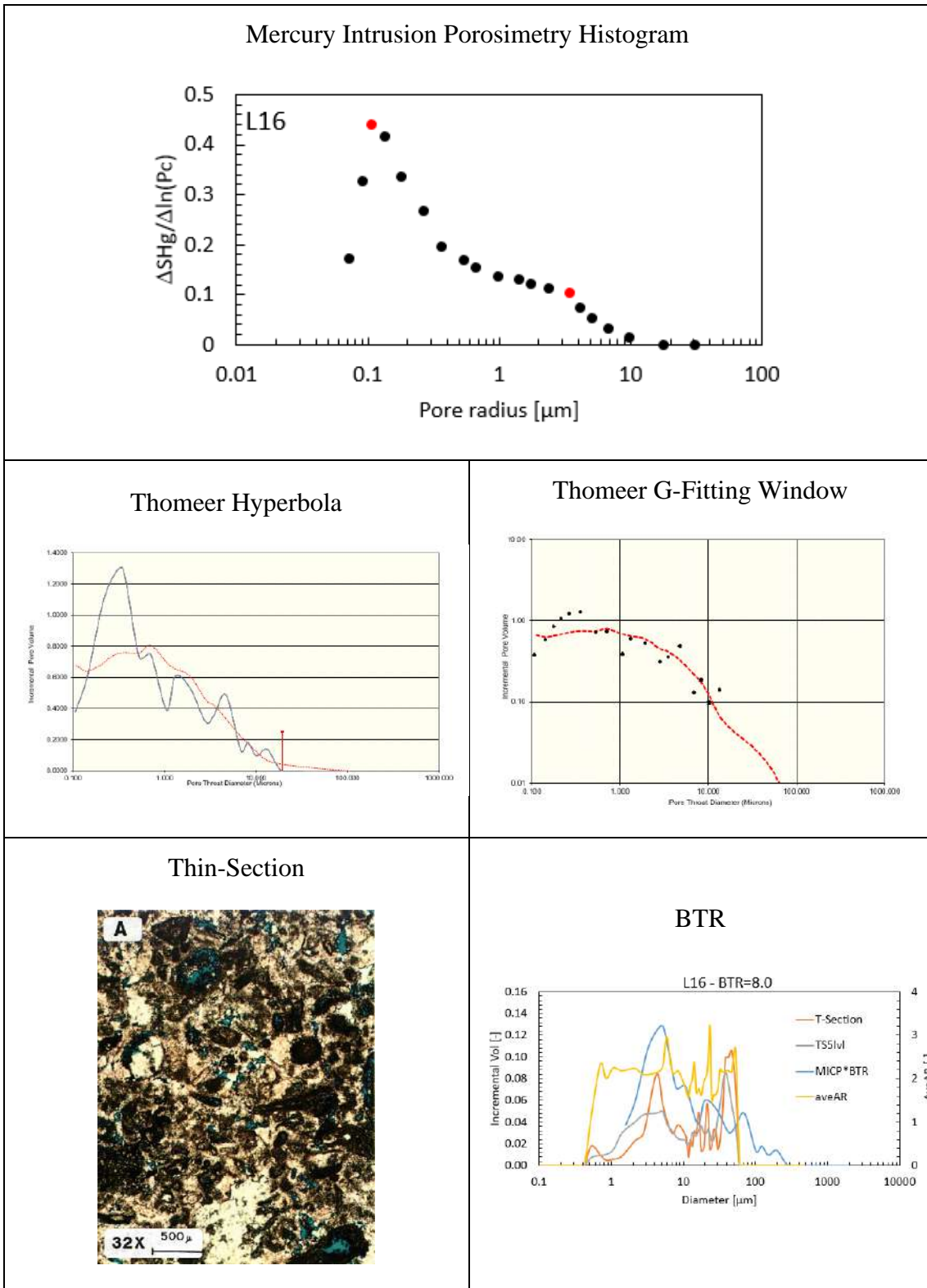


**Sample: L15**

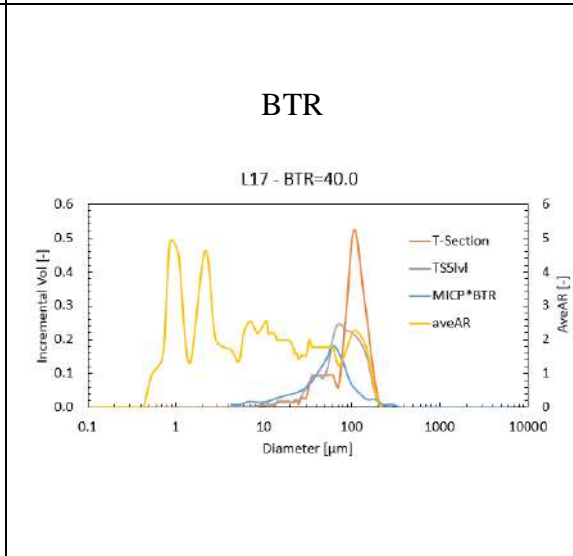
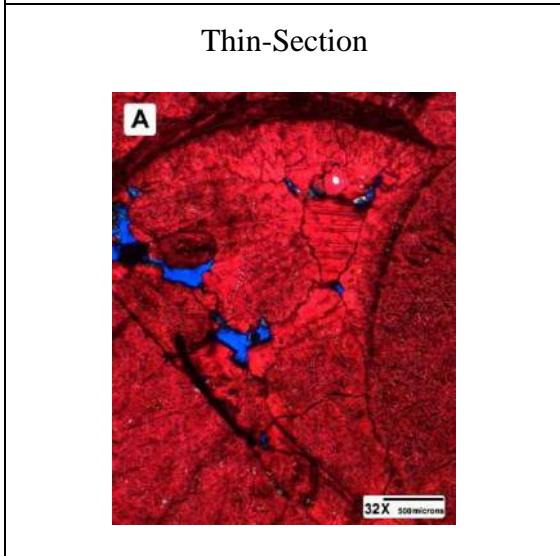
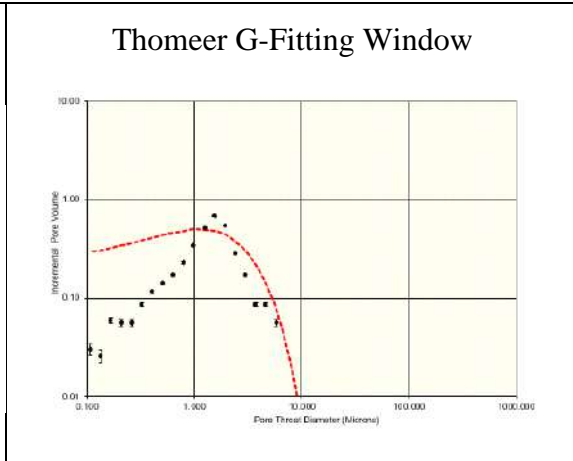
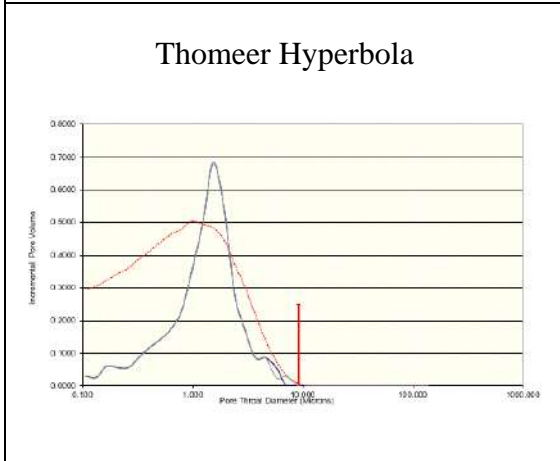
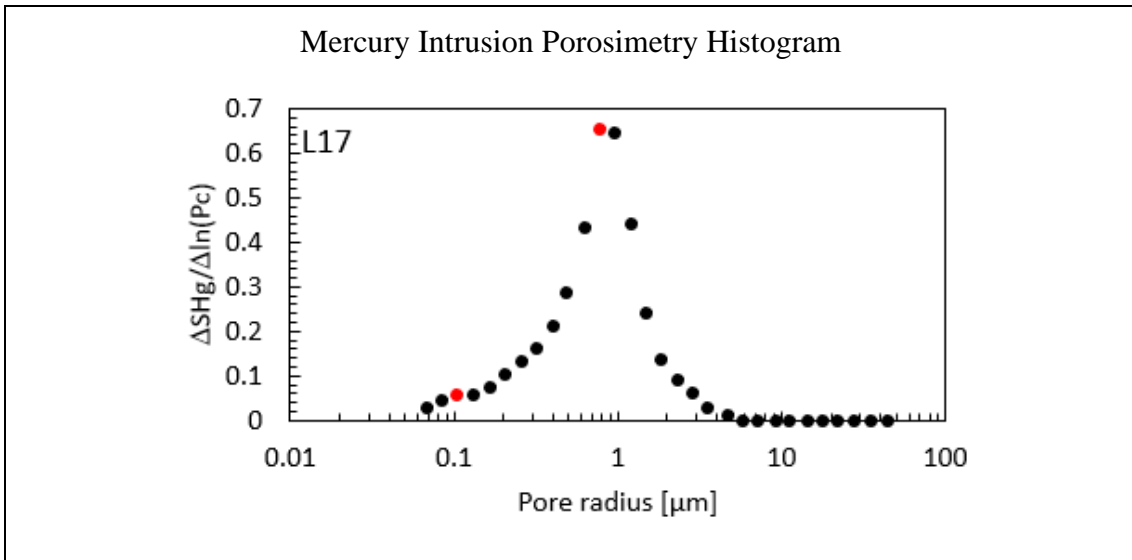




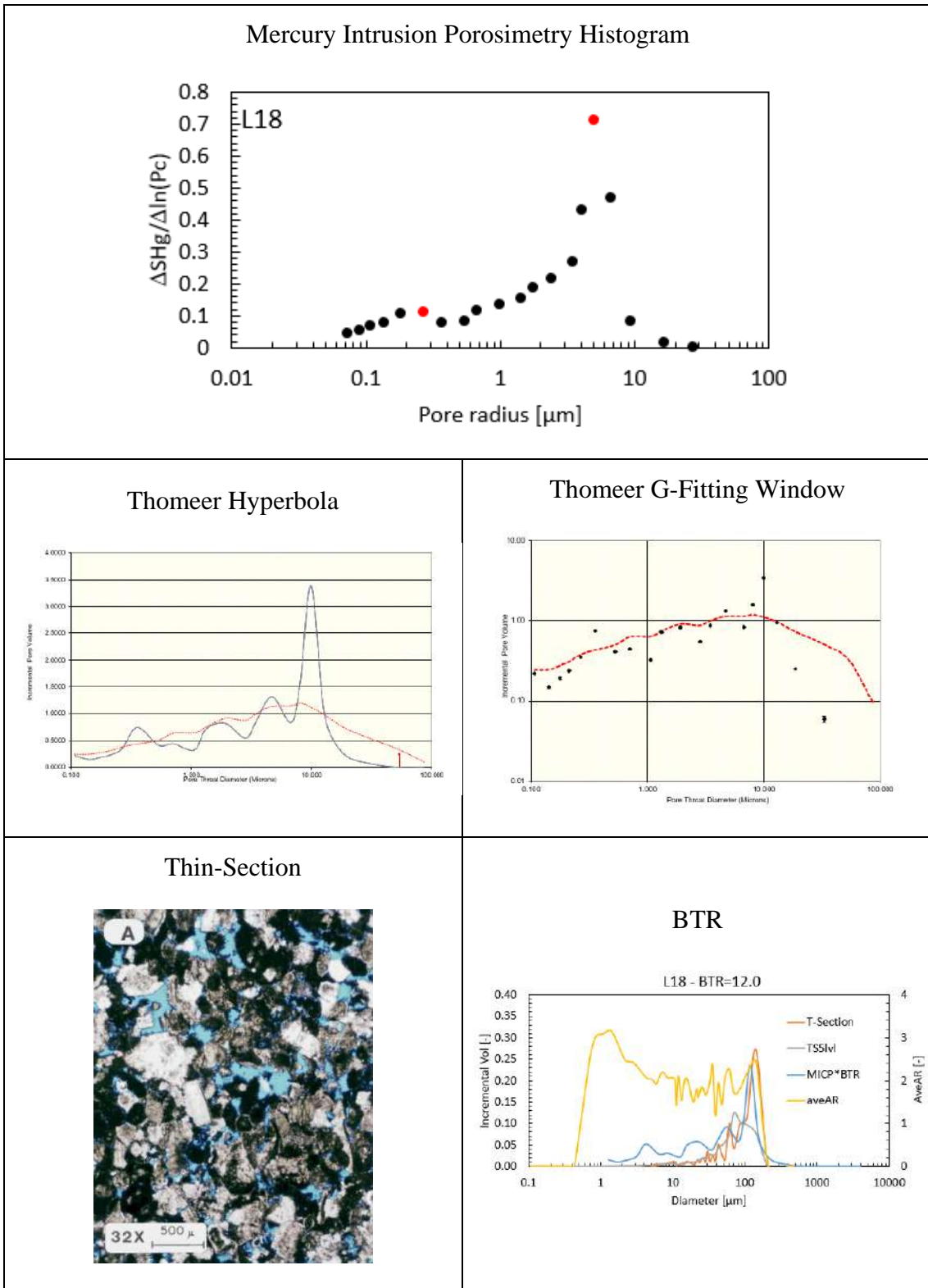
### Sample: L16



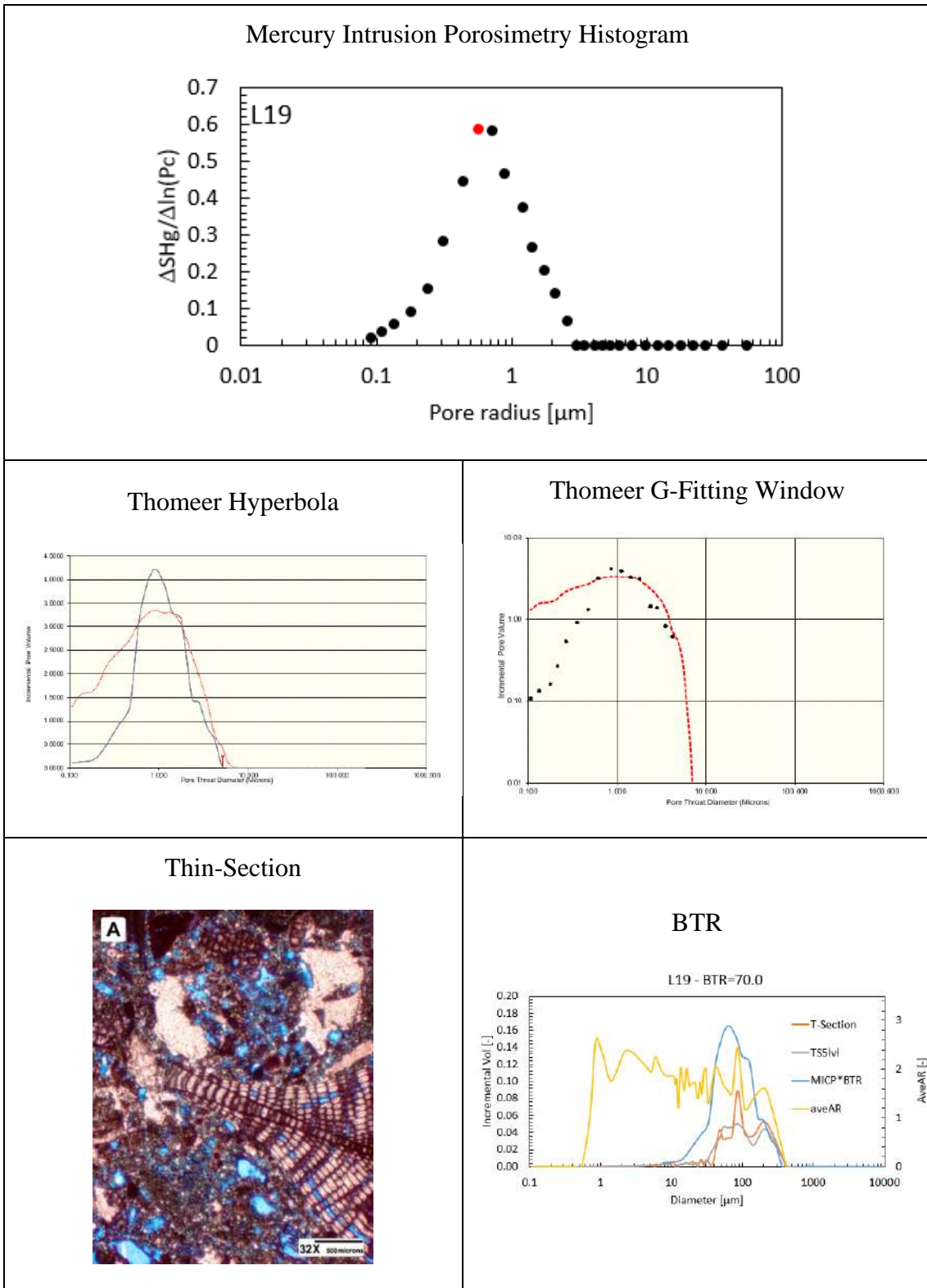
### Sample: L17



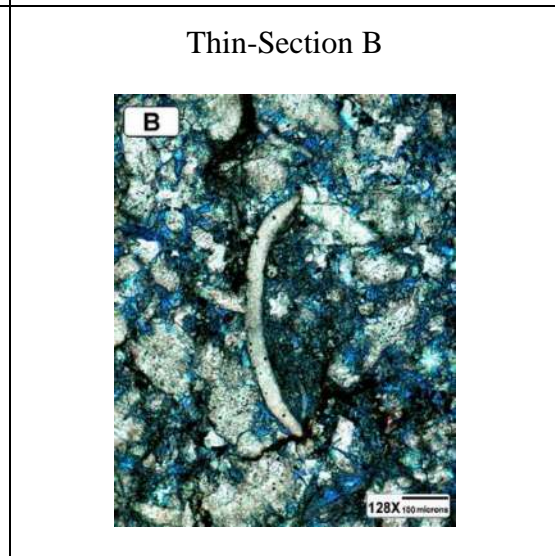
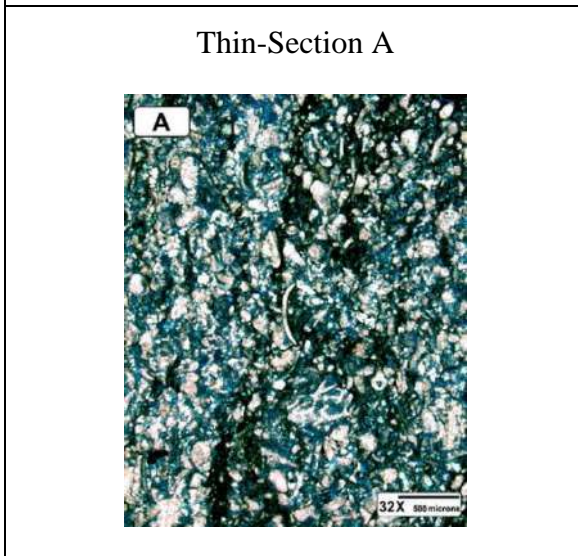
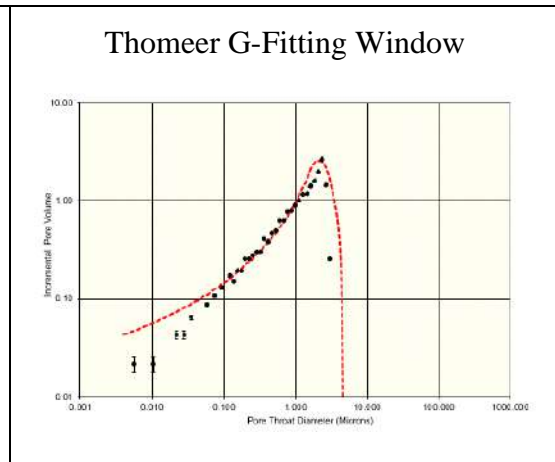
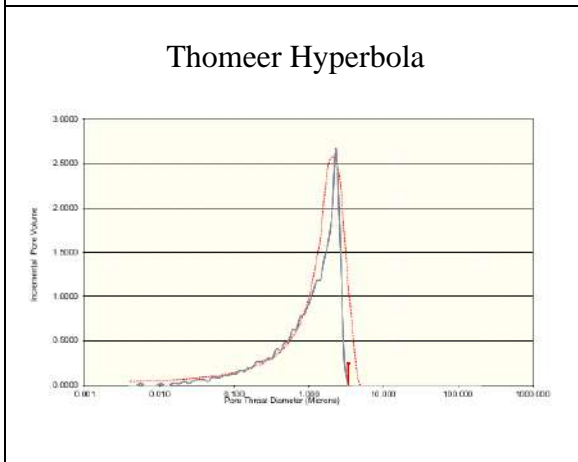
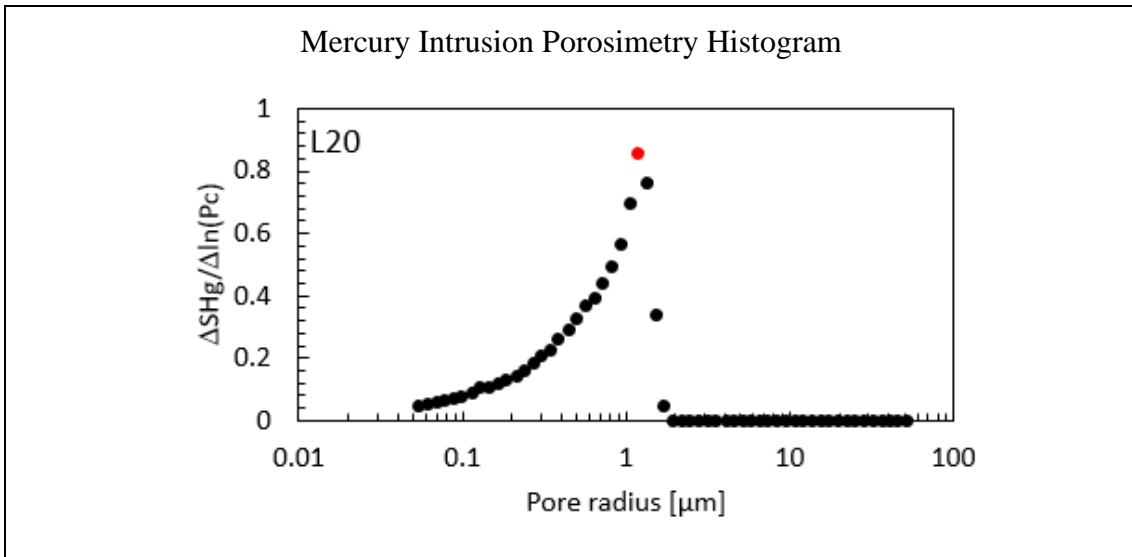
### Sample: L18

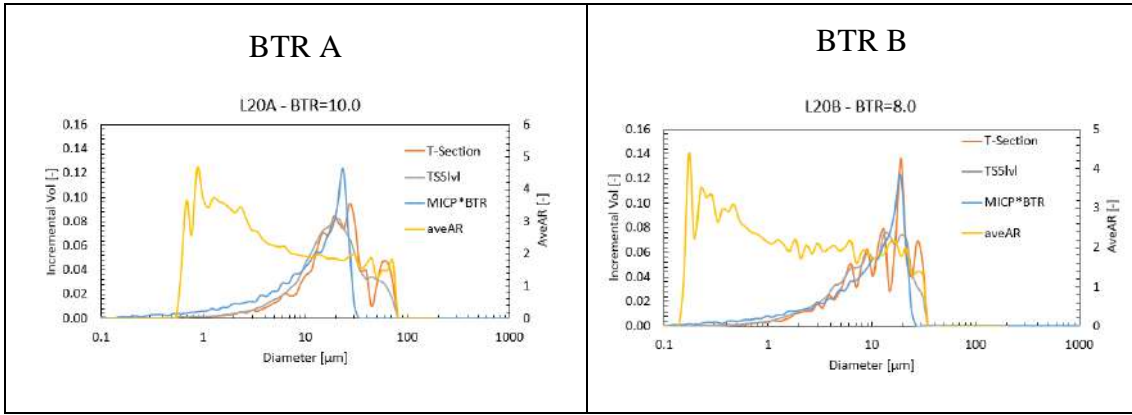


# Sample: L19



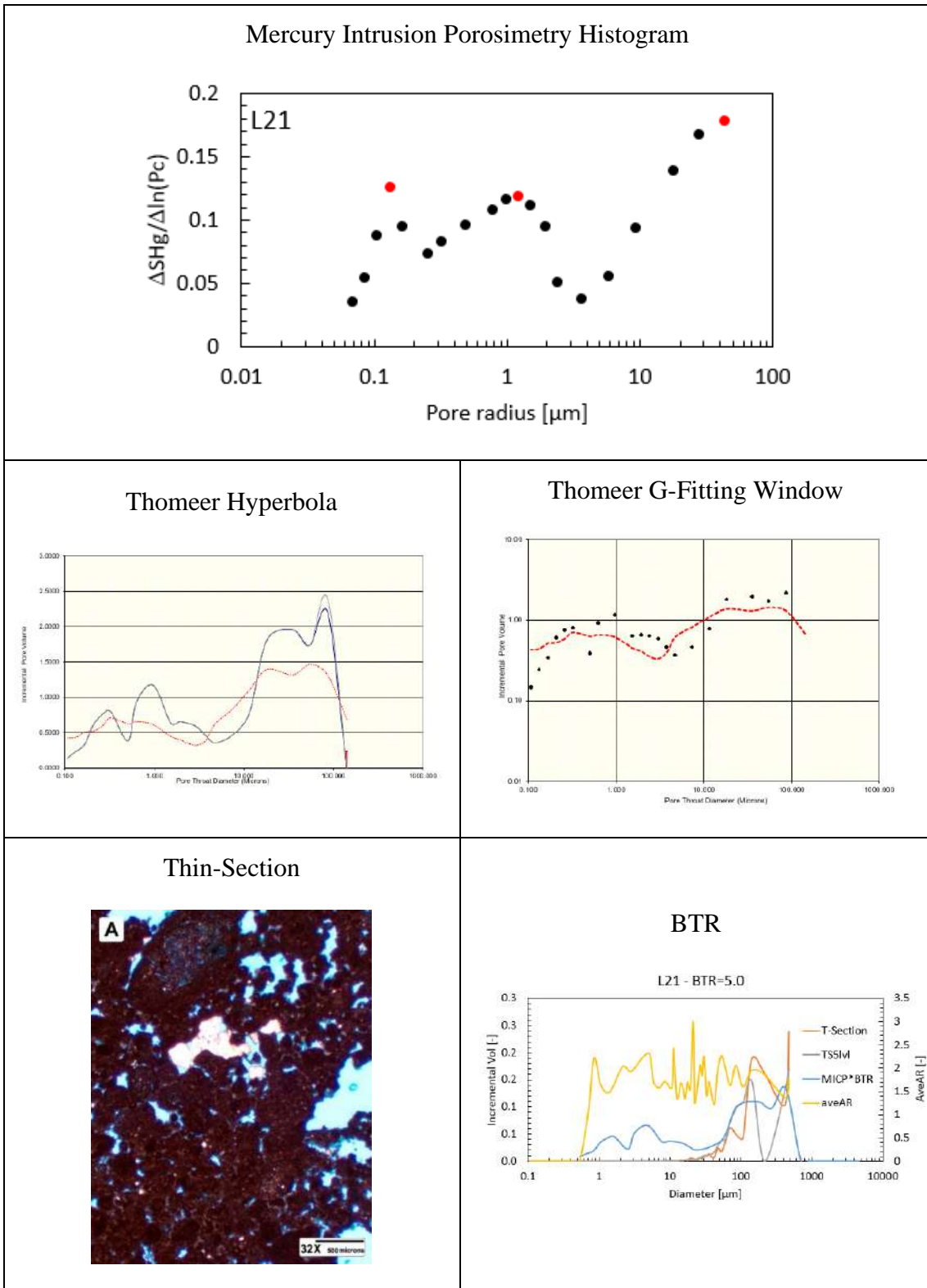
### Sample: L20



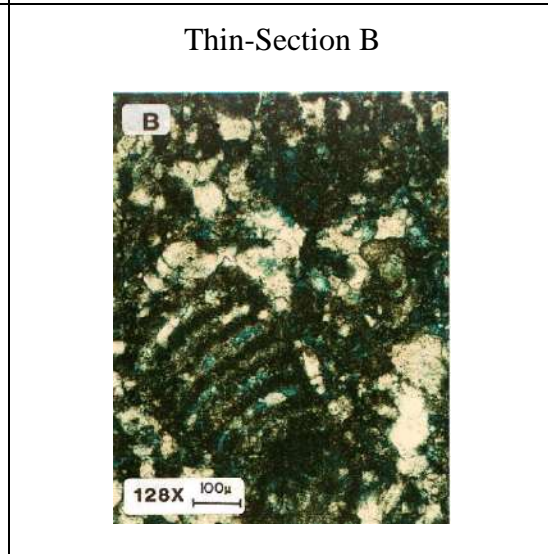
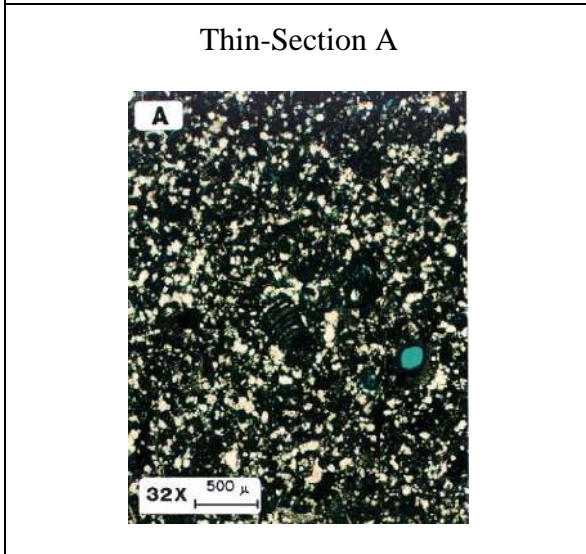
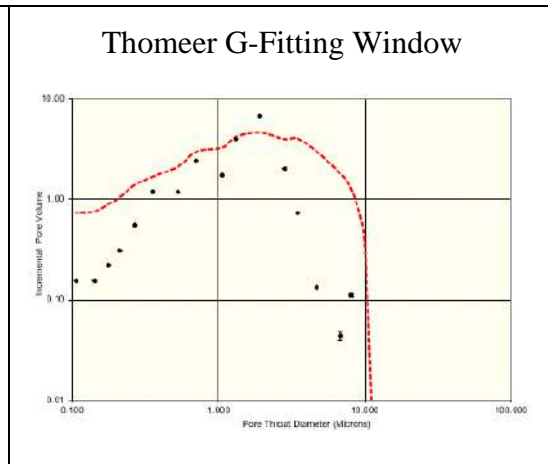
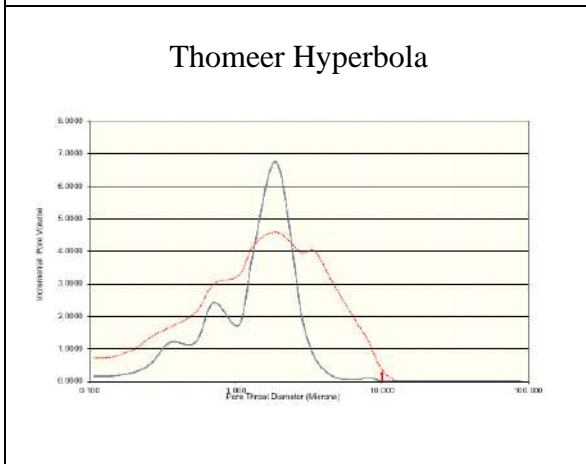
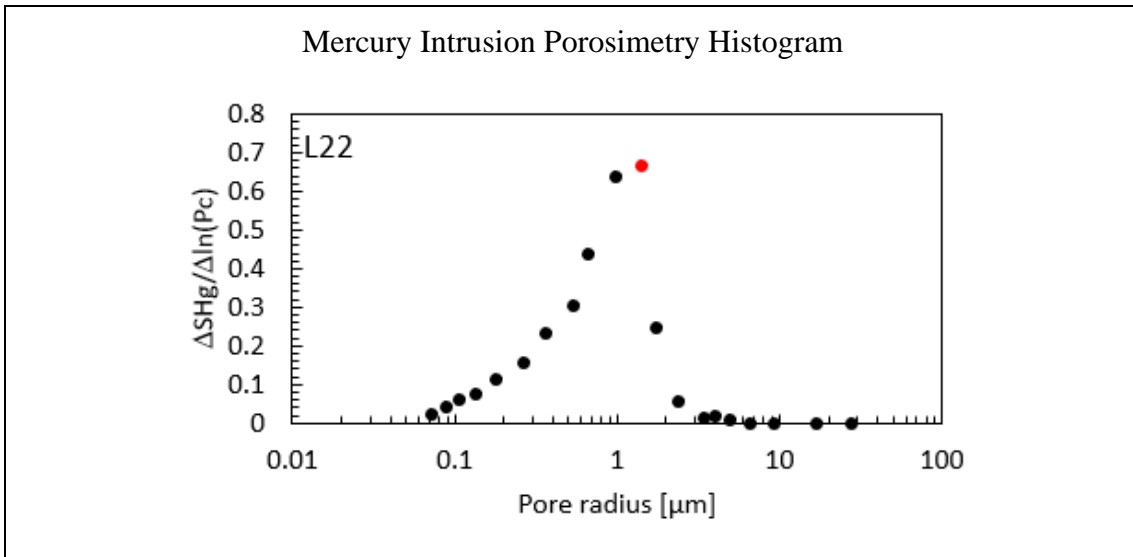




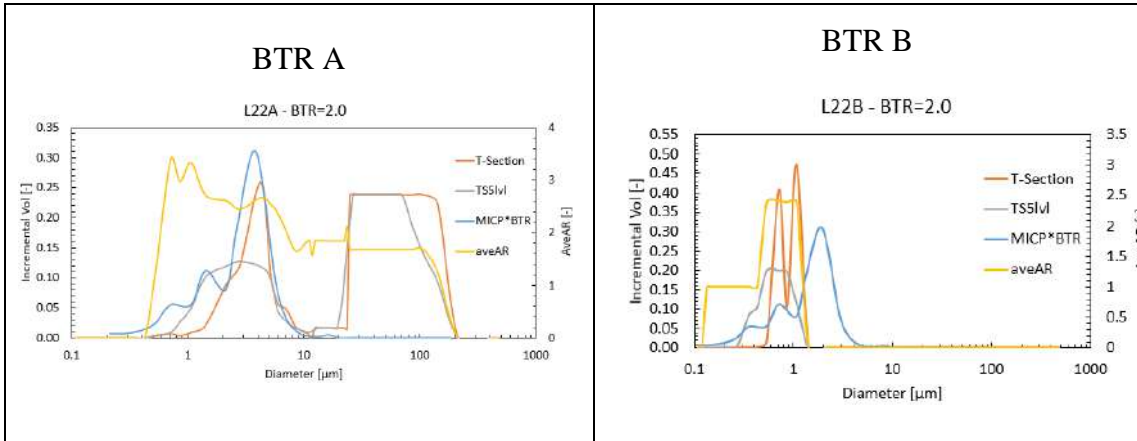
## Sample: L21



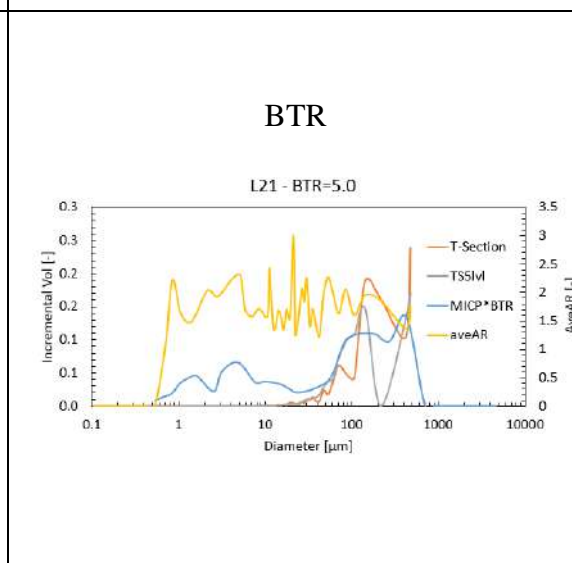
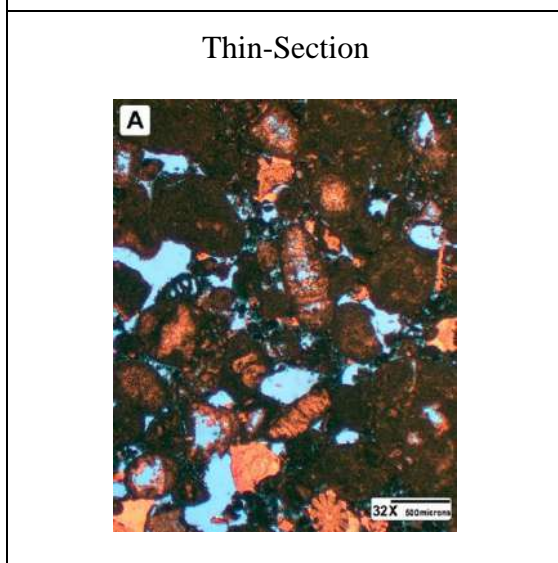
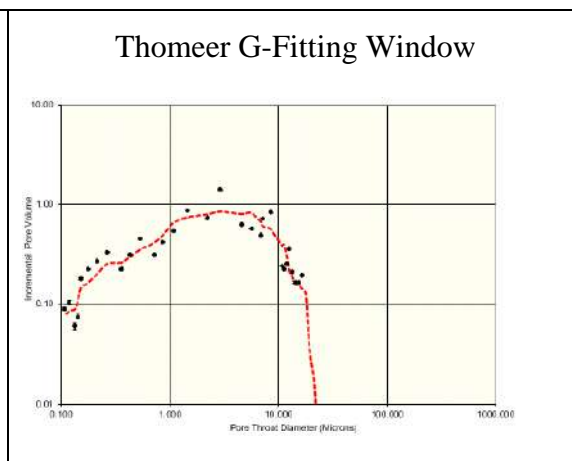
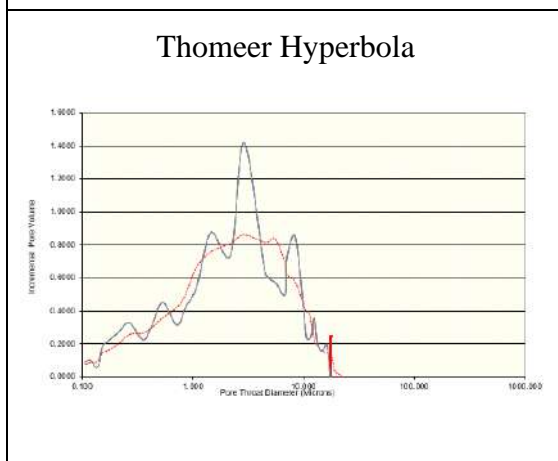
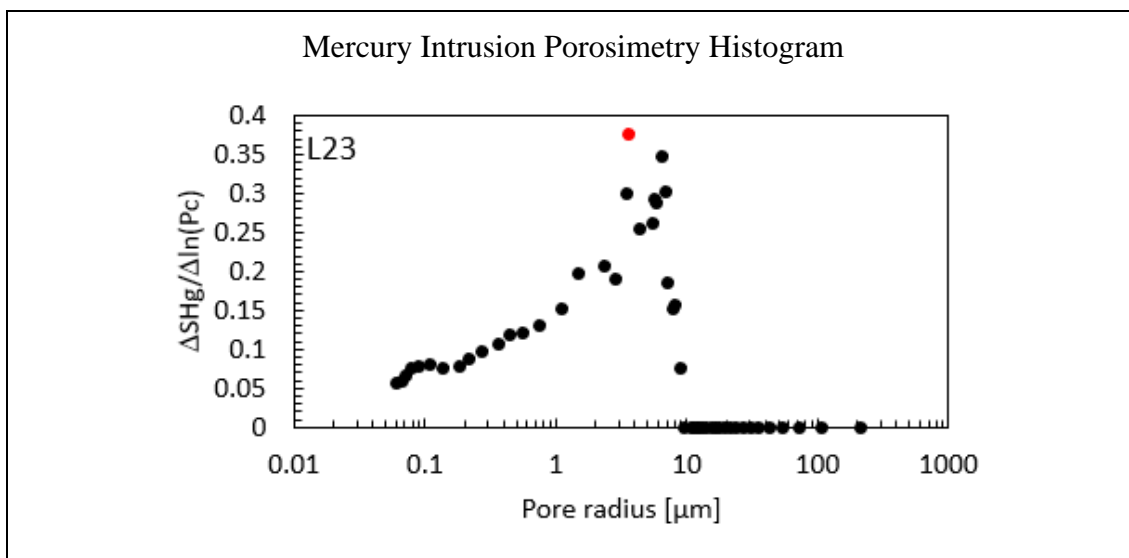
### Sample: L22



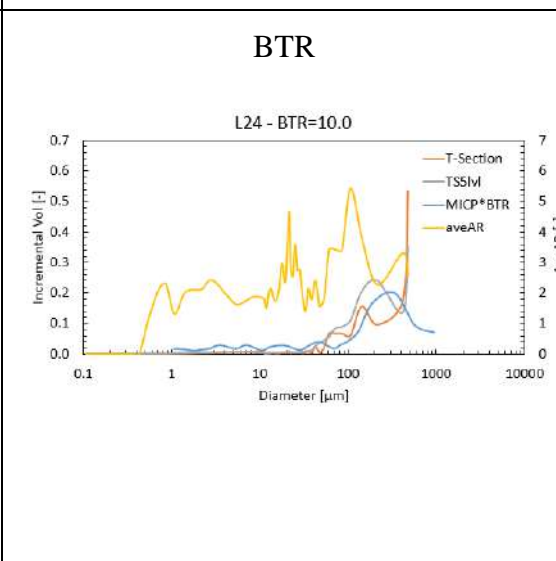
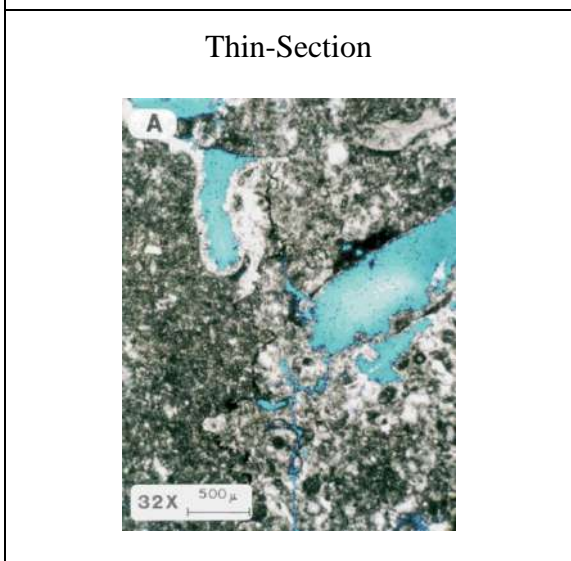
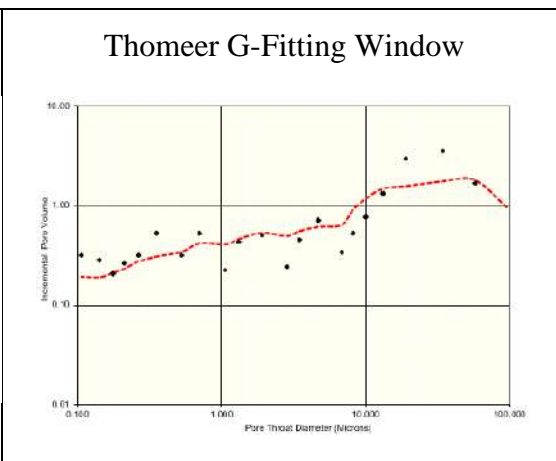
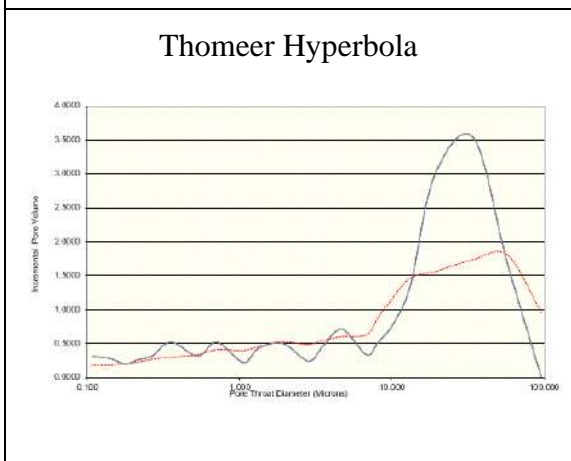
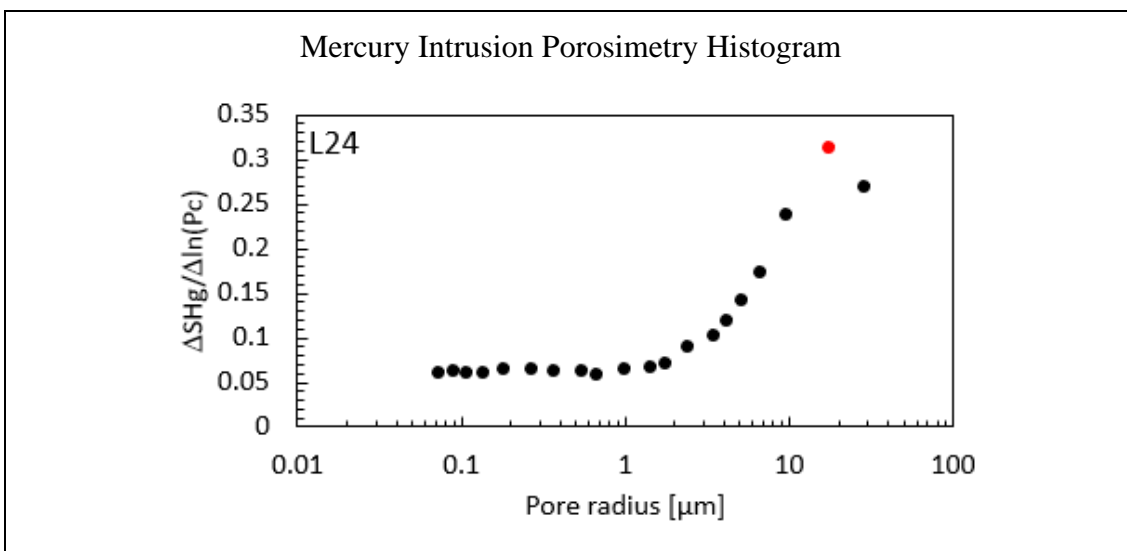




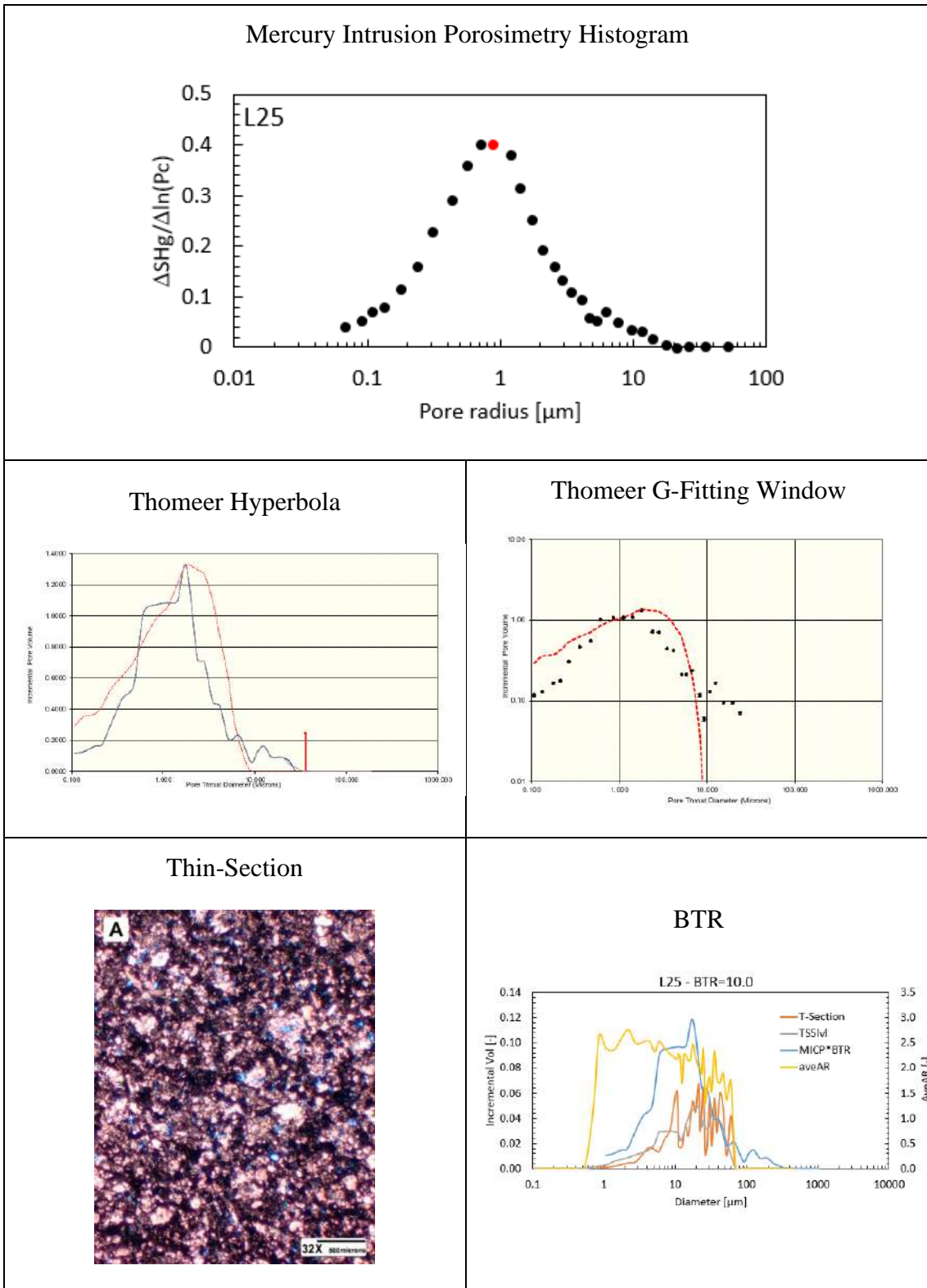
### Sample: L23



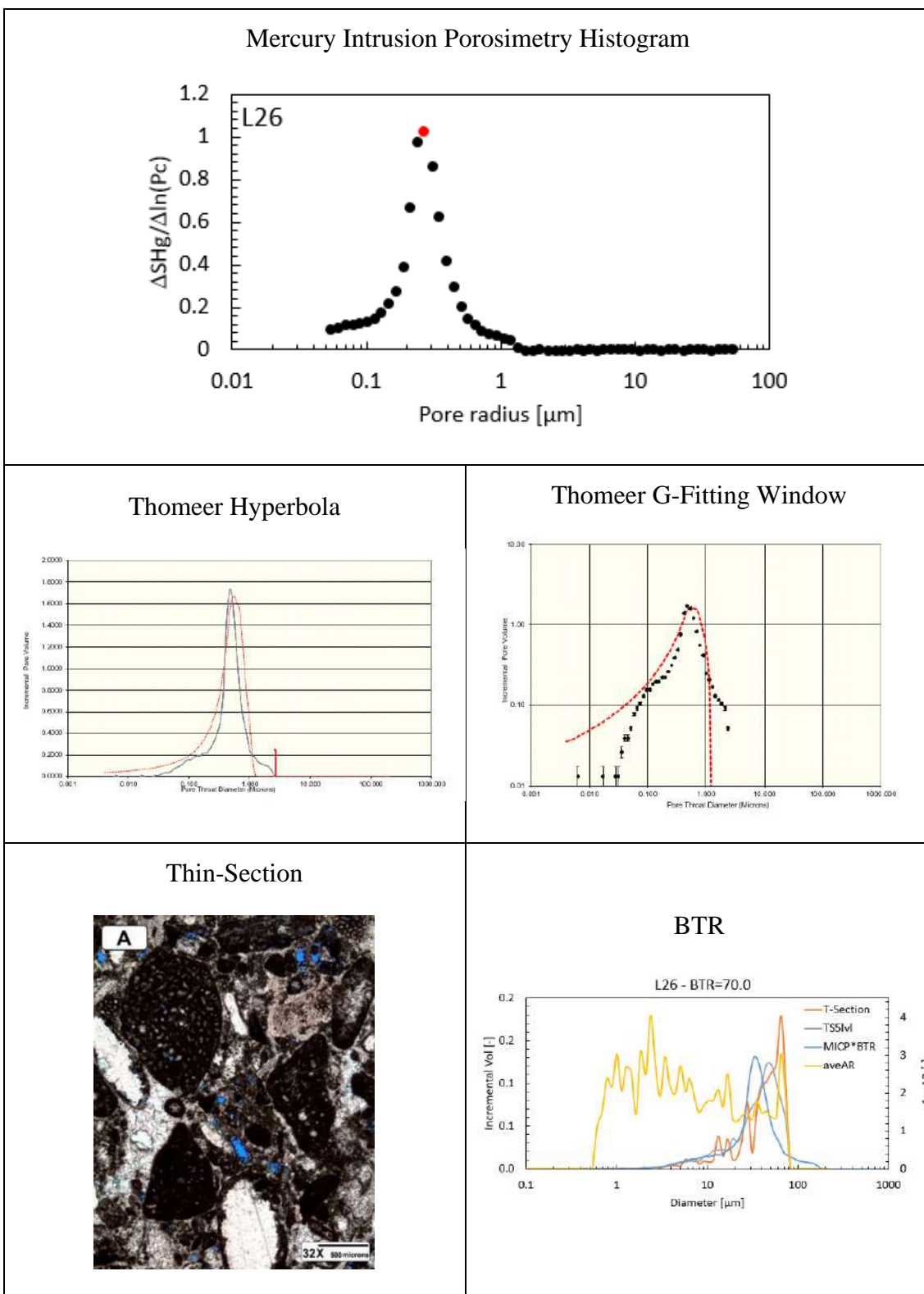
### Sample: L24



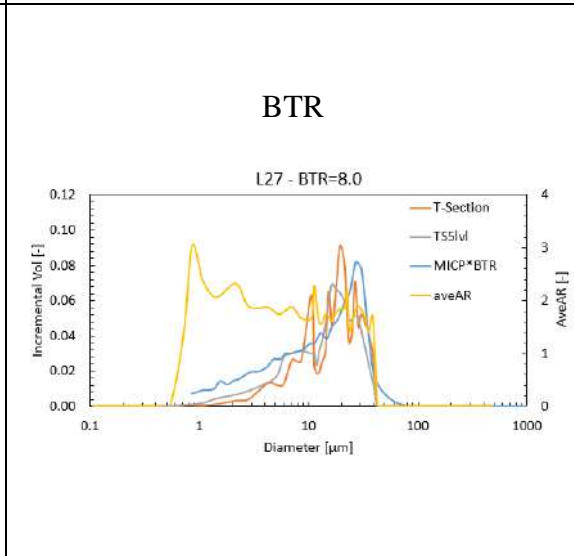
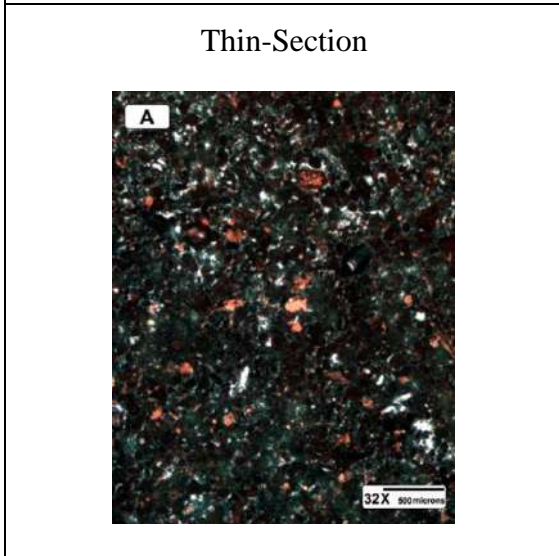
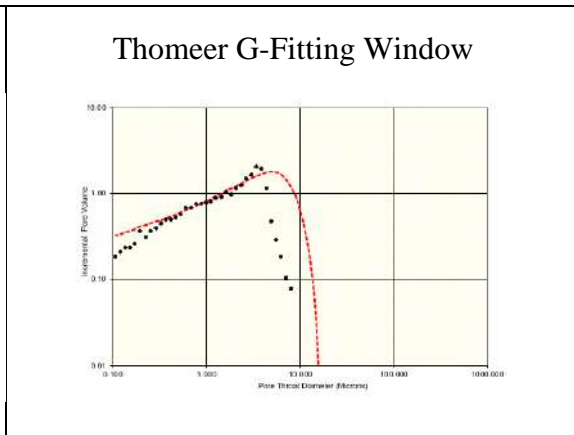
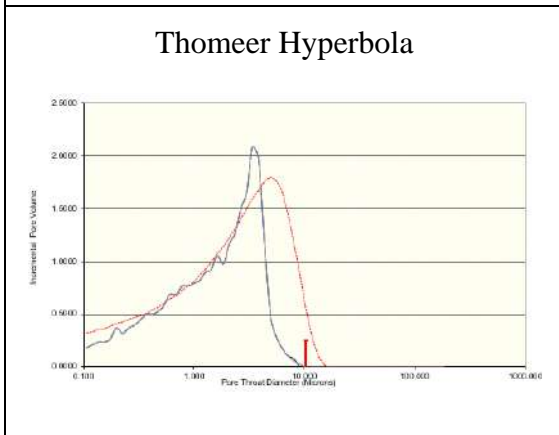
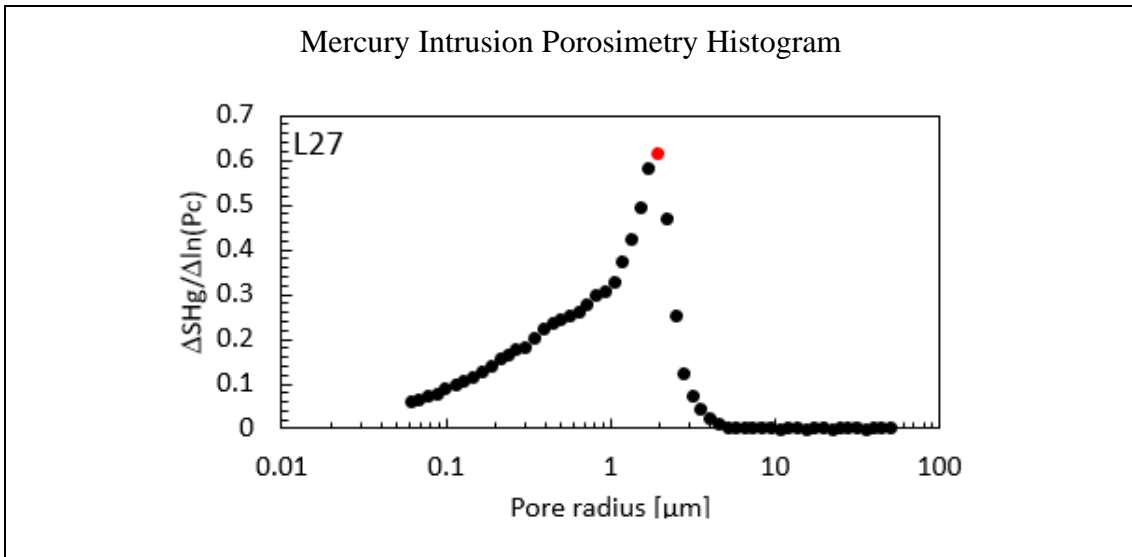
**Sample: L25**



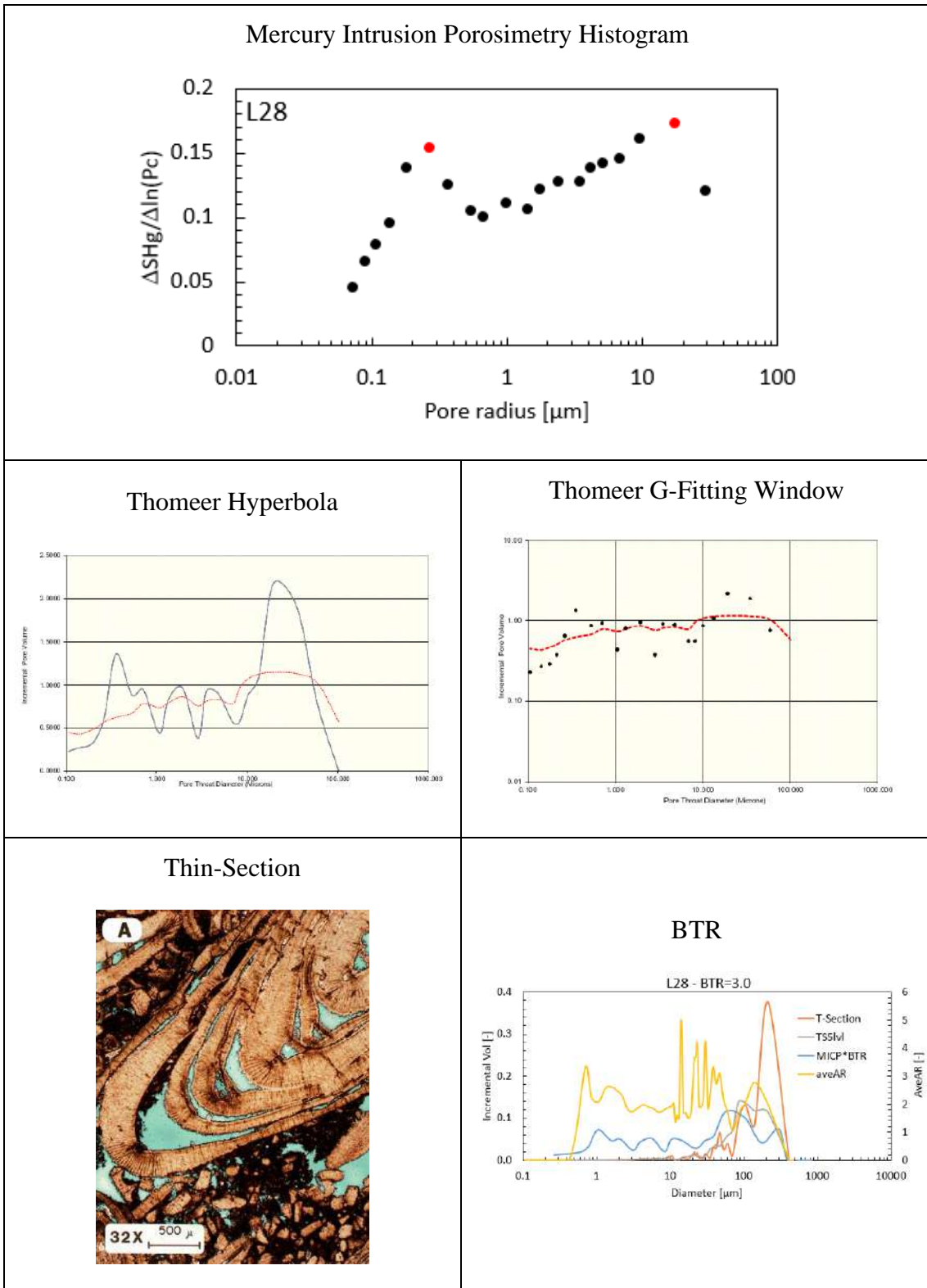
### Sample: L26



# Sample: L27



## Sample: L28





### Sample: L29

